



universität
wien

MASTERARBEIT / MASTER'S THESIS

Titel der Masterarbeit / Title of the Master's Thesis

„A comparison of the velocity fields of the warm ionized gas in massive elliptical galaxies in CALIFA and in cosmological zoom-in simulations“

verfasst von / submitted by

Jan Florian, BSc

angestrebter akademischer Grad / in partial fulfilment of the requirements for the degree of
Master of Science (MSc)

Wien, 2018 / Vienna 2018

Studienkennzahl lt. Studienblatt /
degree programme code as it appears on
the student record sheet:

A 066 881

Studienrichtung lt. Studienblatt /
degree programme as it appears on
the student record sheet:

Masterstudium Astronomie

Betreut von / Supervisor:

Univ.-Prof. Dipl.-Phys. Dr. Bodo Ziegler

We analyze the gas kinematics of massive, early-type galaxies, in simulations and observations, with respect to the effect of AGN feedback on certain quantitative irregularity parameters. Our observational data sample is drawn from the integral-field survey CALIFA, and our simulated data sample is based upon galaxies produced via the code SPHGal. We select objects (observed and simulated) which are currently affected by AGN feedback by means of WHAN analysis in order to compare them. With our simulated data, we have access to two separate simulation runs, the only difference between the two being the implementation of AGN feedback in one, but not the other, which allows us to cleanly isolate AGN feedback's effects. This separation, along with the ability to explore a galaxy's development over time, is not possible with our observational data, and so we use the simulations as a guide to the observations. We find that AGN feedback does increase the value of the irregularity parameters in our simulations, but that other phenomena, such as galactic mergers, can increase them as well. Furthermore, a galaxy which was affected by AGN feedback at some point in its past does not necessarily indicate this in the present. In all, high values for irregularity parameters may be but are not necessarily caused by AGN feedback.

Wir analysieren die Gas kinematik massereicher Galaxien frühen Typs in Simulationen und Beobachtungen in Bezug auf die Auswirkung von AGN-Feedback auf gewisse, quantitative Irregularitätsparameter. Wir beziehen unsere Beobachtungsdaten von der CALIFA-Survey und unsere simulierte Daten wurden anhand des Codes SPHGal produziert. Wir selektieren die Objekte, die momentan durch AGN-Feedback beeinflusst werden, indem wir WHAN-Analyse durchführen, damit wir sie vergleichen können. Mit unseren Simulationsdaten haben wir Zugang zu zwei unterschiedlichen Datensätzen, wobei der einzige Unterschied zwischen den beiden die vorhandene oder nichtvorhandene Implementierung von AGN-Feedback ist. Dies erlaubt es uns, die Auswirkungen von AGN-Feedback klar zu isolieren und diese strikte Trennung, gemeinsam mit der Möglichkeit, die zeitliche Entwicklung der simulierten Galaxien zu erforschen, ist mit den Beobachtungsdaten nicht möglich. Deswegen verwenden wir die Simulationsdaten als Orientierungshilfe für die Beobachtungsdaten. Wir stellen fest, dass AGN-Feedback tatsächlich die Werte der Irregularitätsparameter in den Simulationen erhöht, aber dass andere Phänomene wie z.B. Merger dies auch bewirken können. Desweiteren gibt eine Galaxie, die irgendwann in ihrer Vergangenheit AGN-Feedback ausgesetzt wurde, in der Gegenwart nicht unbedingt Anzeichen darauf. Insgesamt können hohe Werte der Irregularitätsparameter Anzeichen für AGN-Feedback sein, sind dies aber nicht notwendigermaßen.

Contents

1	Introduction, Methods, and Motivation	7
1.1	Introduction	7
1.2	Kinematics	9
1.2.1	Photometry	9
1.2.2	From V/σ to λ_R	13
1.2.3	Generalizing Photometry to Describe Features of Velocity Maps	16
1.2.4	Analysis Methods	18
1.3	Nebular Emission	21
1.3.1	BPT Theory	21
1.3.2	WHAN Theory	24
1.4	Thesis Structure	26
2	Simulations	27
2.1	Introduction to Numerical Galaxy Simulations	27
2.2	Physical Processes	32
2.2.1	Gravity	32
2.2.2	Hydrodynamics	33
2.2.3	Thermal and Chemical Evolution	36
2.2.4	Star Formation, Evolution, and Feedback	37
2.2.5	Black Hole Growth and Feedback	40
2.3	SPHGal	44
2.4	Simulation Sample and Methods	46
2.5	Warm Gas Mass Fraction and Surface Density Profiles	49
2.6	Results from Kinematic Analysis	51
2.6.1	Irregularity Parameters and λ_R	51
2.6.2	Histories	58
2.6.3	Residual Asymmetries	61
2.7	Results from Nebular Emission Analysis	62
2.7.1	WHAN Analysis	62
2.7.2	NII/ $H\alpha$ profiles	63
3	Observations	64
3.1	IFS Surveys	64
3.2	CALIFA	67
3.3	Observational Sample and Methods	68
3.4	Results from Kinematic Analysis	69
3.4.1	Irregularity Parameters and λ_R	69
3.4.2	Residual Asymmetries	79
3.5	Results from Nebular Emission Analysis	80
3.5.1	WHAN Analysis	80
3.5.2	EW($H\alpha$) and NII/ $H\alpha$ profiles	80

4	Comparison and Discussion	82
4.1	Comparison and Discussion of Kinematics Results	82
4.1.1	Irregularity Parameters and λ_R	82
4.1.2	Residual Asymmetries	89
4.2	Comparison and Discussion of Nebular Emission Results	91
4.2.1	EW($H\alpha$) and NII/ $H\alpha$ profiles	91
5	Summary and Conclusion	92
5.1	Summary	92
5.2	Conclusion	93
5.3	Acknowledgements	94
6	Appendix	95
6.1	2D info on all studied simulated galaxy snapshots	95
6.2	2D info on all studied CALIFA galaxies	106

List of Figures

1	“Disky” vs. “boxy” isophotes	10
2	Five classes of stellar kinematics	12
3	$(V/\sigma, \epsilon)$ and (λ_R, ϵ) diagrams	15
4	Application of kinemetry	17
5	BPT diagram	22
6	Sample WHAN diagram	25
7	Time evolution of physical parameters in simulations	30
8	Dynamic range in simulations	31
9	Comparison of recent late-type galaxy simulations	35
10	Warm gas mass fractions for simulated galaxies at $z=0.0$	50
11	Warm gas mass fractions for simulated galaxies at $z=0.5$	50
12	Warm gas surface density profiles for simulated galaxies	50
13	Radial variation of irregularity parameters for simulated galaxies	53
14	Histograms of λ_R and irregularity parameters for simulated galaxies	54
15	λ_R vs. irregularity parameters for simulated galaxies	55
16	Combinations of irregularity parameters for simulated galaxies	56
17	Time evolution of halos 0094, 0204, 0215, 0227, 0290, 0305	60
18	Histograms of the residual asymmetries for simulated galaxies	61
19	Radial $[\text{N II}]/\text{H}\alpha$ profiles for simulated galaxies	63
20	Radial variation of irregularity parameters for observed galaxies	71
21	Histograms of λ_R and irregularity parameters for observed galaxies	72
22	λ_R vs. irregularity parameters for observed galaxies	73
23	Combinations of irregularity parameters for observed galaxies	74
24	Histograms of the residual asymmetries for observed galaxies	79
25	WHAN diagram for observational data	80
26	Radial $\text{EW}(\text{H}\alpha)$ profiles for simulated galaxies	81
27	Radial $\text{NII}/\text{H}\alpha$ profiles for observed galaxies	81
28	Histograms of λ_R and irregularity parameters for simulated and observed galaxies (Simulations not WHAN-separated)	85
29	Histograms of λ_R and irregularity parameters for simulated and observed galaxies (Simulations WHAN-separated)	86
30	λ_R vs. irregularity parameters for simulated and observed galaxies	87
31	Combinations of irregularity parameters for simulated and observed galaxies	88
32	Histograms of the residual asymmetries for simulated and observed galaxies (Simulations non-WHAN separated)	89
33	Histograms of the residual asymmetries for simulated and observed galaxies (Simulations WHAN-separated)	89

List of Tables

1	Parameter space for nebular-emission models in simulations	48
2	Means and standard deviations of λ_R and irregularity parameters for simulated galaxies	54
3	Correlation coefficients for λ_R vs. irregularity parameters for simulated galaxies	55
4	Correlation coefficients for combinations of irregularity parameters for simulated galaxies	56
5	Values of λ_{Re} and irregularity parameters for simulated galaxies with AGN feedback	57
6	Values of λ_{Re} and irregularity parameters for simulated galaxies without AGN feedback	57
7	Means and standard deviations of the residual asymmetries for simulated galaxies	61
8	Total values for $\log([\text{N II}]/\text{H}\alpha)$ for simulated galaxies	62
9	Comparison of IFU surveys	66
10	Means and standard deviations of λ_R and irregularity parameters for observed galaxies	72
11	Correlation coefficients for λ_R vs. irregularity parameters for observed galaxies	73
12	Correlation coefficients for combinations of irregularity parameters for observed galaxies	74
13	Values of λ_{Re} and irregularity parameters for observed galaxies with current AGN activity	75
14	Values of λ_{Re} and irregularity parameters for observed galaxies without current AGN activity	78
15	Means and standard deviations of the residual asymmetries for observed galaxies	79
16	Means and standard deviations of λ_R and irregularity parameters for simulated and observed galaxies (Simulations not WHAN-separated)	85
17	Means and standard deviations of λ_R and irregularity parameters for simulated and observed galaxies (Simulations WHAN-separated) . . .	86
18	Correlation coefficients for λ_R vs. irregularity parameters for simulated and observed galaxies	87
19	Correlation coefficients for combinations of irregularity parameters for simulated and observed galaxies	88
20	Means and standard deviations of the residual asymmetries for simulated and observed galaxies	90

1 Introduction, Methods, and Motivation

1.1 Introduction

Extragalactic astronomy has existed as a separate specialization for less than a hundred years, only since it could be conclusively proven that objects exist beyond the edge of the Milky Way. Starting from the discovery that there are more galaxies than just the one we inhabit, we have learned much about these other “island universes” (Kant, 1755).

The late-type galaxies (spirals, including the Milky Way) seem, at first glance, to be the most interesting, with their distinct spiral arms, apparent ongoing star formation, and other clear features. In contrast, at the other end of Hubble’s (1926) tuning fork, early-type galaxies (ETGs, ellipticals and lenticulars) are generally defined as such by their lack of such features (specifically, spiral arms). This impression was first formed based on the limited amount of detail discernible in the photographic plates with which the galaxies were first studied. New techniques, developed over the following decades, revealed that ETGs are more interesting than they might seem at first glance. Low-brightness features such as shells and ripples (e.g. Struck, 1999) hint at past merger events, which can provide fuel for ongoing low-level star formation (e.g. Kaviraj et al., 2008). This contrasts with the standard image of ETGs as “red and dead” objects with simple histories, old stellar populations, and little to no gas. Furthermore, not all ETGs are alike. More massive ETGs tend to rotate more slowly than their less massive counterparts (Bender, 1988). As technology improved, the dichotomy between two separate classes of ETG became ever clearer (see Cappellari 2016 for a review).

In addition to these insights from photometry and stellar kinematics, the recently discovered presence of nebular emission in many ETGs provides evidence of a pervasive warm interstellar medium (WIM, $T \sim 10^4$ K). The ubiquity of this emission and, thus, of the WIM, was first demonstrated by Kehrig et al. (2012), with confirmation from follow-up studies by Papaderos et al. (2013) and Singh et al. (2013). The WIM’s kinematics can differ greatly from that of the stars, and it can be ionized by several different sources, including young, massive stars, old, evolved stars, and active galactic nuclei. These excitation mechanisms leave spectral traces via the flux ratios and equivalent widths of certain characteristic emission lines.

As these improvements in observational equipment and techniques increased our understanding of the nature of ETGs, and the 20th century gave way to the 21st, the field of numerical galaxy simulations came into being and became an important part of attempting to understand how galaxies form and develop. Being able to simulate a galaxy’s life cycle requires deep knowledge of the underlying processes at work. Thus, there is interplay between the two fields: observations deliver empirical knowledge that shapes the simulations, which in turn provide possible outcomes that can be checked for plausibility (see Naab and Ostriker 2016 as well as Somerville and Davé 2015 for reviews of the current state of galaxy simulations).

In this thesis, we examine sets of simulated and observed data, derived with modern techniques, with respect to the kinematics, nebular emission characteristics, and (for the simulated data) the relative mass fractions and surface density profiles of the WIM, comparing and contrasting where possible. The kinematics of simulated ETGs are often compared to their observed counterparts for accuracy (see e.g. Serra et al., 2014; Wu et al., 2014), but not as much work has been done regarding nebular emission (Hirschmann et al. 2017 is one example, and provides the methods used in this thesis).

One specific aspect we will be investigating is the effect of feedback from an active galactic nucleus (AGN). Many ETGs host supermassive black holes (SMBH) at their centers, and a host of observational and theoretical work has painted the following picture of the way galaxies and the black holes they host influence one another: when SMBHs accrete matter, they produce large amounts of energy. This energy is transferred to the gas within the galaxy, which disturbs the gas's kinematics and causes it to heat up and expand, to the point that it is driven out of the galaxy into the surrounding halo. In simulations, this process is necessary in order to quench star formation and produce realistic massive galaxies, as the cold gas from which stars form is ejected and prevented from re-accreting. Observationally, however, the picture is far less clear. The degree to which the gas kinematics become irregular, and the extent to which the emission characteristics of the gas are affected, are the focus of this thesis.

When comparing and contrasting simulations and observations, care must be taken to ensure that one is examining both sets of data under similar circumstances and comparing the most similar aspects of each (e.g. the kinematics of only the stars or only the warm gas, or the fluxes of certain specific emission lines). This is generally accomplished by attempting to make the simulated data resemble the observations as much as possible, instead of vice versa, for the reason that one has much more flexibility in manipulating simulated data. One can orient a simulated galaxy any way one chooses, at any single spatial scale or range thereof, isolating parts of the galaxy based on any desired criteria, e.g. density, temperature, mass, age, etc. A real galaxy is observed at a single inclination, at a fixed spatial scale, and attempting to isolate specific parts for further study is somewhat more difficult. Furthermore, observations (at least in theory) capture nature objectively, whereas simulations will always be influenced by the assumptions of those who create them. It is important to remain aware of and understand these assumptions. Thus, an attempt has been made to treat the simulated and observed data analyzed in this thesis in similar ways. For details, see the following sections. We will first describe some of the theory of stellar and gas kinematics and the analysis of nebular emission in galaxies, before describing numerical galaxy simulations in general and our simulated data sample in particular, along with the results of its analysis, followed by a description of integral-field observations of galaxies, our observed data sample, and our analysis thereof, followed by a comparison of these analyses and a conclusion.

1.2 Kinematics

In this section, we will provide an overview of the kinematic data that can be gained via integral field spectroscopy (IFS) as well as the methods used to analyze the data. We begin by describing the beginnings of kinematic analysis of ETGs based on photometry and long-slit spectrography, to provide context.

1.2.1 Photometry

As stated previously, for many decades, the main source of information about galaxies (including ETGs) was photometry. One can use a photo of a galaxy to, for example, derive a radial surface brightness profile. Since brightness correlates with mass, this provides information about a galaxy’s mass distribution. The surface brightness of most ETGs is well described by the Sérsic (1968) profile:

$$I(r) = I_e \exp \left\{ -b(n) \left[\left(\frac{r}{r_e} \right)^{1/n} - 1 \right] \right\}, \quad (1)$$

where I_e is the brightness at the half-light radius r_e , n is the so-called Sérsic index, and $b(n) \approx 1.9992n - 0.3271$ for $0.5 < n < 10$ (Capaccioli, 1989). Higher Sérsic indices correspond to steeper central brightness profiles and shallower slopes at higher radii.

Radial surface brightness profiles are generally produced after fitting shapes to an ETG’s isophotes. ETG isophotes are best described by ellipses. In the standard approach (e.g. Peletier et al., 1990), the best-fitting ellipse is determined as a first approximation, then the deviation from this ellipse is measured, as follows. First, the surface brightness is approximated by a Fourier series, truncated after the first two terms:

$$\Sigma(\psi) = \Sigma_0 + A_1 \sin(\psi) + B_1 \cos(\psi) + A_2 \sin(2\psi) + B_2 \cos(2\psi), \quad (2)$$

where ψ is the eccentric anomaly. The ellipse parameters are adjusted so that the Fourier coefficients A_1 , B_1 , A_2 , and B_2 are minimized. Then, the deviations from this best-fitting ellipse are described by the next two terms of the Fourier series:

$$\Sigma(\psi) = \Sigma_0 + A_3 \sin(\psi) + B_3 \cos(\psi) + A_4 \sin(2\psi) + B_4 \cos(2\psi), \quad (3)$$

A first indication of the difference between two classes of ETG arises from the magnitude of this deviation from perfect ellipticity, as measured by the amplitude of the term a_4 , defined as $a_4 = \sqrt{A_4^2 + B_4^2}$. Positive values of a_4 indicate “boxy” isophotes while negative values indicate “disky” isophotes (see Fig. 1 for a comparison). Beyond these photometric differences, boxy and disky ETGs were found to differ in other respects as well. Disky ETGs tend to rotate more quickly than non-disky ETGs (Bender, 1988), for example.

Overall, the differences between the two classes of ETGs that were discerned before the advent of IFS can be summarized as follows:

Giant ellipticals ($M_V \lesssim -21.5$ mag):

- Are best fitted with Sérsic indices $n \gtrsim 4$ (Caon et al., 1993),
- Rotate slowly (Illingworth, 1977),
- Are, on average, rounder (Tremblay and Merritt, 1996),
- Are anisotropic and triaxial (Binney, 1978),
- Can, but must not have, boxy isophotes (Bender, 1988).

In contrast, smaller ellipticals ($M_V \gtrsim -21.5$ mag):

- Are best fitted with Sérsic indices $n \lesssim 3$ (Graham and Guzmán, 2003),
- Rotate quickly (Davies et al., 1983),
- Can, but must not be, rather flat,
- Are close to isotropic and oblate (Kormendy and Bender, 1996),
- Can, but must not have, diskly isophotes.

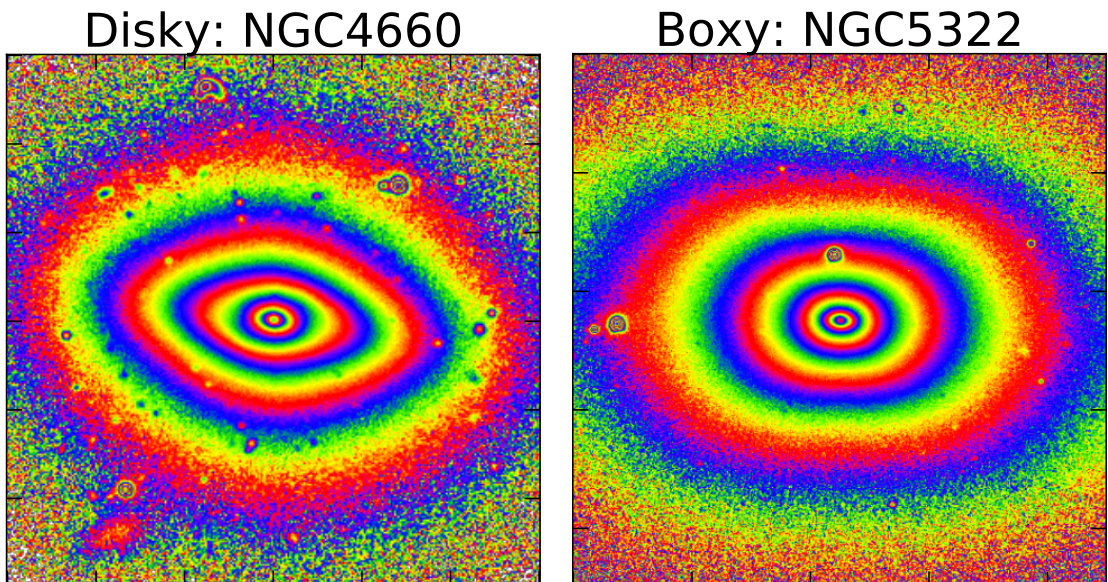


Figure 1 The difference between “disky” and “boxy” isophotes. NGC 4660, on the left, has “disky” isophotes ($a_4 \approx 3$ %). NGC 5322, on the right, has “boxy” isophotes ($a_4 \approx -1$ %). The choice of these two galaxies to represent the two types come from Bender (1988). The photometry is from the Sloan Digital Sky Survey (SDSS) (Cappellari, 2016).

With photometry, one can derive spatial information about quantities such as the surface brightness distribution and thus derive a brightness profile that contains information regarding a galaxy’s shape and some details regarding mass distribution. Kinematic information, particularly two-dimensional kinematic information, however, is also important (e.g. Franx et al., 1991) but harder to derive. This is based on spectroscopy, as the deviation of the observed wavelength of a spectral line from the rest wavelength determines the radial velocity of the emitting material. This technique is used, for example, with the 21cm line emitted by neutral hydrogen to determine galactic rotation curves (e.g. Bosma, 1978). However, to derive a rotation curve in this manner, one derives only one spectrum for the galaxy in question. There is no spatial information.

Ideally, one would derive a spectrum for each pixel in an image, and this is the principle of integral field spectroscopy (IFS). The earliest IFS observations accomplished this by simply moving the spectrograph’s slit, recording several spectra, and thus capturing 2D information about an object. This approach works well for nearby, well-resolved objects such as Centaurus A, the nearest elliptical galaxy (Wilkinson et al., 1986), but is not feasible for most objects. Later, more modern integral field units (IFUs) would split an image into sub-images by means of lenslets or fibers and then produce a spectrum based on each sub-image, a concept first theorized by G. Courtes (1982). Early IFUs such as TIGER (Bacon et al., 1995) and the MPFS (Sil’chenko et al., 1997) proved the efficacy of the technique, but the SAURON survey (de Zeeuw et al., 2002) conducted using the IFU of the same name (Bacon et al., 2001) was the first to provide kinematic information for a significant sample of nearby ETGs.

The quality of the resulting kinematic data is not the same for every pixel (or “spaxel” with the addition of spectral information), and the signal-to-noise ratio between spaxels often varies across orders of magnitude. For this reason, IFS data is often locally averaged before analysis. This has the benefit of increasing the signal-to-noise ratio, at the cost of some spatial resolution. One common averaging technique is Voronoi binning (Cappellari and Copin, 2003). In this adaptive binning scheme, many spaxels with low signal-to-noise are combined into large bins while spaxels with high signal-to-noise remain separate, with the goal of achieving roughly the same signal-to-noise ratio in each bin. Since signal-to-noise generally decreases as the radial distance from the center of a galaxy increases, this generally results in small bins with high spatial resolution near the center of a galaxy, with bin size increasing and spatial resolution decreasing further outward (for an application of this technique to data from the SAURON survey, see Fig. 2).

From a visual inspection of this kinematic data, it became clear that there were indeed two separate types of ETG: one with and one without a degree of ordered rotation. From this insight, a quantitative measure of a galaxy’s angular momentum distribution was developed.

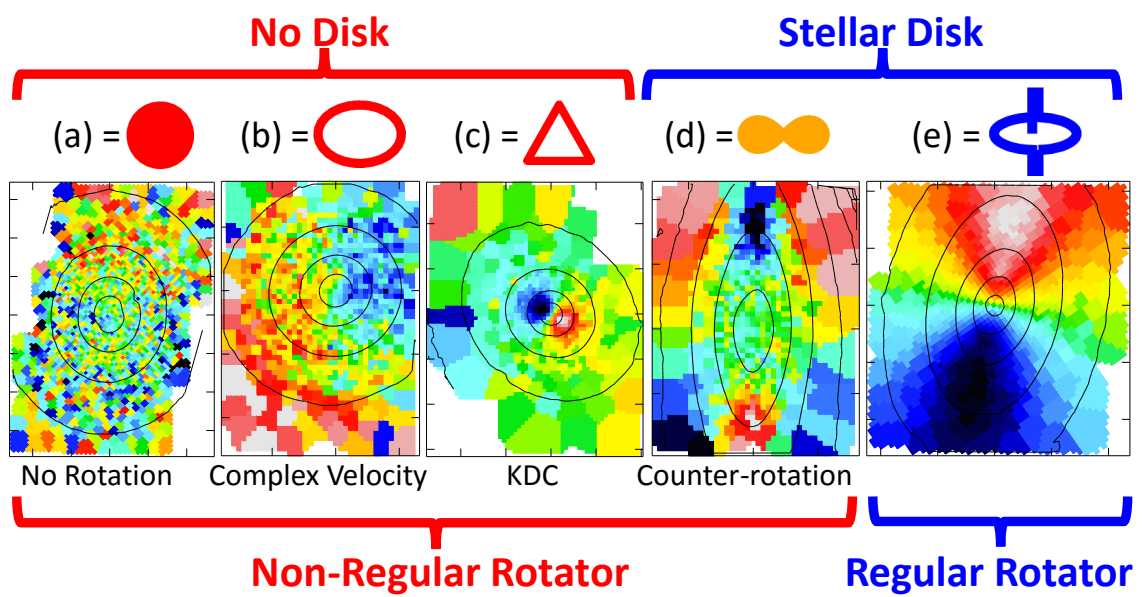


Figure 2 The five classes of stellar kinematics, as introduced by Krajnović et al. (2011). From left to right: (a) No detectable rotation, (b) detectable but irregular rotation, (c) a kinematically decoupled core (KDC), (d) two counterrotating disks, and (e) regular disk-like rotation. Types (a)-(d) represent one class of ETG, with non-ordered rotation, and (e) represents the other, with ordered rotation. The example Voronoi-binned velocity maps are from Emsellem et al. (2004).

1.2.2 From V/σ to λ_R

First attempts at quantifying the degree of ordered rotation present in an ETG’s kinematics predate IFS. It was discovered, for example, that observed stellar kinematics in ETGs showed much lower velocities than theoretical models with isotropic velocity dispersion tensors had predicted (Illingworth, 1977). Motivated by this discovery, Binney (1978) proposed the $(V/\sigma, \epsilon)$ diagram (see the left side of Fig. 3), which plots the ratio between the ordered (V) and random (σ) motion in a galaxy as a function of the galaxy’s apparent ellipticity ϵ . Ideally, these quantities would be measured in such a way that they describe the entire galaxy. For decades, however, V/σ could only be measured through long-slit spectrography, with only one value each for the maximum rotational velocity V_{max} and the central velocity dispersion σ_0 for each galaxy. The advent of IFS would bring about the same level of improvement as to the other areas of research discussed previously.

IFS allowed, first, for luminosity-weighted measures of V and σ integrated over a characteristic length scale, e.g. an ellipse containing half a galaxy’s projected total light (Cappellari et al., 2007):

$$\frac{\langle V^2 \rangle}{\langle \sigma^2 \rangle} \approx \left(\frac{V}{\sigma} \right)_e^2 \equiv \frac{\sum_{n=1}^N F_n V_n^2}{\sum_{n=1}^N F_n \sigma_n^2}, \quad (4)$$

where F_n is the flux enclosed within bin n , V_n and σ_n are, respectively, the mean stellar velocity and velocity dispersion within bin n , and N is the number of bins that fall within the half-light ellipse. One half-light radius has proven to be an effective length over which to bin, resulting in values only slight lower ($\delta(V/\sigma) \lesssim 0.1$) than theoretical models in which the binning extended to infinity (e.g. Emsellem et al., 2011).

When this approach was applied to SAURON IFS data, it was discovered that galaxies with kinematic morphologies suggesting non-regular rotation (Fig. 2a-d) are generally located significantly below the $(V/\sigma, \epsilon)$ diagram’s isotropic line (Cappellari et al., 2007). For the most part, these galaxies corresponded closely to the giant ellipticals described previously in that they are generally bright (Emsellem et al., 2007) and triaxial, with the exception of type (d), the counter-rotating disks. The regular rotators (e) occupied a larger area in the plot, corresponding to a larger range of anisotropies.

The V/σ approach, however, still does not incorporate the spatial information that IFS brought with it that previous long-slit spectrographic methods did not. This means, for example, that a galaxy with a feature such as a kinematically decoupled core (KDC, Fig. 2c) occupies the same region of the $(V/\sigma, \epsilon)$ diagram as an inclined regular rotator, despite these objects having very different kinematics (Emsellem et al., 2007).

For this reason, a new parameter was developed that adds spatial information to the quotient of ordered and random motion. A measure of the projected average

angular momentum, $\langle \mathbf{L} \rangle = \langle \mathbf{R} \times \mathbf{V} \rangle$, takes the place of V . Determining these vectors' directions from observations is no easy task, however, and thus the definition is altered to the more easily observable $\langle R|V| \rangle$, where R is the apparent distance to the galaxy's center, and the brackets meaning a flux-weighted average, as before. This quantity can then be made dimensionless and, to aid in comparisons, normalized with a quantity that is proportional to mass, such as $V_{\text{rms}} \equiv \sqrt{V^2 + \sigma^2}$ (Binney and Tremaine, 2008). The final parameter, λ_R , is then defined as follows (from Emsellem et al. 2007, in the continuous definition just explained as well as the two-dimensional discretized formulation applicable to two-dimensional IFS data):

$$\lambda_R \equiv \frac{\langle R|V| \rangle}{\langle R\sqrt{V^2 + \sigma^2} \rangle} = \frac{\sum_{n=1}^N F_n R_n |V_n|}{\sum_{n=1}^N F_n R_n \sqrt{V_n^2 + \sigma_n^2}} \quad (5)$$

One can plot a (λ_R, ϵ) diagram, which contains similar information to the $(V/\sigma, \epsilon)$ diagram (see the right side of Fig. 3). A point on the latter can be projected onto the former using the following empirical relation (Emsellem et al., 2007, 2011):

$$\lambda_R \approx \frac{k(V/\sigma)}{\sqrt{1 + k^2(V/\sigma)^2}} \quad \text{with} \quad k = 1.1. \quad (6)$$

Different ETGs with different kinematic properties have different values of (V/σ) and λ_R . But which values separate the ETGs with ordered rotation from those without?

A relation derived with respect to V/σ to distinguish between the two classes of ETG is the so-called ‘‘anisotropy parameter’’ $(V/\sigma)^*$ (e.g. Kormendy and Illingworth, 1982). It is defined as $(V/\sigma)^* \equiv (V/\sigma)/(V/\sigma)_{\text{iso}}$, where (V/σ) is the actual observed ratio and $(V/\sigma)_{\text{iso}}$ is the theoretical ratio for an isotropic galaxy of the same ellipticity. Cappellari et al. (2007) found that $(V/\sigma)^* \lesssim 0.4$ roughly separates non-regular, or ‘‘slow’’ rotators, from regular (‘‘fast’’) rotators. Results from the ATLAS^{3D} survey (Cappellari et al., 2011a) confirmed these findings, and found a better value for the separating line between fast and slow rotators at $(V/\sigma)^* \approx 1/3$ (Emsellem et al., 2011). Furthermore, all of the discovered slow rotators were rounder than $\epsilon < 0.4$.

The equivalent separating line, derived for the λ_R parameter described in the previous section, was first placed at $\lambda_R < 0.1$ in Emsellem et al. (2007). Taking into account data from the CALIFA and SAMI surveys as well as the inherent roundness of slow rotators, the current definition of a slow rotator is (from Cappellari, 2016):

$$\lambda_R < 0.08 + \epsilon/4 \quad \text{with} \quad \epsilon < 0.4. \quad (7)$$

λ_R is useful as a first descriptor of a galaxy's kinematics, based on the stellar component, for a first separation into one of the two classes, and we calculate it for every galaxy in our sample. For a more detailed description, however, a new method is necessary.

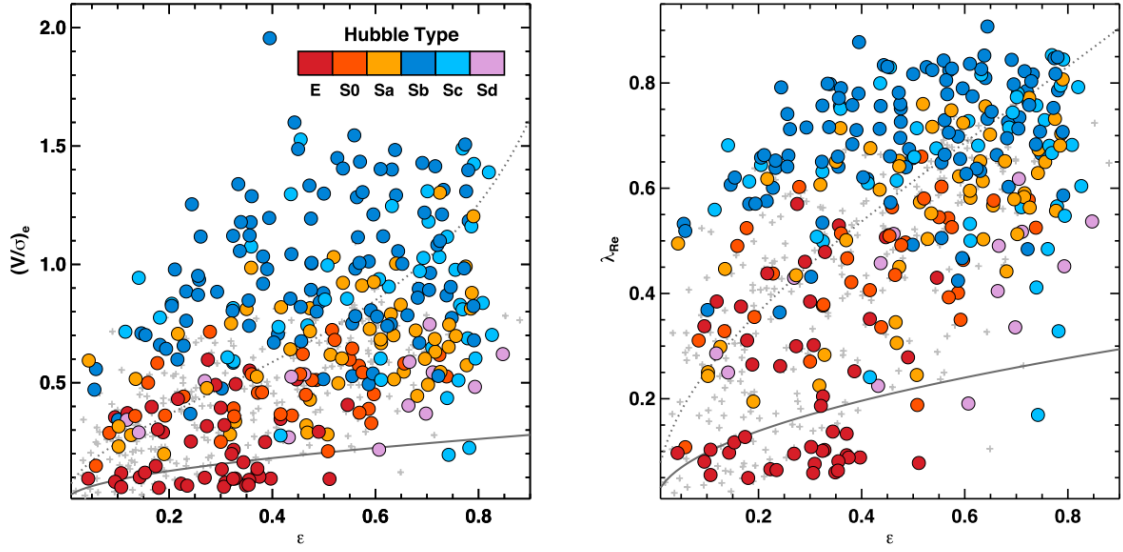


Figure 3 An overview of the $(V/\sigma, \epsilon)$ and (λ_R, ϵ) diagrams, from Fálcon-Barroso et al. (in prep). R_e is the effective (half-light) radius. Left: The $(V/\sigma, \epsilon)$ diagram for 300 galaxies from the CALIFA survey (Sánchez et al., 2012), the data for which come from Falcón-Barroso et al. (2017). The symbols are color-coded by Hubble type. Values for early-type galaxies from the ATLAS^{3D} survey (Emsellem et al., 2011) are plotted as gray crosses. The theoretical values of an edge-on isotropic rotator are plotted as a dotted line. The solid line represents the $(V/\sigma)^* = 1/3$ limit that approximately separates fast from slow rotators. Right: The (λ_R, ϵ) diagram for the same galaxies as on the left, with the same lines as well. Equation 6 is used to find the λ_R equivalent to the $(V/\sigma)^* = 1/3$ separating line between fast and slow rotators, which are better separated on the (λ_R, ϵ) diagram than on the $(V/\sigma, \epsilon)$ diagram (Emsellem et al., 2011).

1.2.3 Generalizing Photometry to Describe Features of Velocity Maps

This new method, called “kinemetry” and developed by Krajnović et al. (2006), works as follows.

For a collisionless stellar system such as an ETG, the distribution function $f = f(\mathbf{x}, \mathbf{v}, t)$ (e.g. Binney and Tremaine, 1987) fully specifies the dynamics of the system. However, this information is not directly observable. In general, when we observe an ETG, the properties we measure are integrated along our line of sight (LOS). In addition, the angle at which we view the object introduces projection effects.

The information that can be gained through observation are the surface brightness of a galaxy, given by

$$\mu(x, y) = \int_{\text{LOS}} dz \int \int \int d\vec{v} f(\vec{r}, \vec{v}), \quad (8)$$

and the velocity profile, or line-of-sight velocity distribution (LOSVD), given by

$$\mathcal{L}(v; x, y) = \int_{\text{LOS}} dz \int \int dv_x dv_y f(\vec{r}, \vec{v}). \quad (9)$$

Here, x , y , and z are the three spatial coordinates and the line of sight is defined as the projection along the z axis. From these equations, it follows that photometry provides the zeroth moment of the LOSVD and it is possible to derive higher moments. Commonly derived higher moments include the mean velocity V and the velocity dispersion σ .

These higher moments can be derived in a similar way as in photometry (hence the name “kinemetry”). First, a grid of possible ellipse parameters spanning the range of possible position angles and axis ratios is generated, and the best-fitting ellipse is determined by minimizing the coefficients of a truncated Fourier series, as before (Eq. 2). It was discovered that a simple cosine law of the form $V(\psi) = V_0 + B_1 \cos(\psi)$ approximates the velocity field of an ETG along the best-fitting ellipse quite accurately, so the number of necessary harmonic terms is comparatively low:

$$V(\psi) = V_0 + A_1 \sin(\psi) + B_1 \cos(\psi) + A_2 \sin(2\psi) + B_2 \cos(2\psi) + A_3 \sin(3\psi) + B_3 \cos(3\psi), \quad (10)$$

A_1 , A_2 , B_2 , A_3 , and B_3 are minimized. Then, the velocity along this best-fitting ellipse is given by the next Fourier terms:

$$V(\psi) = V_0 + A_4 \sin(4\psi) + B_4 \cos(4\psi) + A_5 \sin(5\psi) + B_5 \cos(5\psi). \quad (11)$$

The series can also be defined in the following, more compact way:

$$K(a, \psi) = A_0(a) + \sum_{n=1}^N k_n(a) \cos[n(\psi - \phi_n(a))], \quad (12)$$

and the amplitude coefficients k_n and phase coefficients ϕ_n are the following functions of the A_n and B_n coefficients:

$$k_n = \sqrt{A_n^2 + B_n^2} \quad \text{and} \quad \phi_n = \arctan\left(\frac{A_n}{B_n}\right). \quad (13)$$

Generally, A_n and B_n coefficients describe different properties of a map, but this does not apply to triaxial systems such as ETGs. It thus makes sense to combine the same-order coefficients in the manner described.

Two of these k_n coefficients deserve special mention: $k_1 = \sqrt{A_1^2 + B_1^2}$ describes the bulk motion, or the rotation curve, of the kinematics in question, and $k_{3,5} = \sqrt{A_3^2 + B_3^2 + A_5^2 + B_5^2}$ represents higher-order deviations from the simple rotation model, similar to the a_4 parameter in the photometric approach described previously. Another common definition of this deviation from simple rotation is simply $k_5 = \sqrt{A_5^2 + B_5^2}$. The position angles (defined as the angle from North to the receding component of the velocity) and flattenings (defined as the axis ratio b/a) of the best-fitting ellipses can change from radius to radius, or they can be held constant. They can also be given as output parameters and can be used to further describe the kinematics.

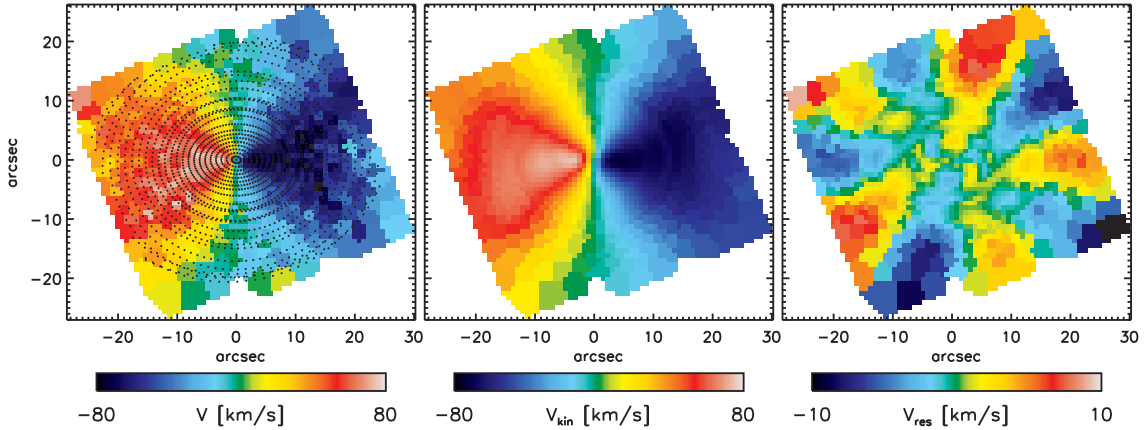


Figure 4 Applying kinemetry to a velocity map. From left to right: (a) The velocity map with the best-fitting ellipses. (b) The reconstructed velocity field on the basis of cosine-law rotation along each ellipse. (c) Residuals between the reconstructed and observed map. The five-fold symmetry suggests the presence of a significant k_5 term, the result of a separate kinematic component from the ordered rotation (from Krajnović et al., 2006).

1.2.4 Analysis Methods

Kinemetry can be applied to any available kinematic information (e.g. gas or stellar kinematics). As the WIM is the focus of this thesis, the results of applying kinemetry to it will be emphasized. Specifically, we calculated the values of the following irregularity parameters, first defined as such in Kutdemir (2010):

- $k_{3,5}/k_1$ (the deviation from simple rotation normalized to the amplitude of the simple rotation of the gas kinematics) at the galaxy’s effective radius,
- $\Delta\phi$ (the smallest difference between the position angles of the stellar and gas kinematics) at the effective radius, and
- σ_{PA} (the standard deviation of the position angles of the gas kinematics measured at different radii) between 0.1 and 2 effective radii.

Kinemetry was run first on the stellar kinematics at the effective radius to determine the stellar position angle, then on the gas kinematics at radii between 0.1 and 2 r_e at steps of 0.1 r_e , with the position angle and flattening of the ellipses allowed to vary between radii, to determine the range of gas position angles in order to calculate σ_{PA} , with the “global” (median) gas position angle subtracted from the stellar position angle to calculate $\Delta\phi$. If the value for $\Delta\phi$ calculated in this manner exceeded 180° , we subtracted it from 360° in order to obtain the smallest angle. Finally, kinemetry was run again on the gas kinematics with the position angle and flattening fixed at their global values to calculate $k_{3,5}/k_1$ at the effective radius. We define a galaxy’s kinematics as “regular” if the calculated value for $k_{3,5}/k_1$ does not exceed 0.15, the value for $\Delta\phi$ does not exceed 25, and the value for σ_{PA} does not exceed 20. These values are taken from Kutdemir (2010), who determined them by examining the parameter space occupied by non-peculiar, non-cluster galaxies with mostly regular kinematics from the SINGS survey (Daigle et al., 2006).

In order to calculate error estimates for these quantities, it is necessary to provide measurement errors for the velocities to kinemetry. Measurement errors for the velocities of both gas and stars in each pixel of the velocity maps were provided for the observational data. The spurious, saturated error pixels were replaced with the median of the non-zero errors for each galaxy. For the simulated data, however, no measurement errors were available (as the data were not “measured” per se) and we had to provide velocity errors for the simulated velocities by other means. We accomplished this by compiling a list each of all the corrected stellar and gas velocity errors from the observational data, then randomly choosing errors from the relevant list and assigning them to each pixel of the simulated stellar and gas velocity maps. This means that the chosen measurement errors are based on empirical results, but has the disadvantage that the distribution of errors is different every time they are randomly assigned, leading to slightly different values for the irregularity parameters and their errors. This variation does not significantly impact our results, but we plan on assigning measurement errors differently in future work.

The estimated errors for $k_{3,5}/k_1$ and $\Delta\phi$ were calculated by means of the formulae

$$err(k_{3,5}/k_1) = \frac{\sqrt{(k_{3,5}/k_1 * err(k_1))^2 + err(k_{3,5})^2}}{k_1} \quad (14)$$

and

$$err\Delta\phi = \sqrt{err(\phi_{stars})^2 + err(\phi_{gas})^2} \quad (15)$$

respectively, where

$$err(k_1) = \frac{\sqrt{A_1^2 * err(A_1)^2 + B_1^2 * err(B_1)^2}}{k_1}, \quad (16)$$

$$err(k_{3,5}) = \frac{\sqrt{A_3^2 * err(A_3)^2 + B_3^2 * err(B_3)^2 + A_5^2 * err(A_5)^2 + B_5^2 * err(B_5)^2}}{k_1}, \quad (17)$$

ϕ_{stars} and ϕ_{gas} are the stellar and gas position angle, respectively, and the individual errors (e.g. $err(A_1)$) are the 1-sigma errors output by kinemetry.

We also analyzed the residuals between the measured velocity fields and the rotation models generated by a further set of kinemetry runs (see Fig. 4 for an example of this approach from the literature), allowing the position angle and flattening of the ellipses to vary along the full radial extent. In order to quantify how “ordered” the residuals are, we calculate a version of the asymmetry index defined in Conselice et al. (2000), which involves taking an image, rotating it by 180° , and subtracting it from the original, as

$$A = \frac{\Sigma|I_0 - I_\phi|}{2\Sigma|I_0|} \quad (18)$$

where I_0 is the original data value in a pixel and I_ϕ is the data value in the pixel rotated by an angle ϕ . A can take on any value from 0 (fully symmetric) to 1 (fully asymmetric). This approach was originally used to describe the photometric asymmetry of galaxies as a further means of classification, but a similar approach has been applied to kinematics by e.g. Dumas et al. (2007). For the results of these kinematic analyses, see subsections 2.6 and 3.4.

In order to run kinemetry on a kinematic map, the center of the map must be defined. This was not a problem for the simulated data, in which the map is designed so that its center coincides with the center of the galaxy, but this is not the case for the observational data. Determining the kinematic center of a galaxy is not trivial, and there are several different approaches, including finding the point with the steepest velocity gradient (Arribas et al., 1997) or the highest velocity dispersion. Certain harmonic coefficients (A_0 , A_2 , and B_2) are also sensitive to miscentering (Krajnović et al., 2006). These methods require regular kinematics, however, which cannot always be expected of our data. For this reason, we assumed that the center

of each of our observed galaxies was the point with the highest continuum flux (within a certain distance of the center of the map determined by half the length of each side, to avoid centering on neighboring objects).

Kinometry automatically stops its fitting when it encounters the edge of the map. It was found, however, that the fitting continued to larger radii than it should in the case of the observational data, resulting in artificial drop-offs of measured parameters, and so we constrained the fit to points within the convex hulls containing all the pixels with non-zero velocities.

1.3 Nebular Emission

Nebular emission is a valuable source of information about the kinematics of the interstellar medium (ISM), as just described, and also of its composition and the sources of ionizing radiation, as follows.

1.3.1 BPT Theory

The ISM in a galaxy is generally mainly ionized by one of the following sources: young, massive stars, an AGN, or post-asymptotic giant branch (pAGB) stars.

Baldwin, Phillips, and Terlevich (hereafter BPT), in their landmark 1981 paper, described a method to use the ratios of the intensities of certain optical emission lines to determine which of these objects is the dominant ionization source for a given galaxy. Their reasoning was as follows: Each of these ionization sources results in a different spectrum. Therefore, one could use the relative strength of emission lines as a basis for quantitative analysis. This method had been applied to HII regions, in the form of the $I([\text{O III}]\lambda 5007)/I(\text{H}\beta)$ or $I([\text{O II}]\lambda 3727)/I([\text{O III}]\lambda 5007)$ ratios (e.g. Searle, 1971). It was found, for example, that HII regions in a galaxy's bulge had different values of these ratios than HII regions in the spiral arms. Single-parameter schemes that result from examining only one line ration, however, do not offer an ideal separation between the different mechanisms described previously, and thus one should compare two different line ratios to each other. The examined lines should fulfill the following criteria:

- They should be prominent and easily measurable,
- They should be insensitive to instrumental effects such as reddening, and
- Different line ratios should indicate high ionization and low ionization.

BPT identified the following lines as fulfilling these criteria: $[\text{Ne V}]\lambda 3246$, $[\text{O II}]\lambda 3727$, $[\text{He II}]\lambda 4686$, $\text{H}\beta$, $[\text{O III}]\lambda 5007$, $[\text{O I}]\lambda 6300$, $\text{H}\alpha$, and $[\text{N II}]\lambda 6584$. BPT, and later Veilleux and Osterbrock (1987), then identified the three most useful two-dimensional combinations of these lines: $[\text{O III}]/\text{H}\beta$ vs. $[\text{N II}]/\text{H}\alpha$ (the “classic” BPT diagram), $[\text{S II}]/\text{H}\alpha$, and $[\text{O I}]/\text{H}\alpha$. $[\text{O III}]/\text{H}\beta$ is sensitive to high ionization, while the other three ratios are sensitive to low ionization. For an example diagram, see Fig. 5.

Using these line ratios, it was possible to separate star-forming galaxies from those hosting AGN (Seyfert galaxies). AGN produce very “hard” ionizing spectra, i.e. the fraction of high-energy photons they produce is very high (Kewley et al., 2001), which results in high values of $[\text{O III}]/\text{H}\beta$ and $[\text{N II}]/\text{H}\alpha$. For this reason, they generally occupy the region in the upper right of the BPT diagram. In contrast, stars produce comparatively “soft” spectra, and thus purely star-forming galaxies tend to occupy the bottom left of a BPT diagram. These are only general trends, however, and do not hold under all circumstances. Galaxies with high star-formation rates (and thus high ionization parameters) and low metallicities (and thus high electron

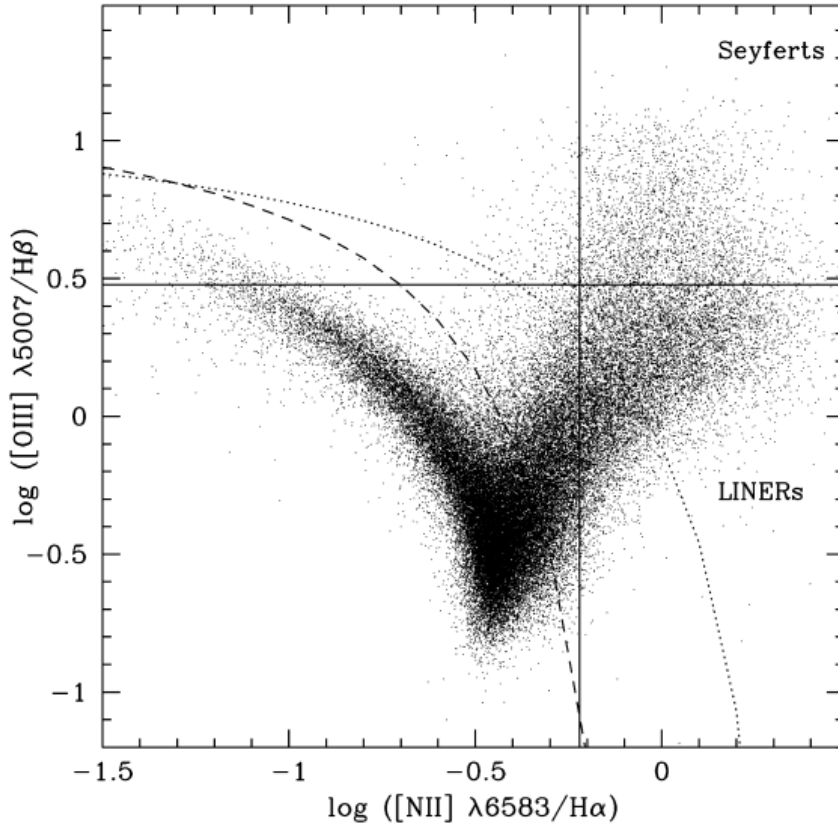


Figure 5 A sample BPT diagram (Fig. 1 from Kauffmann et al. 2003) with data for 55,575 objects from the SDSS for which all four lines were detected with a signal-to-noise ratio of at least 3. Kewley et al. (2001)’s theoretical demarcation line is the dotted curve, and the dashed curve is Kauffmann et al. (2003)’s empirical separation line. The solid, straight lines are the traditional separation lines for Seyfert galaxies ($[\text{O III}]/\text{H}\beta > 3$, $[\text{N II}]/\text{H}\alpha > 0.6$) and LINERs ($[\text{O III}]/\text{H}\beta < 3$, $[\text{N II}]/\text{H}\alpha > 0.6$) from e.g. Ho et al. (1997). Note: BPT diagrams such as this one are often also referred to as “seagull” diagrams due to their bird-like shapes.

temperatures and collisional $[\text{O III}]$ excitation probabilities in ionized gas, see e.g. Gutkin et al. 2016) can exhibit very high values of $[\text{O III}]/\text{H}\beta$, pushing them high up the BPT diagram into regions normally only occupied by AGN (Hirschmann et al., 2017). These conditions are particularly prevalent at high redshift.

Thus, it is possible to separate star-forming galaxies (and regions in galaxies, with IFS) from galaxies and galactic regions dominated by emission from AGN and young, massive stars. As with the kinematics described previously, before the introduction of IFS, it was only possible to measure one or, at most, a few spectra for a single galaxy using long-slit or single-aperture spectrography. Being able to measure a spectrum for every pixel in an image of a galaxy, for the entire galaxy, opens many new avenues of inquiry into the excitation mechanisms for this ionizing radiation.

The precise location of the demarcation line between star-forming and active galaxies, however, is difficult to define without further information. Kewley et al. (2001), using stellar population synthesis and photoionization models, placed a first theoretical separating line (the dotted line in Fig. 5). Kauffmann et al. (2003)

introduced a new line (the dashed line in Fig. 5), based on empirical data from the SDSS. The area between the two lines is traditionally thought to be occupied by intermediate objects.

The bottom right of BPT diagrams is typically occupied by a class of objects referred to as LINERs (Low-Ionization Nuclear Emission Regions,¹ Heckman 1980). As their name suggests, these objects exhibit strong low-ionization lines such as [N II] while their high-ionization lines (such as [O III]) and their overall luminosities are comparatively low. The precise nature of LINERs, in contrast to star-forming or clearly active galaxies, was long considered a mystery. Their spectra resemble those of Seyfert galaxies, and so they were long considered to simply be low-luminosity Seyfert galaxies (e.g. Ho, 1999), but their spectra can also be replicated through combinations of other processes, such as fast shocks (e.g. Dopita and Sutherland, 1995) or emission from evolved, post-AGB (pAGB) stars (e.g. Binette et al., 1994; Stasińska et al., 2008). Of these possible causes, pAGB stars are assumed to play an important role.

This idea is supported by the finding (from modern IFS studies) that LINER emission in galaxies is not confined to the center, as the name would suggest, but is in fact found all throughout galaxies, tracing old stellar populations (e.g. Belfiore et al., 2016). Shocks were found only to play a major role in specialized merger and interaction scenarios. The matter has not yet been conclusively settled, however, and it can be difficult to disentangle the contributions of evolved stars and central AGN in observations. In light of this finding that LINERs are not necessarily simply low-luminosity Seyfert galaxies, and could represent the work of a different ionization mechanism, the fact that the two classes of objects are not more clearly separated in BPT diagrams has been a recent point of criticism.

¹The objects hosting these regions are also referred to as LINERs.

1.3.2 WHAN Theory

Since their introduction, BPT diagrams have been the standard approach to describing the source of a galaxy’s ionizing radiation. Recently, however, several possible problems have been pointed out. Placing a galaxy on a BPT diagram requires the detection of all four required emission lines ($[\text{O III}]$, $\text{H}\beta$, $[\text{N II}]$, $\text{H}\alpha$) at reasonable quality. As shown by Cid Fernandes et al. (2010), this requirement excludes about one third of the emission-line galaxies in the SDSS. Furthermore, as just described, there is no clear delineation between Seyfert galaxies with active AGN and LINERs, which are thought to be ionized at least partially by their old, evolved stars. In the BPT diagram, these objects are all located in the right “wing.”

Several alternative emission-line diagnostic diagrams have been proposed, but we will focus here on the $W_{\text{H}\alpha}$ vs. $[\text{N II}]/\text{H}\alpha$ (WHAN) diagram proposed by Cid Fernandes et al. (2010). In their paper, Cid Fernandes et al. argue that using only two lines, $[\text{N II}]$ and $\text{H}\alpha$, is much more economical than using four. The $[\text{N II}]/\text{H}\alpha$ ratio, the existing x-axis of the BPT diagram, can be used to separate star-forming from active galaxies. In order to further separate LINERs from Seyfert galaxies, Cid Fernandes et al. write, it makes sense to change the paradigm somewhat: instead of working only with ratios of line fluxes, as before, one can also use the equivalent width of $\text{H}\alpha$ ($W_{\text{H}\alpha}$), which describes the relative power of the ionization source compared to the stellar component. $W_{\text{H}\alpha}$ tends to be higher in Seyfert galaxies than in LINERs, with a local minimum separating the two populations to some degree, and so it seems to provide a better criterion for their separation than the $[\text{O III}]/\text{H}\beta$ ratio used previously. This empirical separation has not yet been theoretically examined, however.

Nevertheless, the ability of the diagram to use the $[\text{N II}]/\text{H}\alpha$ ratio to separate star-forming from active galaxies is preserved, and one need only measure two lines. Based on empirical studies, Cid Fernandes et al. were able to define five classes of galaxies based on their location on the WHAN diagram (see Fig 6):

- “Classic” star-forming galaxies ($\log[\text{N II}]/\text{H}\alpha < -0.4$, $W_{\text{H}\alpha} > 3 \text{ \AA}$),
- Seyfert galaxies (or “strong” AGN, $\log[\text{N II}]/\text{H}\alpha > -0.4$, $W_{\text{H}\alpha} > 6 \text{ \AA}$),
- Weak AGN ($\log[\text{N II}]/\text{H}\alpha > -0.4$, $3 \text{ \AA} < W_{\text{H}\alpha} < 6 \text{ \AA}$),
- “Retired” galaxies (LINERs, $W_{\text{H}\alpha} < 3 \text{ \AA}$),
- Passive (lineless) galaxies ($W_{\text{H}\alpha} < 0.5 \text{ \AA}$, $W_{[\text{NII}]} < 0.5 \text{ \AA}$).

The purpose of this thesis is to examine the effect of AGN feedback on a galaxy’s kinematics. With our simulations, we have the luxury of being able to “switch” AGN activity on or off at will, and we can examine a galaxy’s entire history, from the present through high redshift. We do not have these abilities regarding observed galaxies, and so we must determine whether or not they are affected by AGN by

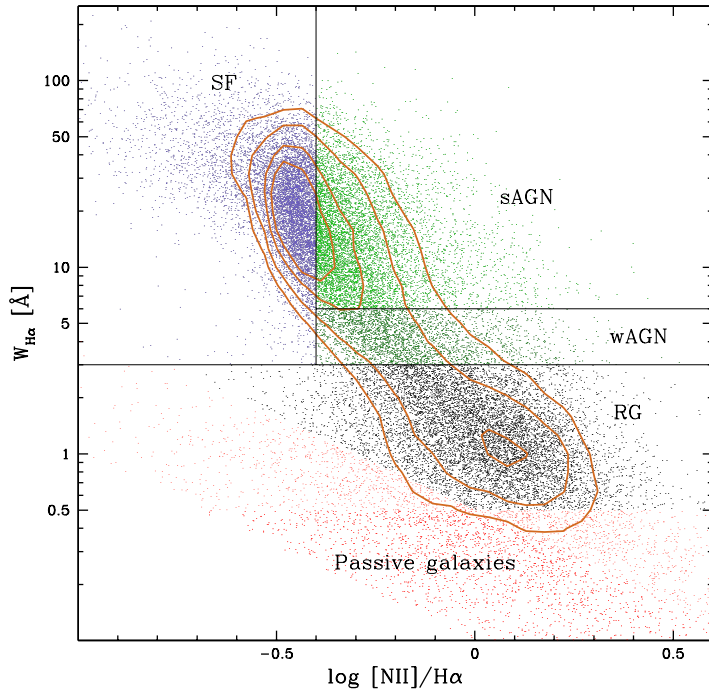


Figure 6 A sample WHAN diagram (Fig. 6 from Cid Fernandes et al. 2011). Included are the names of the five categories of galaxies introduced by Cid Fernandes et al. based on their positions in the diagram: star-forming (SF), strong AGN (sAGN), weak AGN (wAGN), retired galaxies (RG), and passive galaxies (PG).

other means. We use the WHAN diagram to do so, with the caveat that a galaxy that is not currently classified as hosting an AGN may have been affected by one at some point during its past, and may still feel its effects (a point confirmed by our analysis of our simulated data in the next section). In our analysis of the simulated data on its own (Section 2), we rely on the distinction between sets of simulations run with and without AGN feedback to separate the two groups. In our comparison to the observational data (Section 4), however, we will also perform WHAN analysis on the simulated data in order to compare the two samples in as similar a manner as possible.

We will also briefly compare the emission data in its own right. Simulated and observed galaxies are not yet often compared regarding their emission characteristics, and this work represents a proof of concept.

1.4 Thesis Structure

In this thesis, we will examine a sample of recent data from simulations and observations of early-type galaxies. First, for the simulation data (Section 2), we will describe numerical galaxy simulations in general to provide context, followed by the specific simulated galaxies in our data sample. We follow this with the results from kinematic (Subsections 1.2.2 and 1.2.4) analysis in Subsection 2.6, and the results from emission (Subsubsection 1.3.2) analysis in Subsection 2.7. We will then do the same for the observational data (Section 3). A comparison and discussion of the results will be given in Section 4. Finally, we will summarize and conclude in Section 5. In the appendix (Section 6), we will give an overview of all studied galaxies, simulated (Subsection 6.1) and observed (Subsection 6.2).

2 Simulations

From the huge amounts of observational data that have been gathered during the last few decades and the theoretical framework that has been developed to explain what we observe, certain questions have arisen. How do the initially small density fluctuations that emerged shortly after the Big Bang develop into the structures at large and small scales present in today's universe? How do galaxies come to exhibit their wide ranges of shapes, sizes, scaling relations, and other properties? Which processes play which roles in galaxy formation and development? The main force driving structure formation at these scales is gravity, which follows certain known rules. By applying these rules to simulated massive particles, it is possible to model their interactions. Gravity is not the only force at work, however. Attempting to model the full picture analytically is impossible, and thus an important tool in attempting to answer the questions raised by observation and theory is numerical simulation.

A full treatment of numerical galaxy simulations is beyond the scope of this thesis, and the reader is urged to read e.g. the reviews on the subject by Somerville and Davé (2015) and Naab and Ostriker (2016). Instead, in this section we will provide an overview of simulations, drawing on the aforementioned reviews as well as a lecture on the topic given by Michaela Hirschmann at the University of Vienna in the winter semester of 2016/17.

2.1 Introduction to Numerical Galaxy Simulations

Numerical galaxy simulations simultaneously face the luxury of having decades of observational data to draw on and the challenge of having to reproduce a wide variety of physical processes across huge ranges of temporal and spatial scales. Modern simulations have been largely successful at reproducing the formation of structures as described by current Lambda-Cold Dark Matter (Λ CDM) based cosmological models on large scales, as shown in Fig. 7. The general approach to galaxy simulations is as follows:

1. Initial conditions are specified,
2. Rules defining key physical processes (gravity, hydrodynamics, and various complex baryonic processes) are defined,
3. The system is evolved in time,
4. The results are analyzed and compared to observations.

Initial conditions are generally specified in the same manner for all simulations. First, a volume is defined, and the isotropic and homogeneous density field within this volume is discretized into particles with periodic boundary conditions. Then, perturbations are introduced into the density field. These perturbations are described by a power spectrum $P(k)$. $P(k)$ is derived by means of the Harrison-Zel'dovich approximation, as $P_i(k) = Ak^n$. Because the power spectrum changes over time, a transfer function is introduced to describe the power spectrum at any point in time: $P(k) = T^2(k)P_i(k)$ (e.g. Eisenstein and Hu, 1999). The effect of the perturbations on the positions and velocities of the particles in the simulation volume is described via the Zel'dovich approximation (e.g. Bertschinger, 1998). At the end of this process, one has a simulated volume full of massive particles with a distribution of positions and velocities at high redshift, before nonlinear structure formation has begun to occur. The free parameters of the initial conditions generated in this way are the chosen cosmology, the size of the volume, the number of particles, and the initial redshift (Bertschinger, 1998; Hahn and Abel, 2011).

In contrast to the mostly universal approach to initial conditions, there are many different approaches to describing physical processes. There are three main approaches to modelling galaxies, roughly in order from least to most explicit: semi-empirical models, semi-analytical models, and hydrodynamic models.

Semi-empirical models, such as sub-halo abundance matching (SHAM) models (e.g. Behroozi et al., 2010), attempt to derive relations between theoretical properties of dark matter halos on the one hand and observed properties of galaxies on the other. These models do not involve explicit descriptions of physical processes, however, and will not be further described in this thesis.

A more explicit family of methods are the so-called “semi-analytical models” (SAM, see e.g. Benson 2010 for a review). These models do describe physical processes, but the focus here is on each of the bulk components in a system and the rates of conversion between them rather than on individual elements and processes. A SAM can track, for example, the rate at which cold gas forms stars, or how quickly dark-matter halos accrete gas. This approach has many advantages, including the ability to explore a wide range of physical parameters with a reasonable amount of computational resources, as well as an avoidance of the numerical issues that arise with more in-depth methods.

However, there are approaches that enable even more extensive examinations of galaxy formation and evolution, and they are the focus of this thesis. With hydrodynamic techniques, mass is discretized into particles and/or space is discretized into grid cells, and the equations describing gravity and hydrodynamics are simultaneously solved for all components (stars, gas, black holes, and dark matter) as the system evolves in time. This means that one can obtain information about gas temperatures, or stellar velocities, or dark matter densities, or a number of other quantities, depending on one’s scientific goals. As the complexity rises, however, so does the computational cost, and it becomes difficult to represent a large range

of physical scales in the same simulation. A simulated cluster of massive galaxies cannot resolve individual stars. The details of certain baryonic processes, such as the feedback from black hole accretion, are also currently poorly understood and thus even more difficult to implement accurately in simulations, especially when the affected areas cannot be spatially resolved. As a result, these processes are often included in the form of physically motivated, empirical sub-resolution or “sub-grid” models, which represent their larger-scale effects, rather than modelling them explicitly.

Ideally, one would be able to analyze a huge volume in order to take into account environmental effects and consider large-scale structures containing many objects, but simultaneously be able to resolve tiny spatial scales in order to examine contributions from e.g. individual stars. In practice, one must choose a spatial scale to analyze. For an example of the range in spatial scales that a single modern simulation can describe, see Fig. 8. As simulations become able to encompass higher dynamic ranges, progress will be made from both “ends”: large-scale simulations will be better able to resolve small-scale processes, while more detailed simulations will be able to grow and describe larger and larger volumes. However, there is still much work to be done.

One common way to increase the resolution in areas of interest is the so-called “zoom-in” technique. In zoom-in simulations, the simulation is run once with the same resolution for all particles and, often, only dark matter particles. After simulated time has passed and structures have formed, the particles comprising the structures are identified and the simulation is reset to its initial conditions. Then, the particles of interest are replaced with a higher number of smaller particles, increasing the resolution, and the simulation is run again, this time with hydrodynamics and sub-resolution baryonic processes being described in addition to the interactions of the dark matter. This technique is especially useful in examining single galaxies and their environments.

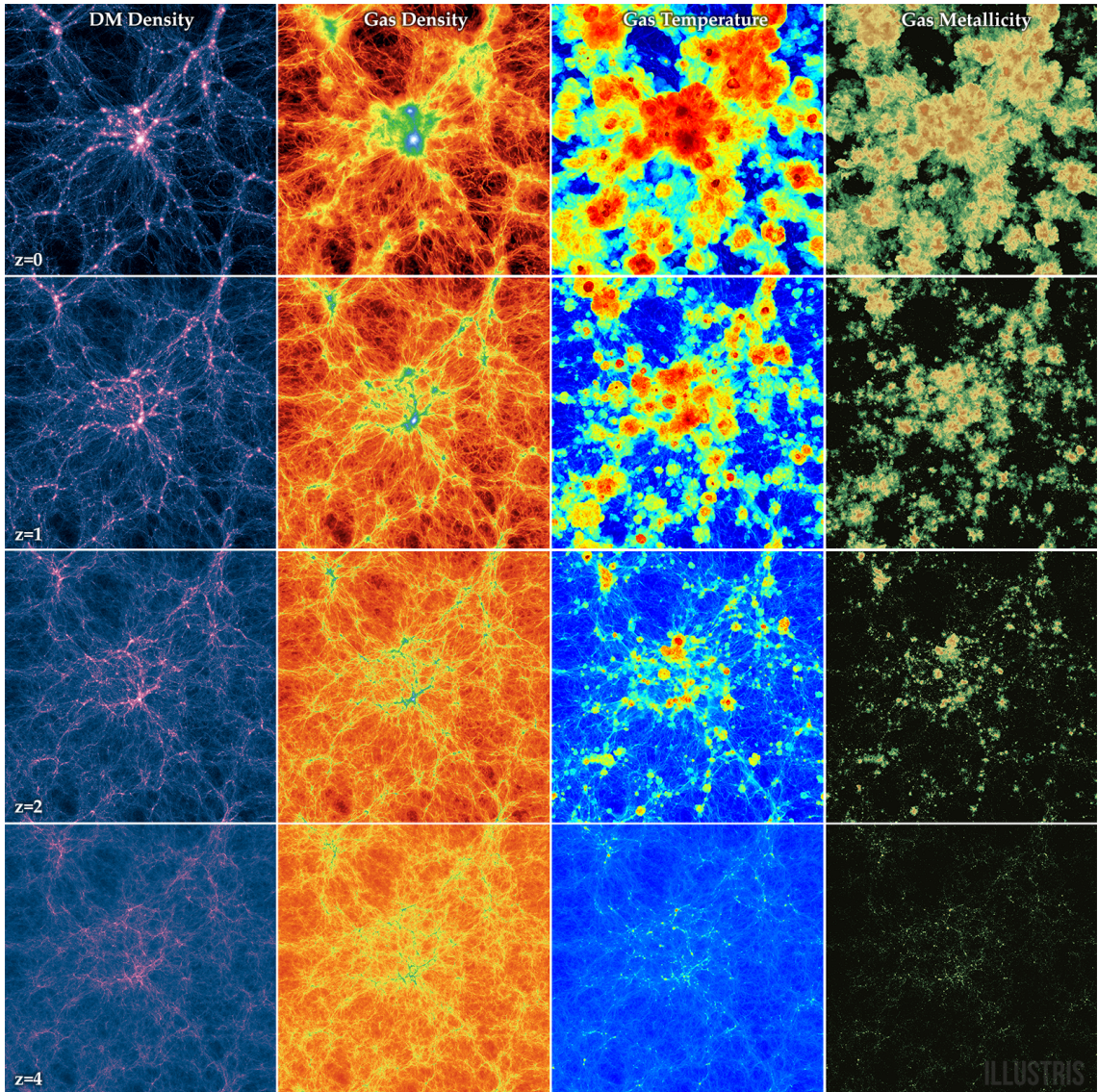


Figure 7 The evolution of certain key physical parameters (left to right: density of dark matter, density of gas, temperature of gas, metallicity of gas) over the course of cosmic time (bottom to top: $z=4$, $z=2$, $z=1$, $z=0$), as modelled by the Illustris simulation (from Vogelsberger et al., 2014). Each box has a side length of 106.5 cMpc and a projected “depth” of 21.3 cMpc. One can see in the first column on the left that structures arise in the form of dark matter filaments and the formation of halos where filaments meet. In the second column, the distribution of gas on large scales closely mirrors that of dark matter. The gas around massive halos increases in heat over time due to feedback processes from the galaxies they host as well as shock heating as the halos collapse, as can be seen in the third column. Finally, in the fourth column, metals spread from halos and fill ever larger regions of comoving space.

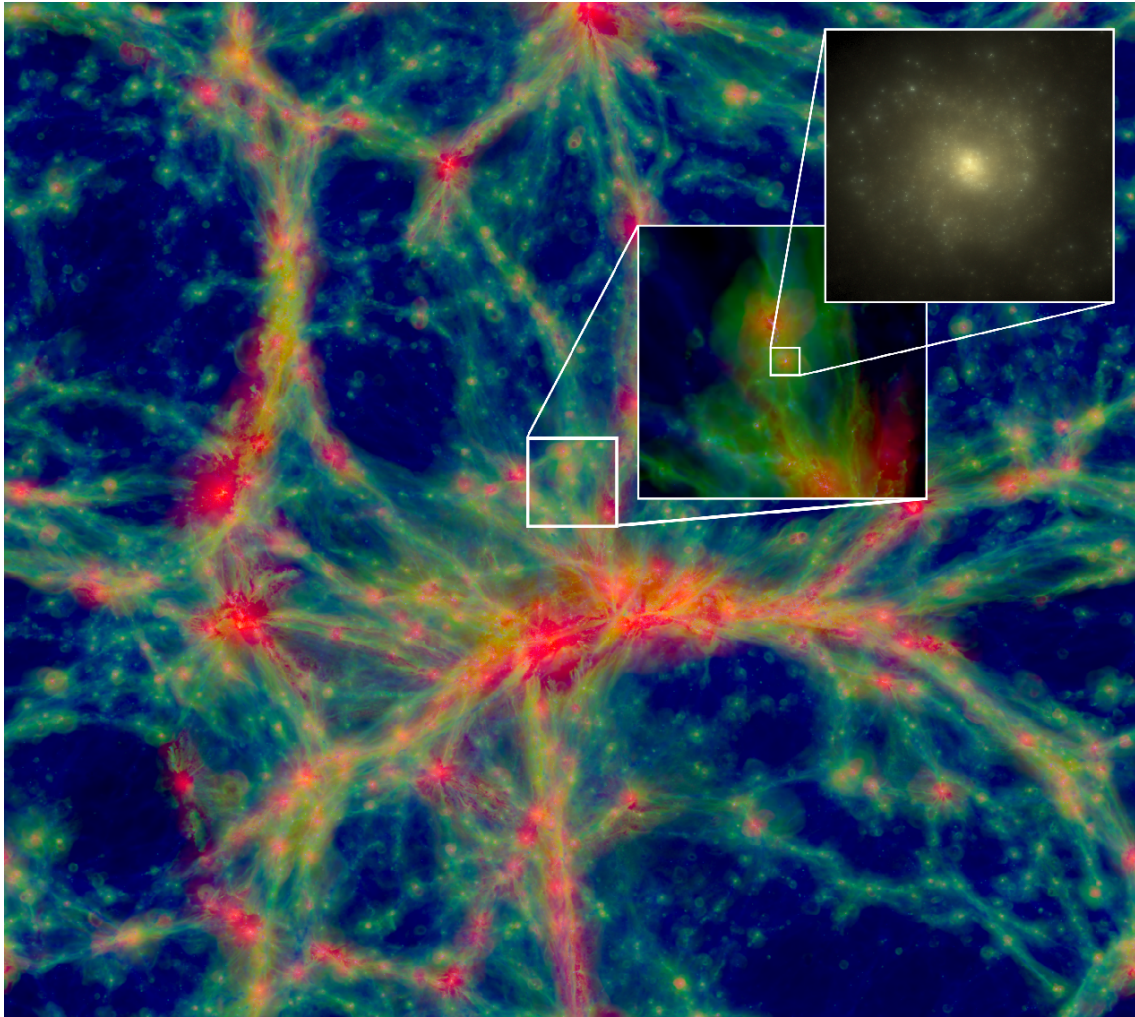


Figure 8 The dynamic range possible in current hydrodynamic simulations, and the small size of galaxies compared to large-scale structures. The largest box is $100 \times 100 \times 20$ cMpc, the first zoomed-in box is 10×10 cMpc, and the second zoomed-in box, showing an individual galaxy, is 60 ckpc \times 60 ckpc. The color describes the gas temperature (blue to green to red representing cold to warm to hot) and the brightness describes the gas density. The simulation shown is EAGLE, and the image with insets is reproduced from Schaye et al. (2015).

2.2 Physical Processes

Certain physical processes have been determined to play important roles in galaxy formation and evolution and are commonly included in simulations. Their general implementation will be described in the following subsections, followed by the specific details of SPHGal, the code used to generate the simulations in our data sample.

2.2.1 Gravity

The gravitational force exerted on each mass element in a simulation by all others is calculated by numerically solving Poisson’s equation. This is carried out by codes referred to as gravity solvers.

First, a volume is defined to contain the simulation, as described previously. The forces on each massive particle within the volume are calculated, and the system develops forward in time, taking discrete time-steps. To reflect the expansion of space over cosmic time, the volume is assumed to be co-moving, with the expansion rate calculated from the Friedmann equation, but the actual equations solved by the codes do not include relativistic corrections, which are generally assumed to be negligible.

The most straightforward approach to calculating the force on each mass element is to directly sum up the contribution of every other mass element. The computational effort involved with this approach, however, scales with the number of particles N as N^2 , which is quite high. Other, more efficient methods are mesh-based, particle-based, or a combination of the two.

A popular mesh-based method is the particle-mesh (PM) approach (Hockney and Eastwood, 1988) in which particle mass is transformed to a density, then the fast Fourier transform of the density contrast in a cell is computed, the Poisson equation is solved in Fourier space, and the potential is transformed back into real space through an inverse fast Fourier transform. This approach is faster than direct summation ($t \propto N \log N$), but the resolution is limited by the simulation’s cell size.

Popular particle-based methods include tree codes (Barnes and Hut, 1986), which operate by grouping distant particles together and approximating the force they exert through their multipole expansions. The computational effort involved with tree codes also scales with $N \log N$, as with PM codes, but PM codes are more efficient and accurate at larger scales.

In order to combine tree codes’ superior resolution with PM codes’ speed and efficiency, hybrid methods were developed. These include, for example, TreePM approaches, in which forces at short ranges are calculated using the tree approach, and forces at longer ranges are calculated with particle meshes (see e.g. Dolag et al. 2008 and references therein for details regarding these and other gravity solving schemes).

2.2.2 Hydrodynamics

All massive matter in simulations is subject to gravity. In addition, gas is subject to the laws of hydrodynamics. At each time-step of the simulation, the effects of gravity and hydrodynamics must both be determined, which significantly increases the complexity of the required calculations. In most cases, hydrodynamics are handled by numerically solving the Euler equations, which describe conservation of mass, momentum, and energy. The equation of state is generally assumed to be that of an ideal, non-relativistic gas. Depending on whether the equations are solved in the fixed or the fluid frame, the approaches to solving the Euler equations are either Eulerian or Lagrangian, respectively.

In Eulerian methods, gas is discretized onto grid cells. Then, the advection of gas properties is computed across the cells' boundaries. The details of this approach are many and varied, but most implementations have a few things in common. In most codes, the pressure at each cell face is determined by solving the Riemann problem. The pressure results in force exerted on the gas in the cell, and the gas is advected, along with all its properties, according to this force. In most modern codes, cell properties are calculated by interpolating the properties in neighboring cells, with the interpolation functions generally being parabolic. This is referred to as the Piecewise Parabolic Method (PPM, e.g. Colella and Woodward 1984).

The spatial resolution of a simulation using Eulerian methods is determined by the grid size, which can in principle be set to any arbitrary value according to one's needs. Dynamic range, however, is still a problem. A similar technique to the zoom-in technique (used with Lagrangian simulations) described previously to increase dynamic range in Eulerian simulations is Adaptive Mesh Refinement (AMR). With AMR, cells that fulfill certain (usually mass-based) criteria are split into smaller cells, increasing the spatial resolution in that area. Modern Eulerian codes include RAMSES (Teyssier, 2010), Enzo (Bryan et al., 2014), and H-ART (Kravtsov et al., 1997).

With Lagrangian methods, the Euler equations are instead solved for gas that has been discretized into particles. As with Eulerian methods, there are many ways of accomplishing this, but the most popular approach is referred to as Smooth Particle Hydrodynamics (SPH, described e.g. in reviews by Monaghan 1992 or Springel 2010b). Information, such as density or temperature, is carried directly by the particles and calculated by means of a sum over particles which are closer than a certain smoothing length h , and weighted by a spherical kernel function W of the distance separating particles, as follows:

$$X_i = \sum_j m_j (X_j / \rho_j) W(|\mathbf{r}_i - \mathbf{r}_j|, h_i, h_j), \quad (19)$$

where X_i is the desired information, and m and ρ are mass and density, respectively. In the classic implementation, the first information calculated is the density, then the thermal energy, then the pressure, then the acceleration.

This method has several advantages, including simple implementation in three spatial dimensions and good spatial adaptivity, and a variant of it is used in the code GASOLINE (Wadsley et al., 2004). On the downside, however, energy and entropy are not explicitly conserved with variable smoothing lengths in adiabatic flows. To solve this problem, entropy-conserving (EC-)SPH (Springel, 2005) was developed, and it is used e.g. in the code GADGET-2 (Springel, 2005). EC-SPH brought with it new problems, however. It was discovered, for example, that it creates artificial pressure and thus an artificial surface tension between hot and cold gas phases. This means that cold gas clumps moving through hotter gas are able to resist disruption more effectively than they should (Agertz et al., 2007).

Several approaches have been defined to deal with these problems. Saitoh and Makino (2013), basing their work on Ritchie and Thomas (2001), argued that the density distribution is non-differentiable at contact discontinuities and that classic and EC-SPH fails to account for this. Instead, a density-independent (DI-)SPH formulation, in which the internal energy and energy density are separately calculated and then used to calculate density, should describe contact discontinuities more accurately. This turned out to be the case. In order to incorporate the conservation properties of EC-SPH, Hopkins (2013) adapted DI-SPH into pressure-entropy (PE-)SPH and this, along with other improvements including new artificial viscosity descriptions (e.g. Hu et al., 2014), means that modern SPH methods can accurately describe surface instabilities and a range of other phenomena. However, an SPH simulation’s resolution is still determined by the masses of its simulated particles, in contrast to grid-based methods.

Eulerian methods accurately model hydrodynamics, including shocks and contact discontinuities (which Lagrangian methods can have trouble with, as described), but they do not conserve angular momentum as well as Lagrangian methods. Additionally, numerical diffusion can lead to artifacts. Lagrangian methods conserve angular momentum and entropy more exactly, and are more adaptive spatially, as described, but they converge more slowly than Eulerian methods (Dolag et al., 2008).

Ideally, one would combine Eulerian methods’ accurate representations of difficult scenarios with Lagrangian methods’ automatic density refinement. This can be done e.g. by using a grid, as in standard Eulerian methods, but allowing the grid to change its shape and follow the movements of the gas instead of remaining fixed. This is the principle on which the AREPO code (Springel, 2010a) operates. In AREPO, the grid is generated by means of a Voronoi tessellation around the particles so that each grid cell contains the space that is closer to its particle than any other (see Subsubsection 1.2.1 for information regarding the application of a similar technique to photometric data). The force on each particle is calculated by solving the Riemann problem across the cell faces, as before, and then the grid is re-formed when the particles move. At the cost of some additional computational resources to re-generate the grid at each timestep, this approach neatly combines the advantages of Lagrangian and Eulerian methods.

In the last few sections, we have discussed several different approaches to modelling gravity and hydrodynamics in numerical simulations, each with its own advantages and disadvantages. It is important to note, however, that there is not one method that is clearly superior to all others. Furthermore, the modern versions of all the methods discussed produce fairly similar, broadly accurate results (see Fig. 9 for a comparison of modern simulations). The major differences between the results of different models arise not necessarily from the choice of large-scale gravity or hydrodynamics solvers, but rather from the details of the sub-grid physical processes discussed in the next few sections (Scannapieco et al., 2012).

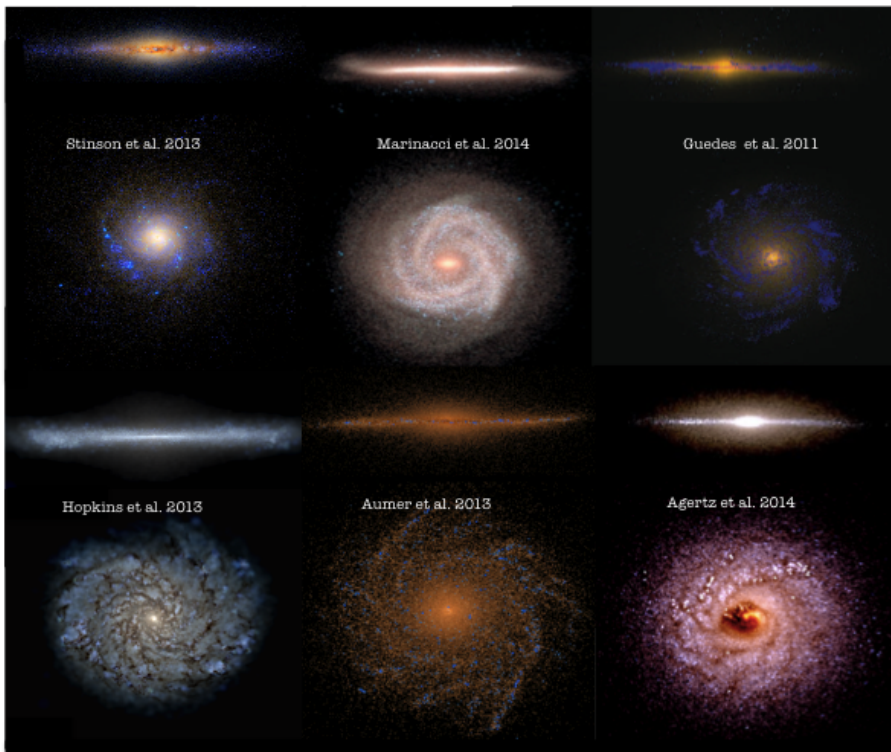


Figure 9 Results from recent numerical galaxy simulations modelling late-type galaxies. Each image shows an edge-on and a face-on view of the stellar light of the simulated galaxy. Top row, left to right: Lagrangian (SPH, GASOLINE) simulation by Stinson et al. (2013), Lagrangian-Eulerian (AREPO) simulation by Marinacci, Pakmor and Springel (2014), Lagrangian (SPH, GASOLINE) simulation by Guedes et al. (2011). Bottom row, left to right: Lagrangian (SPH, GASOLINE) simulation by Hopkins et al. (2014), Lagrangian (SPH, GADGET) simulation by Aumer et al. (2013a), Eulerian (AMR, RAMSES) simulation by Agertz and Kravtsov (2015). This overview is reproduced from Naab and Ostriker (2016).

2.2.3 Thermal and Chemical Evolution

Baryons in simulations are subject to radiative processes. They can radiate away portions of their potential energy and thus decrease their temperature, but they can also experience heating when they themselves receive radiation from stars and AGN. These mechanisms are included in some form in most modern simulations.

Radiation can heat gas directly, and it can also photo-ionize the gas, changing its characteristics further. Stellar radiation, in particular, is typically mainly produced by young, massive stars (e.g. Leitherer et al., 1999), which can release up to $\sim 10^{53}$ erg of energy as radiation by the time they explode as supernovae (which themselves release on the order of 10^{51} erg). Modelling radiative transfer fully and accurately is difficult to accomplish, and so stellar feedback is usually implemented in one of several phenomenological ways, described in the next subsection.

In terms of cooling, gas at temperatures higher than $T \gtrsim 10^7$ K is fully ionized and mainly cools via free-free emission (bremsstrahlung). At slightly lower temperatures, between $\sim 10^4$ and $\sim 10^7$ K, ionized atoms in the gas can release energy by decaying to their ground states or through recombination with electrons. At even lower temperatures, below 10^4 K, cooling takes place when heavy elements experience collisional excitation/de-excitation. This is also referred to as metal-line cooling.

Metal-line cooling is generally included in simulations, often by tracking emission from individual elements (Scannapieco et al., 2005, 2006). In order to properly describe the effect metals have on the temperature of the gas, their production and transport must be accurately described, and most modern simulations also describe the chemical enrichment of the ISM by supernovae and old, evolved stars, e.g. by tracking the production of oxygen by Type II supernovae, the production of iron by Type Ia supernovae, and the production of carbon by asymptotic giant branch (AGB) stars. As with other processes, the details of metal production models, especially at extremely high masses and low metallicities, have not yet been completely determined, and so absolute predictions are not as reliable as relative trends with respect to other galaxy properties (e.g. stellar mass). Properly describing chemical enrichment is also important because it affects the color and luminosity of stellar populations.

Furthermore, heavy elements are important to the production of dust, which further changes a galaxy's spectral energy distribution by absorbing energy in the optical and UV wavelength ranges and re-radiating it in the infrared. This scattering and re-radiation also results in pressure exerted on the dust, which can be transferred to the gas, proportional to the dust's optical depth τ_{IR} to the infrared radiation, in the form $\dot{P}_{rad} \sim (1 + \tau_{IR})L/c$. However, the extent to which this pressure drives the gas, e.g. resulting in outflows, has not yet been settled. Recent studies (e.g. Rosdahl et al., 2015) suggest that radiation pressure has less of an effect than is often currently assumed.

2.2.4 Star Formation, Evolution, and Feedback

An important aspect of galaxy simulations is the conversion of gas into stars. This process is difficult to model in simulations for several reasons. On the one hand, the physical processes involved in star formation are complex, with the interstellar medium (ISM) out of which stars form consisting of several different co-existing gas phases, each exhibiting different temperatures and densities (McKee and Ostriker, 1977). Turbulence, magnetic fields, and other processes are generally assumed to affect star formation (McKee and Ostriker, 2007), but are not generally included well, or in some cases at all, in simulations. On the other hand, the spatial scales at which star formation takes place are very small compared to entire galaxies (see the discussion on dynamic range in previous sections). One approach to modelling star formation and similar phenomena in simulations is not to attempt to resolve and explicitly model the processes in question, but to make use of empirical findings to describe them instead. One such empirical finding is that roughly 1% of the dense, cold molecular gas in galaxies per free-fall time becomes stars (e.g. Leroy et al., 2013). This rate applies to the majority of current observations. The implementation of this finding in galaxy simulations generally takes a straightforward form (first described by Katz 1992) that relates the star formation rate to the local gas density divided by the free-fall time, in the form of a Schmidt (1959) law, as follows:

$$\dot{\rho}_* = \frac{\epsilon_* \rho_{\text{gas}}}{t_{\text{ff}}}. \quad (20)$$

ϵ_* is a free parameter, the value of which is calculated from the Kennicutt (1998) relation in isolated, idealized simulated galaxy disks. Another free parameter is the threshold at which gas is deemed dense enough to form stars. This can be related, for example, to the Jeans mass (Springel and Hernquist, 2003): as soon as the Jeans mass falls below the mass of one gas particle, star formation can occur. From the gas particle masses possible at the time, this resulted in a density threshold of $\approx 0.1 \text{ atoms cm}^{-3}$.

This approach is fine for a first approximation, but it has several problems in practice. The Kennicutt relation describes the ISM well at spatial scales of roughly 1 kpc, but not much smaller, and so it does not make sense to calibrate the star-formation rate based on it if one can resolve smaller scales. A density threshold of $\approx 0.1 \text{ atoms cm}^{-3}$ is also unrealistic. More realistic treatments incorporate higher thresholds (e.g. Governato et al., 2007) or calculate the star-formation rate directly from the density of the molecular gas instead of all the gas, eliminating the need for arbitrary thresholds altogether (e.g. Kuhlen et al., 2012). However, this requires modelling the molecular gas separately, which in turn requires a new set of empirical assumptions, as the temperatures and densities typical of molecular gas are not generally resolved in current simulations.

Only including star formation in simulations, however, is not enough. Applying only these methods, with nothing to stop the gas from collapsing, results in dense, clumpy disks that do not resemble local galaxies, as all the available gas is converted into stars. Clearly, whole stellar lifetimes after formation must be taken into account.

Stars, especially massive stars, begin to influence their surroundings from the beginning of their existence and distribute momentum and energy throughout the ISM as long as they exist and after they die. The low (1%) star formation rate described earlier is generally explained as a consequence of turbulence caused by newly-formed stars and supernovae from massive, short-lived stars (e.g. Krumholz et al., 2012). Another somewhat unexpected observational finding has been that the relative fraction of stars and baryons in halos of galactic size is substantially lower than elsewhere. Something is either preventing the accretion onto the galaxy of gas out of which stars could form, or removing the gas from the galaxy before stars can form. The explanation for this low baryon fraction came from the observation of galactic-scale outflows supposedly driven by supernovae and massive stars, with mass-loss rates comparable to the star-formation rate, in many star-forming galaxies (Veilleux et al., 2005).

There are many different ways this stellar feedback is implemented in simulations. The first attempts (e.g. Katz et al., 1996) consisted of calculating the thermal energy produced by supernovae, then injecting it into the surrounding medium in an attempt to overpressurize the ISM. This was, however, ineffective: because the cooling times in the medium surrounding the supernovae are so low, the energy is radiated away almost immediately, long before it has the chance to drive an outflow. To get around this, simulators have devised several tactics: they either “turn off” cooling for a certain time to allow the outflow to develop (e.g. Stinson et al., 2006) or they super-heat the gas by only selecting certain particles to heat up (Dalla Vecchia and Schaye, 2012).

Another way to incorporate stellar feedback is through kinetic energy instead of thermal energy. This approach was first developed by Navarro and White (1993) and is used in the GADGET-2 (Springel and Hernquist, 2003) code. Instead of receiving thermal energy, gas particles receive “kicks.” The wind velocity v_{wind} and a mass loading factor $\eta \equiv \dot{M}_{\text{out}}/\dot{M}_*$ determine the strength and distribution of the kicks. In Springel and Hernquist’s original formulation, the wind velocity and mass loading factor are held constant. According to Oppenheimer and Davé (2006), however, a different approach, derived from “momentum-driven” wind models (Murray et al. 2005, based on the assumption that the majority of the thermal energy dissipates away quickly), produces results that correspond more closely to many observed galaxy characteristics (e.g. Davé et al., 2013). In this approach, $v_{\text{wind}} \propto \sigma$ and $\eta \propto \sigma^{-1}$ (σ is the galaxy’s velocity dispersion).

These are only some of the ways stellar feedback is implemented, however. The aforementioned methods either only include the effects of supernovae, or they include pre-supernova effects in very simple ways, and they do not explicitly model each of the individual phases a supernova goes through as it develops (e.g. Governato et al., 2010; Agertz et al., 2013). Protostellar objects, before they truly become stars, can produce powerful jets. Massive stars, in addition to exploding as Type II supernovae, drive powerful winds of their own. Less massive stars drive less powerful winds as they evolve, and may also explode as Type I supernovae under the right conditions. All of these effects result in a transfer of mass, momentum, metals, and energy to the surrounding ISM and can be included in simulations individually or in various combinations. One attempt to include all these aspects in a self-consistent way can be found in the FIRE simulations (Hopkins et al., 2014), which explicitly derive their feedback parameters from stellar evolution models. Another approach is taken in the simulations used to generate our data, and will be described shortly.

2.2.5 Black Hole Growth and Feedback

After dark matter (which only interacts gravitationally), gas particles (which also follow the laws of hydrodynamics), and stars (which interact gravitationally but influence their surroundings as mentioned), black holes remain to be described.

The standard explanation for the existence of supermassive black holes at the centers of galaxies is that they came into being as the end result of the evolution of the first massive stars to form in the universe. These first black holes would be roughly as massive as their progenitor stars ($\sim 100 M_\odot$) and then, over billions of years, accrete material and grow to supermassive size. However, the presence of luminous quasars at high redshift ($z \sim 6-7$) powered by black holes with $\sim 10^9 M_\odot$ means that either the initial mass was higher ($10^4 - 10^6 M_\odot$), or the growth rate was substantially higher than the theoretical ceiling at the Eddington limit, at which the outward force produced by feedback balances the inward gravitational force. This issue is not yet resolved (see e.g. Volonteri 2010 for a discussion of mechanisms for producing more massive early black holes), but is not the focus of this thesis. In simulations, the general approach is to place massive ($\sim 10^5 M_\odot$) black holes by hand into massive ($M_H \gtrsim 10^{10} - 10^{11} M_\odot$) dark-matter halos. Sometimes the black holes all have the same, fixed mass, sometimes their masses correspond to their host halo's $M_{\text{BH}} - \sigma$ relation, but the details do not generally greatly influence the outcomes.

Once the black holes are in place, the rate at which they grow in mass is generally described through a variation on the Bondi-Hoyle-Littleton (Bondi, 1952; Hoyle and Lyttleton, 1939) formula for accretion, as follows:

$$\dot{M}_{\text{Bondi}} = \alpha \frac{4\pi G^2 M_{\text{BH}}^2 \rho}{(c_s^2 + v^2)^{3/2}}. \quad (21)$$

M_{BH} is the black hole's mass, ρ is the gas density, c_s is the gas sound speed, v is the relative velocity between the gas and the black hole, and α is a parameter introduced to compensate for the fact that the Bondi sphere of influence is generally too small to be spatially resolved, and to reflect the higher temperatures and lower densities in the vicinities of black holes. Simulations are getting to the point where this is no longer a problem, however, and in these situations $\alpha = 1$. Otherwise, in the first implementations of this model α was mostly held constant (at ~ 100), but in more recent cases (e.g. Booth and Schaye, 2009) its value is dependent on the gas density.

The Bondi model provides a physically motivated estimate of the accretion rate, but it assumes very idealized conditions. The gas being accreted is expected to be unaffected by feedback, self-gravity, or magnetic fields, and the accretion flow is expected to be steady, unperturbed, adiabatic, and spherically symmetrical. Simulations of more realistic conditions, involving local heating and cooling as well as turbulence, have shown that thermal instabilities develop in the accreting gas and grow in a nonlinear manner, leading to the development of cold gas filaments and

clouds, which decouple from the surrounding hot gas and boost the accretion rate by several orders of magnitude compared to the Bondi model (e.g. Gaspari et al., 2013). Thus, the Bondi model is unlikely to accurately describe cold, turbulent gas. Nevertheless, variations of it are commonly used to describe the mass growth rate of black holes through gas accretion.

When the accretion rate is low, the accretion is efficient, meaning that very little of the energy contained in the infalling matter is radiated away (“jet mode” or “radio mode” feedback). At higher accretion rates, however, much more energy and momentum is distributed amongst the black hole’s surroundings, producing the outflows and radiation associated with observations of strongly accreting black holes (Krolik, 1999). This is referred to as “radiative mode” feedback. Observationally, these outflows exhibit excess energy at IR, UV, and X-ray wavelengths as well as highly ionized emission lines. By heating up the surrounding gas (thermal feedback), or by ionizing and photo-dissociating the gas (radiative feedback), or by imparting momentum to the gas and physically driving it (kinetic feedback), strongly accreting black holes can eject gas from galaxies or prevent it from cooling and forming stars as well as regulating their own growth by limiting the amount of gas they can accrete. There is also the possibility that the produced outflows simply escape their host galaxies without much interaction with the surrounding gas, however.

Springel et al. (2005b) and Di Matteo et al. (2005) were some of the first to implement radiative-mode black hole feedback in simulations. Their approach was to calculate black hole accretion rates using the previously described Bondi model, then to calculate a bolometric luminosity proportional to the accretion rate:

$$L_{\text{bol}} = \epsilon_r \frac{dM_{\text{BH}}}{dt} c^2, \quad (22)$$

where ϵ_r is the radiative efficiency, equal to 0.1, and c is the speed of light. They then converted a fixed fraction of the luminosity to thermal energy and distributed it amongst nearby gas particles. This process did not take place in a cosmological context (the galaxies in question were not modeled with hot gas halos, for example), but the feedback resulting from this implementation was able, by converting about 5% of the luminosity into energy, to remove most of the galaxies’ cold gas, regulating the black holes’ growth and the galaxies’ star formation (Springel et al., 2005a).

Radio-mode feedback is associated with jets containing relativistic particles, detected at radio wavelengths coming from massive early-type galaxies. Instead of interacting with the matter in their host galaxies, as just described, these highly collimated beams generally deposit their energy in the intra-cluster medium (ICM) in which their host galaxies reside. Observationally, these jets are associated in many cases with large bubbles in the ICM, heated to X-ray-emitting temperatures. It is unclear, however, how such narrow, bipolar jets can heat the ICM seemingly isotropically, resulting in bubbles (Vernaleo and Reynolds, 2006).

The first simulations combining both radiative mode and jet mode feedback were carried out by Sijacki et al. (2007). Below a certain accretion rate threshold ($\sim 1\%$

of the Eddington limit), jet mode feedback is implemented by including the bubbles caused by jets (the bubbles were not directly caused by the jets, but were instead placed by hand, with radii and energies proportional to the black hole masses). Above the critical threshold, radiative mode feedback is implemented by depositing a fraction of the accreting black hole’s luminosity into the surrounding medium as thermal energy, as before. Other groups implement black hole feedback with similar methods used with stellar feedback, described previously, with cooling either “switched off” for a duration of time or the thermal energy stochastically distributed to nearby gas particles.

In addition to implementations based mainly on thermal energy, as just described, there are other implementations also based on radiation and mechanical energy. AGN produce characteristic spectra, with peaks at infrared, UV, and X-ray wavelengths (e.g. Sazonov et al., 2004), which describe the way the energy from electromagnetic radiation is distributed. The overall strength of the radiation as a function of the accretion rate can be calculated by means of the Soltan (1982) argument. AGN are also seen to produce winds from their broad-absorption-line regions (Yuan and Narayan, 2014) which are capable of transporting significant amounts of momentum. The strength of these winds can also be empirically related to the accretion rate (Arav et al., 2013). Thus, by calculating the thermal, mechanical, and radiative energy produced by a black hole as a function of its accretion rate, one should be able to accurately model AGN feedback in a physically motivated way, without having to resort to the “tricks” mentioned previously. The implementation of mechanical and radiative feedback in a cosmological context is described by Choi et al. (2016) and is shown to produce X-ray luminosities and black hole mass relations that better correspond to observations as well as more realistically quenched star formation than the results of purely thermal, isotropic feedback.

AGN feedback has several effects on simulated galaxy properties. By preventing cooling flows in group and cluster environments, AGN feedback prevents star formation in simulated group and cluster galaxies (e.g. McCarthy et al., 2010). Because the rate of in-situ star formation thus decreases, but the ratio of accreted stars is not significantly affected, these simulated galaxies grow in size, but the overall velocity dispersion increases (Martizzi et al., 2014). In this way, AGN feedback tends to turn simulated fast rotators into slow rotators and late-type galaxies into early types (Dubois et al. 2013, Frigo et al. in prep.). The work to confirm these predictions with observational results is ongoing.

Galaxies with different masses and in different environments will feel the effects of stellar and AGN feedback to different degrees. Low-mass, more isolated (typically late-type) galaxies tend to grow by accreting gas from their surroundings and forming stars in-situ. They are more affected by stellar feedback than AGN feedback. In contrast, more massive early-type galaxies (the focus of this thesis) in denser environments feel the effects of AGN feedback more strongly. Certain observational trends, e.g. the increasing relative fraction of slow rotators compared to fast rotators among ETGs as environmental density increases (Cappellari et al., 2011b) have not yet been confirmed by statistically meaningful simulated studies, but this work is also ongoing.

2.3 SPHGal

Following the general description of simulation codes from the last few sections, we will describe the details of the code used to generate our simulations: SPHGal.

SPHGal (Hu et al., 2014) is based on the SPH code GADGET3 (Springel, 2005). SPHGal computes gravitational forces via a TreePM approach, in which short-range forces are calculated based on a “tree” algorithm and long-range forces are calculated by particle-mesh algorithms, as described previously. One significant difference between GADGET3 and SPHGal is its treatment of gas hydrodynamics. GADGET3 suffers from the problems described previously when describing fluid mixing. SPHGal offers several improvements:

- A density-independent pressure-entropy (PE) formulation of SPH,
- A Wendland C^4 kernel that takes into account 200 neighboring particles,
- Improved artificial viscosity,
- Artificial thermal viscosity, and
- A limit on the degree to which neighboring particles can experience different time-steps.

Star formation, evolution, and the resulting chemical enrichment are implemented as described by Aumer et al. (2013b) and Núñez et al. (2017). Gas particles above a certain density threshold, set by $n_{\text{th}} = n_0(T_{\text{gas}}/T_0)^3(M_0/M_{\text{gas}})^2$, where $T_0 = 30000$ K, $n_0 = 2\text{cm}^{-3}$, are Jeans unstable. For these gas particles, the star formation rate is given by $d\rho_*/dt = \eta\rho_{\text{gas}}/t_{\text{dyn}}$, where $t_{\text{dyn}} = 1/\sqrt{4\pi G\rho_{\text{gas}}}$ is the gas dynamical timescale and η is the star-formation efficiency, set to 0.025 to reproduce the Schmidt-Kennicutt relation. Each formed stellar particle represents a stellar population, with its own age and metallicity, and the mass distribution described by a Kroupa (2001) IMF and upper and lower mass limits of $100 M_{\odot}$ and $0.1 M_{\odot}$, respectively. Feedback is implemented in the form of ultraviolet radiative heating and energy input from winds produced by young, massive stars, which then explode as Type Ia and II supernovae, further releasing metals, mass, and momentum into their surroundings, and less massive, evolved stars driving weaker winds. More specifically, young stars transfer momentum to neighboring gas particles for the first few Myr of their existence, and gas particles within the Strömgren spheres of young stars are heated. Thermal and mechanical energy from supernovae is transferred to neighboring gas particles, with the relative fraction of each depending on how close the receiving gas particle is to the star particles when the supernova takes place (the full amount of energy being given by $E = \frac{1}{2}m_{\text{ejected}}v_{\text{out}}^2$, with $v_{\text{out,SN}} = 4500$ km/s), with the free expansion, Sedov-Taylor, and snowplow phases each treated separately. AGB stars are treated similarly, with significantly slower winds ($v_{\text{out,AGB}} = 10$ km/s). Supernovae of types Ia and II and AGB stars produce metals via yields described

by Iwamoto et al. (1999), Woosley and Weaver (1995), and Karakas (2010), respectively. The abundances of eleven elements (H, He, C, N, O, Ne, Mg, Si, S, Ca, and Fe) in star and gas particles are tracked explicitly and used to calculate cooling rates, with diffusion calculated for gas particles to model metal mixing.

AGN feedback, the most important physical process for this thesis, is implemented as follows (based on Choi et al. 2015, 2016). Black holes with masses of $10^5 M_{\odot}$ are seeded in dark-matter halos with masses of at least $10^{11} M_{\odot}$. These black hole particles grow according to a statistical form of Bondi accretion (Eq. 21), with the probability of a gas particle being accreted onto the black hole proportional to the fractional part of its volume that lies within the Bondi radius. With a probability based on the accretion efficiency, gas particles in the vicinity of the black hole are randomly selected to receive kinetic energy in the form of velocity “kicks” of 10,000 km/s in a direction perpendicular to the gas disk, to replicate broad-absorption-line (BAL) winds. The resulting momentum is shared with the two gas particles closest to the kicked particle. To include the effects of the X-ray radiation produced by the AGN, each gas particle is affected by Compton and photoionization heating via formulae described in Sazonov et al. (2005), with the magnitude of the heating determined by the amount of radiation the gas particle receives (i.e. the luminosity flux at the gas particle’s position). In addition, each fluid element which absorbs radiation in this manner is also subject to radiation pressure, in the form of additional momentum proportional to the amount of absorbed energy and directed away from the black hole.

2.4 Simulation Sample and Methods

The initial conditions of the simulations are taken from dark-matter-only simulations in Oser et al. (2010, 2012), based on a WMAP3 cosmology (Spergel et al., 2007). Specifically, $h = 0.72$, $\Omega_\Lambda = 0.74$, $\sigma_8 = 0.77$, and $n_s = 0.95$. These simulations included $(2^9)^3$ dark-matter particles, each with a mass $m_{\text{DM}} = 2 \times 10^8 M_\odot h^{-1}$, within a volume of $(72 \text{ Mpc } h^{-1})^3$, and were run from $z=43$ to $z=0$, with a total of 95 snapshots taken at different redshifts. The previously discussed “zoom-in” technique was then applied to these simulations, with a total of 39 halos with masses between 7×10^{11} and $2.7 \times 10^{13} M_\odot h^{-1}$ selected for re-simulation. All particles within $2 \times r_{200}$, or two times the radius at which the mean density equals 200 times the universe’s critical density, were flagged, and their positions were traced back to the simulations’ initial conditions. These particles were then replaced with higher-resolution dark-matter particles ($m_{\text{DM}} = 2.5 \times 10^7 M_\odot h^{-1}$, or 1/8 the original value) as well as gas particles ($m_{\text{gas}} = 4.2 \times 10^6 M_\odot h^{-1}$) and the simulations were run again. For each halo, one simulation run was performed with AGN feedback and one without. Of these re-simulated halos, twenty of the most massive, with virial masses at $z=0$ between $3 \times 10^{12} M_\odot$ and $3 \times 10^{13} M_\odot$, corresponding to galaxy masses (stellar masses within 1/10 of the virial radius) of $3 \times 10^{12} M_\odot$ – $3 \times 10^{11} M_\odot$, were selected for further study. It was found that, at $z=0$, AGN feedback had removed a substantial portion of the warm gas from many of the galaxies (see the next section), making it impossible to compare them with the observations. For this reason, we decided to examine the same halos at slightly higher redshift ($z=0.5$). The ten halos found to host galaxies with significant warm gas components with and without AGN feedback comprise our sample (see Subsection 6.1 for an overview of each halo). In addition, for six of these halos, we performed our analysis on snapshots representing a range of redshifts from $z = 3$ to $z \sim 0.5$ in order to examine these galaxies’ histories.

In order to compare the snapshots’ kinematic properties to those from observations, we generated mock two-dimensional velocity maps using the Python code `voronimaps` described in Frigo et al. (in prep.), based on previous codes by Jesseit et al. (2007), Jesseit et al. (2009), and Naab et al. (2014), in order to generate data similar to that produced by IFS. With this code, a snapshot is loaded and centered on the most massive galaxy. The galaxy is oriented such that the velocity at its center of mass is zero, and its inclination with respect to the observer is user-defined and can be anything from completely edge-on to completely face-on. In this thesis, all snapshots were oriented at an inclination of 52° , chosen to represent the possible range of observed inclinations. To reproduce the observational effects of “seeing,” each particle (star or gas, depending on the kinematics being analyzed) is replaced with 60 “pseudoparticles.” Each pseudoparticle retains the original particle’s properties, but its position is randomly distributed according to a Gaussian function centered on the original particle’s position. The resulting 3D distribution of pseudoparticles is then mapped onto a 2D grid. The purpose of the code is then

to produce Voronoi-binned maps of quantities, e.g. age, metallicity, or line-of-sight velocity (hence the name), and so an initial, regular grid is produced and its cells are then joined together, with the resulting grid having a similar signal-to-noise ratio (defined here as the number of particles) in each cell (see Subsubsection 1.2.1 for a review of the application of this technique to IFS data). For the purposes of this thesis, however, regular grids were generated in order to facilitate comparison with the observed data, which is also provided in the form of regular, non-Voronoi-binned grids. The value of the relevant quantity (in this case, the line-of-sight velocity) in each grid cell is calculated by means of a weighted sample average. The resolution of the resulting grids was 1 kpc x 1 kpc per pixel, corresponding to the typical spatial resolution of the observational data, for the snapshots at $z=0.5$. For the six snapshots of which we examine the histories since $z = 3$, we generated grids with pixel sizes of 0.4 kpc x 0.4 kpc, corresponding to the simulation’s smoothing length.

Specifically, our analysis consisted of generating maps of the line-of-sight velocities of the star particles and the warm (defined here as $10^3 < K < 4 \times 10^4$) gas particles. With the resulting kinematic maps, values for the irregularity parameters $k_{3,5}/k_1$, $\Delta\phi$, and σ_{PA} as well as the angular momentum parameter λ_R (see Subsubsections 1.2.4 and 1.2.2 for details) were calculated for each halo.

In this section, we distinguish between galaxies with and without AGN feedback simply based on whether or not the simulations were run with AGN feedback included. When we compare the simulations to the observed data (Section 4), we will classify both simulated and observed data as being affected by an AGN by means of the WHAN analysis described previously.

In order to do so, we require information as to each simulated galaxy’s nebular emission. The kinematic information can be extracted directly from the simulation snapshots, as described. Nebular emission, however, is not included explicitly and must be added through post-processing. The details of this process are explained in Hirschmann et al. (2017), which is the first work to include contributions from each of the three ionization sources discussed in Section 1.3 in simulated galaxies in a self-consistent way. Nebular emission from young, massive stars as well as AGN narrow-line regions are described using methods described by Gutkin et al. (2016) and Feltre et al. (2016), while contributions from pAGB stars are calculated based on methods originally described by Hirschmann et al. (2017), all based on the photoionization code CLOUDY (Ferland et al., 2013). For each of the three ionization sources, a grid of models covering a representative range of key parameters such as interstellar metallicity, dust/metal mass ratio, or ionized gas density is generated (see Table 1 from Hirschmann et al. 2017, their Table 1), and the model with the parameters that resemble those of the galaxy being post-processed the most closely is applied.

Parameter space	SF models (Gutkin et al. 2016)	AGN models (Feltre et al. 2016)	PAGB models (this work)
Ionizing spectrum (<i>matched/fixed</i>)	10 Myr-old stellar population with const SFR (<i>fixed</i>), stellar metallicity same as that of gas (<i>matched</i>)	UV slope $\alpha = -1.2, -1.4, -\mathbf{1.7}, -2.0$ (<i>fixed</i>)	3, 5, 7, 9 Gyr-old stellar populations (<i>matched</i>) $Z_{\odot, \text{stars}} = 0.008, 0.014, 0.017, 0.02$ (<i>matched</i>)
Interstellar metallicity Z (<i>matched</i>)	$Z_{\star} = 0.0001, 0.0002, 0.0005, 0.001, 0.002, 0.004, 0.006, 0.008, 0.014, 0.017, 0.02, 0.03$	$Z_{\bullet} = 0.0001, 0.0002, 0.0005, 0.001, 0.002, 0.004, 0.006, 0.008, 0.014, 0.017, 0.02, 0.03, 0.04, 0.05, 0.06, 0.07$	$Z_{\diamond} = 0.0001, 0.0002, 0.0005, 0.001, 0.002, 0.004, 0.006, 0.008, 0.014, 0.017, 0.02, 0.03, 0.04, 0.05, 0.06, 0.07$
Ionization parameter $\log U$, function of the average gas density (<i>matched</i>)	$\log U_{\star} = -0.65, -1.15, -1.65, -2.15, -2.65, -3.15, -3.65$	$\log U_{\bullet} = -0.65, -1.15, -1.65, -2.15, -2.65, -3.15, -3.65, -4.65$	$\log U_{\diamond} = -2.15, -2.65, -3.15, -3.65, -4.15, -4.65$
Dust/metal mass ratio ξ_d (<i>fixed</i>)	0.1, 0.3 , 0.5	0.1, 0.3 , 0.5	0.1, 0.3 , 0.5
Ionized-gas density $\log(n_{\text{H}}/\text{cm}^3)$ (<i>fixed</i>)	$\log(n_{\text{H}, \star}) = \mathbf{2.0}, 3.0, 4.0$	$\log(n_{\text{H}, \bullet}) = 2.0, \mathbf{3.0}, 4.0$	$\log(n_{\text{H}, \diamond}) = \mathbf{1.0}, 2.0, 3.0$
C/O abundance ratio in solar units (<i>matched</i>)	$(\text{C/O})_{\star}/(\text{C/O})_{\odot} = 0.1, 0.2, 0.27, 0.38, 0.52, 0.72, 1.0$	$(\text{C/O})_{\bullet}/(\text{C/O})_{\odot} = 0.1, 0.2, 0.27, 0.38, 0.52, 0.72, 1.0$	$(\text{C/O})_{\diamond}/(\text{C/O})_{\odot} = 1.0$
Model normalization (<i>matched</i>)	Star formation rate SFR	AGN luminosity L_{AGN}	Mass of evolved stars $M_{\odot, \text{stellar}}$

Table 1 Overview of the parameter space of the nebular-emission models for young stars, AGN and post-AGB stars. To select the SF, AGN and PAGB models appropriate for each galaxy at each simulation time step, we adopt a fixed spectral slope of AGN ionizing radiation ($\alpha = -1.7$), fixed dust-to-metal mass ratio ($\xi_d = 0.3$), and fixed ionized-gas density ($n_{\text{H}, \star} = 10^2 \text{ cm}^{-3}$, $n_{\text{H}, \bullet} = 10^3 \text{ cm}^{-3}$ and $n_{\text{H}, \diamond} = 10 \text{ cm}^{-3}$). We further match the AGN, SF and PAGB ionization parameters, interstellar (i.e. gas + dust-phase) metallicity, C/O abundance ratio and age and metallicity of post-AGB stars to those of the simulated galaxy. The emission-line luminosities are scaled to the SFR, AGN luminosity and mass of post-AGB stellar population of the galaxy (from Hirschmann et al. 2017, their Table 1).

2.5 Warm Gas Mass Fraction and Surface Density Profiles

Figures 10 and 11 show the relative mass fractions of the cold, warm, and hot gas components as a function of total stellar mass within $1/10$ of each simulated galaxy's virial radius with and without AGN feedback at $z=0.0$ and $z=0.5$, respectively.

By $z=0.0$, AGN feedback has removed the majority of the warm and cold gas in each galaxy. Only one galaxy retains any cold gas, and only two manage to keep warm gas. Almost all of the galaxies (9/10) manage to retain hot gas, however. In contrast, of the galaxies without AGN feedback, all but one manage to retain some amount of cold and warm gas, and all galaxies hold some amount of hot gas. The mean stellar mass is also higher without AGN feedback compared to with AGN feedback, by a factor of about 3 ($3.07 \times 10^{11} M_{\odot}$ vs. $1.16 \times 10^{11} M_{\odot}$, respectively).

The picture is somewhat different at $z=0.5$. Here, eight galaxies with AGN feedback have cold gas, and all ten have warm and hot gas. Without AGN feedback, nine galaxies have cold gas, and all ten galaxies have warm and hot gas. The mean cold, warm, and hot gas fractions are 0.007, 0.066, and 0.049 with AGN feedback, and 0.024, 0.131, and 0.069 without, respectively. Each of the three fractions is, on average, reduced for galaxies with AGN feedback compared to those without, with the cold fraction reduced to roughly a third of its value, the warm fraction reduced to roughly half, and the hot fraction reduced to roughly five sevenths. The cold fraction is seemingly affected the most, with the warm fraction feeling the effects of feedback slightly less strongly, but more strongly than the hot fraction, as the gas is heated up and ejected by the released energy and momentum.

Furthermore, with AGN feedback, the mean stellar mass is $1.10 \times 10^{11} M_{\odot}$. This is not markedly different from the stellar mass at $z=0.0$. Without AGN feedback, the stellar mass is $1.92 \times 10^{11} M_{\odot}$ at $z=0.5$, or roughly two thirds its value at $z=0.0$. From these numbers, we conclude that AGN feedback efficiently removes gas from its host galaxy between $z=0.5$ and $z=0.0$, inhibiting star formation during this time period. Without AGN feedback, the reservoir of cold gas remains, and stars continue to form. We take a closer look at these diverging histories in the following sections.

Figure 12 shows the surface density profiles of the warm gas within $0.1 r_{\text{vir}}$ of our simulated galaxies with and without AGN feedback. Without AGN feedback, surface densities seem to be higher overall and profiles seem to be smoother and more continuous, whereas with AGN feedback there are several cases in which the profile cuts off or features gaps along its radial extent (Halos 0175, 0215, 0259) and one only begins at roughly $0.025 r_{\text{vir}}$, suggesting a central gap (Halo 0305). Without AGN feedback, only Halo 0259 shows gaps, and the rest of the profiles feature generally smooth declines, with some (e.g. Halos 0094, 0175, 0215) exhibiting local minima between 0.05 and $0.1 r_{\text{vir}}$. Higher stellar masses also generally seem to correlate with higher surface densities.

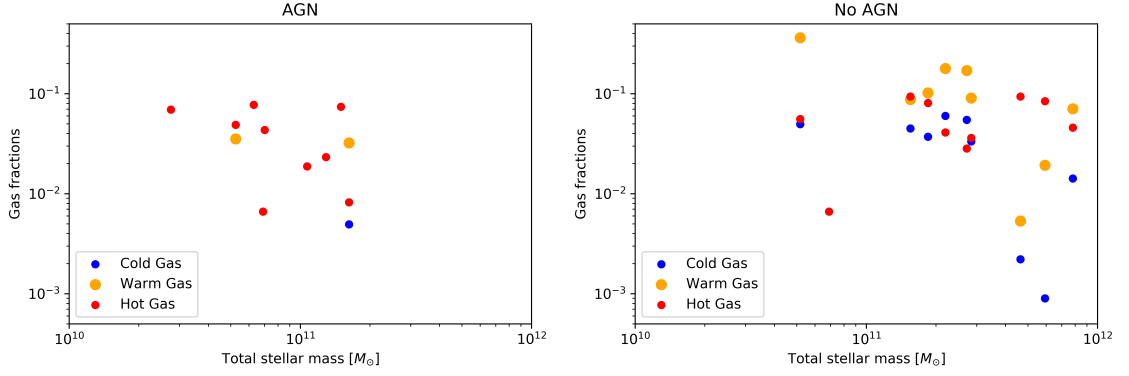


Figure 10 Cold, warm, and hot mass fractions (cold/warm/hot gas mass divided by the sum of the total gas mass and the total stellar mass) vs. total stellar mass within 1/10 of the virial radius for simulated galaxies with AGN feedback (left) and without AGN feedback (right) at $z=0.0$. AGN feedback has succeeded in removing much of the gas from the galaxies in which it is included, and the gas that remains is generally hot.

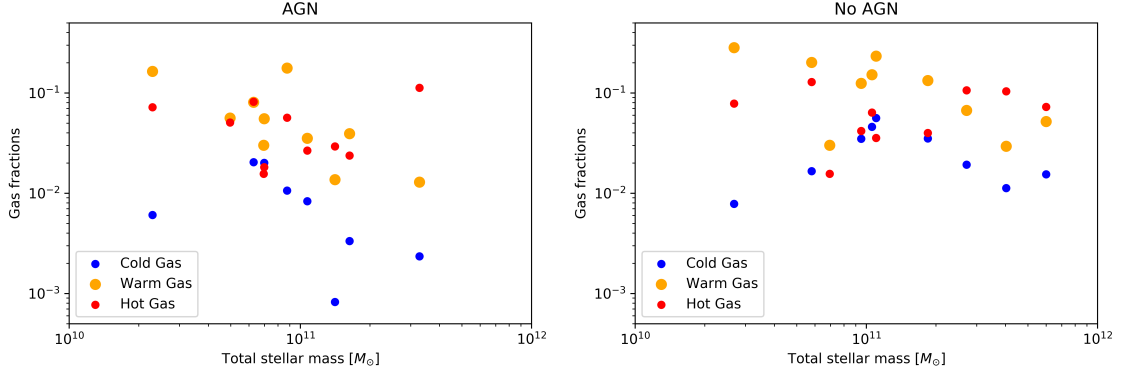


Figure 11 Cold, warm, and hot mass fractions (cold/warm/hot gas mass divided by the sum of the total gas mass and the total stellar mass) vs. total stellar mass within 1/10 of the virial radius for simulated galaxies with AGN feedback (left) and without AGN feedback (right) at $z=0.5$. AGN feedback results in lower overall stellar masses as well as reduced gas masses, but the gas has not yet been completely removed.

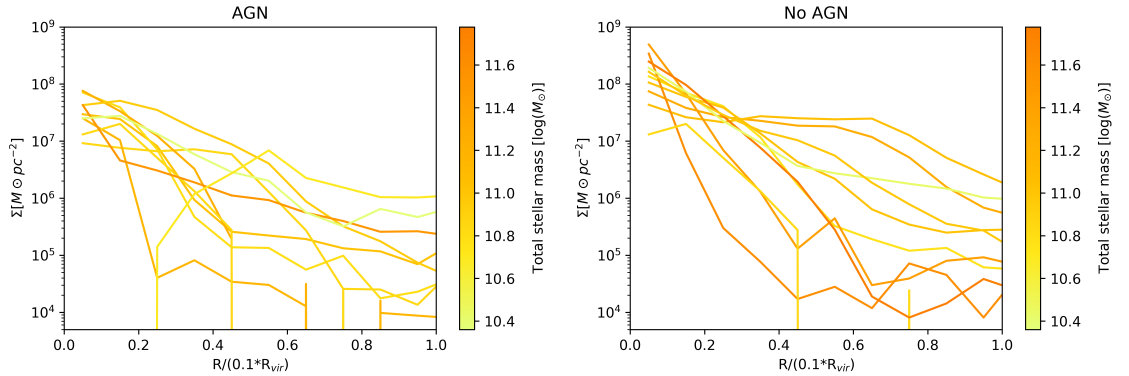


Figure 12 Surface density profiles of the warm gas within 1/10 of the virial radius in galaxies with (left) and without (right) AGN feedback. AGN feedback results in lower surface densities overall, as well as less regular profiles, with several cutting off or only beginning at higher radii. Higher total stellar masses tend to correlate with higher warm gas surface densities.

2.6 Results from Kinematic Analysis

2.6.1 Irregularity Parameters and λ_R

Figure 14 shows histograms for the values of λ_R as well as the irregularity parameters $k_{3,5}/k_1$, $\Delta\phi$, and σ_{PA} for our simulated galaxies with and without AGN feedback. Figure 15 shows scatter plots in which galaxies' λ_R values are plotted against the values of each irregularity parameter, while Figure 16 shows each of the irregularity parameters plotted against each other, color-coded with the value of the respective third parameter. In Figures 15 and 16, for galaxies with AGN feedback, each point is annotated with the accretion rate of that galaxy's black hole. Finally, Tables 5 and 6 list the values of each of these parameters for each simulated galaxy. We will briefly discuss these results here, then discuss them in more detail in Section 4.

In this thesis, we calculated σ_{PA} by examining the development of the position angle of the gas kinematics across a galaxy's radial range, but we analyzed $\Delta\phi$ and $k_{3,5}/k_1$ only at each galaxy's effective radius. A preliminary examination of the values of $k_{3,5}/k_1$ and $\Delta\phi$ across the full examined radial range (Fig. 13) shows that, in general, the values at the effective radius are representative of the full range, but that there can be differences at different radii, with trends toward lower values at lower radii. Values for k_1 across the full radial extent of each galaxy are given in the Appendix, and a more detailed examination will be the focus of planned future work.

Table 2 lists the average values and standard deviations of λ_R and the irregularity parameters for simulated galaxies with and without AGN feedback. In general, we would expect the values for the irregularity parameters to be lower without AGN feedback than with it, and this does seem to be the case. The scatter is lower as well, further strengthening the conclusion that AGN feedback disrupts the gas kinematics to a significant degree. Somewhat surprisingly, however, the mean value for λ_R is lower for galaxies without AGN feedback. The difference is lower than the standard deviation, suggesting the difference is not necessarily significant, but all of the galaxies with AGN feedback are fast rotators and one of the galaxies without it is a slow rotator, suggesting that there may indeed be a difference. It is important to mention, however, that λ_R is sensitive to a number of parameters, including the inclination angle under which a galaxy is viewed and the radius at which the measurements are taken. Frigo et al. (in prep.) carried out a similar analysis using the same simulations, and found that AGN feedback does result, overall, in a significant decline in a galaxy's λ_R value. Their analysis was carried out based on Voronoi-binned velocity maps with the galaxies oriented edge-on, using a different method to calculate the effective radius (manual calculation of the half-mass radius instead of relying on the values given in the simulation snapshots' trace-files, as we used), which might at least partially explain the differences to our results.

Table 3 lists the correlation coefficients of λ_R vs. each of the irregularity parameters. We would expect λ_R to correlate negatively with each of the irregularity

parameters, as a high degree of ordered vs. chaotic rotation implies orderly kinematics. For the most part, we found this to be the case as well.

Table 4 lists the correlation coefficients of each of the irregularity parameters vs. each other. The values of the irregularity parameters do not necessarily correlate with one another. For example, a galaxy could have stellar and gas disks that exhibit high degrees of ordered rotation and thus low values of $k_{3,5}/k_1$, but the two disks could be oriented at an angle to each other, or be located in the same plane but rotate in opposite directions, resulting in a high value of $\Delta\phi$. This conclusion is borne out by the data. On the other hand, a high value of σ_{PA} could suggest inherent irregularities in the gas disk, which $k_{3,5}/k_1$ should be sensitive to and which could result in a higher value for $\Delta\phi$ as well. Indeed, this seems to be the case. The correlations are never particularly strong, however. This is visible both in the values of the correlation coefficients and in the distribution of the color-coded points. Also, neither λ_R nor the irregularity parameters seem to correlate with the current black hole accretion rate. Their values may be more closely related to the black hole’s recent accretion history, which we explore in the next subsection.

Judging by the σ_{PA} vs. $k_{3,5}/k_1$ plot, 7/10 galaxies with AGN feedback fall within the “ordered” parameter range, as opposed to 10/10 without AGN feedback. For σ_{PA} vs. $\Delta\phi$, the numbers are 6/10 with AGN feedback and 8/10 without, and for $k_{3,5}/k_1$ vs. $\Delta\phi$ the numbers are 5/10 with AGN feedback and 8/10 without. On the whole, galaxies without AGN feedback are more ordered than those with it. The “regular” parameter ranges given in Kutdemir (2010) are somewhat arbitrarily chosen, however, and could be refined with new data.

With AGN feedback, Halo 0094 lies just barely within the regular parameter space with respect to $k_{3,5}/k_1$ and σ_{PA} , and its $\Delta\phi$ value ($\sim 180^\circ$) indicates that its gas and stellar kinematics are in almost exact counter-rotation. Halo 0204 is irregular in all three parameters. Halo 0290 is regular with respect to $\Delta\phi$ and σ_{PA} , and this fact (in combination with an irregular $k_{3,5}/k_1$ value) suggests gas kinematics which are orderly on the whole and correspond closely to the stellar kinematics, but which may harbor additional kinematic components. Halo 0300 is only regular with respect to σ_{PA} , and there only barely, suggesting quite turbulent kinematics. Finally, Halo 0305 is only irregular in $\Delta\phi$. Its gas kinematics seem to be quite ordered, but happen to rotate almost perpendicular to the stellar disk. The other five halos (0175, 0215, 0224, 0227, and 0259) are regular in all three parameters. All in all, there are an average of 2.2 regular parameters per galaxy.

Without AGN feedback, almost all ten galaxies are regular in all three parameters. The two exceptions are Halo 0215, whose value for $\Delta\phi$ near 180° suggests counter-rotation between the gas and the stars, and Halo 0300, which also exhibits a heightened value for $\Delta\phi$, though not high enough to imply full counter-rotation. These two galaxies are regular in their remaining two parameters. On average, each galaxy is regular in 2.8 parameters.

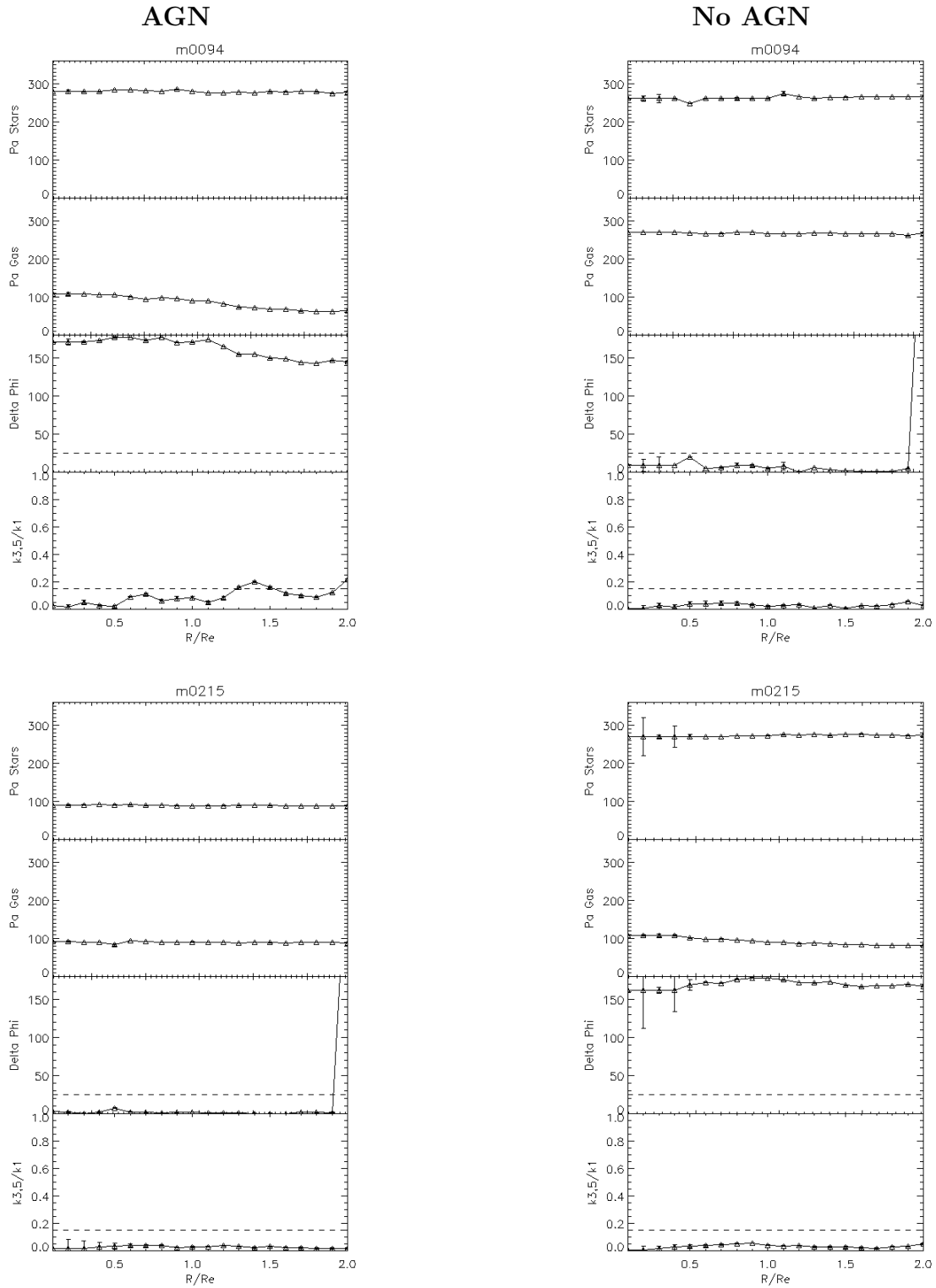


Figure 13 The values of the stellar position angle, the gas position angle, $\Delta\phi$, and $k_{3,5}/k_1$, at increments of $0.1r_e$ between 0.1 and $2r_e$, for Halos 0094 (top) and 0215 (bottom), with (left column) and without (right column) AGN feedback. In most cases, the values of the irregularity parameters do not vary significantly as a function of radius.

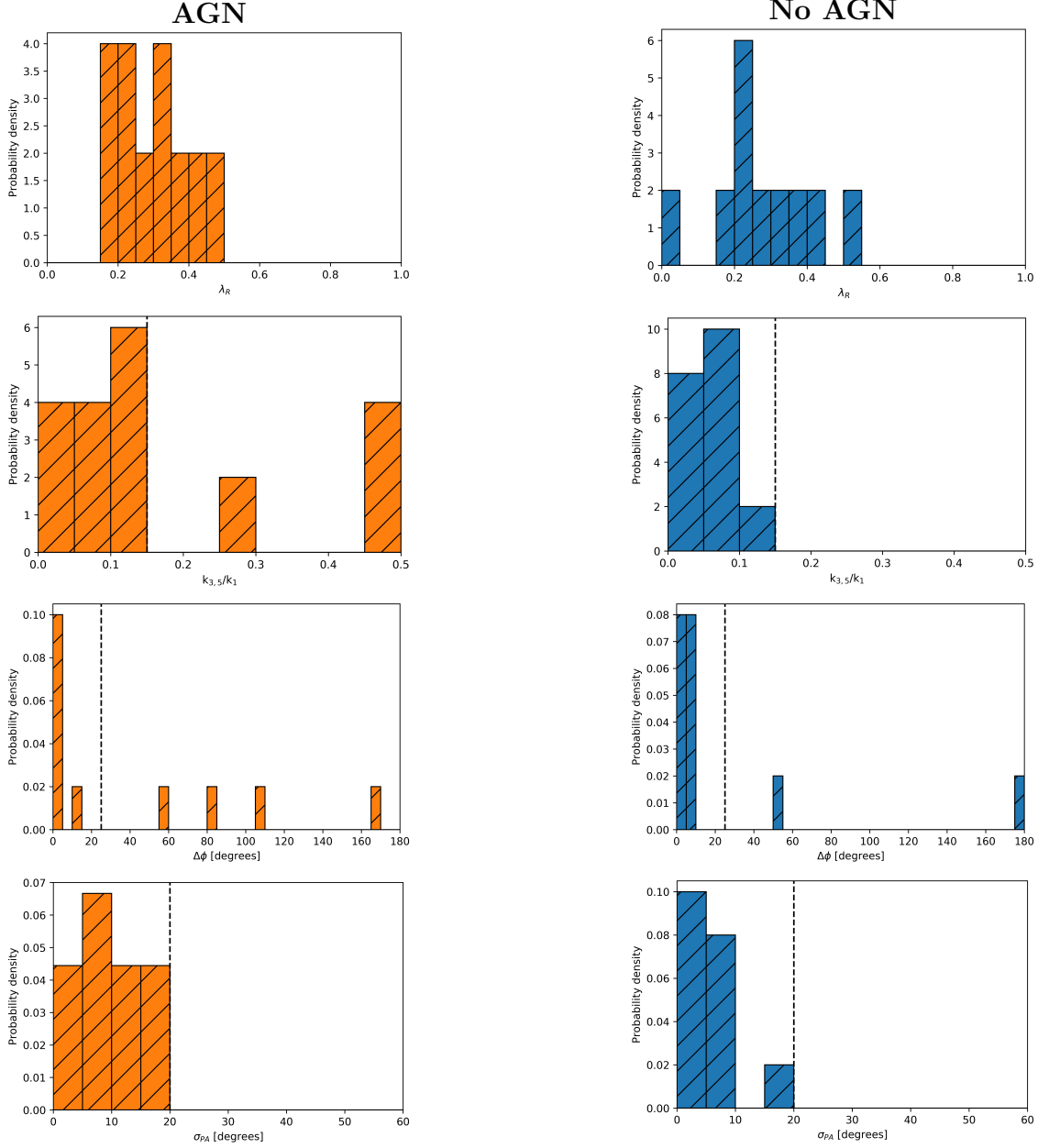


Figure 14 Histograms of λ_R (top row), $k_{3,5}/k_1$ (second row), $\Delta\phi$ (third row), and σ_{PA} (bottom row), for simulated galaxies with AGN feedback (left column) and without AGN feedback (right column). Values to the left of the dashed black lines fall within the respective “regular” ranges of each irregularity parameter.

	$\mu(\lambda_R)$	$\sigma(\lambda_R)$	$\mu(k_{3,5}/k_1)$	$\sigma(k_{3,5}/k_1)$	$\mu(\Delta\phi)$	$\sigma(\Delta\phi)$	$\mu(\sigma_{PA})$	$\sigma(\sigma_{PA})$
AGN	0.293	0.097	0.18	0.15	44	56	15	16
NoAGN	0.276	0.134	0.06	0.03	27	53	6	5

Table 2 Means and standard deviations of λ_R and irregularity parameters for simulated galaxies with and without AGN feedback.

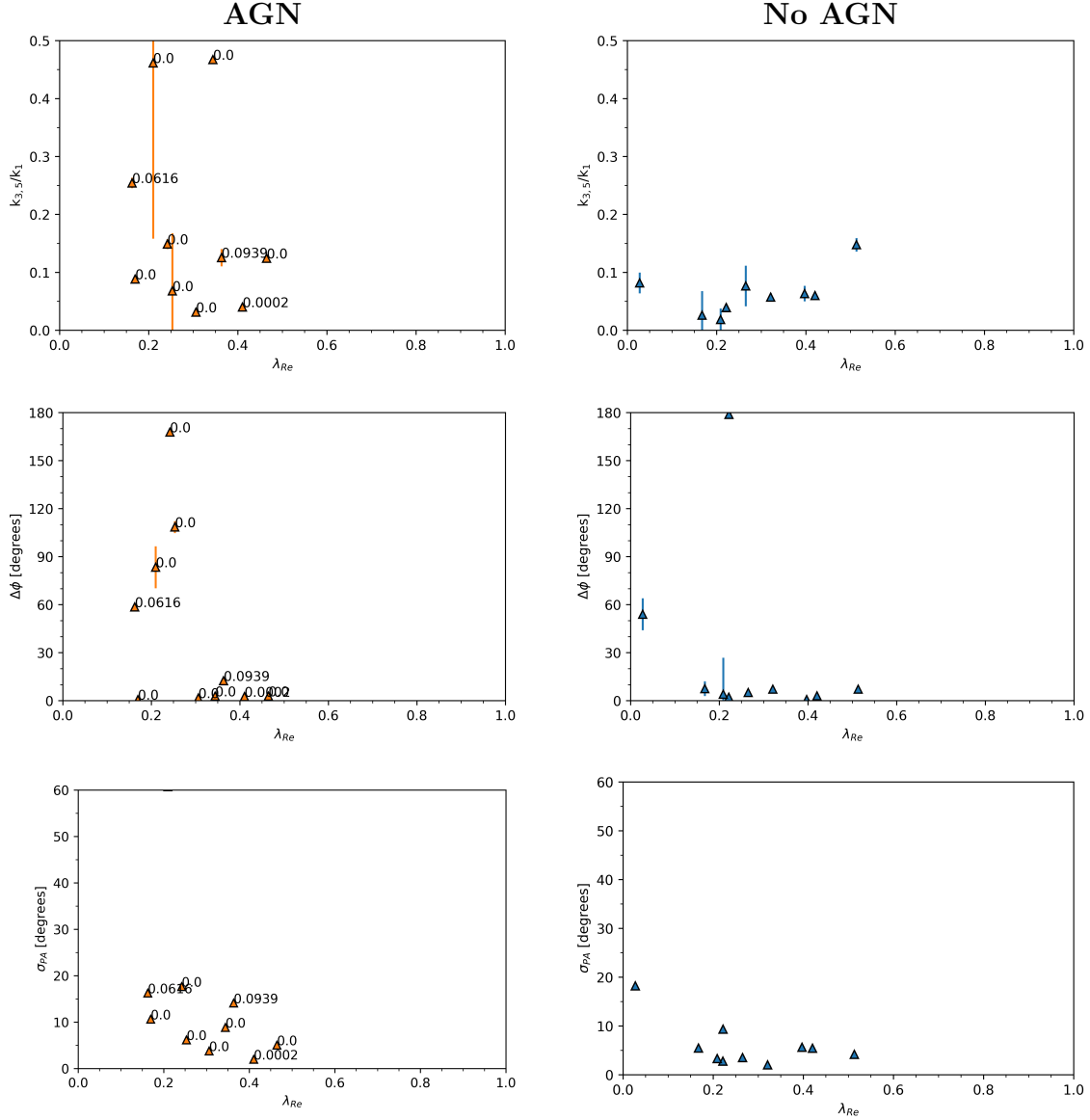


Figure 15 λ_R vs each of the irregularity parameters $k_{3,5}/k_1$ (top row), $\Delta\phi$ (middle row), and σ_{PA} (bottom row), for simulated galaxies with AGN feedback (left column) and without AGN feedback (right column). The numbers by the points in the left column are the black hole accretion rates for each galaxy, in $\log(M_\odot/\text{year})$.

	λ_R vs. $k_{3,5}/k_1$	λ_R vs. $\Delta\phi$	λ_R vs. σ_{PA}
AGN	-0.218	-0.478	-0.446
NoAGN	0.518	-0.311	-0.585

Table 3 The values of the Pearson correlation coefficient for λ_R vs. each of our irregularity parameters.

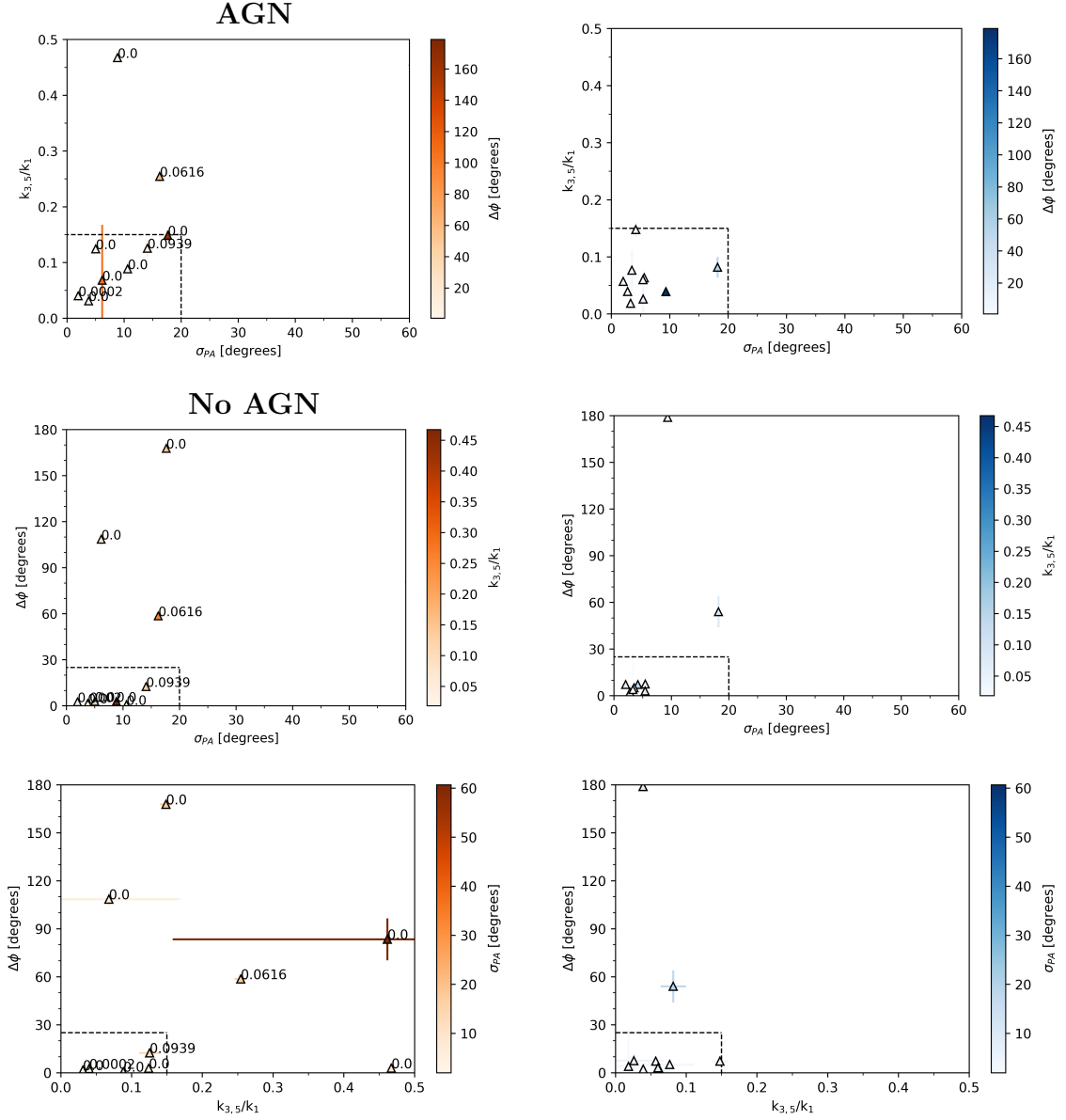


Figure 16 σ_{PA} vs. $k_{3,5}/k_1$ (top row), σ_{PA} vs. $\Delta\phi$ (middle row), and $k_{3,5}/k_1$ vs. $\Delta\phi$ (bottom row), for simulated galaxies with AGN feedback (left column) and without AGN feedback (right column). The numbers by the points in the left column are the black hole accretion rates for each galaxy, in $\log(M_{\odot}/\text{year})$.

	σ_{PA} vs. $k_{3,5}/k_1$	σ_{PA} vs. $\Delta\phi$	$k_{3,5}/k_1$ vs. $\Delta\phi$
AGN	0.666	0.385	0.109
NoAGN	0.128	0.494	-0.142

Table 4 The values of the Pearson correlation coefficient for each combination of irregularity parameters.

Name	r_e (kpc)	λ_{Re}	Fast/Slow	r_{max}/r_e	$k_{3,5}/k_1$	$\Delta\phi$	σ_{PA}	# Reg.
0094	2.906	0.242	Fast	2.0	$0.15^* \pm 0.01$	168 ± 0	18^*	2
0175	5.362	0.464	Fast	1.9	$0.12^* \pm 0.05$	$3^* \pm 0$	5^*	3
0204	2.229	0.208	Fast	2.0	0.46 ± 0.30	83 ± 13	61	0
0215	2.871	0.411	Fast	2.0	$0.04^* \pm 0.00$	$3^* \pm 1$	2^*	3
0224	1.997	0.302	Fast	2.0	$0.03^* \pm 0.01$	$2^* \pm 0$	4^*	3
0227	2.218	0.364	Fast	2.0	$0.13^* \pm 0.01$	$12^* \pm 1$	14^*	3
0259	2.781	0.168	Fast	2.0	$0.09^* \pm 0.00$	$1^* \pm 1$	11^*	3
0290	4.554	0.344	Fast	2.0	0.47 ± 0.01	$3^* \pm 0$	9^*	2
0300	4.440	0.164	Fast	2.0	0.25 ± 0.01	59 ± 0	16^*	1
0305	1.360	0.252	Fast	2.0	$0.07^* \pm 0.10$	108 ± 4	6^*	2
Mean	3.072	0.293		1.99	0.18 ± 0.05	44 ± 2	15	2.2

Table 5 The values of λ_{Re} and the irregularity parameters for simulated galaxies with AGN feedback. Starred values for irregularity parameters indicate that these values lie within their respective ranges signifying “regular” kinematics. The last column indicates the number of irregularity parameters that exhibit values within the regular range for each galaxy.

Name	r_e (kpc)	λ_{Re}	Fast/Slow	r_{max}/r_e	$k_{3,5}/k_1$	$\Delta\phi$	σ_{PA}	# Reg.
0094	2.579	0.222	Fast	2.0	$0.04^* \pm 0.00$	$2^* \pm 1$	3^*	3
0175	2.546	0.420	Fast	2.0	$0.06^* \pm 0.01$	$3^* \pm 0$	5^*	3
0204	2.379	0.321	Fast	2.0	$0.06^* \pm 0.01$	$7^* \pm 0$	2^*	3
0215	1.865	0.222	Fast	2.0	$0.04^* \pm 0.00$	179 ± 0	9^*	2
0224	1.936	0.264	Fast	2.0	$0.08^* \pm 0.04$	$5^* \pm 1$	4^*	3
0227	1.864	0.396	Fast	2.0	$0.06^* \pm 0.01$	$1^* \pm 1$	6^*	3
0259	2.781	0.170	Fast	2.0	$0.03^* \pm 0.04$	$8^* \pm 5$	5^*	3
0290	5.043	0.513	Fast	1.9	$0.15^* \pm 0.01$	$7^* \pm 1$	4^*	3
0300	1.622	0.024	Slow	2.0	$0.08^* \pm 0.02$	54 ± 10	18^*	2
0305	1.429	0.207	Fast	2.0	$0.02^* \pm 0.02$	$4^* \pm 23$	3^*	3
Mean	2.404	0.276		1.99	0.06 ± 0.02	27 ± 4	6	2.8

Table 6 The values of λ_{Re} and the irregularity parameters for simulated galaxies without AGN feedback. Starred values for irregularity parameters indicate that these values lie within their respective ranges signifying “regular” kinematics. The last column indicates the number of irregularity parameters that exhibit values within the regular range for each galaxy.

2.6.2 Histories

In addition to cleanly separating simulated galaxies affected by AGN from those that are not, we are able to look at the histories of certain quantities in order to examine causes and effects.

Figure 17 shows the development in time between $z \sim 3$ and $z \sim 0.5$ of the halos 0094 (chosen because of the counter-rotating gas and stellar disks with AGN feedback), 0204 (chosen because of its central warm gas gap), 0215 (chosen because of the counter-rotating gas and stellar disks without AGN feedback), 0227 (chosen because of its complex kinematics with AGN feedback), 0290 (chosen because of its orderly kinematics), and 0305 (chosen because of the 90° offset between its stellar and gas disks with AGN feedback). Specifically, the quantities analyzed are the stellar mass within $1/10$ of the virial radius (chosen as a proxy for the galaxy's mass), the black hole accretion rate (for galaxies that can experience AGN feedback), the warm gas mass fraction (as described earlier), and the irregularity parameters $k_{3,5}/k_1$, $\Delta\phi$, and σ_{PA} . We broadly expect the irregularity parameters and the warm gas fraction to react to spikes in the black hole accretion rate (which can in turn be caused by mergers, indicated by jumps in the total stellar mass) which lead to increased feedback. We have seen that the momentary black hole accretion rate does not seem to have an effect on the magnitude of irregularity parameters, but perhaps the overall history does.

A general trend can be seen among all the galaxies. In the cases with AGN feedback, mergers (jumps in the stellar mass) generally lead to spikes in the black hole accretion rate and thus in the strength of the feedback from the AGN. The accretion rate subsequently falls back down to zero as the increased feedback regulates the amount of infalling matter. This spike and subsequent drop in the accretion rate seems to happen quite quickly, with the peaks in the accretion rate present in single simulation snapshots at individual redshifts (for Halo 0094, for example, the spike occurs at $z = 1.0$, between a snapshot at $z = 0.96$ and one at $z = 1.04$, for a total duration of roughly 400 Myr). As the effects of feedback spread out from the central AGN, the values of the irregularity parameters increase after a delay (for Halo 0094, the increase seems to begin around $z \sim 0.75$, or roughly 1.4 Gyr after the spike in the black hole accretion rate at $z=1.0$). For the most part, they then remain elevated until $z=0.5$ (a further ~ 2 Gyr), but there are exceptions. In Halo 0094, for example, σ_{PA} and $k_{3,5}/k_1$ seem to be dropping by $z=0.5$, while $\Delta\phi$ stays high, as the gas disk seemingly settles into its new configuration. The warm gas fractions also initially decrease at roughly the same time (with increases near $z=0.5$ in the cases of Halos 0094 and 0305), as the gas is heated and driven out of the galaxy. These effects, and the resulting increase in the irregularity parameters compared to the case without AGN feedback, take effect mainly at relatively low redshift (between $z \sim 1.0$ and $z \sim 0.5$, a timespan of roughly 3 Gyr). For the galaxies without AGN feedback, mergers seemed also to result in increases in the irregularity parameters (and the warm gas fraction) at the time of the merger, with the gas seemingly settling down (and the

irregularity parameters decreasing to nearly 0) again quite quickly. For Halo 0094, the time period between a merger causing an increase in irregularity parameters and the parameters decreasing back to nearly zero in the case without AGN feedback was nearly the same period of time as the delay between the spike in the black hole accretion rate and the increase in the irregularity parameters in the case with AGN feedback (between $z \sim 1.0$ and $z \sim 0.75$, or roughly 1.4 Gyr).

The same trend as for Halo 0094 seems to hold for Halo 0204, but $\Delta\phi$ is far less affected. In contrast, Halo 0215 experiences a fairly quiet history with and without AGN feedback, with no real spikes in stellar mass, black hole accretion rate, warm gas fraction, or irregularity parameters to speak of, with the exception of the merger just before $z = 0.5$ that seemingly reverses the direction of the stellar rotation compared to the gas rotation. Halo 0227 shows a spike in the black hole accretion rate after $z = 1.0$, which seems to increase the irregularity parameters, and another one at $z = 0.5$, which seems to increase them further. Halo 0290 experiences several spikes in its black hole accretion rate, with the one at $z \sim 1.0$, just before the merger, seeming to have the largest effect on the irregularity parameters. Finally, Halo 0305 experiences a major spike earlier than the other halos, at $z \sim 1.5$, which leads to increased irregularity parameters from then on. In all six cases (except Halo 0215), with AGN feedback, the last major merger and associated spike in the black hole accretion rate seem to result in the total stellar mass staying the same for the rest of the galaxy's development (through $z = 0.5$, at least) as few to no new stars form. This is not the case without AGN feedback. For each halo without AGN feedback, the total stellar mass was higher (sometimes significantly so) and still increasing at $z = 0.5$.

In these plots, we see that increased black hole activity tends to lead to increased irregularity parameters, but that mergers in cases without AGN feedback can increase them as well. Therefore, galaxies with high irregularity parameters may have been subject to AGN feedback, but this is not necessarily the case.

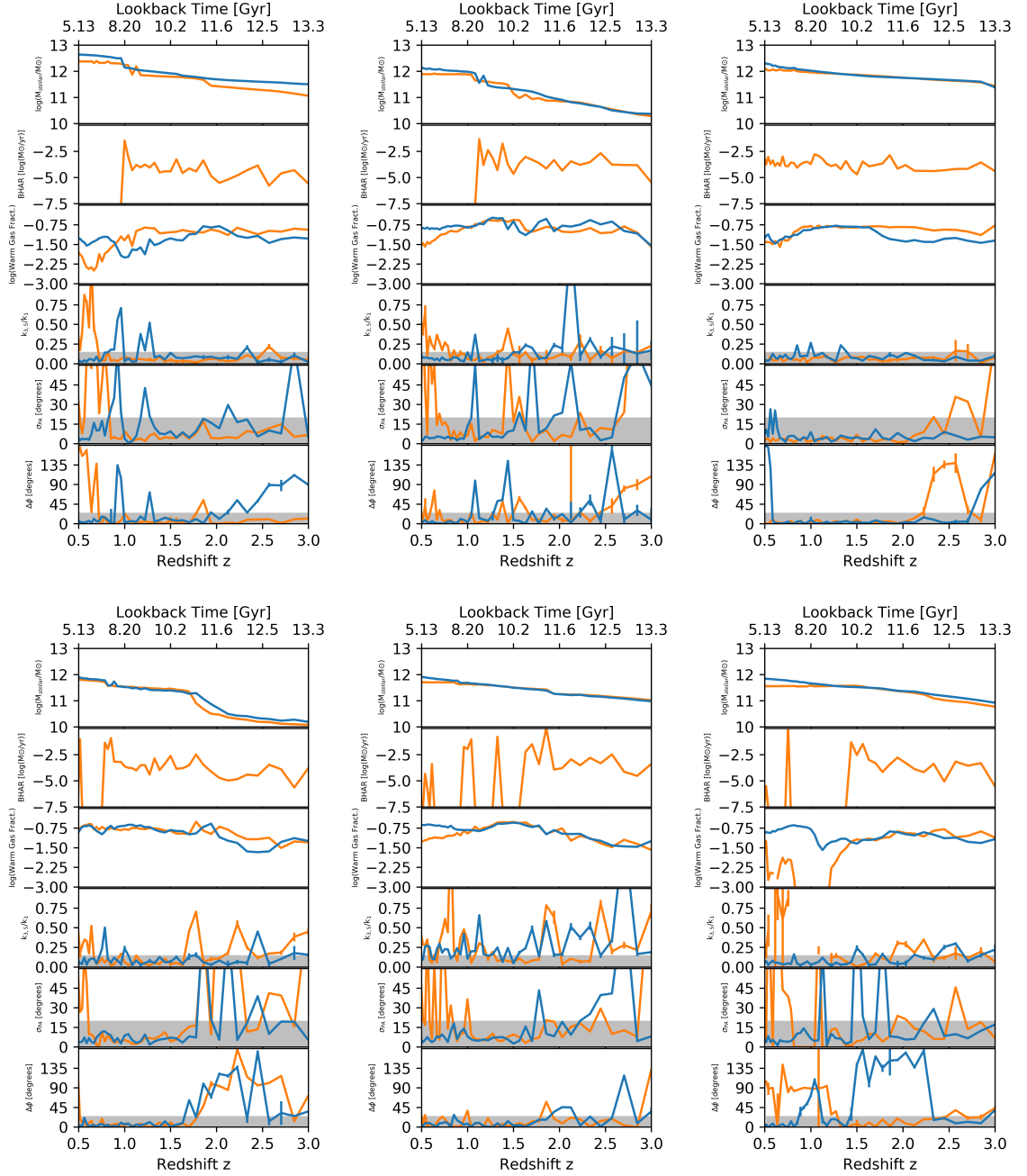


Figure 17 For each of the halos 0094 (top left, chosen because of the counter-rotating gas and stellar disks with AGN feedback), 0204 (top middle, chosen because of its central warm gas gap), 0215 (top right, chosen because of the counter-rotating gas and stellar disks without AGN feedback), 0227 (bottom left, chosen because of its complex kinematics with AGN feedback), 0290 (bottom middle, chosen because of its orderly kinematics), and 0305 (bottom right, chosen because of the 90° offset between its stellar and gas disks with AGN feedback), the values of (from top to bottom) the stellar mass within 1/10 of the virial radius, the black hole accretion rate, the warm gas mass fraction, and the irregularity parameters $k_{3,5}/k_1$, $\Delta\phi$, and σ_{PA} , with (orange) and without (blue) AGN feedback, at redshifts between 3 and 0.5. The gray areas in the irregularity parameter plots indicate the “regular” ranges.

2.6.3 Residual Asymmetries

Figure 18 shows histograms of the asymmetries of the residuals generated by subtracting the full rotation model generated by kinemetry from the gas velocity fields of simulated galaxies with and without AGN feedback. The means and standard deviations of the asymmetries are given in Table 7. We expect the asymmetries to be higher in the case of AGN feedback, as the kinematics are subject to additional turbulence. With AGN feedback, asymmetries range from 0.632 to 0.821, with a mean of 0.736, whereas without AGN feedback, asymmetries range from 0.655 to 0.785, with a mean of 0.725.

The mean asymmetry is, indeed, very slightly higher for galaxies with AGN feedback than without, but the difference is well below the scatter, and so we assume the actual difference to be marginal.

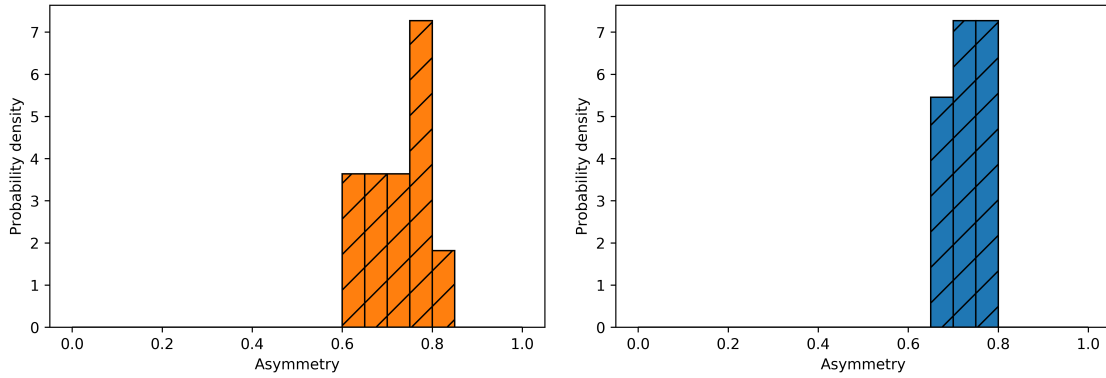


Figure 18 Histograms for the asymmetries of the residuals generated by subtracting the full rotation model generated by kinemetry from the simulated gas velocity fields for galaxies with (left) and without (right) AGN feedback.

	μ (Asymmetry)	σ (Asymmetry)
AGN	0.736	0.063
NoAGN	0.725	0.043

Table 7 The means and standard deviations of the asymmetries of the residuals generated by subtracting models of the rotation of the gas velocity fields of simulated galaxies with and without AGN feedback.

2.7 Results from Nebular Emission Analysis

2.7.1 WHAN Analysis

In order to be observationally classified as hosting an AGN, a galaxy needs to have both a total $\log([\text{N II}]/\text{H}\alpha) > -0.4$ and $W_{\text{H}\alpha} > 3$. Surprisingly, each of our galaxies (with and without AGN feedback) exhibited a total $\log([\text{N II}]/\text{H}\alpha)$ value lower than -0.4 , failing the first criterion (see Table 8). Thus, none of our galaxies would be classified as hosting AGN in a WHAN diagram, irrespective of the $W_{\text{H}\alpha}$ values, despite demonstrably feeling the effects of AGN feedback. For the purposes of our comparison to the observations, all halos will be classified as without AGN, as they do not fulfill the criteria at the time we “observe” them. In simulations, a galaxy is theoretically classified as black hole-dominated if the ratio of its black hole accretion rate to its star-formation rate exceeds 0.01, which was the case for one halo: Halo 0300. Halo 0300’s total $\log([\text{N II}]/\text{H}\alpha)$ value is -0.999 , which puts it some distance to the left of the dividing line between active and inactive galaxies in a WHAN diagram.

In the last subsection, we saw that irregularity parameters can be increased by AGN-related as well as non-AGN-related processes. This finding, that not all galaxies hosting AGN are recognized as such (at least not these galaxies, classified according to this scheme) further complicates things.

Name	$\log([\text{N II}]/\text{H}\alpha)$ (AGN)	$\log([\text{N II}]/\text{H}\alpha)$ (NoAGN)
0094	-0.730	-0.880
0175	-0.506	-0.858
0204	-0.936	-0.716
0215	-0.633	-1.176
0224	-0.694	-0.948
0227	-0.987	-0.925
0259	-0.642	-0.642
0290	-1.311	-0.796
0300	-0.999	-1.068
0305	-1.897	-0.721

Table 8 The total values of $\log([\text{N II}]/\text{H}\alpha)$ of simulated galaxies with and without AGN feedback. Each value is below -0.4 , which means that no galaxy would be classified as hosting an AGN on a WHAN diagram.

2.7.2 N II/H α profiles

The radial [N II]/H α profiles do show differences between galaxies with and without AGN feedback. Similarly to the surface density profiles shown before, galaxies with AGN feedback tend to display more irregular profiles than those without. They also exhibit a wider range of values. All in all, though, there is a more or less constant [N II]/H α presence throughout the entire radial extent, which is in line with the results of Kehrig et al. (2012), Papaderos et al. (2013), and others who have detected a ubiquitous ionized medium.

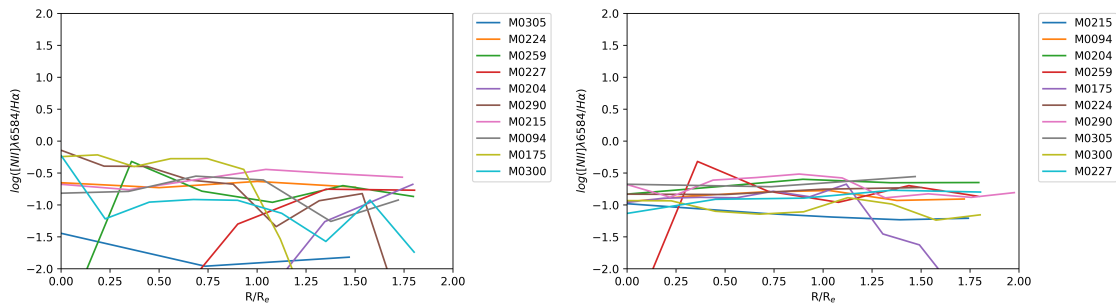


Figure 19 Radial [N II]/H α profiles for simulated galaxies with (left) and without (right) AGN feedback.

3 Observations

This section is structured similarly to Section 2. We will begin with an overview of IFS surveys before describing the specifics of CALIFA, from which the data on our observed galaxies comes. Finally, we will discuss our data sample and the results of our analyses.

3.1 IFS Surveys

In the 1990s, the first prototypes of integral-field units were developed, and the first large-scale surveys using IFS began to be carried out in the early 2000s. Over the course of the following decade, several surveys were carried out in which one galaxy was observed at a time. These surveys include SAURON (de Zeeuw et al., 2002), ATLAS^{3D} (Cappellari et al., 2011a), DiskMass (Bershady et al., 2010) and the source of the data in this thesis, CALIFA (Sánchez et al., 2012). Currently, a new generation of surveys has begun. In these multiplexed surveys, including SAMI (Bryant et al., 2015) and MaNGA (Bundy et al., 2015), multiple galaxies can be observed simultaneously, which significantly increases the total number of galaxies that can be analyzed. For a summary of the basic characteristics of these surveys, see Table 9 (Bundy et al. from 2015, their Table 3).

The role of the SAURON and ATLAS^{3D} surveys in recognizing and quantifying the difference between the two different classes of ETG kinematics has been described in the introduction and will not be repeated here. The recognition of this difference was facilitated by the higher spatial resolution of this sample compared to the other surveys. Compared to the other surveys, however, the sample is smaller and restricted to ETGs within a comparatively narrow wavelength range, choices motivated by the goal of observing mainly stellar kinematics in these galaxies.

Where ATLAS^{3D} focused mainly on ETGs, DiskMass focused mainly on late-type galaxies, specifically on the relative mass contributions of dark and baryonic matter at different radii. To accomplish this, a sample of mostly face-on galaxies was examined with an instrument setup that maximized the measurable velocity resolution (~ 14 km/s) in order to capture the stellar and gas velocity components normal to the disk plane and thus parallel to the viewer. These velocity components are difficult to measure in face-on galaxies due to most of the velocity being oriented within the disk plane.

CALIFA aimed to be the first IFS survey not to examine specific morphological types, as the previously described surveys had done, but instead to present data on a representative sample of local galaxies over their full radial extents within the full optical spectral range, albeit at the cost of somewhat lower spatial resolution than the other surveys. CALIFA will be described in more detail in the following subsection.

SAMI and MaNGA, the multiplexed surveys, use multiple IFUs in order to be able to analyze multiple galaxies simultaneously. SAMI can observe 12 galaxies and

1 standard star at the same time, while MaNGA features 17 simultaneously usable IFUs. MaNGA analyzes galaxies within fixed radial ranges (1.5 and 2.5 effective radii) with, on average, 5 spatial elements per radius, but the radial extents and spatial resolutions achieved by SAMI cover wider distributions. SAMI's spatial resolution tends to be better in the central regions of its massive galaxies, but this increased resolution does not always extend to all galaxies' outer reaches. Finally, MaNGA covers a larger wavelength range, but SAMI's spectral resolution at ~ 7000 Å is higher, circa double MaNGA's.

Specification	MaNGA	SAMI	CALIFA	DiskMass (H α)	DiskMass (stellar)	ATLAS ^{3D}
Sample size	10,000	3,400	600	146	46	260
Selection	$M_* > 10^9 M_\odot$	$M_* > 10^{8.2} M_\odot$	$45'' < D_{25} < 80''$	S/SAab-cd, b/a>0.75, $10'' < h_R < 20''$		$M_* \gtrsim 10^{9.8} M_\odot$ ^e E/S0
Redshift	0.01–0.15	0.004–0.095	0.005–0.03	0.001–0.047	0.003–0.042	$z \lesssim 0.01$
Radial coverage	$1.5 R_e(\text{P+})$ $2.5 R_e(\text{S})$	$1.1\text{--}2.9 R_e$	$1.8\text{--}3.7 R_e$	$1.4\text{--}3 R_e$	$1.1\text{--}2.3 R_e$	$0.6\text{--}1.5 R_e$
S/N ^a at $1R_e$ (per spatial sample)	14–35	12–28	10–50	6	9–16	15
λ range (nm)	360–1030	370–570 (580V) 625–735 (1000R)	375–750 (V500) 370–475 (V1200)	648–689	498–538	480–538
$\sigma_{\text{instrument}}$ (km s ⁻¹)	50–80	75 28	85 150	13	16	98
Angular sampling ^b (diameter)	2''	1''.6	2''.7	4''.7	2''.7	0''.8
Angular FWHM (reconstructed)	2''.5	2''.1 ^c	2''.5	6''	3''.5	1''.5
Spatial FWHM (physical)	$1.3\text{--}4.5 \text{ kpc}(\text{P+})$ $2.2\text{--}5.1 \text{ kpc}(\text{S})$	$1.1\text{--}2.3 \text{ kpc}$	$0.8\text{--}1.0 \text{ kpc}$	$0.4\text{--}4.2 \text{ kpc}$	$0.3\text{--}3.0 \text{ kpc}$	0.15 kpc
Spatial FWHM (in R_e)	$0.2\text{--}0.6(\text{P+})$ $0.3\text{--}0.9(\text{S})$	$0.3\text{--}0.8$	0.2	$0.2\text{--}0.4$	$0.1\text{--}0.2$	0.09
IFU fill factor With gradients measurable ^d to	56%	73%	53%	25%	53%	100%
1.0 R_e :	4070	720	580	128	39	112
1.5 R_e :	6050	790	521	122	20	47
2.0 R_e :	2570	680	462	80	5	26
2.5 R_e :	2340	460	340	26	0	13
3.0 R_e :	670	350	111	3	0	1

Table 9 When ranges are given (other than redshift and wavelength), we use 20th and 80th percentile estimates. D_{25} is related to the SDSS “isoA_r” major-axis diameter of the 25 AB arcsec⁻² r -band isophote. For MaNGA and SAMI, radii are defined in terms of R_e as measured for Sérsic fits performed in the NASA Sloan Atlas. For CALIFA, half-light radii were remeasured from the imaging data by the CALIFA team, and for DiskMass, R_e are estimated from measured disk radial scale lengths (h_R) adopting $R_e/h_R \sim 1.67$ (Lackner and Gunn, 2012). For MaNGA, “P+” refers to the Primary+ Sample which accounts for $\sim 2/3$ of the survey targets. The Secondary sample ($\sim 1/3$) is designated by “S.”

^a S/N is given per λ resolution element, per spatial element (e.g., per fiber), in the r -band.

^b The angular sampling diameter is either that of a fiber or the width of the lenslet in the case of ATLAS^{3D}.

^c The expected SAMI FWHM averaged over the full survey is 2''.1 (S. Croom, private communication). Results from the first year indicate a value of 2''.4 (Sharp et al., 2015).

^d A target galaxy is defined to have a “measurable gradient” within the specified radius if the IFU field-of-view covers this radius with more than 2.5 spatial resolution elements with size given by the reconstructed FWHM. In the case of MaNGA, the same galaxy may be included in multiple bins (i.e., the total number of measurable gradients is ~ 1.5 times the final sample size). For SAMI, the bins are unique.

^e This is only approximate. ATLAS^{3D} selected visually-classified early-type galaxies with $M_K < -21.5$, $D < 42\text{Mpc}$, $|\text{Dec} - 29^\circ| < 35^\circ$, and $|b| > 15^\circ$. (from Bundy et al. 2015, their Table 3).

3.2 CALIFA

The Calar Alto Legacy Integral Field Area (CALIFA) survey was designed to characterize a statistically significant portion of the galaxies in the Local Universe by examining galaxies of all morphological types, all across the luminosity function and exhibiting a wide range of other possible characteristics, over their full radial extents, in terms of the emission characteristics of their ionized gas, the kinematics of their gas and stars, and the properties of their stellar populations. According to these specifications, an initial “mother sample” of 937 galaxies located at redshifts between 0.005 and 0.03 was identified, from which the final sample of 667 galaxies was drawn based on their visibilities. Most ($\sim 2/3$) of these galaxies ended up being disk-dominated, including interacting and irregular galaxies, with the remaining ~ 200 galaxies being early types. The majority of the galaxies in the sample are field galaxies, with some galaxies belonging to groups as well as the Coma cluster. There is still some selection bias present, despite the stated goal of representing all galaxy types, with the sample skewing toward more massive, brighter galaxies.

Once a galaxy is selected, it is observed using the PMAS/PPak (Roth et al., 2005; Kelz et al., 2006) spectrograph, which is mounted at the Calar Alto observatory on the 3.5m telescope and features a $74'' \times 62''$ hexagonal field of view, with 331 fibers of $2.7''$ diameter each, sampling the FOV and a further 36 fibers sampling the sky around the FOV. Observations are carried out in a low-spectral-resolution (V500, with $R \sim 850$ and a spectral coverage between $3750\text{-}7500 \text{ \AA}$) and a medium-spectral-resolution (V1200, with $R \sim 1700$ and a spectral coverage between $3700\text{-}4200 \text{ \AA}$) mode, with two to three dithered exposures per mode. The resulting data are then processed by means of the CALIFA pipeline (Husemann et al., 2013), in which cosmic rays are removed, flux calibration is carried out, extinction effects are corrected and the data are interpolated onto a $78'' \times 72''$ grid. The resulting data, as more and more galaxies are observed in the course of the survey, are provided to the community in the form of data cubes which comprise regular Data Releases, the most recent of which is DR3 in the spring of 2016 (Sánchez et al., 2016).

In Sánchez et al. (2012), the authors of the collaboration prove that their data meets the goals outlined in their proposal and is of lasting, legacy value to the community. A number of publications have since made use of the data, on such topics as the mass-metallicity relation (González Delgado et al., 2014a), stellar age gradients (Sánchez-Blázquez et al., 2014), aperture effects (Iglesias-Páramo et al., 2013) or investigations into the nature of the excitation mechanisms of the ionized medium of early-type galaxies (Kehrig et al., 2012; Papaderos et al., 2013; Gomes et al., 2016).

3.3 Observational Sample and Methods

A portion (~ 120) of the early-type galaxies with V500 CALIFA data available were selected for further study. Some of these galaxies have been analyzed in the course of the previously mentioned studies by Papaderos et al. and Gomes et al. In order to perform the emission analyses described in these studies, the CALIFA data were processed spaxel-by-spaxel by means of a pipeline developed by Papaderos et al. called PORTO3D (Kehrig et al., 2012; Gomes et al., 2016), designed to carry out post-processing and spectral fitting of IFS data. PORTO3D works in the following way: first, after data quality assessments are carried out, individual spectra are extracted from the data cubes. These spectra are then fitted using the stellar population synthesis code STARLIGHT (Cid Fernandes et al., 2005) and the resulting stellar fits are subtracted from the spectra, resulting in emission lines as well as the properties (e.g. ages and metallicities) of the best-fitting stellar populations. All in all, for each galaxy in the sample there is a data cube with a two-dimensional map each for stellar velocities, median-smoothed stellar velocities, errors to stellar velocities, stellar velocity dispersions, $H\alpha$ -emitting gas velocities, smoothed velocities, velocity errors, velocity dispersions, $H\alpha$ fluxes and equivalent widths and the $[N II]/H\alpha$ ratio in every spaxel. At the typical distances of the galaxies, the pixel scale of $1'' \times 1''$ corresponds to a spatial resolution of roughly 1 kpc/pixel. For an overview of each galaxy, including characteristic parameters and stellar and gas velocity maps, see Subsection 6.2.

The data were then analyzed in the manner described in Subsection 1.2, as previously done with the simulated data. Because the distinction between galaxies with AGN and those without was not known a priori, as with the simulated galaxies, galaxies were first placed on a WHAN diagram (Subsubsection 3.5.1) and those meeting the criteria for either weak or strong AGN were selected as AGN-hosting galaxies, with the rest treated as non-AGN-hosting. Values for the irregularity parameters $k_{3,5}/k_1$, $\Delta\phi$, and σ_{PA} as well as the specific angular momentum λ_R were calculated for AGN and non-AGN galaxies, radial profiles of the $H\alpha$ equivalent width as well as $[N II]/H\alpha$ flux ratios were calculated, and models of the stellar and gas rotation were generated and subtracted from the respective kinematic maps, with the residuals analyzed with regard to their asymmetry. The results of these analyses are presented in the following sections. Five galaxies (IC1079, NGC0677, NGC0741, NGC4874, and NGC6173) were too large to allow the calculation of irregularity parameters. For these galaxies, only the asymmetries of the residuals and the emission-line profiles were generated.

3.4 Results from Kinematic Analysis

3.4.1 Irregularity Parameters and λ_R

This subsection is structured similarly to the corresponding subsection in the Simulations section (2.6.1), but there is one important difference. In the last section, we separated galaxies into those with AGN feedback and those without. We cannot do this for our observed galaxies, and so we separate them into those classified as hosting AGN at the time of observation and those not hosting AGN, by means of WHAN analysis. Figure 21 shows histograms for the values of λ_R as well as the irregularity parameters $k_{3,5}/k_1$, $\Delta\phi$, and σ_{PA} for our observed galaxies classified as AGN-hosting and non-AGN hosting. Figure 22 shows scatter plots in which galaxies' λ_R values are plotted against the values of each of the irregularity parameters, while Figure 23 shows each of the irregularity parameters plotted against each other. Finally, Tables 13 and 14 list the values of each of these parameters for each observed galaxy. As before, we will briefly discuss our results here, then discuss them in more detail in Section 4.

A first examination of the values of the irregularity parameters across the full radial extent of each galaxy, not just the effective radius (Fig. 20), has revealed that the values can change significantly depending on the radius at which they are measured. For the most part, lower radii result in lower values for irregularity parameters, but the variation is much higher than it is for the simulated galaxies. Future work will take this fact into account.

Table 10 lists the average values and standard deviations of λ_R and the irregularity parameters for observed galaxies with and without current AGN activity. Here, λ_R is lower for galaxies currently experiencing AGN feedback, but the values of the irregularity parameters (with the exception of $\Delta\phi$) are also lower. There is a difference between our λ_R values and those in the literature (e.g. Falc3n-Barroso et al. 2015) for some of our objects. All of our objects are classified as fast rotators, whereas this is not the case in the literature. We believe that the differences arise due to the fact that the values in the literature were calculated within the elliptical effective radius of radially binned data which was not post-processed by PORTO3D as ours was.

Table 11 lists the correlation coefficients of λ_R vs. each of the irregularity parameters. For the most part, there seems to be no significant correlation between λ_R and any of the parameters in either case, except for a negative correlation between λ_R and $\Delta\phi$ and a slight positive correlation between λ_R and σ_{PA} .

Table 12 lists the correlation coefficients of each of the irregularity parameters vs. each other. Parameters seem to be more strongly anti-correlated in the cases without ongoing AGN activity.

Judging by the σ_{PA} vs. $k_{3,5}/k_1$ plot, 0/6 galaxies with current AGN activity fall within the ‘‘ordered’’ parameter range, as opposed to 2/106 without. For σ_{PA} vs. $\Delta\phi$, the numbers are 0/6 with and 2/106 without current AGN activity, and for

$k_{3,5}/k_1$ vs. $\Delta\phi$ the numbers are 0/6 with current activity and 4/106 without.

Of the galaxies with current AGN activity, NGC0160 is regular with respect to $\Delta\phi$, as both the stellar and gas components seem to rotate in more or less the same plane. NGC0932 is regular with respect to $k_{3,5}/k_1$, and its gas kinematics do seem to be more or less orderly. Each of these galaxies' other irregularity parameters, however, and all three of the other four galaxies' parameters, fall within the irregular range. On average, there are 0.33 regular parameters per galaxy.

There are more regular galaxies among those without current AGN activity, but a greater amount of irregular galaxies as well. 15 galaxies are regular with respect to one parameter (most commonly $\Delta\phi$), 4 were regular with respect to 2 parameters, and one (NGC7722) was regular with respect to all three. The greater number of galaxies irregular in all parameters, however, means that the average number of regular parameters per galaxy is 0.27, slightly lower than for galaxies with ongoing AGN activity.

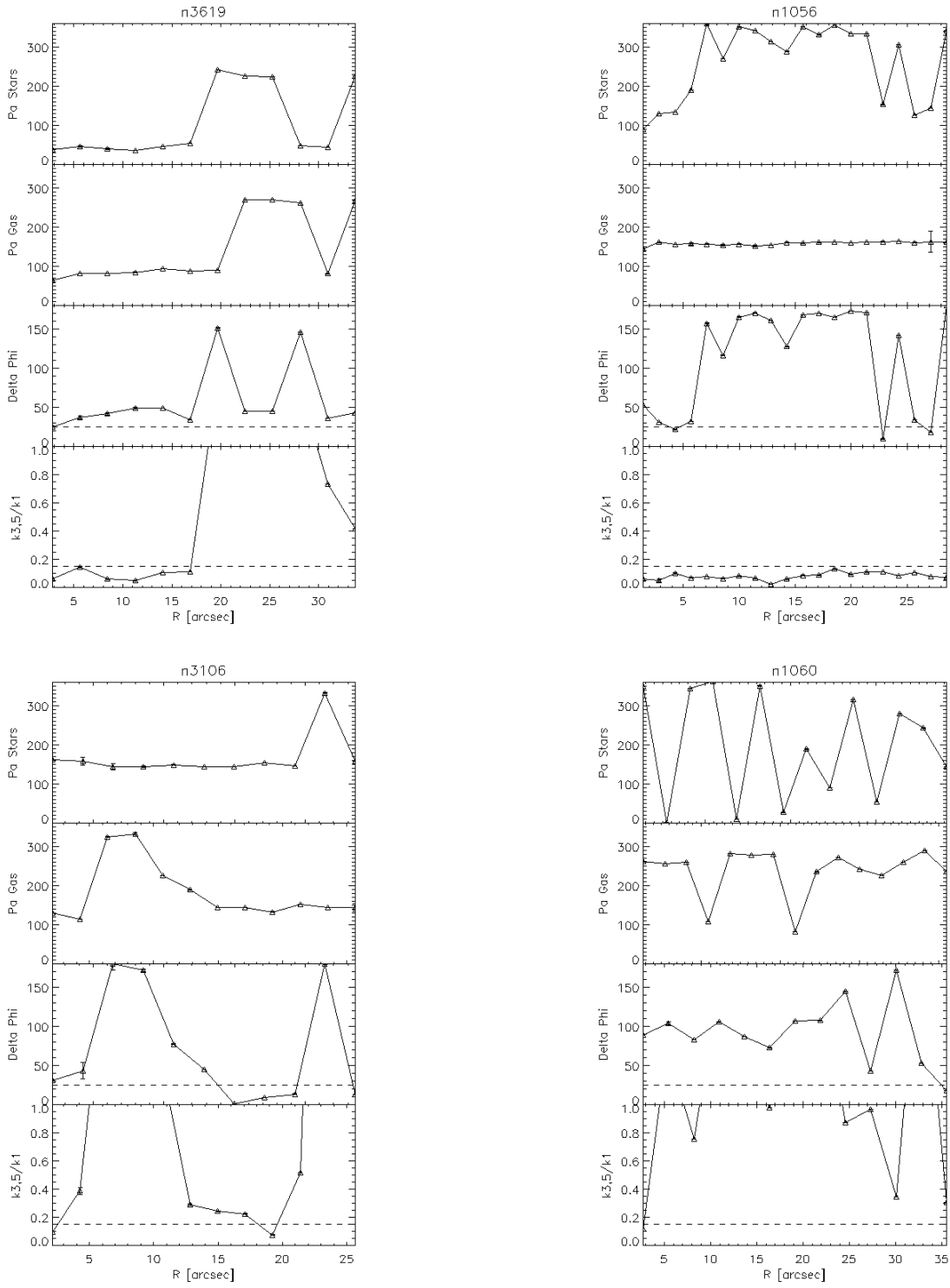


Figure 20 The values of the stellar position angle, the gas position angle, $\Delta\phi$, and $k_{3.5}/k_1$, at increments of $0.1 \cdot r_e$ between 0.1 and $2 r_e$, for NGC 3619 (top left), NGC 1056 (top right), NGC 3106 (bottom left), and NGC 1060 (bottom right). The value of the irregularity parameters can vary significantly as a function of radius.

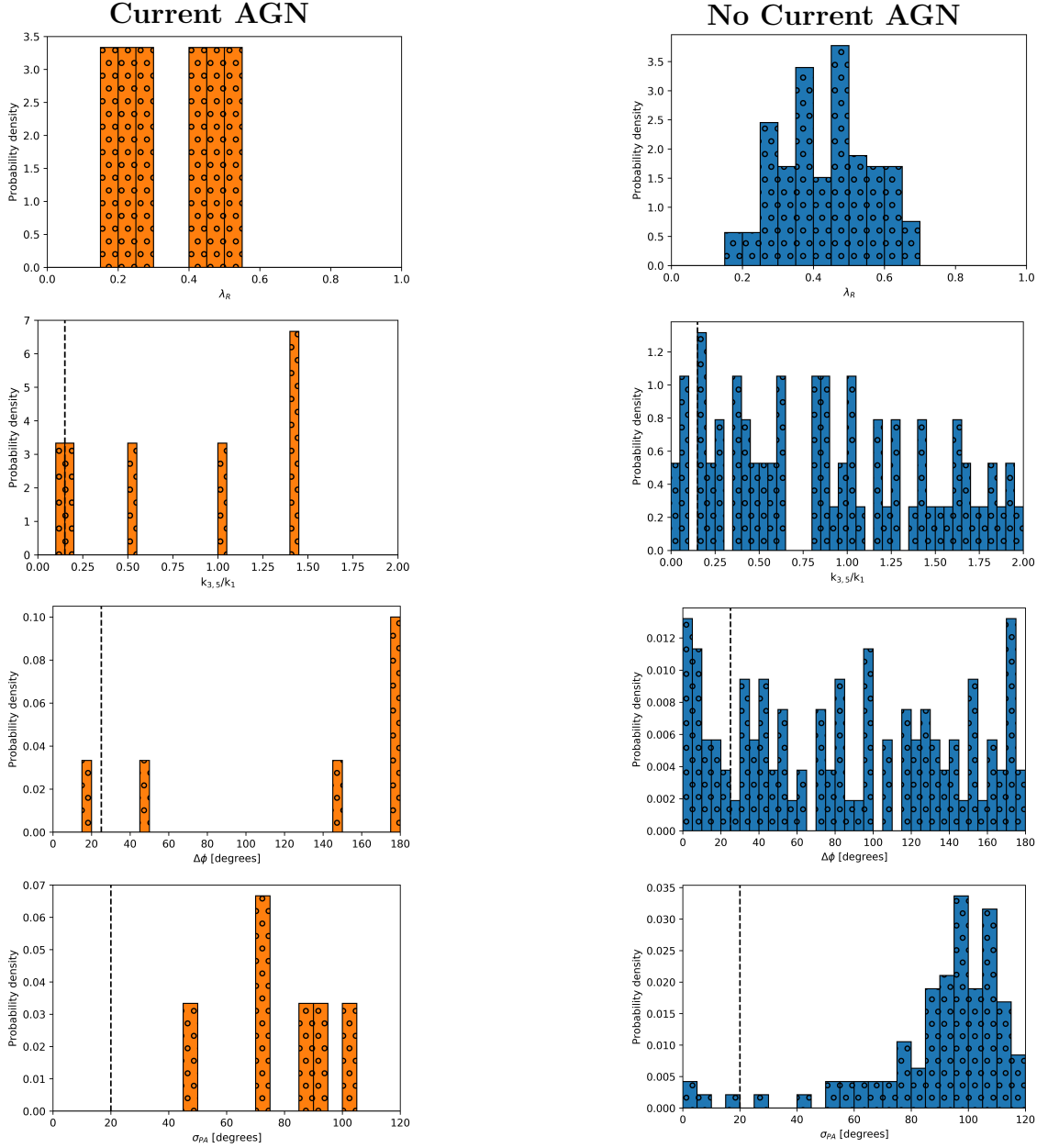


Figure 21 Histograms of $k_{3,5}/k_1$ (top row), $\Delta\phi$ (middle row), and σ_{PA} (bottom row), for observed galaxies with (left column) and without (right column) current AGN activity.

	$\mu(\lambda_R)$	$\sigma(\lambda_R)$	$\mu(k_{3,5}/k_1)$	$\sigma(k_{3,5}/k_1)$	$\mu(\Delta\phi)$	$\sigma(\Delta\phi)$	$\mu(\sigma_{PA})$	$\sigma(\sigma_{PA})$
AGN	0.351	0.127	0.78	0.53	125	67	79	17
NoAGN	0.434	0.125	1.66	1.49	85	57	94	26

Table 10 Means and standard deviations of λ_R and irregularity parameters for observed galaxies with and without current AGN activity.

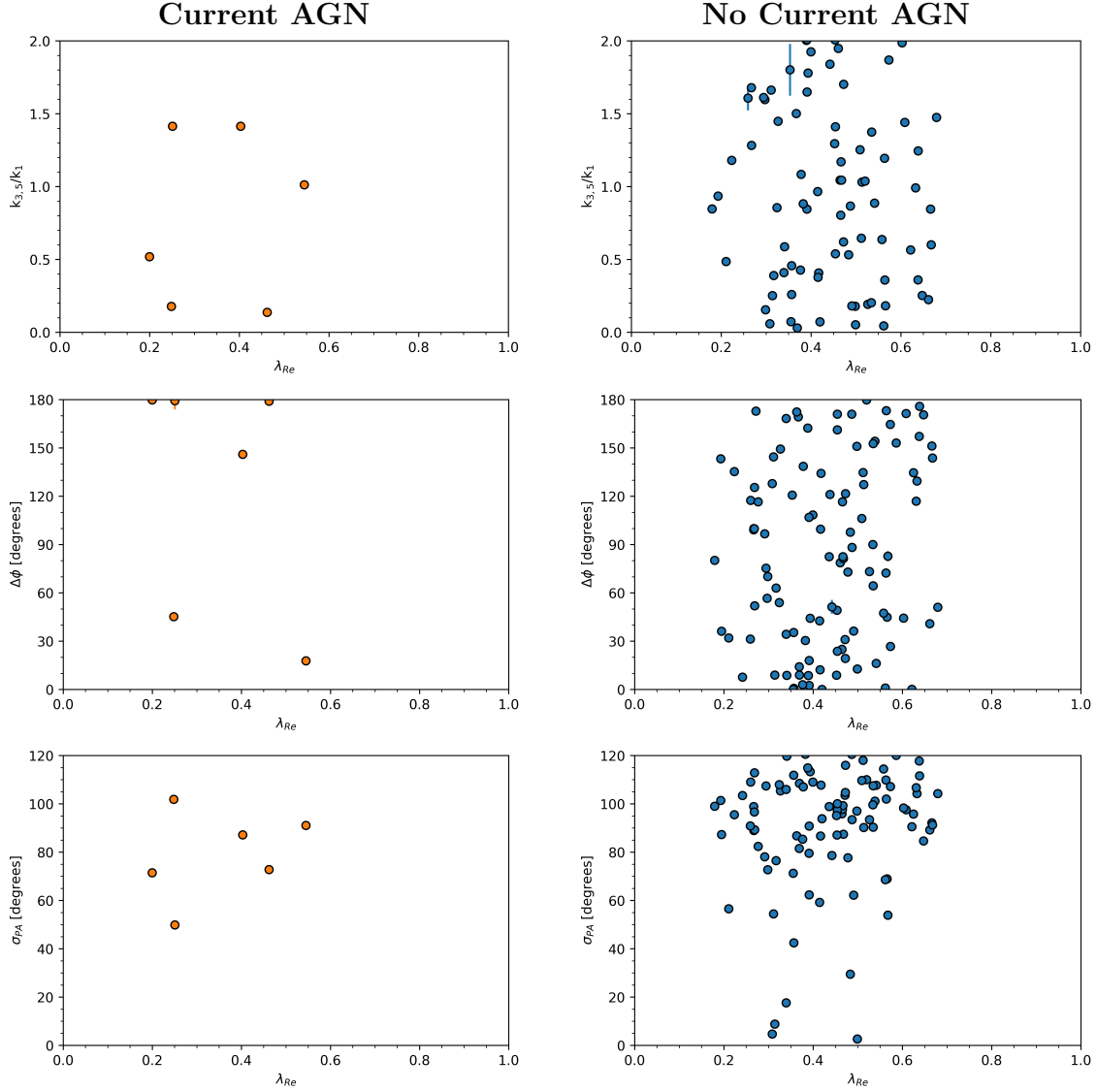


Figure 22 λ_R vs each of the irregularity parameters $k_{3,5}/k_1$ (top row), $\Delta\phi$ (middle row), and σ_{PA} (bottom row), for observed galaxies with (left column) and without (right column) current AGN activity.

	λ_R vs. $k_{3,5}/k_1$	λ_R vs. $\Delta\phi$	λ_R vs. σ_{PA}
AGN	0.110	-0.376	0.298
NoAGN	-0.103	0.161	0.116

Table 11 The values of the Pearson correlation coefficient for λ_R vs. each of the irregularity parameters.

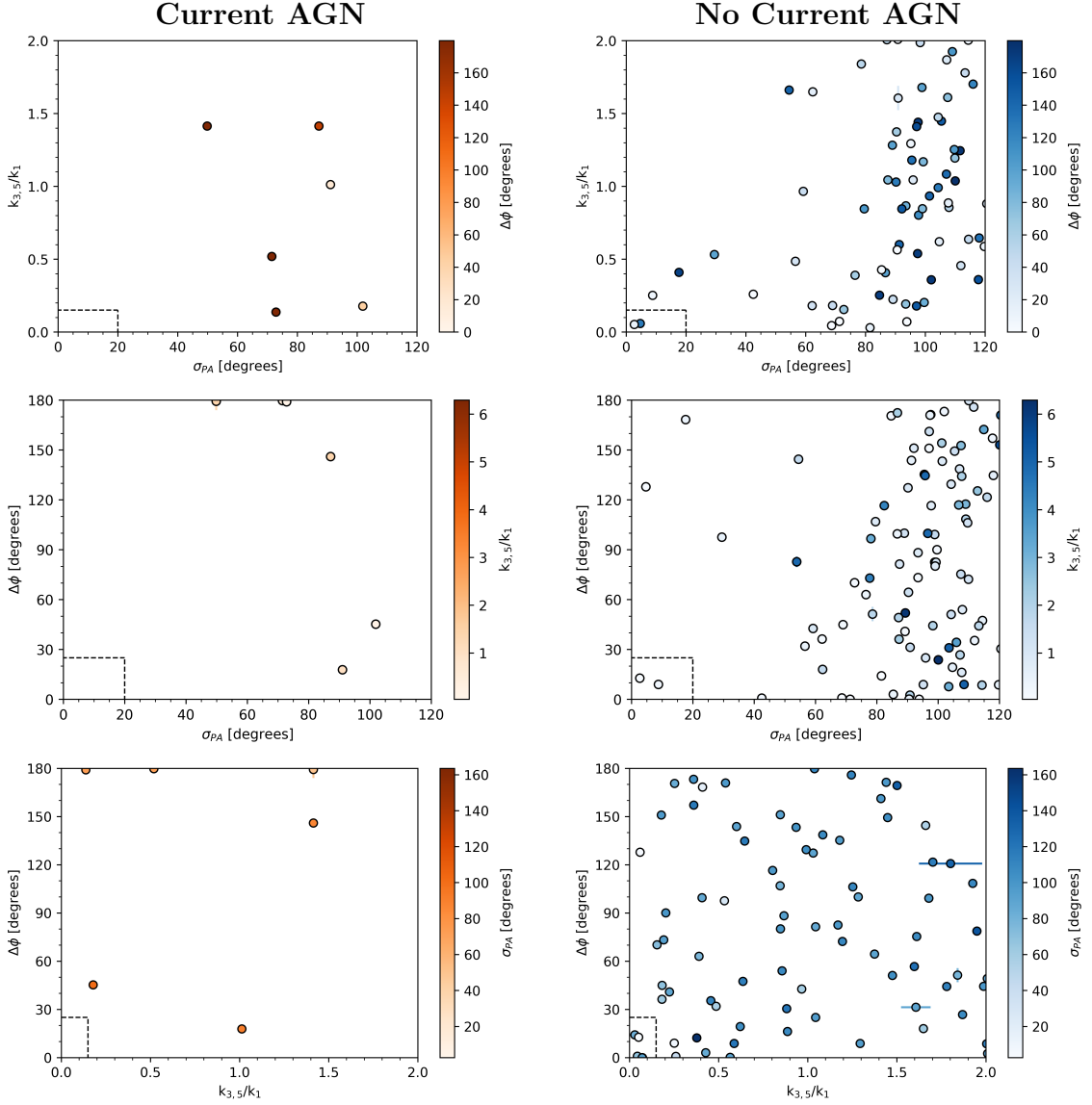


Figure 23 σ_{PA} vs. $k_{3,5}/k_1$ (top row), σ_{PA} vs. $\Delta\phi$ (middle row), and $k_{3,5}/k_1$ vs. $\Delta\phi$ (bottom row), for observed galaxies with (left column) and without (right column) current AGN activity.

	σ_{PA} vs. $k_{3,5}/k_1$	σ_{PA} vs. $\Delta\phi$	$k_{3,5}/k_1$ vs. $\Delta\phi$
AGN	-0.343	-0.781	0.101
NoAGN	0.250	0.194	0.120

Table 12 The values of the Pearson correlation coefficient for each combination of irregularity parameters.

Name	r_e (")	λ_{Re}	Fast/Slow	r_{max}/r_e	$k_{3,5}/k_1$	$\Delta\phi$	σ_{PA}	# Reg.
NGC0160	22.176	0.545	Fast	1.6	1.01 ± 0.0	$18^* \pm 0$	91	1
NGC0932	18.612	0.462	Fast	1.8	$0.14^* \pm 0.0$	179 ± 1	73	1
NGC1349	17.028	0.251	Fast	1.3	1.41 ± 0.0	179 ± 5	50	0
NGC3106	21.384	0.200	Fast	1.2	0.52 ± 0.0	180 ± 1	71	0
NGC3619	28.116	0.403	Fast	1.2	1.41 ± 0.0	146 ± 0	87	0
UGC10205	19.404	0.248	Fast	1.1	0.18 ± 0.0	45 ± 0	102	0
Mean		0.351		1.4	0.78 ± 0.00	125 ± 1	79	0.33

Table 13 The values of λ_{Re} and the irregularity parameters for observed galaxies with current AGN activity. Starred values for irregularity parameters indicate that these values lie within their respective ranges signifying “regular” kinematics. The last column indicates the number of irregularity parameters that exhibit values within the regular range for each galaxy.

Name	r_e (")	λ_{Re}	Fast/Slow	r_{max}/r_e	$k_{3,5}/k_1$	$\Delta\phi$	σ_{PA}	# Reg.
IC2341	11.088	0.498	Fast	1.8	0.18 ± 0.0	151 ± 0	97	0
IC4534	13.464	0.603	Fast	2.0	1.99 ± 0.0	44 ± 0	98	0
LSBCF560	8.370	0.464	Fast	2.0	1.04 ± 0.0	$25^* \pm 0$	96	1
NGC0155	15.84	0.513	Fast	2.0	1.03 ± 0.0	127 ± 0	90	0
NGC0364	15.84	0.609	Fast	2.0	1.44 ± 0.0	171 ± 0	98	0
NGC0472	4.620	0.661	Fast	2.0	0.22 ± 0.0	41 ± 1	89	0
NGC0499	21.384	0.378	Fast	1.6	1.08 ± 0.0	139 ± 0.0	107	0
NGC0517	10.296	0.573	Fast	2.0	2.68 ± 0.0	165 ± 1	141	0
NGC0528	12.276	0.520	Fast	2.0	1.04 ± 0.0	180 ± 0	110	0
NGC0529	12.672	0.541	Fast	2.0	0.89 ± 0.0	$16^* \pm 0$	108	1
NGC0731	11.484	0.558	Fast	2.0	0.64 ± 0.0	47 ± 1	114	0
NGC0774	12.276	0.562	Fast	2.0	$0.04^* \pm 0.0$	$1^* \pm 1$	69	2
NGC0810	17.424	0.324	Fast	2.0	0.86 ± 0.0	54 ± 0	108	0
NGC0842	11.484	0.534	Fast	2.0	0.20 ± 0.0	90 ± 0.0	100	0
NGC0924	12.672	0.638	Fast	2.0	0.36 ± 0.0	157 ± 0.0	118	0
NGC0938	13.86	0.526	Fast	2.0	0.19 ± 0.0	73 ± 1	93	0
NGC0962	13.86	0.472	Fast	2.0	5.12 ± 0.0	31 ± 2	104	0
NGC1026	17.424	0.454	Fast	1.9	1.41 ± 0.0	161 ± 0	97	0
NGC1041	17.028	0.269	Fast	2.0	6.17 ± 0.0	52 ± 0	89	0
NGC1056	14.256	0.308	Fast	2.0	$0.06^* \pm 0.0$	128 ± 1	5*	2
NGC1060	27.324	0.415	Fast	1.5	0.97 ± 0.0	43 ± 0	59	0
NGC1132	32.868	0.369	Fast	1.0	5.11 ± 0.0	$9^* \pm 0$	108	1
NGC1167	24.948	0.339	Fast	1.1	0.41 ± 0.0	168 ± 0	18*	1
NGC1270	5.048	0.467	Fast	2.0	1.17 ± 0.0	82 ± 0	99	0
NGC1361	16.236	0.340	Fast	2.0	3.55 ± 0.0	34 ± 0	106	0
NGC1656	17.424	0.679	Fast	2.0	1.48 ± 0.0	51 ± 0	104	0
NGC1665	23.76	0.631	Fast	1.4	2.93 ± 0.0	117 ± 0	107	0

Continued on next page

Table 14 – *Continued from previous page*

Name	r_e (")	λ_{Re}	Fast/Slow	r_{max}/r_e	$k_{3,5}/k_1$	$\Delta\phi$	σ_{PA}	#	Reg.
NGC1666	12.276	0.621	Fast	2.0	0.56 ± 0.0	$0^* \pm 0$	91	0	
NGC2476	9.504	0.564	Fast	2.0	0.36 ± 0.0	173 ± 0	102	0	
NGC2507	19.8	0.472	Fast	1.6	0.62 ± 0.0	19 ± 0	105	0	
NGC2513	26.532	0.298	Fast	1.5	$0.15^* \pm 0.0$	70 ± 0	73	1	
NGC2577	17.424	0.573	Fast	1.5	1.87 ± 0.0	27 ± 0	107	0	
NGC2592	9.9	0.563	Fast	2.0	1.19 ± 0.0	72 ± 0	110	0	
NGC2767	5.716	0.568	Fast	2.0	4.92 ± 0.0	83 ± 3	54	0	
NGC2918	12.276	0.269	Fast	2.0	2.52 ± 0.24	125 ± 0	113	0	
NGC3158	32.473	0.388	Fast	1.2	3.36 ± 0.0	162 ± 0	115	0	
NGC3182	17.424	0.454	Fast	2.0	6.29 ± 0.0	$24^* \pm 0$	100	1	
NGC3300	13.86	0.391	Fast	1.7	0.85 ± 0.02	107 ± 1	80	0	
NGC3610	13.86	0.512	Fast	2.0	0.65 ± 0.0	135 ± 0	118	0	
NGC3615	15.444	0.317	Fast	1.8	0.39 ± 0.02	63 ± 0	76	0	
NGC3990	5.918	0.647	Fast	2.0	0.25 ± 0.0	171 ± 3	85	0	
NGC4003	14.256	0.416	Fast	1.7	0.38 ± 0.01	$12^* \pm 1$	164	1	
NGC4841a	20.592	0.242	Fast	1.8	3.12 ± 0.0	$8^* \pm 0$	103	1	
NGC4956	9.504	0.491	Fast	2.0	0.18 ± 0.01	36 ± 1	62	0	
NGC5029	25.344	0.417	Fast	1.4	0.41 ± 0.0	100 ± 0	87	0	
NGC5198	16.236	0.391	Fast	2.0	2.01 ± 0.0	$3^* \pm 0$	91	1	
NGC5216	20.196	0.483	Fast	1.7	0.53 ± 0.0	98 ± 0	29	0	
NGC5423	15.444	0.393	Fast	2.0	1.78 ± 0.0	44 ± 0	113	0	
NGC5473	17.82	0.418	Fast	1.9	2.10 ± 0.0	134 ± 0	108	0	
NGC5481	5.918	0.291	Fast	2.0	3.18 ± 0.0	97 ± 0	78	0	
NGC5485	31.68	0.391	Fast	1.2	1.65 ± 0.0	$18^* \pm 0$	62	1	
NGC5513	15.84	0.535	Fast	2.0	1.37 ± 0.0	64 ± 0	90	0	
NGC5532	24.552	0.341	Fast	1.6	0.59 ± 0.0	$9^* \pm 0$	120	1	
NGC5546	17.424	0.327	Fast	2.0	1.45 ± 0.0	149 ± 0	105	0	
NGC5549	14.652	0.454	Fast	2.0	2.01 ± 0.0	49 ± 0	87	0	
NGC5557	24.552	0.363	Fast	1.4	2.18 ± 0.0	172 ± 0	87	0	
NGC5580	15.048	0.625	Fast	2.0	4.94 ± 0.0	135 ± 0	96	0	
NGC5598	9.108	0.442	Fast	2.0	1.84 ± 0.0	51 ± 4	79	0	
NGC5611	7.92	0.461	Fast	2.0	1.95 ± 0	79 ± 1	141	0	
NGC5623	15.444	0.277	Fast	2.0	4.29 ± 0.0	117 ± 0	82	0	
NGC5631	19.008	0.566	Fast	1.8	0.18 ± 0.0	45 ± 0	69	0	
NGC5642	18.612	0.267	Fast	1.9	1.28 ± 0.0	100 ± 0	89	0	
NGC5684	17.82	0.260	Fast	2.0	2.94 ± 0.0	117 ± 0	109	0	
NGC5687	25.344	0.297	Fast	1.5	1.60 ± 0.0	57 ± 0	124	0	
NGC5784	13.464	0.369	Fast	2.0	$0.03^* \pm 0.0$	$14^* \pm 0$	81	2	
NGC5797	18.612	0.539	Fast	1.8	2.14 ± 0.0	154 ± 0	101	0	

Continued on next page

Table 14 – *Continued from previous page*

Name	r_e (")	λ_{Re}	Fast/Slow	r_{max}/r_e	$k_{3,5}/k_1$	$\Delta\phi$	σ_{PA}	#	Reg.
NGC5928	15.84	0.399	Fast	2.0	1.93 ± 0.0	108 ± 0	109	0	
NGC5966	18.612	0.436	Fast	1.7	2.37 ± 0.0	82 ± 0	99	0	
NGC6020	19.008	0.195	Fast	1.9	2.24 ± 0.0	36 ± 0	87	0	
NGC6021	9.504	0.420	Fast	2.0	$0.07^* \pm 0.0$	$0^* \pm 1$	94	2	
NGC6023	8.940	0.180	Fast	2.0	0.85 ± 0.0	80 ± 0	99	0	
NGC6081	12.276	0.357	Fast	1.5	0.26 ± 0.01	$1^* \pm 1$	42	1	
NGC6125	21.78	0.267	Fast	1.7	1.68 ± 0.00	99 ± 0	99	0	
NGC6146	15.048	0.211	Fast	1.4	0.49 ± 0.00	32 ± 1	57	0	
NGC6150	11.88	0.535	Fast	2.0	2.74 ± 0.00	153 ± 0	107	0	
NGC6278	11.088	0.487	Fast	2.0	0.87 ± 0.00	88 ± 0	93	0	
NGC6146	15.048	0.211	Fast	1.4	0.49 ± 0.00	32 ± 1	57	0	
NGC6338	28.116	0.311	Fast	1.2	1.66 ± 0.00	144 ± 0	54	0	
NGC6411	34.056	0.223	Fast	1.1	1.18 ± 0.00	135 ± 0	95	0	
NGC6427	8.316	0.466	Fast	2.0	0.80 ± 0.00	117 ± 2	98	0	
NGC6515	19.008	0.478	Fast	1.8	4.38 ± 0.00	73 ± 1	78	0	
NGC6762	9.504	0.376	Fast	2.0	0.43 ± 0.00	$3^* \pm 0$	85	1	
NGC7025	13.464	0.314	Fast	2.0	0.25 ± 0.00	$9^* \pm 0$	9^*	2	
NGC7194	17.82	0.509	Fast	1.8	1.25 ± 0.00	106 ± 0	110	0	
NGC7236	14.652	0.259	Fast	1.6	1.61 ± 0.08	31 ± 0	91	0	
NGC7436B	27.72	0.193	Fast	1.1	0.94 ± 0.00	143 ± 0	101	0	
NGC7550	24.552	0.268	Fast	1.4	1.04 ± 0.00	81 ± 0	87	0	
NGC6146	15.048	0.211	Fast	1.4	0.49 ± 0.00	32 ± 1	57	0	
NGC7559b	9.957	0.666	Fast	2.0	0.85 ± 0.00	151 ± 0	92	0	
NGC7562	20.988	0.383	Fast	1.8	0.88 ± 0.00	30 ± 0	121	0	
NGC7611	11.088	0.633	Fast	2.0	0.99 ± 0.00	129 ± 1	104	0	
NGC7619	35.64	0.389	Fast	1.1	2.00 ± 0.00	$9^* \pm 0$	114	1	
NGC6146	15.048	0.211	Fast	1.4	0.49 ± 0.00	32 ± 1	57	0	
NGC7671	11.088	0.356	Fast	2.0	0.46 ± 0.00	35 ± 0	112	0	
NGC7683	14.256	0.586	Fast	2.0	5.65 ± 0.00	153 ± 0	120	0	
NGC7711	15.048	0.472	Fast	1.6	1.70 ± 0.00	122 ± 0	116	0	
NGC7722	21.384	0.499	Fast	1.5	$0.05^* \pm 0.00$	$13^* \pm 0$	3^*	3	
NGC6146	15.048	0.211	Fast	1.4	0.49 ± 0.00	32 ± 1	57	0	
UGC0029	17.028	0.294	Fast	1.6	1.61 ± 0.00	75 ± 0	107	0	
UGC3960	8.879	0.638	Fast	2.0	1.25 ± 0.00	176 ± 1	112	0	
UGC5771	12.672	0.355	Fast	2.0	$0.07^* \pm 0.00$	$0^* \pm 0$	71	2	
UGC8234	8.316	0.353	Fast	2.0	1.80 ± 0.18	121 ± 0	131	0	
UGC9518	11.484	0.438	Fast	2.0	2.69 ± 0.00	121 ± 0	125	0	
UGC10097	14.652	0.454	Fast	2.0	0.54 ± 0.00	170 ± 0	97	0	
UGC10693	22.968	0.452	Fast	1.6	1.29 ± 0.00	$9^* \pm 0$	95	1	

Continued on next page

Table 14 – *Continued from previous page*

Name	r_e (")	λ_{Re}	Fast/Slow	r_{max}/r_e	$k_{3,5}/k_1$	$\Delta\phi$	σ_{PA}	#	Reg.
UGC10695	24.552	0.667	Fast	1.3	0.60 ± 0.00	144 ± 1	91	0	
UGC10905	15.444	0.367	Fast	2.0	1.50 ± 0.00	169 ± 0	134	0	
UGC11228	12.276	0.486	Fast	2.0	4.81 ± 0.00	171 ± 0	120	0	
UGC11958	13.464	0.268	Fast	1.9	4.93 ± 0.00	100 ± 0	97	0	
UGC12127	36.432	0.272	Fast	1.0	4.37 ± 0.00	173 ± 0	123	0	
Mean		0.434		1.8	1.66 ± 0.01	85 ± 0	94	0.27	

Table 14: The values of λ_{Re} and the irregularity parameters for observed galaxies without current AGN activity. Starred values for irregularity parameters indicate that these values lie within their respective ranges signifying “regular” kinematics. The last column indicates the number of irregularity parameters that exhibit values within the regular range for each galaxy.

3.4.2 Residual Asymmetries

Figure 24 shows histograms of the asymmetries of the residuals generated by subtracting the full rotation model generated by kinemetry from the gas velocity fields of observed galaxies with and without current AGN activity. The means and standard deviations of the asymmetries are given in Table 15. As before, we expect the asymmetries to be higher in the case of current AGN activity, as the kinematics are subject to additional turbulence. With current AGN activity, the asymmetries range from 0.769 to 0.982, with a mean of 0.875. Without current AGN activity, the asymmetries range from 0.705 to 1.000, with a mean of 0.848.

Also as before, the mean asymmetry for galaxies with AGN feedback is very slightly higher than those without, but the difference is not significant.

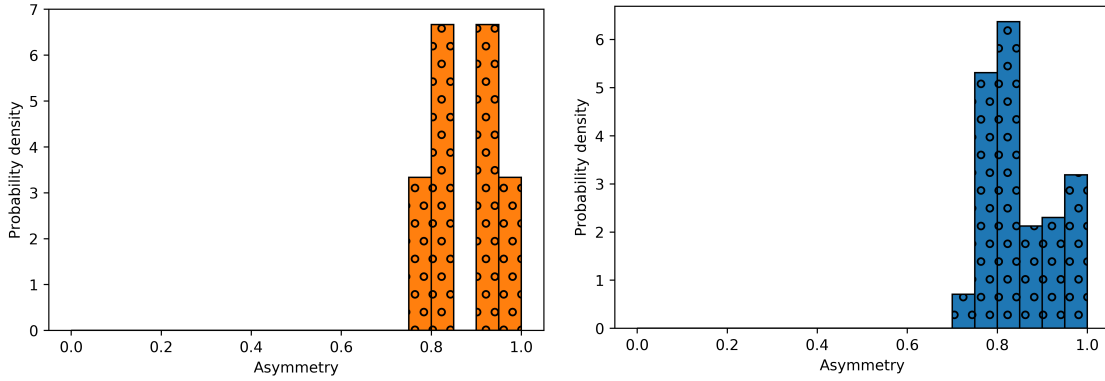


Figure 24 Histograms for the asymmetries of the residuals generated by subtracting the full rotation model generated by kinemetry from the observed gas velocity fields for galaxies with (left) and without (right) current AGN activity.

	μ (Asymmetry)	σ (Asymmetry)
AGN	0.875	0.075
NoAGN	0.848	0.075

Table 15 The means and standard deviations of the asymmetries of the residuals generated by subtracting models of the rotation of the gas velocity fields of observed galaxies with and without current AGN activity.

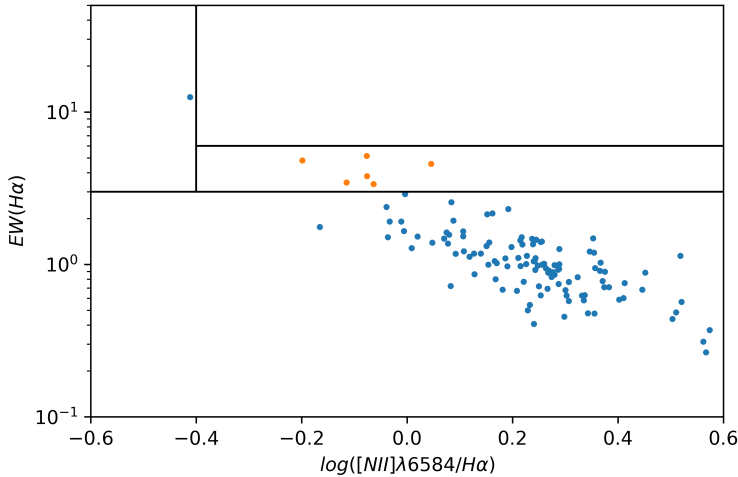


Figure 25 A WHAN diagram for our observational data sample. Galaxies characterized as either strong or weak AGN, and thus currently subject to AGN activity, are plotted in orange, and the rest are plotted in blue.

3.5 Results from Nebular Emission Analysis

3.5.1 WHAN Analysis

Figure 25 shows the WHAN diagram based on our observational data. Only six galaxies (NGC0160, NGC0932, NGC1349, NGC3106, NGC3619, and UGC10205) meet the criteria for current AGN activity, and all six fall within the “weak AGN” parameter range, with no “strong AGN” objects. We consider these six objects to be currently affected by AGN activity and the rest to be currently unaffected, but stress our previous point that a galaxy may have been affected by AGN feedback at points in its past, even if it does not currently indicate this. Furthermore, an AGN can be currently active to the point that it drives outflows, but it may still avoid detection due to fluctuations in activity that take place over small time-scales.

3.5.2 $EW(H\alpha)$ and $NII/H\alpha$ profiles

The ubiquitous ionized component described by Kehrig et al. (2012), Papaderos et al. (2013), and others is also on display here. Galaxies with and without current AGN activity feature mostly constant $[NII]/H\alpha$ and $EW(H\alpha)$ values across their radial extents. Values for $EW(H\alpha)$ tend to start low and rise toward a galaxy’s outer edge, while $[NII]/H\alpha$ values tend to stay mostly constant. $EW(H\alpha)$ traces a galaxy’s specific star formation rate (sSFR), or star formation rate per unit mass, and so a rising profile toward a galaxy’s edge also implies a radial increase in the sSFR. This is consistent with the negative radial age gradient in most CALIFA galaxies (e.g. González Delgado et al. 2014b), suggesting inside-out galaxy growth which may be continuing at the galaxies’ current edges. Galaxies currently affected by AGN tend to have higher $EW(H\alpha)$ values, but this is unsurprising, as this is one

of the criteria by which they were selected.

More details can be found in examinations of galaxies' nebular emission, but the focus of this thesis is on the kinematics of the ionized gas. The reader is urged to consult Kehrig et al. (2012), Papaderos et al. (2013), Gomes et al. (2016), and other works for more in-depth explorations of nebular emission in early-type galaxies.

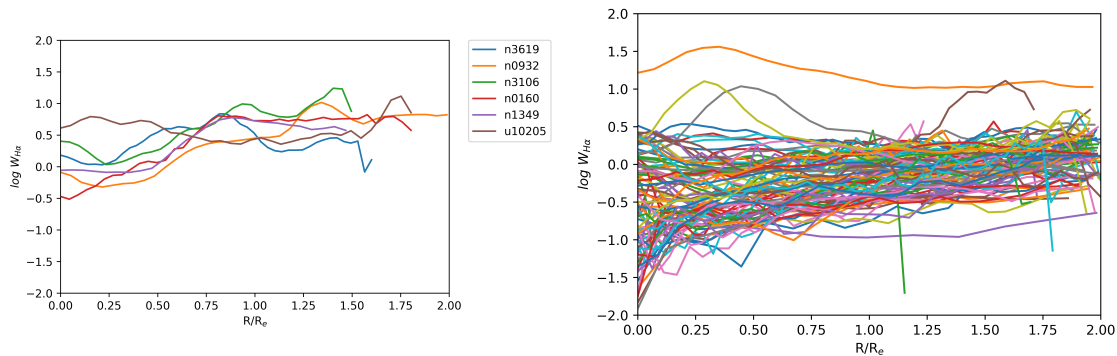


Figure 26 $EW(H\alpha)$ profiles for observed galaxies with (left) and without (right) current AGN activity.

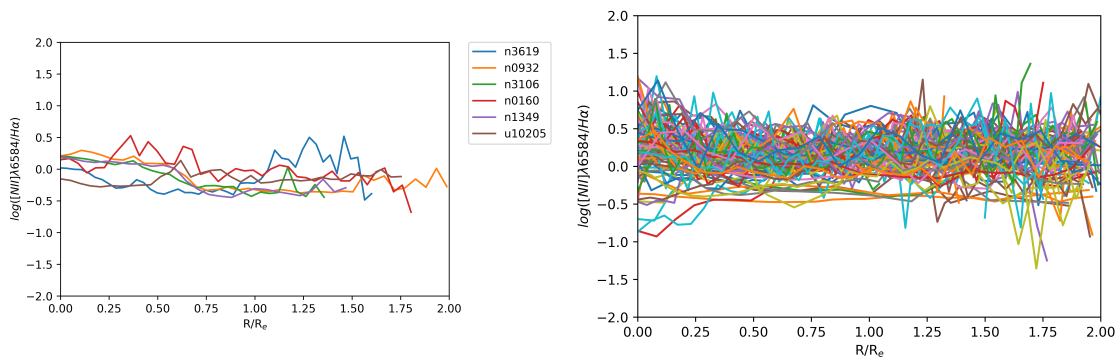


Figure 27 $NII/H\alpha$ profiles for observed galaxies with (left) and without (right) current AGN activity.

4 Comparison and Discussion

4.1 Comparison and Discussion of Kinematics Results

4.1.1 Irregularity Parameters and λ_R

This subsection is structured similarly to the corresponding subsections in the Simulations (2.6.1) and Observations (3.4.1) sections as we summarize and compare our results. As mentioned in Section 3, we separated the observed galaxies into those currently affected and unaffected by AGN feedback by means of WHAN analysis and presented the results of our analyses for both of these groups. We summarize these results again here. When we performed our analyses on the simulated data in Section 2, our separation into galaxies affected and unaffected by AGN feedback was carried out on the basis of whether or not AGN feedback was included in the simulations, and we summarize those results here as well. At the end of Section 2, however, we also separated the simulated galaxies into those currently affected and unaffected by AGN feedback by means of WHAN analysis, and it is this separation we will primarily use to compare the results of our simulated data analyses to those from observations, in order to most closely compare galaxies affected by an AGN at the time of observation.

Figure 28 combines the histograms for the values of λ_R as well as the irregularity parameters $k_{3,5}/k_1$, $\Delta\phi$, and σ_{PA} for our simulated galaxies with and without AGN feedback and our observed galaxies currently affected and unaffected by an AGN from the previous sections. In Figure 29, the same histograms are presented for current AGN and non-AGN galaxies. Figure 30 shows scatter plots in which galaxies' λ_R values are plotted against the values of each of the irregularity parameters, while Figure 31 shows each of the irregularity parameters plotted against each other. In these two plots, the simulated galaxies with AGN feedback included are plotted with reduced opacity on both the current AGN and non-current AGN plots, in order to represent both methods of classification. Under each set of histograms is a table summarizing the means and standard deviations of the quantities plotted (Tables 16 and 17), and under each set of plots comparing two quantities, the relevant correlation coefficients are presented as well (Tables 18 and 19).

In the absence of any other factors, we expect λ_R to be lower for galaxies affected by AGN feedback as opposed to those unaffected. Dubois et al. (2016) showed that AGN feedback is necessary for galaxies to exhibit the typical features of ETGs, e.g. a lack of clear, orderly, disk-like rotation, and thus lower values of λ_R . Frigo et al. (in prep.), using the same simulations as we did, find a similar trend. Indeed, the overall mean λ_R value for simulated and observed galaxies with AGN feedback is lower than that without, with both means of separation. The difference is not large, however, and the scatter is significant. We expect that the difference would be larger if not for one simulated galaxy without AGN feedback with a much lower λ_R value than the rest (Halo 0300).

Frigo et al. find a strong time dependence on the difference between simulations with and without AGN feedback, with the two populations quite similar at $z=1$ and then very different at $z=0$, with AGN feedback presumably working to decrease λ_R along the way (around $z=0.25$ for Halo 0227, for example). We presume that the small difference in λ_R values for our simulated galaxies arises partially due to the fact that, at $z=0.5$, this process has not yet been completed, and partially due to the fact that λ_R is sensitive to the inclination of the galaxy in question and the radius at which it is measured. Inasmuch as we can separate all our galaxies into those currently affected and unaffected by AGN feedback, we find that (current) AGN feedback does seem to result in a reduced value for λ_R , which is in line with the previously discussed works. However, the relatively small magnitude of this reduction, along with the less consistent apparent impact of AGN feedback on the values of irregularity parameters, serve to underscore an important point: *we can only clearly discern whether or not a galaxy is affected by an AGN at the moment we observe it.* AGN activity sometimes leaves traces in the form of “ionization echoes,” such as the famous object Hanny’s Voorwerp (Keel et al., 2012), but these objects are not necessarily captured by diagnostic analysis of the type carried out in this thesis.

For the simulated galaxies, which we are able to clearly separate into those which may have been affected by AGN feedback at some point in their histories from those who remain completely unaffected, we see that the value of each of the three irregularity parameters is, on average, higher for galaxies with AGN feedback than without. Taking all of our simulated and observed galaxies and the WHAN-based separation between current AGN activity and lack thereof into account, however, the picture changes. The average value of $\Delta\phi$ is indeed higher for currently AGN-affected galaxies, but the average value of $k_{3,5}/k_1$ is lower, and there is no clear difference in the average σ_{PA} values. AGN activity may have raised the values of the irregularity parameters before the AGN itself switched off (as we have seen, there is a delay between increases in AGN activity and the corresponding spikes in irregularity parameters), but we have also seen that phenomena such as mergers, completely independent of AGN feedback, can raise the irregularity parameters as well. To summarize: AGN feedback seems to increase the values of irregularity parameters, but it is not the only mechanism able to do so, and a galaxy may have felt the effects of an AGN during its past without indicating so when we observe it in the present.

Figures 26 through 29 show the inherent differences between the simulated and observed galaxies. The simulated galaxies, though they exhibited similar ranges of λ_R values, occupied a much smaller range of values for the irregularity parameters. The simulated galaxies are clustered mainly around the “regular” areas in the bottom left corner of the figures in which two irregularity parameters are plotted against each other, whereas the observed galaxies’ values are far more scattered. A much higher number of simulated galaxies is regular than observed galaxies.

The fact that the simulated gas kinematics are, overall, so well-behaved is surprising, as most of the galaxies lie above the mass threshold ($\log(M) \sim 11.5$) that roughly separates fast from slow rotators. We have seen in our examination of the time development of the halos (and the literature points to a similar conclusion) that the differences between galaxies affected by AGN feedback and those unaffected begins to be felt at low redshift, however, and so our simulated galaxies may simply not be old enough.

On the whole, we expected a negative correlation between λ_R and the irregularity parameters, as a higher degree of ordered rotation should correspond to more orderly kinematics on the whole. For the simulated galaxies, this was the case for every combination, AGN and no AGN feedback (except for a surprisingly high positive correlation between λ_R and $k_{3,5}/k_1$ in the cases without AGN feedback). Observed galaxies seemed to cancel out this trend somewhat, however, and the only negative correlation for all WHAN-separated galaxies was between λ_R and $\Delta\phi$. In principle, we would expect AGN feedback to strengthen the negative correlation, as it tends to lower λ_R while increasing the irregularity parameters. Indeed, the correlations seem to be somewhat more strongly negative in the presence of AGN feedback.

The strongest correlation between irregularity parameters was the anti-correlation found between σ_{PA} and $\Delta\phi$ for all WHAN-separated galaxies currently affected by an AGN, and a weaker positive correlation between those same two parameters for those unaffected by an AGN. Kutdemir (2010) found a correlation between σ_{PA} and $k_{3,5}/k_1$, and we are able to reproduce it to some degree for all WHAN-separated galaxies currently unaffected by an AGN, but this is also cancelled out by an anti-correlation for AGN-affected galaxies.

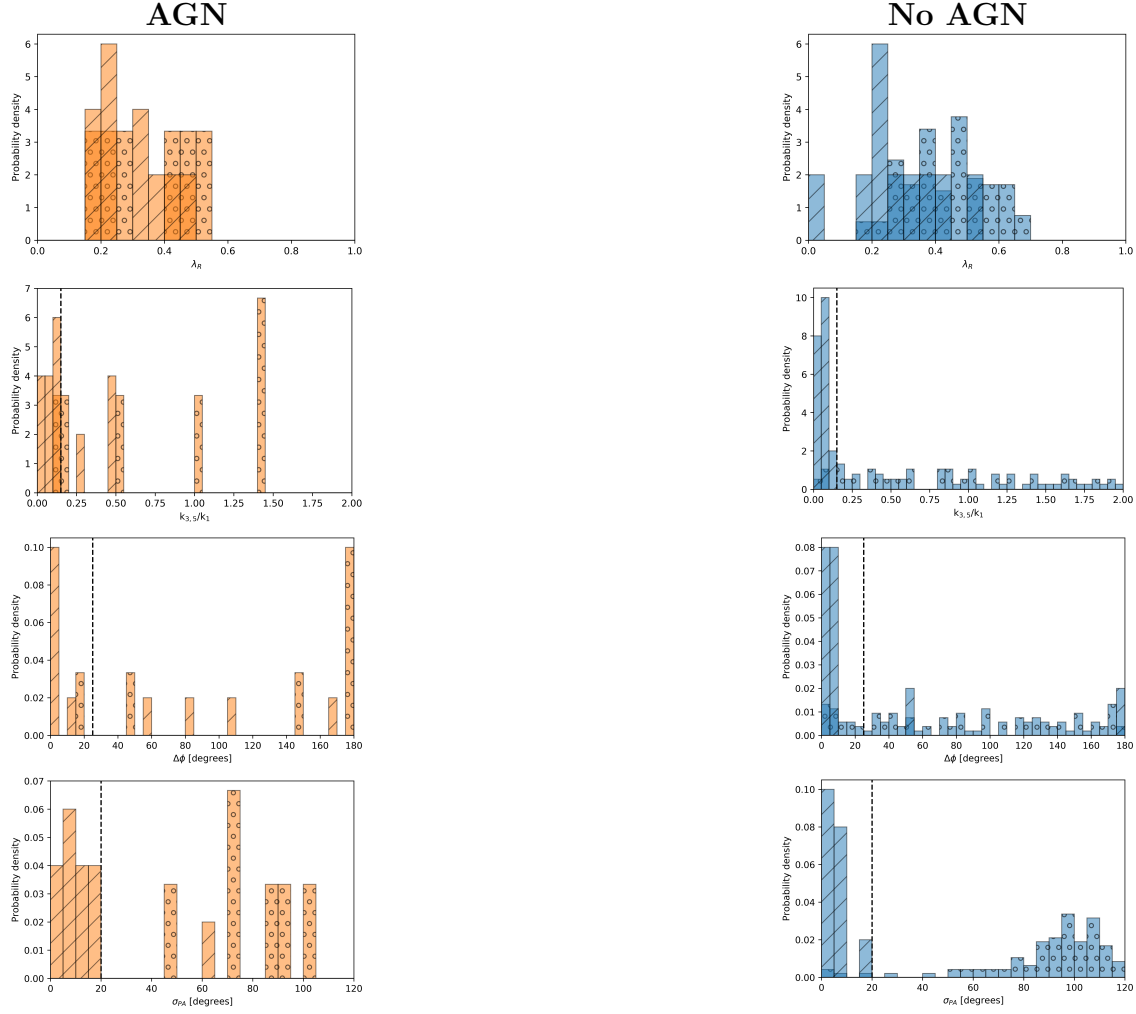


Figure 28 Histograms of λ_R (top row), $k_{3,5}/k_1$ (second row), $\Delta\phi$ (third row), and σ_{PA} (bottom row), for simulated galaxies with AGN feedback and observed galaxies with current AGN activity (left column) and simulated galaxies without AGN feedback and observed galaxies without current AGN activity (right column).

	$\mu(\lambda_R)$	$\sigma(\lambda_R)$	$\mu(k_{3,5}/k_1)$	$\sigma(k_{3,5}/k_1)$	$\mu(\Delta\phi)$	$\sigma(\Delta\phi)$	$\mu(\sigma_{PA})$	$\sigma(\sigma_{PA})$
AGN (Sim.)	0.293	0.097	0.18	0.15	44	56	15	16
NoAGN (Sim.)	0.276	0.134	0.06	0.03	27	53	6	5
AGN (Obs.)	0.351	0.127	0.78	0.53	125	67	79	17
NoAGN (Obs.)	0.434	0.125	1.66	1.49	85	57	94	26
AGN (Mean)	0.322	0.112	0.48	0.34	85	62	47	17
NoAGN (Mean)	0.355	0.130	0.86	0.76	56	55	50	16

Table 16 Means and standard deviations of λ_R and irregularity parameters for both simulated and observed galaxies for simulated galaxies with AGN feedback and observed galaxies with current AGN activity on the one hand, and simulated galaxies without AGN feedback and observed galaxies without current AGN activity on the other hand.

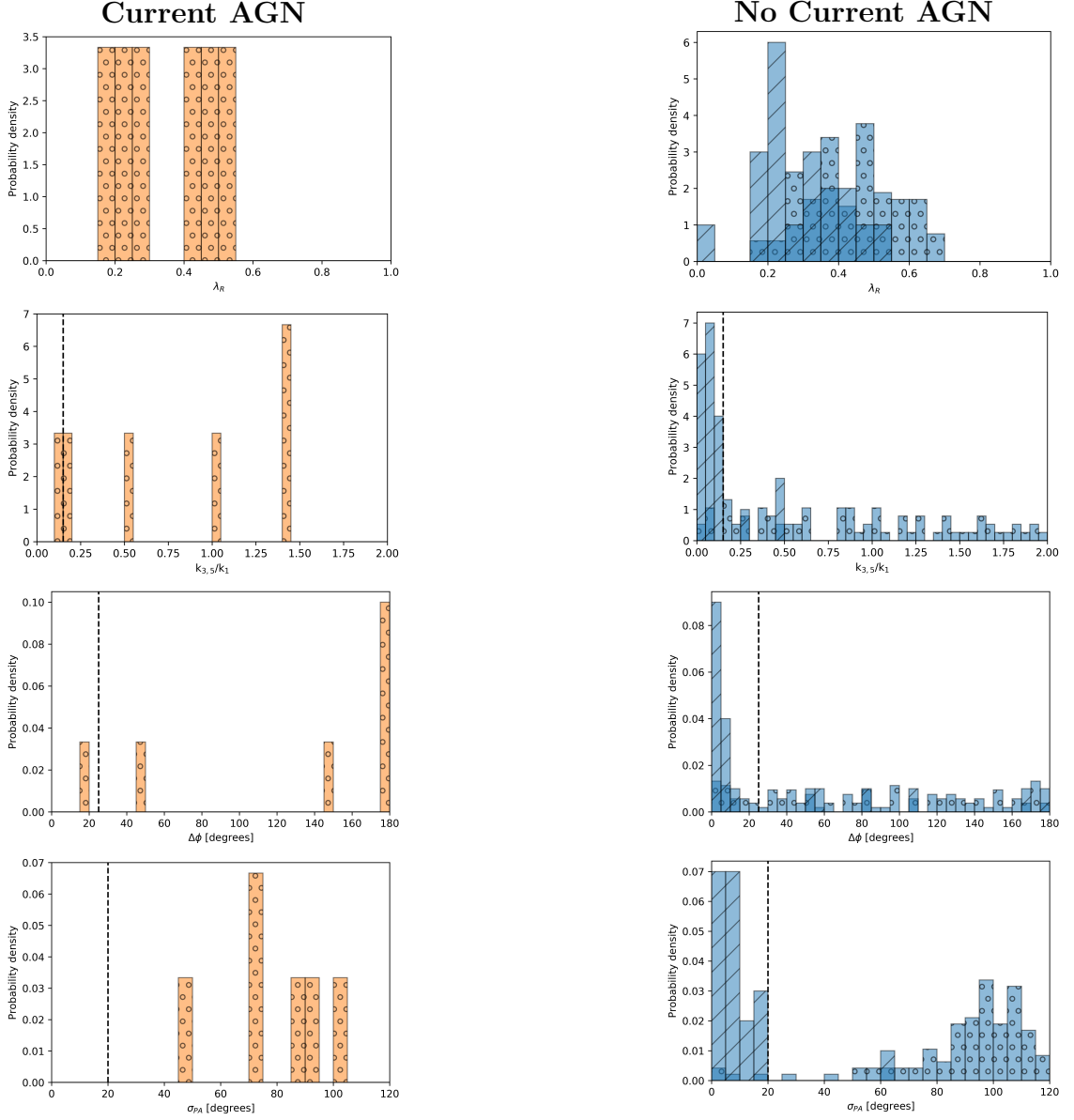


Figure 29 Histograms of λ_R (top row), $k_{3,5}/k_1$ (second row), $\Delta\phi$ (third row), and σ_{PA} (bottom row), for both simulated and observed galaxies classified through WHAN analysis as currently experiencing AGN activity (left column) and those for which that is not the case (right column).

	$\mu(\lambda_R)$	$\sigma(\lambda_R)$	$\mu(k_{3,5}/k_1)$	$\sigma(k_{3,5}/k_1)$	$\mu(\Delta\phi)$	$\sigma(\Delta\phi)$	$\mu(\sigma_{PA})$	$\sigma(\sigma_{PA})$
AGN (Mean)	0.351	0.127	0.78	0.53	125	67	79	17
NoAGN (Mean)	0.411	0.135	1.411	1.48	77	59	81	39

Table 17 Means and standard deviations of λ_R and irregularity parameters for both simulated and observed galaxies for both simulated and observed galaxies classified through WHAN analysis as currently experiencing AGN activity and those for which that is not the case.

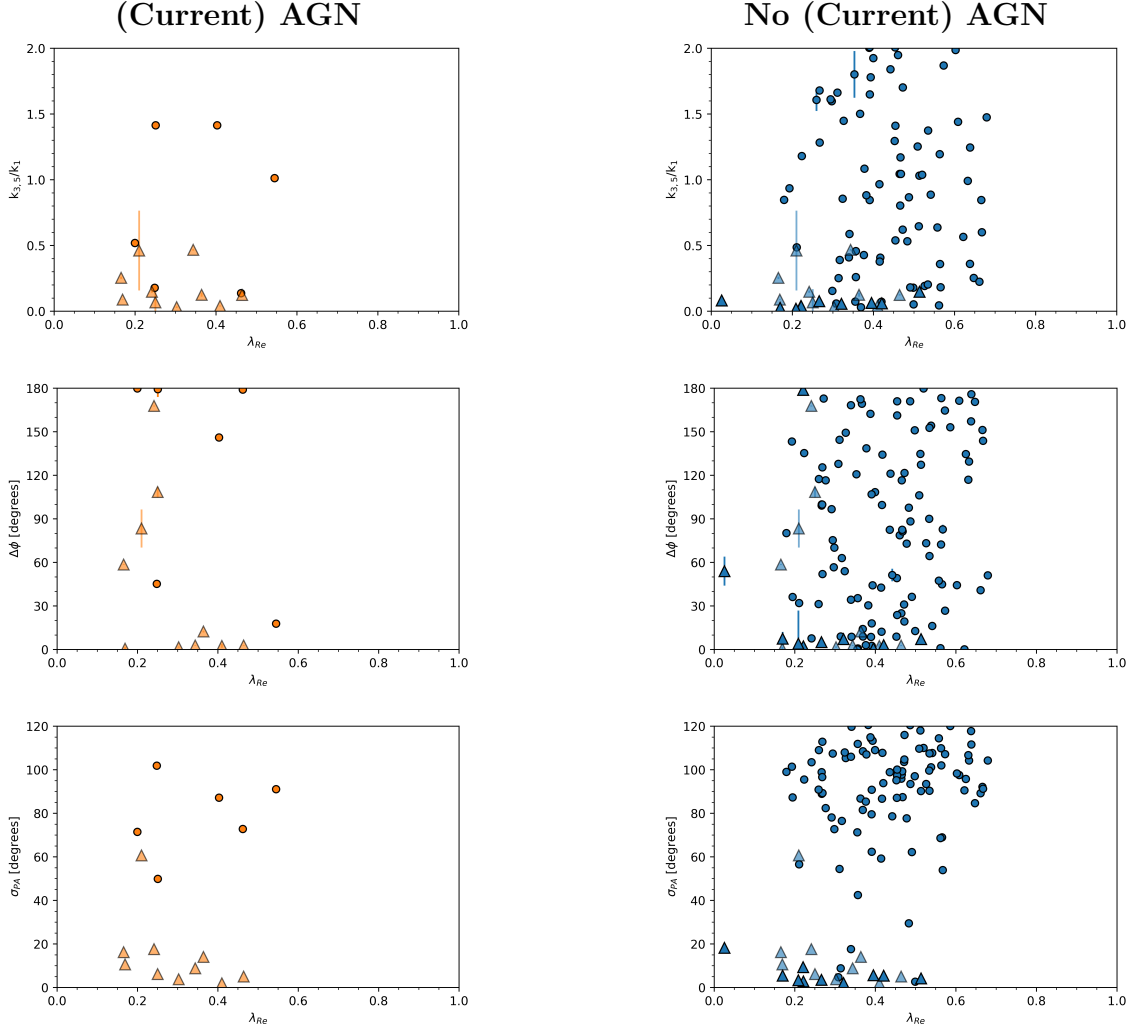


Figure 30 λ_R vs each of the irregularity parameters $k_{3,5}/k_1$ (top row), $\Delta\phi$ (middle row), and σ_{PA} (bottom row), for galaxies currently experiencing AGN feedback (left column) and not (right column). Note: The values for simulated galaxies which have experienced AGN feedback in the past, but are not doing so currently, are plotted with semi-transparent points.

	λ_R vs. $k_{3,5}/k_1$	λ_R vs. $\Delta\phi$	λ_R vs. σ_{PA}
AGN (Sim.)	-0.218	-0.478	-0.446
NoAGN (Sim.)	0.518	-0.311	-0.585
AGN (Obs.)	0.110	-0.376	0.298
NoAGN (Obs.)	-0.103	0.161	0.116
AGN (Mean, non-separated sims.)	-0.054	-0.427	-0.074
NoAGN (Mean, non-separated sims.)	0.208	-0.075	-0.235
AGN (Mean, separated sims.)	0.110	-0.376	0.298
NoAGN (Mean, separated sims.)	0.073	0.198	0.361

Table 18 The values of the Pearson correlation coefficient for λ_R vs. each of our irregularity parameters for simulated and observed galaxies.

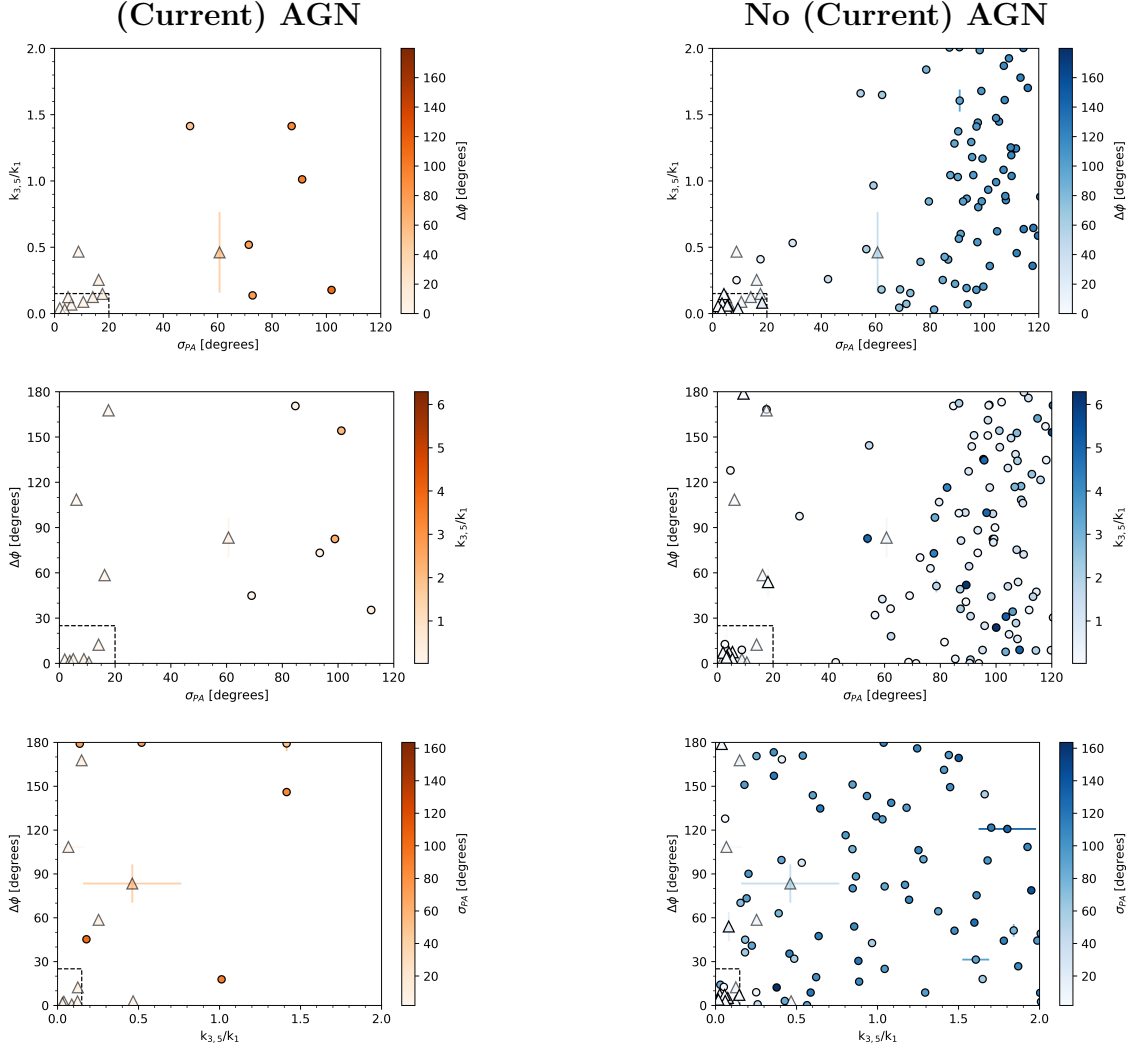


Figure 31 σ_{PA} vs. $k_{3,5}/k_1$ (top row), σ_{PA} vs. $\Delta\phi$ (middle row), and $k_{3,5}/k_1$ vs. $\Delta\phi$ (bottom row), for galaxies currently experiencing AGN feedback (left column) and not (right column). Note: The values for simulated galaxies which have experienced AGN feedback in the past, but are not doing so currently, are plotted with semi-transparent points.

	σ_{PA} vs. $k_{3,5}/k_1$	σ_{PA} vs. $\Delta\phi$	$k_{3,5}/k_1$ vs. $\Delta\phi$
AGN (Sim.)	0.666	0.385	0.109
NoAGN (Sim.)	0.128	0.494	-0.142
AGN (Obs.)	-0.343	-0.781	0.101
NoAGN (Obs.)	0.250	0.194	0.120
AGN (Mean, non-separated sims.)	0.162	-0.198	0.105
NoAGN (Mean, non-separated sims.)	0.189	0.344	-0.011
AGN (Mean, separated sims.)	-0.343	-0.781	0.101
NoAGN (Mean, separated sims.)	0.440	0.362	0.215

Table 19 The values of the Pearson correlation coefficient for each combination of irregularity parameters for both simulated and observed galaxies.

4.1.2 Residual Asymmetries

The residual asymmetries were very slightly higher for simulated galaxies with AGN feedback and for observed galaxies with current AGN activity. When the asymmetries are average for all WHAN-separated galaxies, the difference is somewhat larger, although we believe that this is primarily due to the inherently lower asymmetries of the simulated galaxies. The difference is, overall, not significant, which is in line with similar findings by (e.g. Dumas et al., 2007), who used tilted-ring analysis (similar to kinemetry) with SAURON data and found no significant difference between active and inactive galaxies.

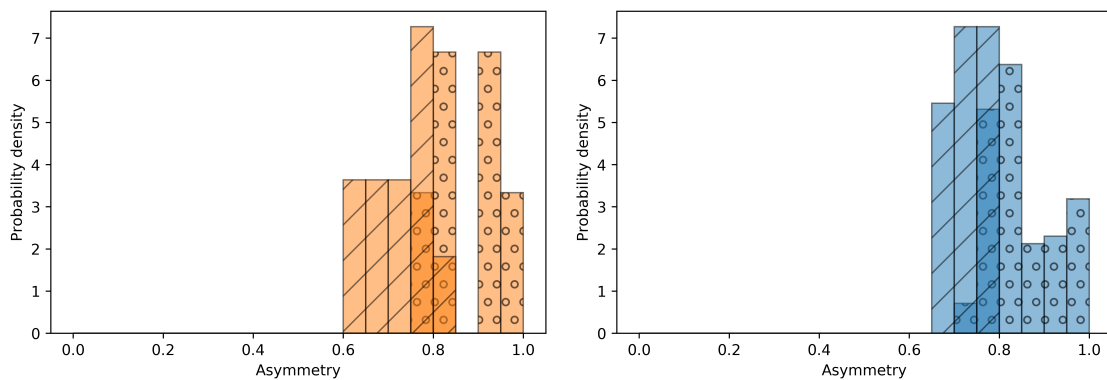


Figure 32 Histograms for the asymmetries of the residuals generated by subtracting the full rotation model generated by kinemetry from the simulated and observed gas velocity fields for simulated galaxies with AGN feedback and observed galaxies with current AGN activity (left) and simulated galaxies without AGN feedback and observed galaxies without current AGN activity (right).

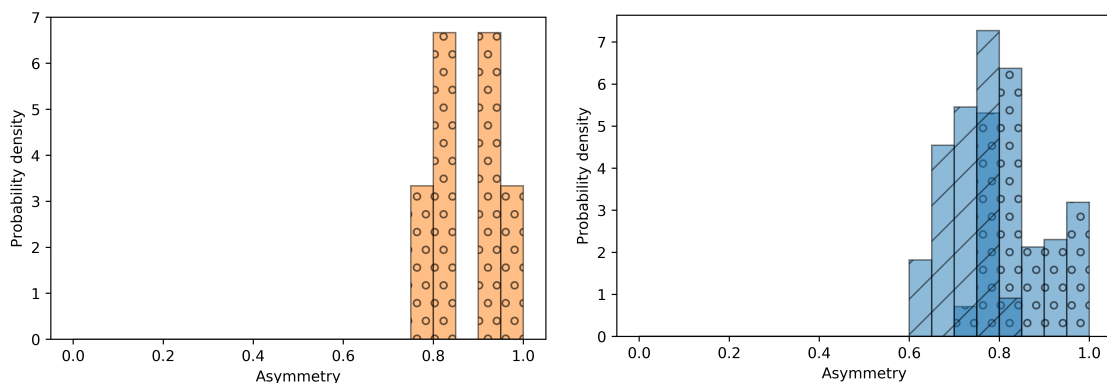


Figure 33 Histograms for the asymmetries of the residuals generated by subtracting the full rotation model generated by kinemetry from the simulated and observed gas velocity fields for both simulated and observed galaxies classified through WHAN analysis as currently experiencing AGN activity (left column) and those for which that is not the case (right column).

	μ (Asymmetry)	σ (Asymmetry)
AGN (Sim.)	0.735	0.063
NoAGN (Sim.)	0.725	0.043
AGN (Obs.)	0.875	0.075
NoAGN (Obs.)	0.848	0.075
AGN (Mean, non-separated sims.)	0.805	0.069
NoAGN (Mean, non-separated sims.)	0.787	0.059
AGN (Mean, separated sims.)	0.875	0.075
NoAGN (Mean, separated sims.)	0.829	0.084

Table 20 The means and standard deviations of the asymmetries of the residuals generated by subtracting models of the rotation of the gas velocity fields of simulated and observed galaxies.

4.2 Comparison and Discussion of Nebular Emission Results

4.2.1 $\text{EW}(\text{H}\alpha)$ and $\text{NII}/\text{H}\alpha$ profiles

We plotted radial $[\text{N II}]/\text{H}\alpha$ profiles for our simulated galaxies in Fig. 19, and radial $[\text{N II}]/\text{H}\alpha$ and $\text{EW}(\text{H}\alpha)$ profiles for our observed galaxies in Figs. 27 and 26, respectively. All galaxies, simulated and observed, seemed to have fairly constant $[\text{N II}]/\text{H}\alpha$ for their full radial extents. In simulated galaxies with AGN feedback, there was a wider range of values, and the profiles were less smooth and regular. In this respect, they are similar to the surface density profiles of the warm gas. As our analysis uncovered, none of the ten galaxies with AGN feedback would be classified as currently experiencing AGN activity through WHAN analysis, and only one would be classified as AGN-dominated based on the ratio of its black hole accretion rate to its star-formation rate: Halo 0300. For the other nine halos, the total $[\text{N II}]/\text{H}\alpha$ values were comparable to those for the observed galaxies, but for Halo 0300, it was a bit lower than expected. This can be explained at least partially by the fact that Halo 0300's central galaxy lies somewhat below the empirical stellar mass/gas metallicity relation at the redshift at which we observe it (Michaela Hirschmann, personal communication, June 5, 2018).

5 Summary and Conclusion

5.1 Summary

In this thesis, we examine a sample of massive early-type galaxies comprised of observed galaxies from the CALIFA survey and simulated galaxies produced by the code SPHGal. By means of WHAN analysis, we separate each of these sub-samples into galaxies subject to and not subject to AGN feedback at the moment of observation. We examine (primarily) the gas kinematics of these galaxies, quantifying the degree of “order” by means of the parameter λ_R and the three irregularity parameters $k_{3,5}/k_1$ (the deviation from simple rotation normalized to the amplitude of the simple rotation), $\Delta\phi$ (the smallest difference between the position angles of the stellar and gas kinematics), and σ_{PA} (the standard deviation of the position angles of the gas kinematics measured at different radii). We examine the effect of AGN feedback on each of these parameters, and on their correlations amongst each other. We find that:

- AGN feedback is very (perhaps too) effective at heating and removing gas from simulated galaxies, with most of the warm and cold gas removed by $z=0.0$,
- None of our ten galaxies that were simulated with AGN feedback were classified as either strong or weak AGNs by WHAN analysis at $z=0.5$, and only one would be considered AGN-dominated based on the ratio of its black hole accretion rate to its star-formation rate,
- AGN feedback, when considered on its own, results in lower overall values of λ_R and higher values of the irregularity parameters, but
- Other phenomena, such as mergers, can also increase the values of irregularity parameters, which means that
- **High irregularity parameters can be caused by, but are not necessarily a sign of, AGN feedback.**
- Overall, galaxies separated into those currently affected by AGN activity and those unaffected by means of WHAN analysis do not show significant differences in their irregularity parameters.
- λ_R anti-correlates with the irregularity parameters to some degree,
- The irregularity parameters do not correlate particularly strongly with one another, and
- The residuals of the subtraction of a model of the rotation of the gas kinematics from the actual kinematics are not significantly less symmetric for galaxies affected by AGN feedback than those not affected.

In this thesis, we measured $k_{3,5}/k_1$ and $\Delta\phi$ at each galaxy's effective radius. A preliminary examination of the values of these parameters across a galaxy's full radial extent has revealed that they do not vary significantly as a function of radius for simulated galaxies, but that the variation as a function of radius can be quite significant for the observed galaxies. This suggests that the values of the irregularity parameters at the effective radius do not tell the whole story, and will be taken into account in future work.

An examination of the development histories of six of the simulated galaxies showed that, generally, the increased values of the irregularity parameters we measure at $z=0.5$ in the cases with AGN feedback were caused by roughly concurrent mergers and spikes in the black hole accretion rate at $z \sim 1.0$, after which the irregularity parameters begin to increase by about $z \sim 0.75$ and stay elevated until $z=0.5$ (time spans of roughly 1.4 and 2 Gyr, respectively). In contrast, in cases without AGN feedback, the mergers that take place around $z=1.0$ result in increased irregularity parameters with little to no delay in time, but the irregularity parameters fall back down again to nearly zero quite quickly.

We also examined the emission characteristics of our sample by plotting radial $[\text{N II}]/\text{H}\alpha$ and $\text{EW}(\text{H}\alpha)$ profiles, finding that all galaxies had fairly constant radial profiles, suggesting a ubiquitous WIM, but that the profiles are less regular for simulated galaxies with AGN feedback and that the values of $[\text{N II}]/\text{H}\alpha$ for one simulated, theoretically (but not observationally) AGN-dominated galaxy lie below those of the observed galaxies by roughly an order of magnitude.

5.2 Conclusion

Part of the purpose of this work is to demonstrate the broad range of possible science topics currently being examined in the field of extragalactics. In the century in which we have been learning about other galaxies, we have gathered mountains of data, which we have used in order to shape our own models of galaxies. We have largely been successful in recreating the galaxies we observe, but so many questions remain. With the rapidly increasing computational power at our disposal, our models grow more and more intricate, with ever larger dynamic ranges and ever more cunningly modelled physics. As instrumentation grows in sophistication, the data with which to compare and refine our models grows more and more useful in its own right.

There are many aspects of this work that could be explored in further study. The emission characteristics of galaxies in simulations are now only starting to be analyzed, and there is much work that can be done here as well. We calculated the values of two of our three irregularity parameters at each studied galaxy's effective radius, in order to determine a representative value for the galaxy, but more information lies in the radial variations of these quantities. Our velocity maps were also analyzed without radial binning, which is something we would do differently in future work.

5.3 Acknowledgements

Thank you to my supervisors, Bodo and Michaela, for giving me the opportunity to work on this project, for pulling strings, for answers, for patience, for time. Thank you to the other members of the Extragalactic Astrophysics group: Asmus Böhm, Christian Maier, Miguel Verdugo, Boris Deshev, and José Perez, for your feedback and technical help. Thank you to Matteo Frigo and Bernhard Röttgers at the MPI in Garching, for quick, helpful, patient answers to my questions about how to handle the simulation snapshots. Thank you to Polychronis Papaderos and Jean-Michel Gomes in Porto for providing the data and tools to handle the observational aspect of my thesis, and for your helpful input in all aspects of this work. Thank you to Davor Krajnović for your answers to my kinemetry questions, especially in person.

Thank you to Philip Winter for providing me with the template I have used to write this thesis, and for your helpful feedback regarding its content. Thank you also to Nina Némec for your feedback, and for helping to keep me sane during the process of working on this thesis. That goes for a few other people as well: Simon Rella, Sarah Stidl, Charles Steenkolk, Cassidy Robertson, Lena Florian, Alice Schimek, Johannes Seelig, I am lucky to have you in my life.

Above all, thank you to my parents. I love you.

This study uses data provided by the Calar Alto Legacy Integral Field Area (CALIFA) survey (<http://califa.caha.es/>). Based on observations collected at the Centro Astronómico Hispano Alemán (CAHA) at Calar Alto, operated jointly by the Max-Planck-Institut für Astronomie and the Instituto de Astrofísica de Andalucía (CSIC).

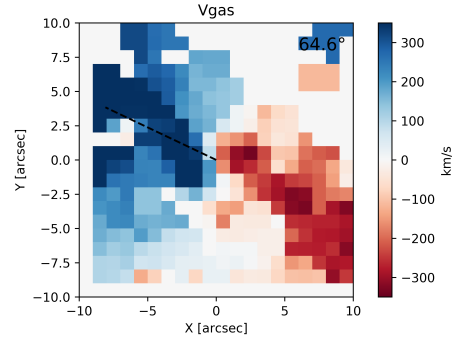
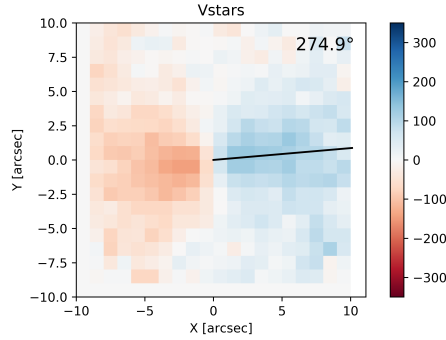
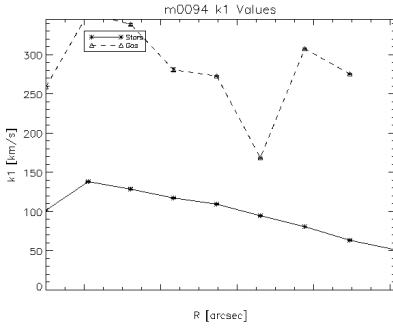
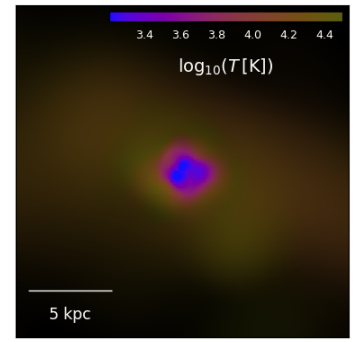
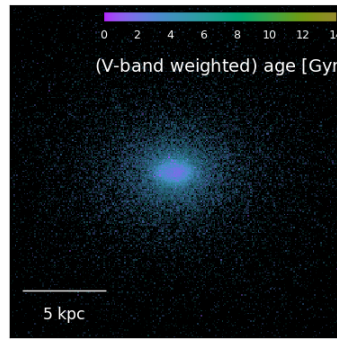
Ich habe mich bemüht, sämtliche Inhaber der Bildrechte ausfindig zu machen und ihre Zustimmung zur Verwendung der Bilder in dieser Arbeit eingeholt. Sollte dennoch eine Urheberrechtsverletzung bekannt werden, ersuche ich um Meldung bei mir.

6 Appendix

6.1 2D info on all studied simulated galaxy snapshots

The following values were either produced in the course of the work described in this thesis (λ_R , residual asymmetry) or were taken from the trace files provided along with the simulation snapshots. Note: the radial k_1 profiles, along with the position angles of the gas and stellar kinematics, are the result of a separate set of kinemetry runs from the analysis described in the thesis and are meant to give general impressions of each simulated galaxy. This means e.g. that the position angles may vary slightly between the values presented here and in the thesis itself.

Snapshot 0094 (AGN)
 log(Stellar Mass): 12.372
 Redshift: 0.515
 r_e : 2.906 kpc
 AGN activity: No
 λ_R value at r_e : 0.242
 Residual asymmetry: 0.710



Snapshot 0094 (No AGN)
 log(Stellar Mass): 12.635
 Redshift: 0.515
 r_e : 2.579 kpc
 λ_R value at r_e : 0.222
 Residual Asymmetry: 0.785

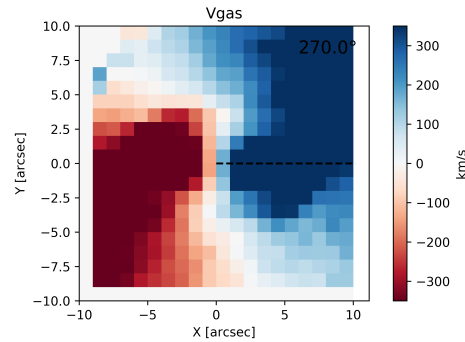
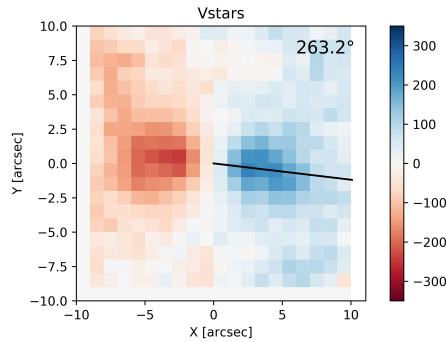
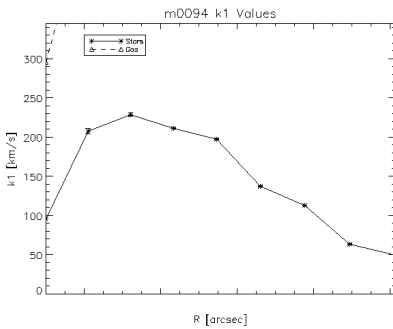
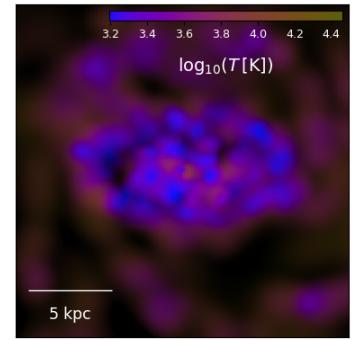
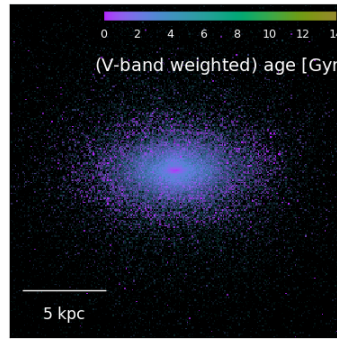
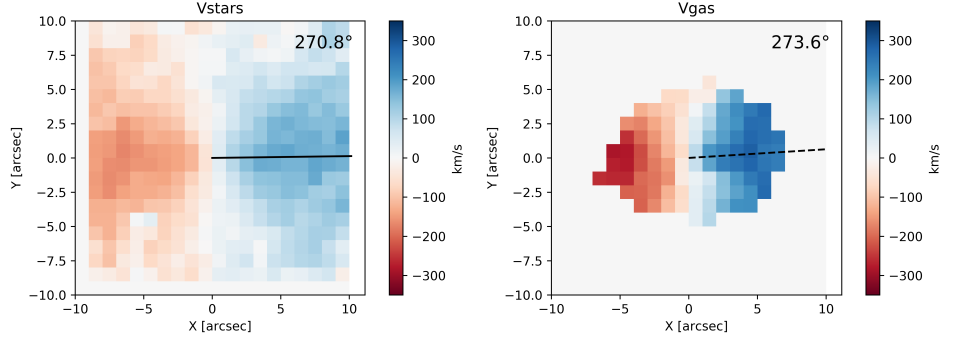
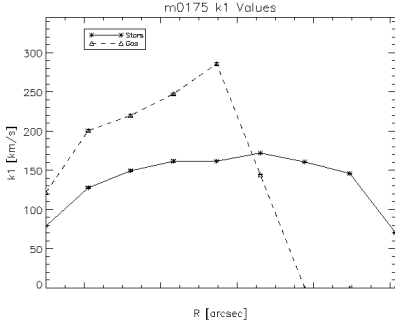
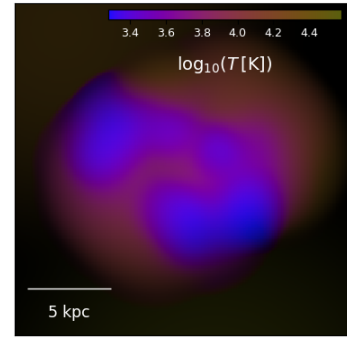
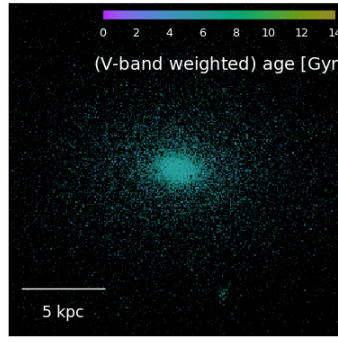


Figure 34 Top row, left to right: Name and characteristic parameters, stellar distribution, and warm gas distribution, respectively. Bottom row, left to right: radial k_1 profiles for stars (solid) and gas (dashed), stellar kinematics, and gas kinematics, respectively. The solid and dashed line in the stellar and gas velocity map, respectively, is the median position angle along which kinemetry coefficients were determined. The number value of this position angle given at the top right of the plot.

Snapshot 0175 (AGN)
 $\log(\text{Stellar Mass}): 12.007$
 Redshift: 0.515
 $r_e: 5.362$ kpc
 AGN activity: No
 λ_R value at r_e : 0.464
 Residual asymmetry: 0.789



Snapshot 0175 (No AGN)
 $\log(\text{Stellar Mass}): 12.462$
 Redshift: 0.515
 $r_e: 2.546$ kpc
 λ_R value at r_e : 0.420
 Residual Asymmetry: 0.774

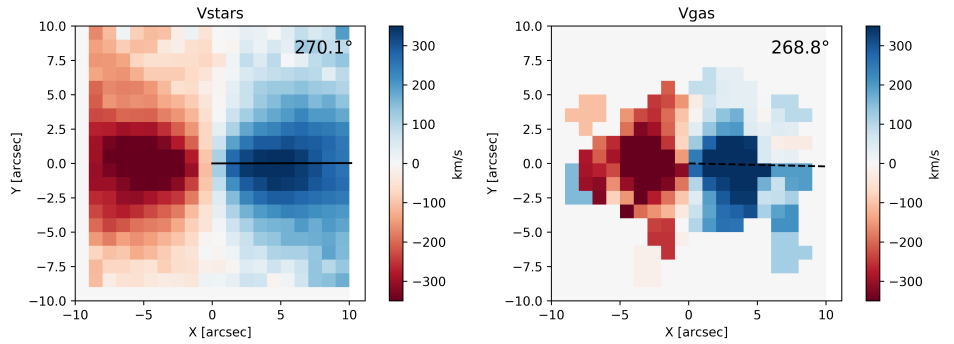
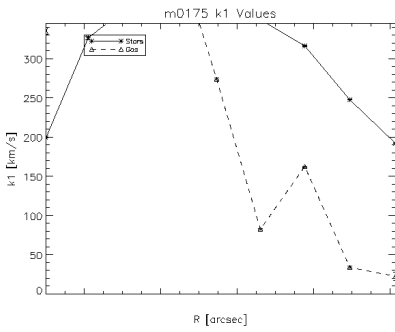
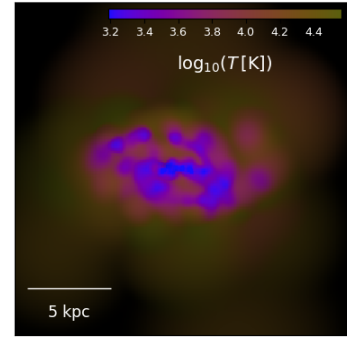
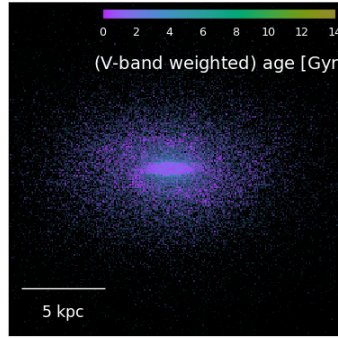
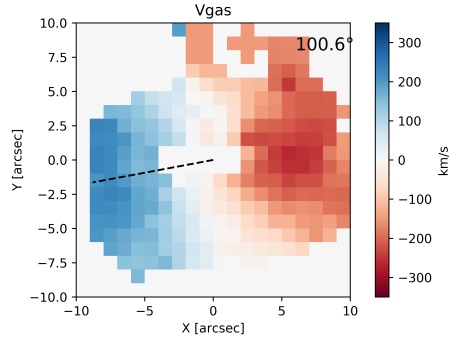
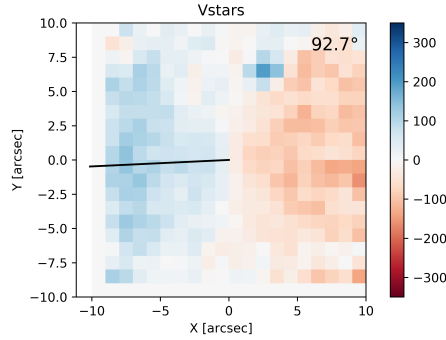
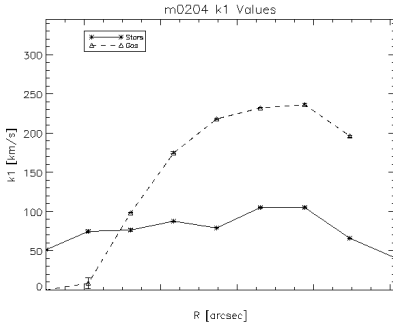
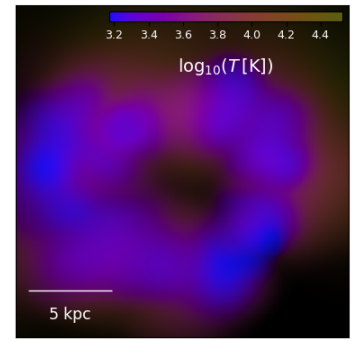
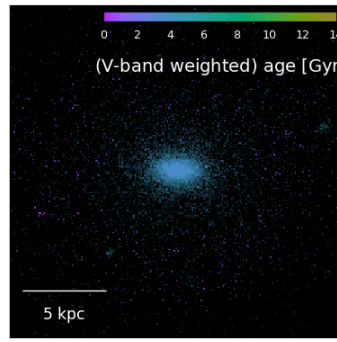


Figure 35 Top row, left to right: Name and characteristic parameters, stellar distribution, and warm gas distribution, respectively. Bottom row, left to right: radial k_1 profiles for stars (solid) and gas (dashed), stellar kinematics, and gas kinematics, respectively. The solid and dashed line in the stellar and gas velocity map, respectively, is the median position angle along which kinemetry coefficients were determined. The number value of this position angle given at the top right of the plot.

Snapshot 0204 (AGN)
 log(Stellar Mass): 11.887
 Redshift: 0.515
 r_e : 2.229 kpc
 AGN activity: No
 λ_R value at r_e : 0.208
 Residual asymmetry: 0.677



Snapshot 0204 (No AGN)
 log(Stellar Mass): 12.123
 Redshift: 0.515
 r_e : 2.379 kpc
 λ_R value at r_e : 0.321
 Residual Asymmetry: 0.720

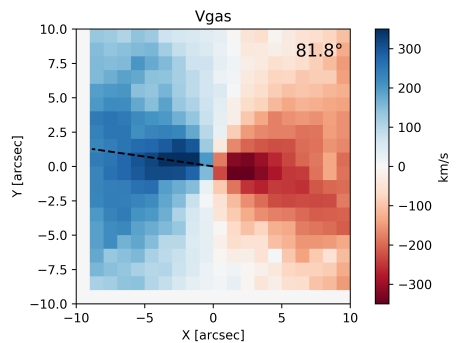
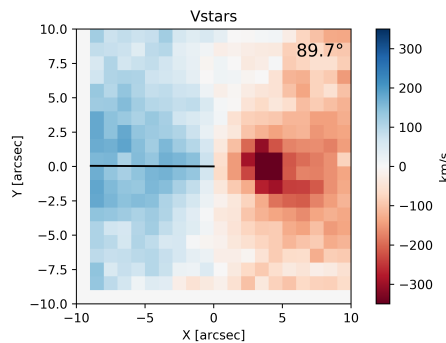
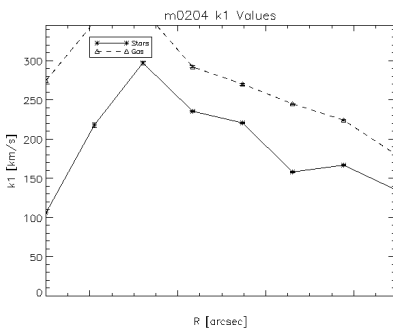
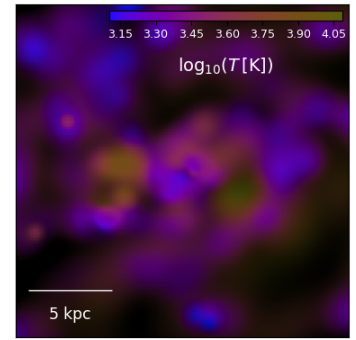
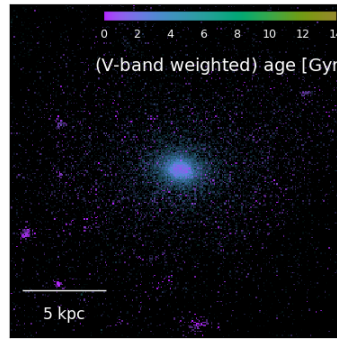
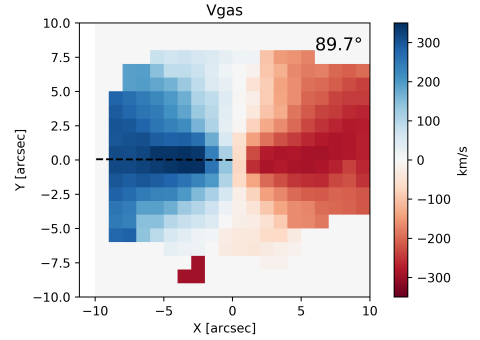
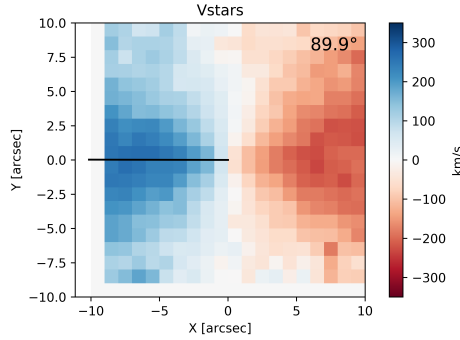
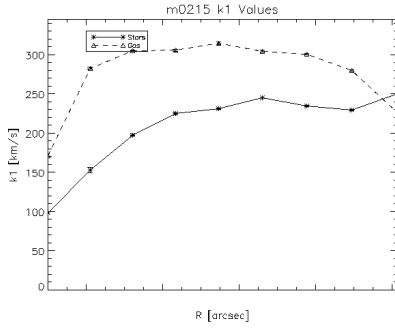
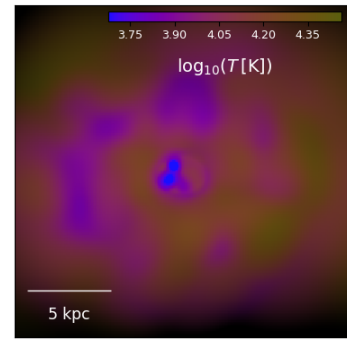
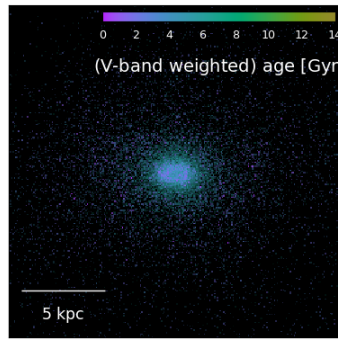


Figure 36 Top row, left to right: Name and characteristic parameters, stellar distribution, and warm gas distribution, respectively. Bottom row, left to right: radial k_1 profiles for stars (solid) and gas (dashed), stellar kinematics, and gas kinematics, respectively. The solid and dashed line in the stellar and gas velocity map, respectively, is the median position angle along which kinemetry coefficients were determined. The number value of this position angle given at the top right of the plot.

Snapshot 0215 (AGN)
 $\log(\text{Stellar Mass}): 12.070$
Redshift: 0.515
 $r_e: 2.871$ kpc
AGN activity: No
 λ_R value at r_e : 0.411
Residual asymmetry: 0.798



Snapshot 0215 (No AGN)
 $\log(\text{Stellar Mass}): 12.291$
Redshift: 0.515
 $r_e: 1.865$ kpc
 λ_R value at r_e : 0.222
Residual Asymmetry: 0.680

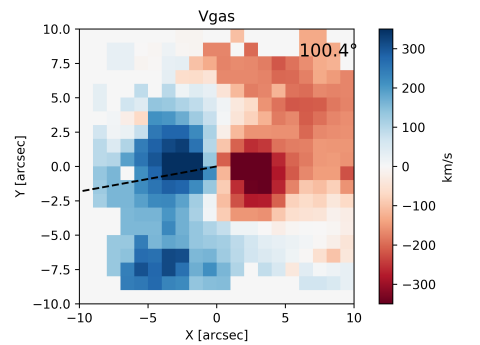
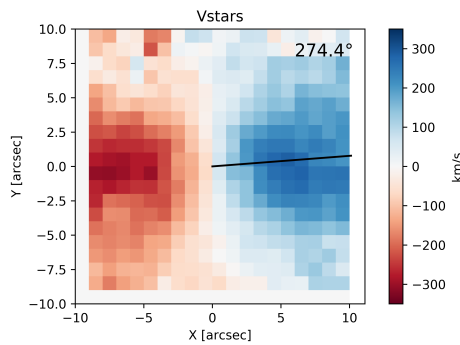
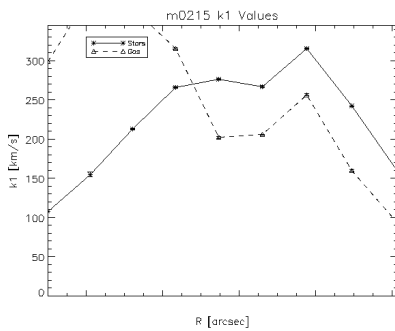
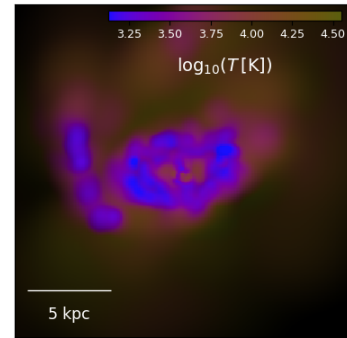
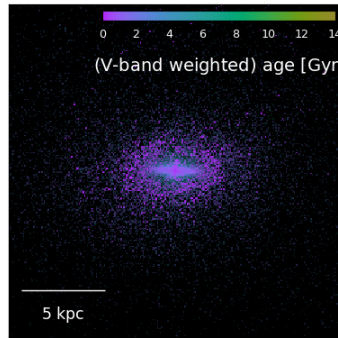
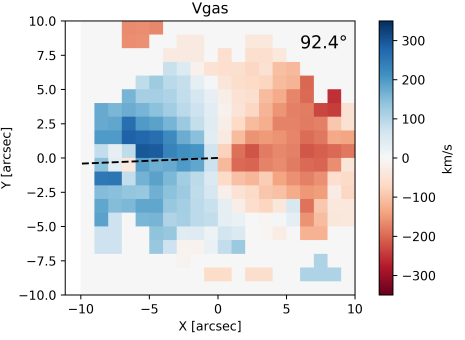
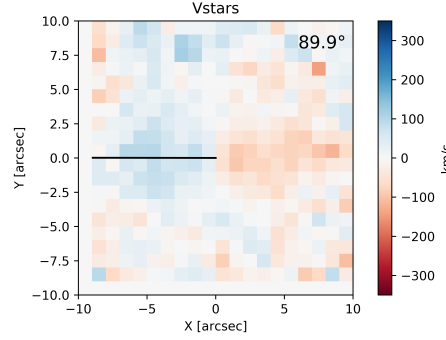
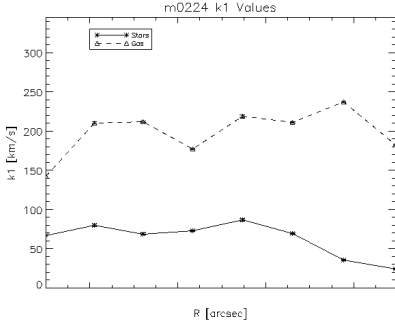
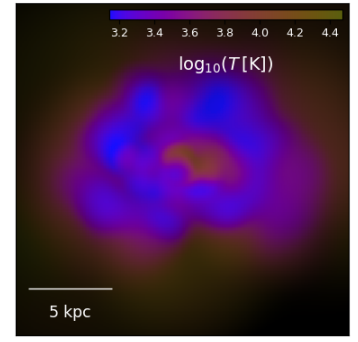
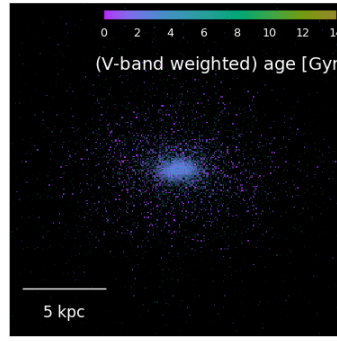


Figure 37 Top row, left to right: Name and characteristic parameters, stellar distribution, and warm gas distribution, respectively. Bottom row, left to right: radial k_1 profiles for stars (solid) and gas (dashed), stellar kinematics, and gas kinematics, respectively. The solid and dashed line in the stellar and gas velocity map, respectively, is the median position angle along which kinemetry coefficients were determined. The number value of this position angle given at the top right of the plot.

Snapshot 0224 (AGN)
 $\log(\text{Stellar Mass}): 11.655$
 Redshift: 0.515
 $r_e: 1.997$ kpc
 AGN activity: No
 λ_R value at $r_e: 0.302$
 Residual asymmetry: 0.746



Snapshot 0224 (No AGN)
 $\log(\text{Stellar Mass}): 11.621$
 Redshift: 0.515
 $r_e: 1.936$ kpc
 λ_R value at $r_e: 0.264$
 Residual Asymmetry: 0.655

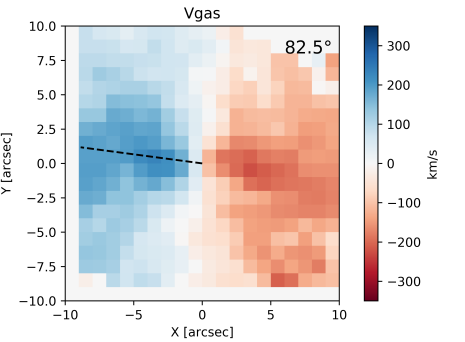
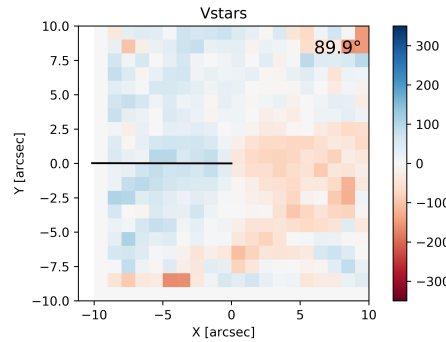
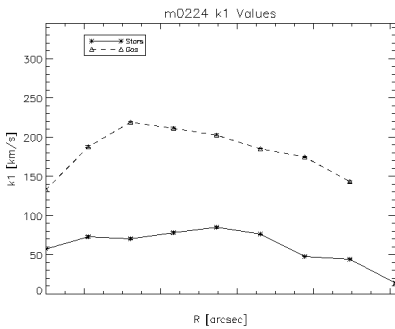
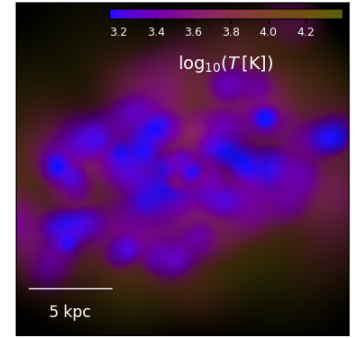
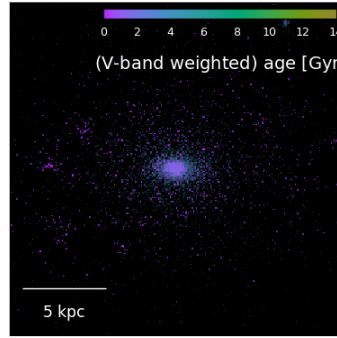
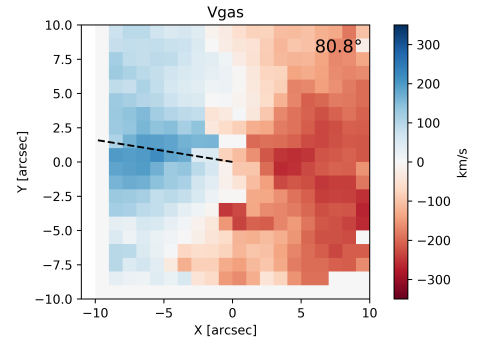
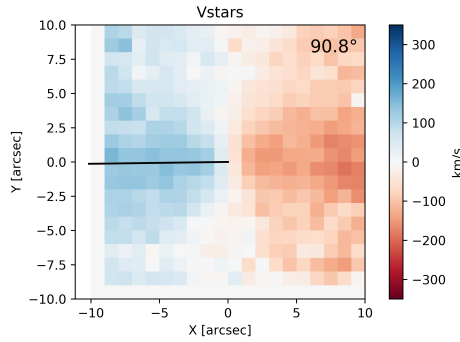
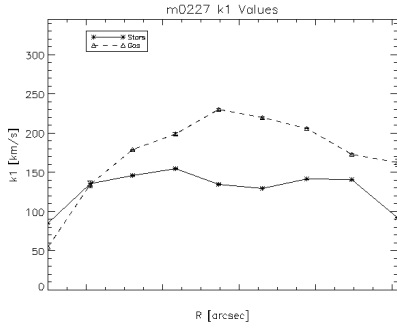
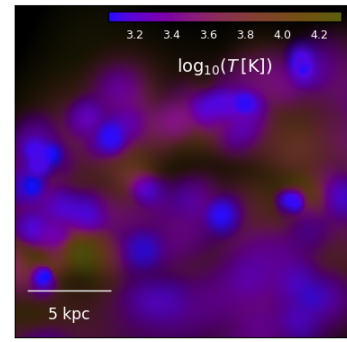
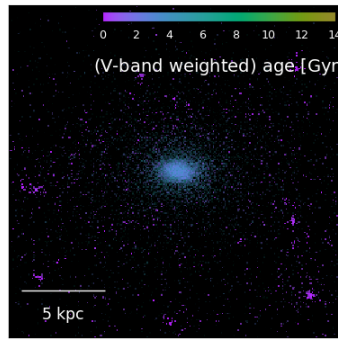


Figure 38 Top row, left to right: Name and characteristic parameters, stellar distribution, and warm gas distribution, respectively. Bottom row, left to right: radial k_1 profiles for stars (solid) and gas (dashed), stellar kinematics, and gas kinematics, respectively. The solid and dashed line in the stellar and gas velocity map, respectively, is the median position angle along which kinemetry coefficients were determined. The number value of this position angle given at the top right of the plot.

Snapshot 0227 (AGN)
 $\log(\text{Stellar Mass}): 11.800$
 Redshift: 0.515
 $r_e: 2.218$ kpc
 AGN activity: No
 λ_R value at r_e : 0.364
 Residual asymmetry: 0.821



Snapshot 0227 (No AGN)
 $\log(\text{Stellar Mass}): 11.882$
 Redshift: 0.515
 $r_e: 1.864$ kpc
 λ_R value at r_e : 0.396
 Residual Asymmetry: 0.721

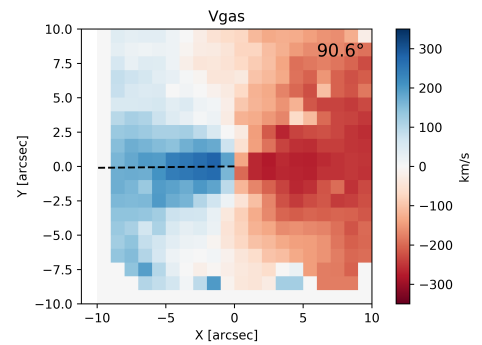
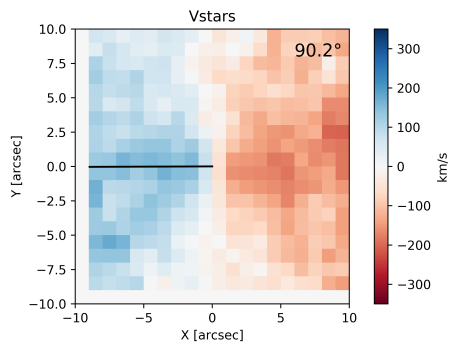
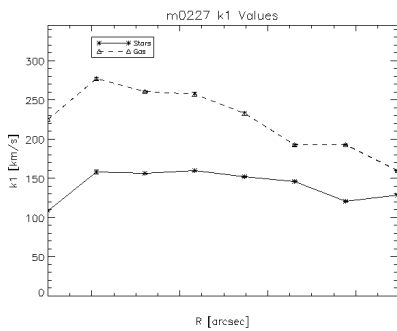
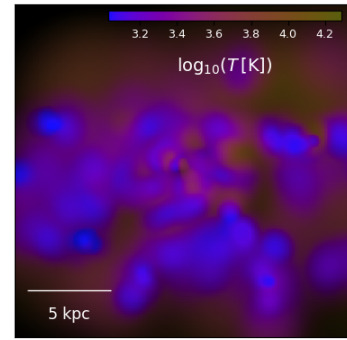
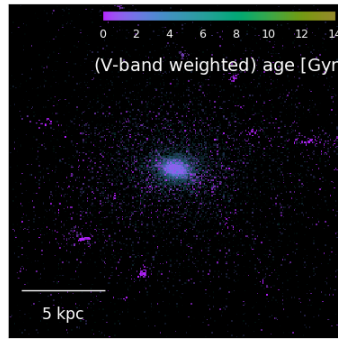
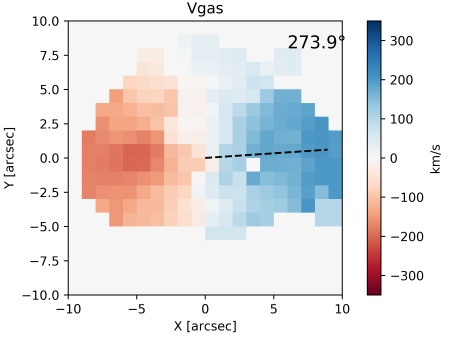
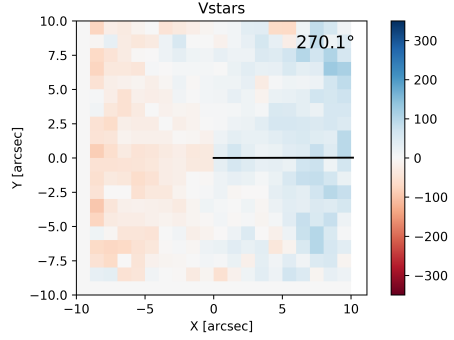
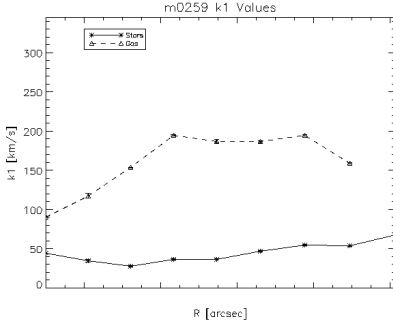
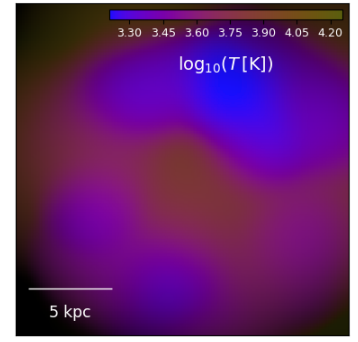
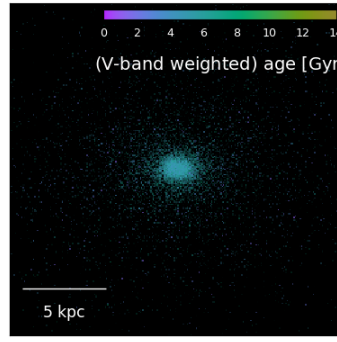


Figure 39 Top row, left to right: Name and characteristic parameters, stellar distribution, and warm gas distribution, respectively. Bottom row, left to right: radial k_1 profiles for stars (solid) and gas (dashed), stellar kinematics, and gas kinematics, respectively. The solid and dashed line in the stellar and gas velocity map, respectively, is the median position angle along which kinemetry coefficients were determined. The number value of this position angle given at the top right of the plot.

Snapshot 0259 (AGN)
 log(Stellar Mass): 11.699
 Redshift: 0.515
 r_e : 2.781 kpc
 AGN activity: No
 λ_R value at r_e : 0.168
 Residual asymmetry: 0.794



Snapshot 0259 (No AGN)
 log(Stellar Mass): 11.699
 Redshift: 0.515
 r_e : 2.781 kpc
 λ_R value at r_e : 0.170
 Residual Asymmetry: 0.703

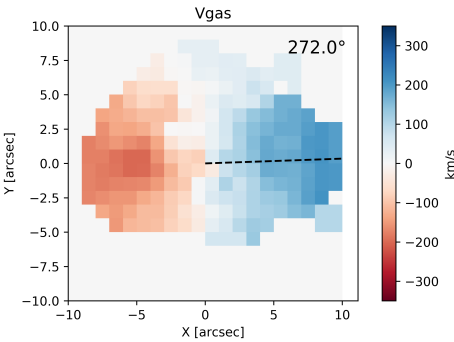
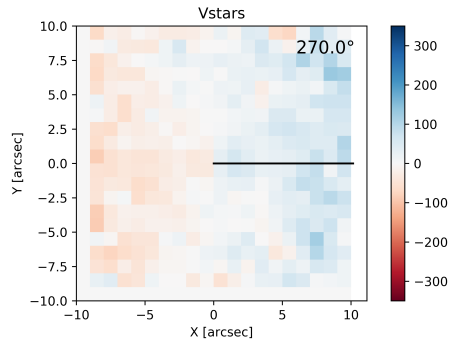
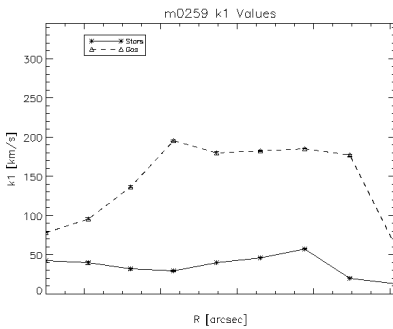
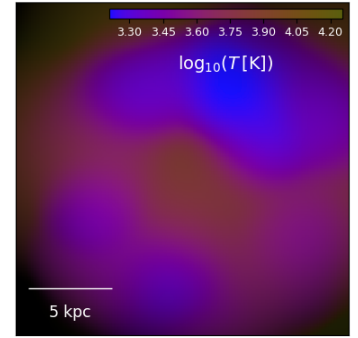
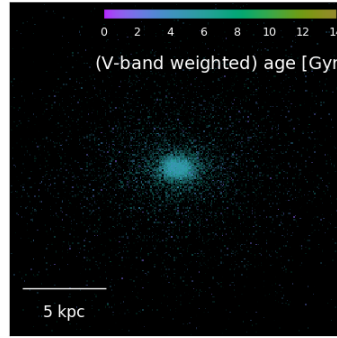
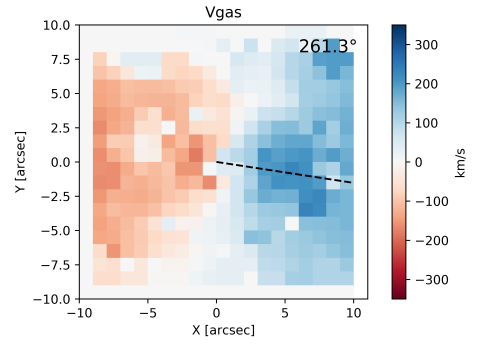
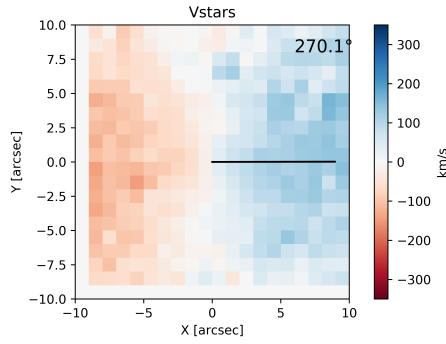
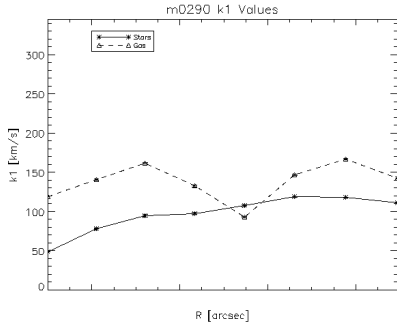
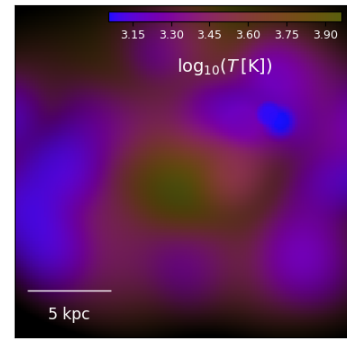
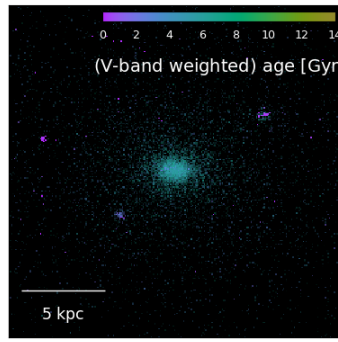


Figure 40 Top row, left to right: Name and characteristic parameters, stellar distribution, and warm gas distribution, respectively. Bottom row, left to right: radial k_1 profiles for stars (solid) and gas (dashed), stellar kinematics, and gas kinematics, respectively. The solid and dashed line in the stellar and gas velocity map, respectively, is the median position angle along which kinemetry coefficients were determined. The number value of this position angle given at the top right of the plot.

Snapshot 0290 (AGN)
 $\log(\text{Stellar Mass}): 11.701$
 Redshift: 0.515
 $r_e: 4.554$ kpc
 AGN activity: No
 λ_R value at r_e : 0.344
 Residual asymmetry: 0.697



Snapshot 0290 (No AGN)
 $\log(\text{Stellar Mass}): 11.899$
 Redshift: 0.515
 $r_e: 5.043$ kpc
 λ_R value at r_e : 0.513
 Residual Asymmetry: 0.758

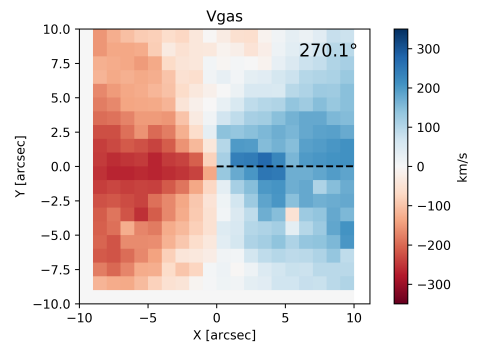
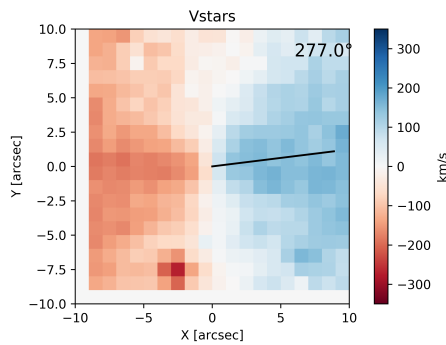
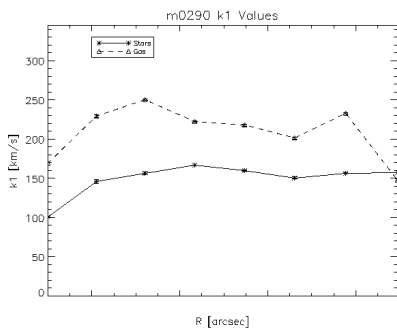
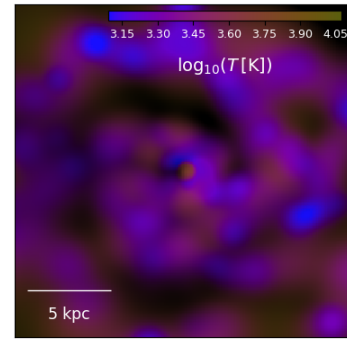
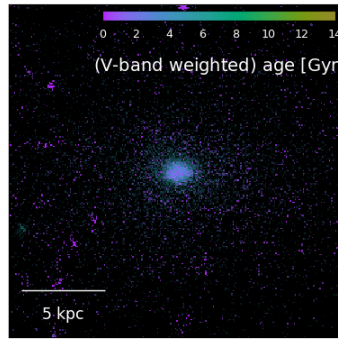
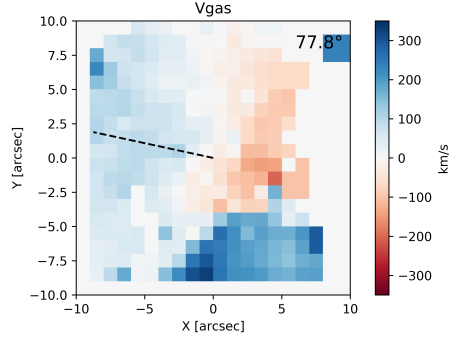
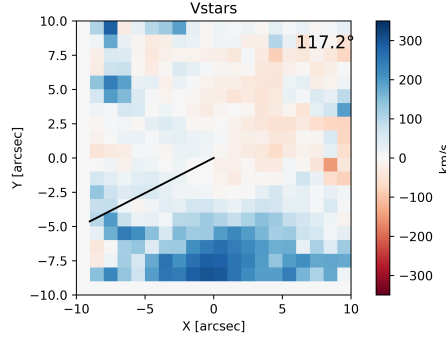
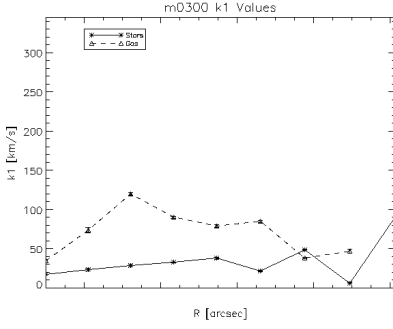
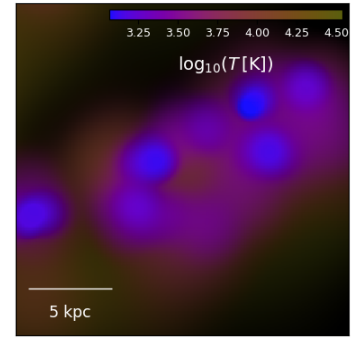
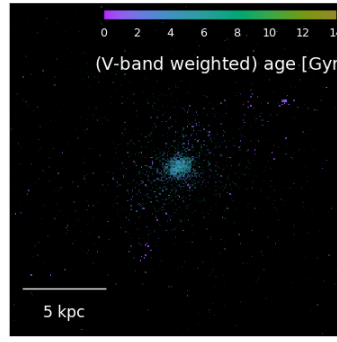


Figure 41 Top row, left to right: Name and characteristic parameters, stellar distribution, and warm gas distribution, respectively. Bottom row, left to right: radial k_1 profiles for stars (solid) and gas (dashed), stellar kinematics, and gas kinematics, respectively. The solid and dashed line in the stellar and gas velocity map, respectively, is the median position angle along which kinemetry coefficients were determined. The number value of this position angle given at the top right of the plot.

Snapshot 0300 (AGN)
 log(Stellar Mass): 11.218
 Redshift: 0.515
 r_e : 4.440 kpc
 AGN activity: No
 λ_R value at r_e : 0.364
 Residual asymmetry: 0.697



Snapshot 0300 (No AGN)
 log(Stellar Mass): 11.286
 Redshift: 0.515
 r_e : 1.622 kpc
 λ_R value at r_e : 0.024
 Residual Asymmetry: 0.664

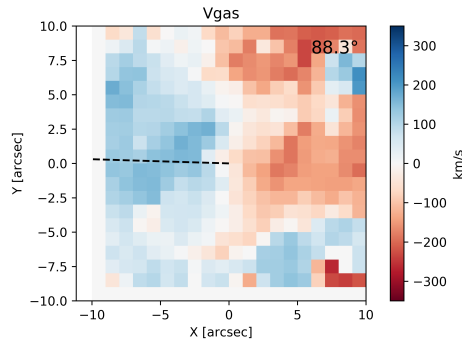
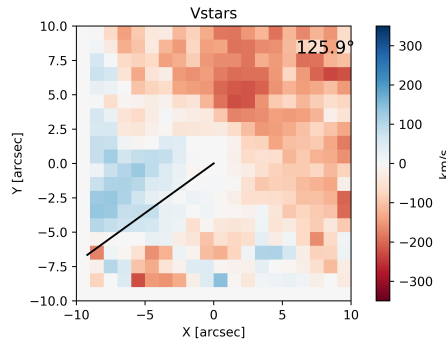
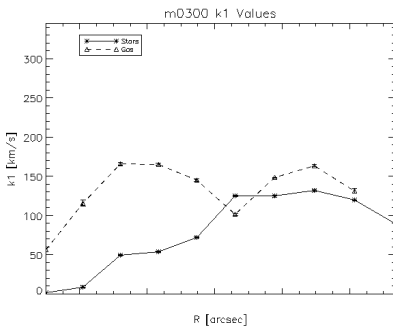
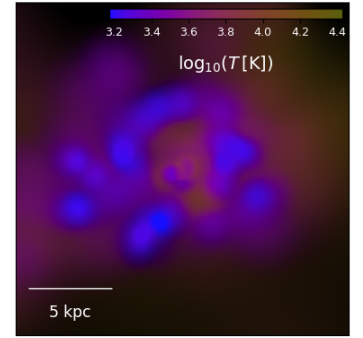
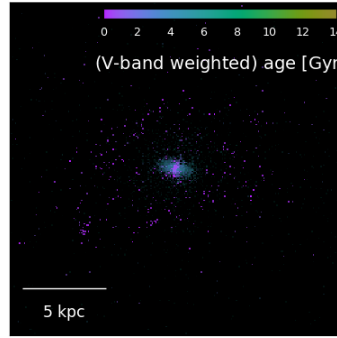
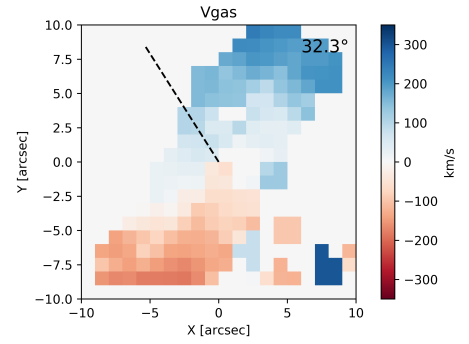
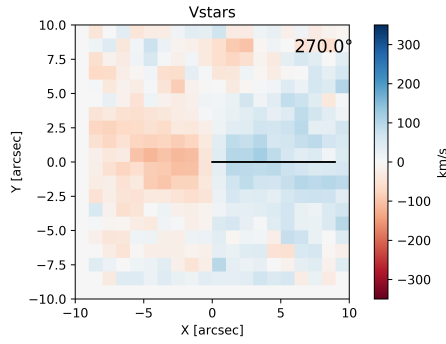
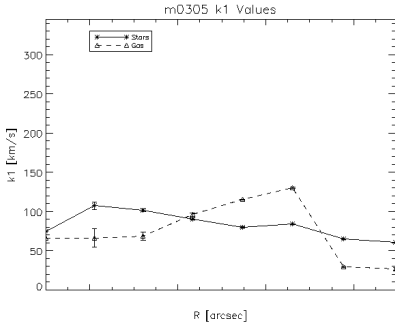
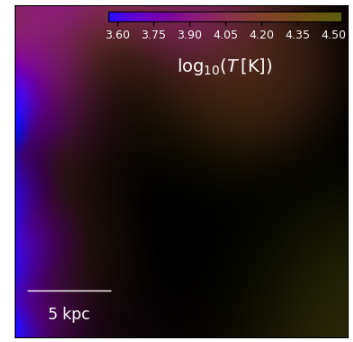
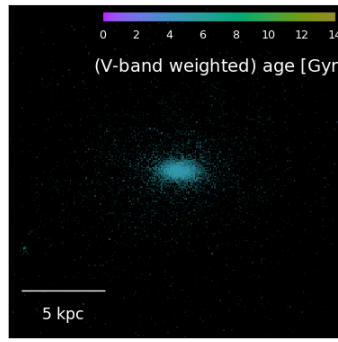


Figure 42 Top row, left to right: Name and characteristic parameters, stellar distribution, and warm gas distribution, respectively. Bottom row, left to right: radial k_1 profiles for stars (solid) and gas (dashed), stellar kinematics, and gas kinematics, respectively. The solid and dashed line in the stellar and gas velocity map, respectively, is the median position angle along which kinemetry coefficients were determined. The number value of this position angle given at the top right of the plot.

Snapshot 0305 (AGN)
 $\log(\text{Stellar Mass}): 11.553$
 Redshift: 0.515
 $r_e: 1.360$ kpc
 AGN activity: No
 λ_R value at r_e : 0.252
 Residual asymmetry: 0.800



Snapshot 0305 (No AGN)
 $\log(\text{Stellar Mass}): 11.835$
 Redshift: 0.515
 $r_e: 1.429$ kpc
 λ_R value at r_e : 0.207
 Residual Asymmetry: 0.773

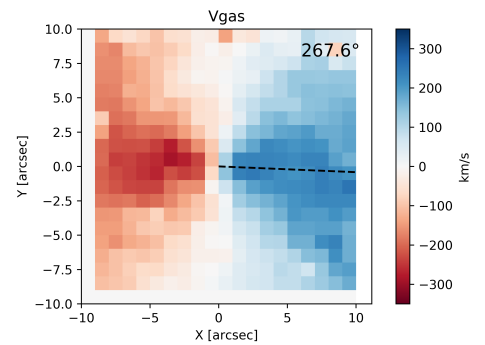
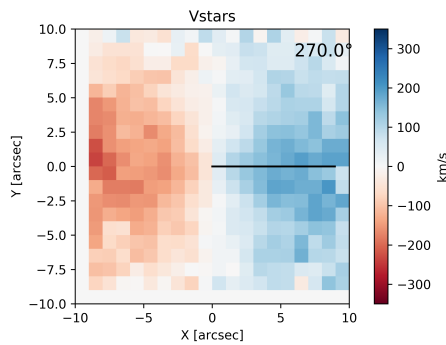
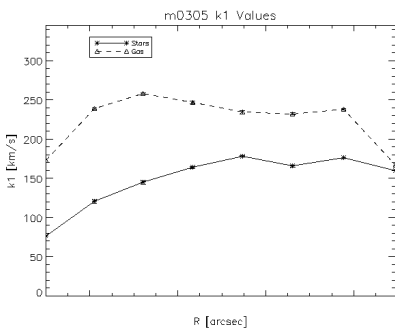
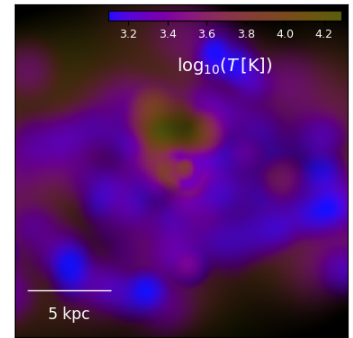
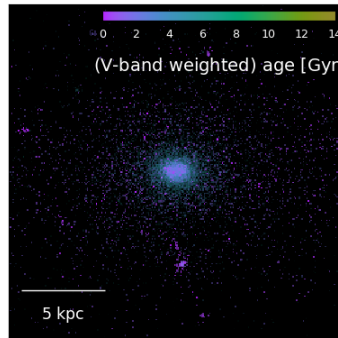


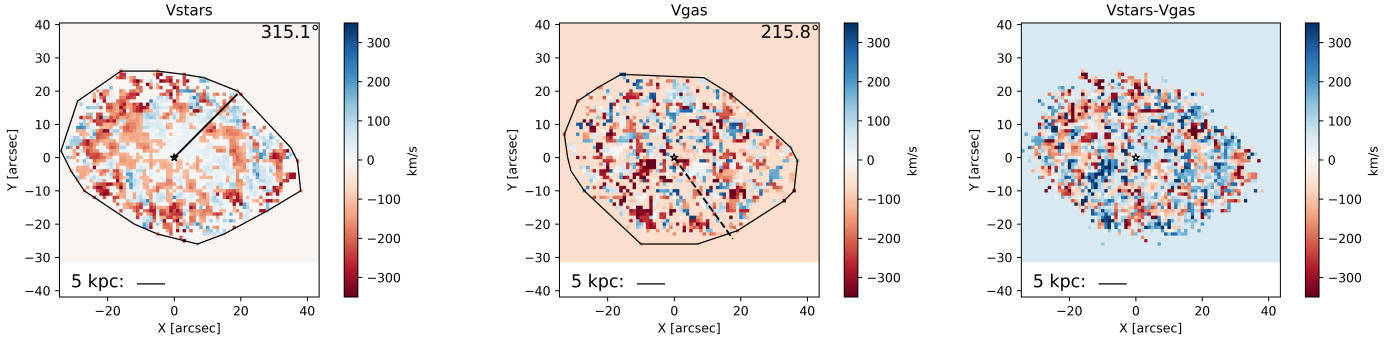
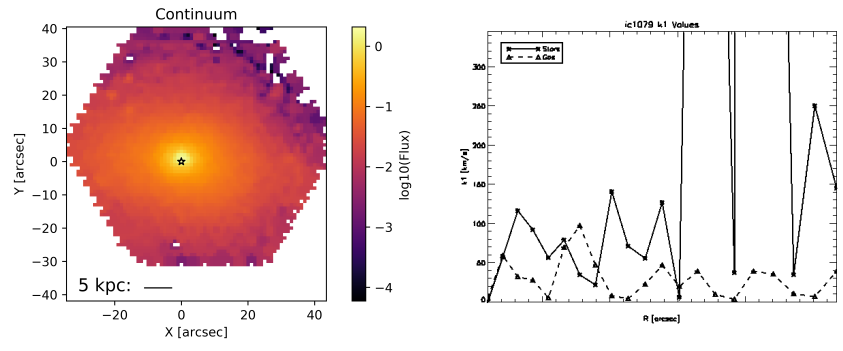
Figure 43 Top row, left to right: Name and characteristic parameters, stellar distribution, and warm gas distribution, respectively. Bottom row, left to right: radial k_1 profiles for stars (solid) and gas (dashed), stellar kinematics, and gas kinematics, respectively. The solid and dashed line in the stellar and gas velocity map, respectively, is the median position angle along which kinemetry coefficients were determined. The number value of this position angle given at the top right of the plot.

6.2 2D info on all studied CALIFA galaxies

The following values were either produced in the course of the work described in this thesis (λ_R , residual asymmetry) or were taken from our reduced data cubes (distance) or from the third data release (DR3) of CALIFA (stellar mass, R-band absolute magnitude, redshift, effective radius) described in Sánchez et al. (2016), unless noted otherwise. Data for one galaxy was taken from the 2MASS survey (Crook et al., 2007). Note: the galaxy referred to in this appendix (and the rest of the thesis) as UGC11958 is actually the galaxy NGC7237, but we retain this nomenclature for consistency.

IC 1079

$\log(\text{Stellar Mass}): 11.327$
 $D = 127.9 \text{ Mpc}$
 $M_r = -23.211 \text{ mag}$
 Redshift: 0.029
 $r_e = 37.62 \text{ arcsec}$
 AGN activity: No
 λ_R value at r_e : N/A
 Residual asymmetry: 0.830



IC 2341

$\log(\text{Stellar Mass}): 10.806$
 $D = 73.6 \text{ Mpc}$
 $M_r = -21.451 \text{ mag}$
 Redshift: 0.017
 $r_e = 11.088 \text{ arcsec}$
 AGN activity: No
 λ_R value at r_e : 0.498
 Residual asymmetry: 0.921

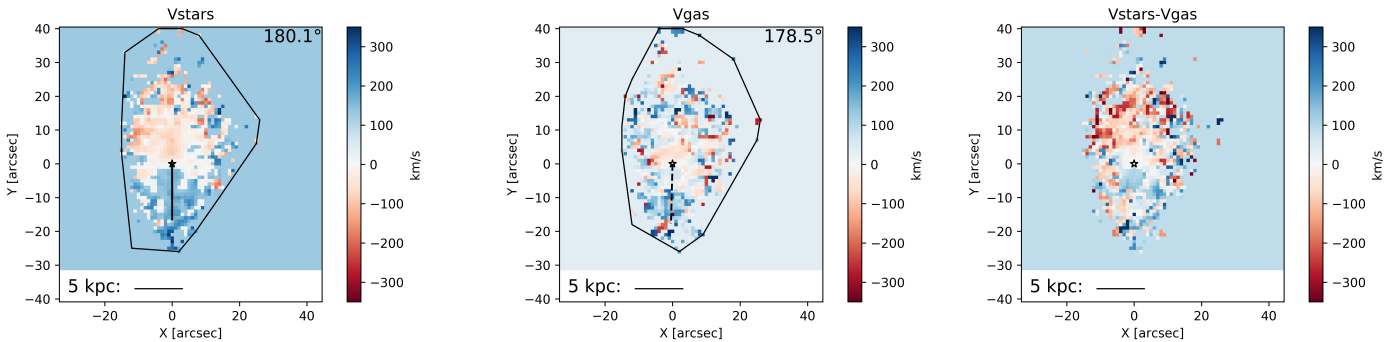
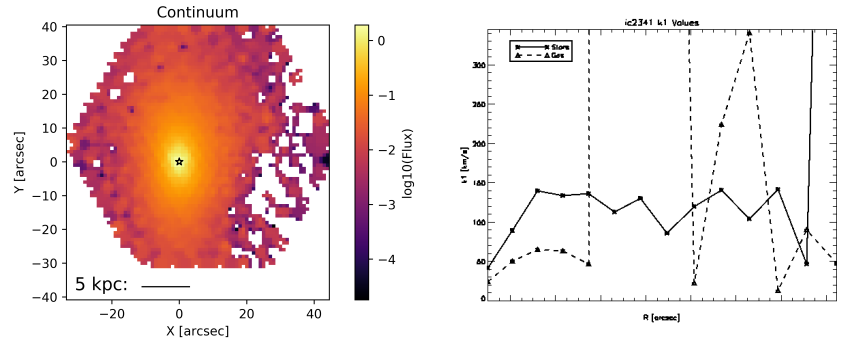
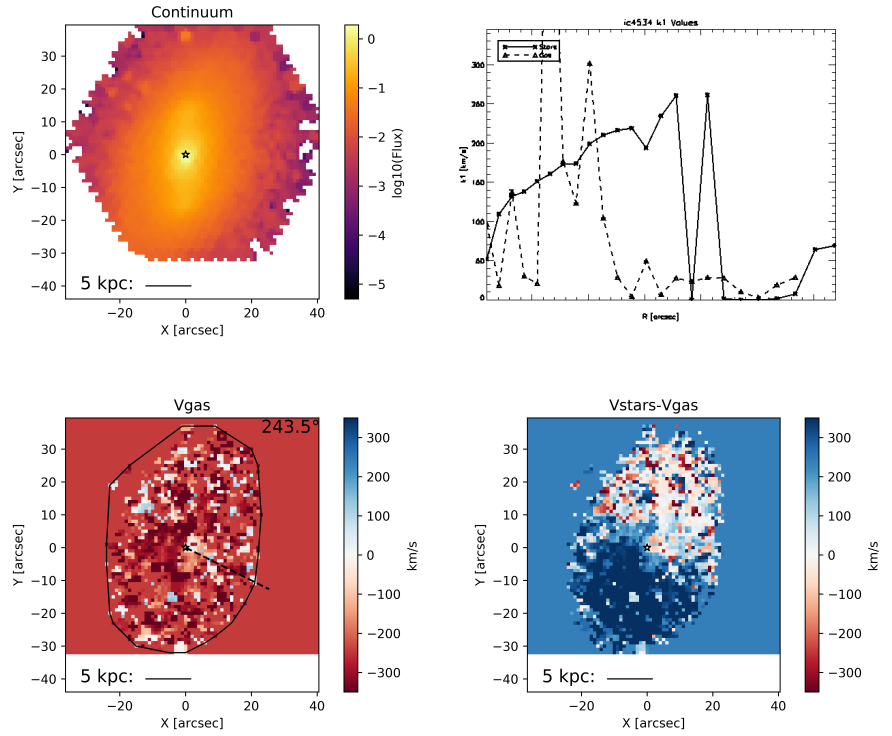


Figure 44 Top row, left to right: Name and characteristic parameters, continuum flux, and radial k_1 profiles for stars (solid) and gas (dashed), respectively. Bottom row, left to right: stellar kinematics, gas kinematics, and the difference between stellar and gas kinematics, respectively. The curves containing the data points are the convex hulls used to define the 'edge' of the map. The brightest continuum pixel (used as the center for kinemetry) is marked by a white star. The solid and dashed line in the stellar and gas velocity map, respectively, is the median position angle along which kinemetry coefficients were determined. The number value of this position angle is given at the top right of the plot. A scale bar is given along the bottom of each velocity map.

IC 4534

$\log(\text{Stellar Mass}): 10.925$
 $D = 76.2 \text{ Mpc}$
 $M_r = -21.63 \text{ mag}$
 Redshift: 0.016
 $r_e: 13.464 \text{ arcsec}$
 AGN activity: No
 λ_R value at $r_e: 0.603$
 Residual asymmetry: 0.814



LSBCF 560

$\log(\text{Stellar Mass}): 11.89$
 $D = 217.4 \text{ Mpc}$
 $M_r = -23.36 \text{ mag}$
 Redshift: 0.053
 $r_e: 8.370 \text{ arcsec}$
 AGN activity: No
 λ_R value at $r_e: 0.464$
 Residual asymmetry: 0.882

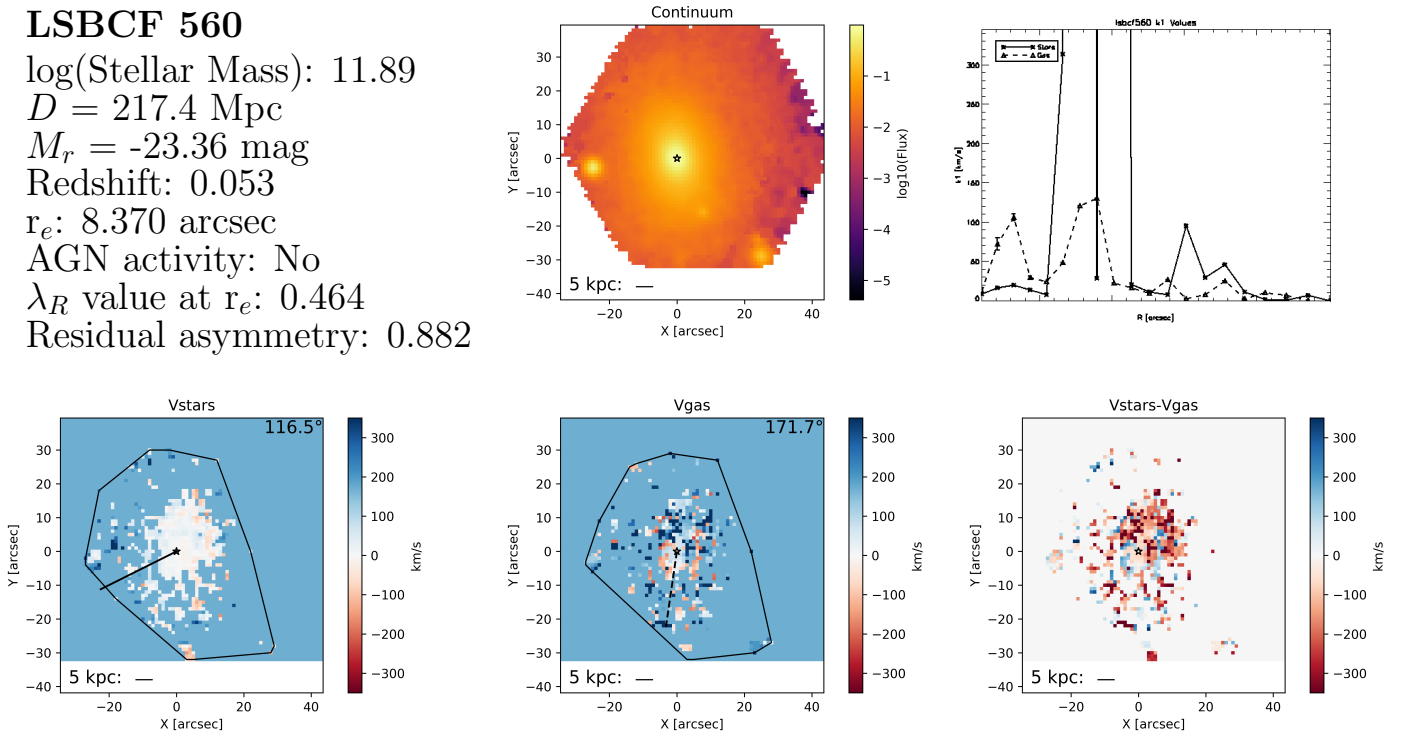
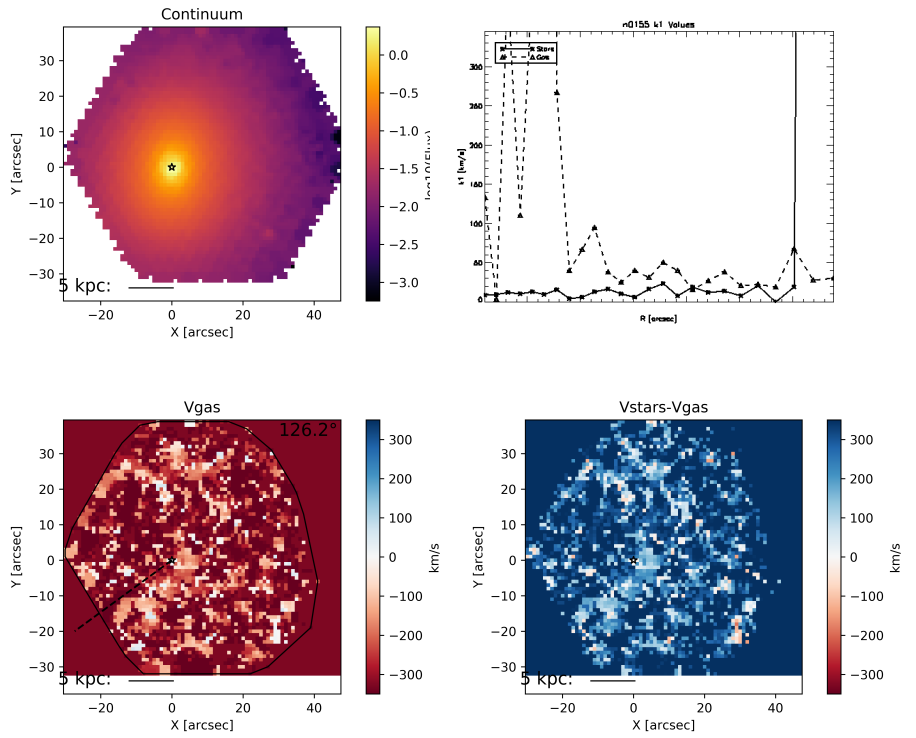


Figure 45 Top row, left to right: Name and characteristic parameters, continuum flux, and radial k_1 profiles for stars (solid) and gas (dashed), respectively. Bottom row, left to right: stellar kinematics, gas kinematics, and the difference between stellar and gas kinematics, respectively. The curves containing the data points are the convex hulls used to define the 'edge' of the map. The brightest continuum pixel (used as the center for kinemetry) is marked by a white star. The solid and dashed line in the stellar and gas velocity map, respectively, is the median position angle along which kinemetry coefficients were determined. The number value of this position angle is given at the top right of the plot. A scale bar is given along the bottom of each velocity map.

NGC 0155

$\log(\text{Stellar Mass}): 11.176$
 $D = 83.4 \text{ Mpc}$
 $M_r = -22.412 \text{ mag}$
 Redshift: 0.021
 $r_e: 15.84 \text{ arcsec}$
 AGN activity: No
 λ_R value at r_e : 0.513
 Residual asymmetry: 0.856



NGC 0160

$\log(\text{Stellar Mass}): 11.030$
 $D = 70.5 \text{ Mpc}$
 $M_r = -22.18 \text{ mag}$
 Redshift: 0.018
 $r_e: 22.176 \text{ arcsec}$
 AGN activity: Yes
 λ_R value at r_e : 0.545
 Residual asymmetry: 0.944

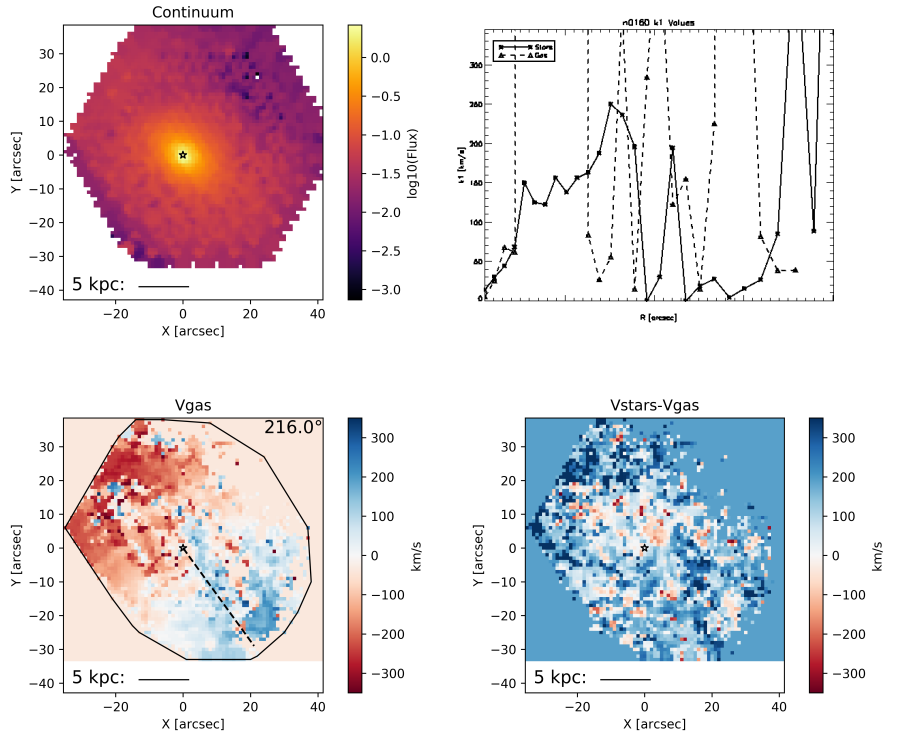
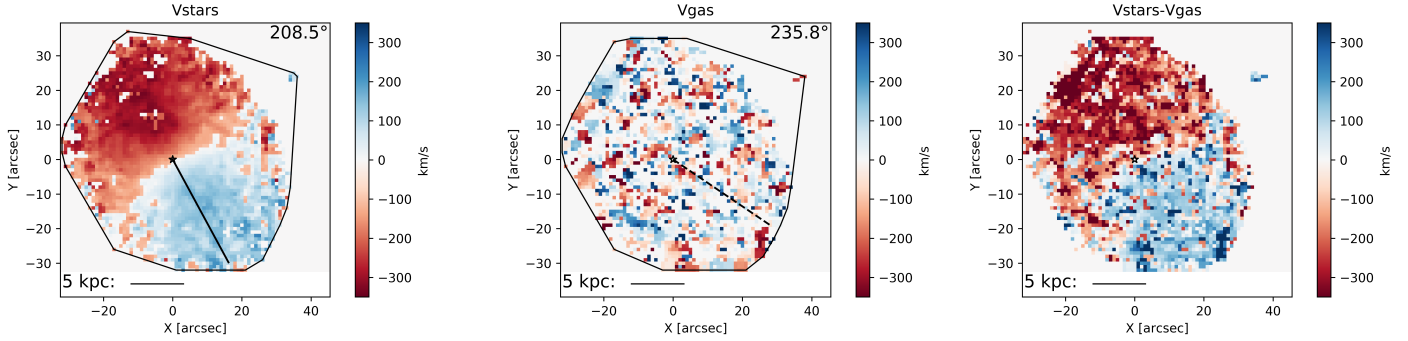
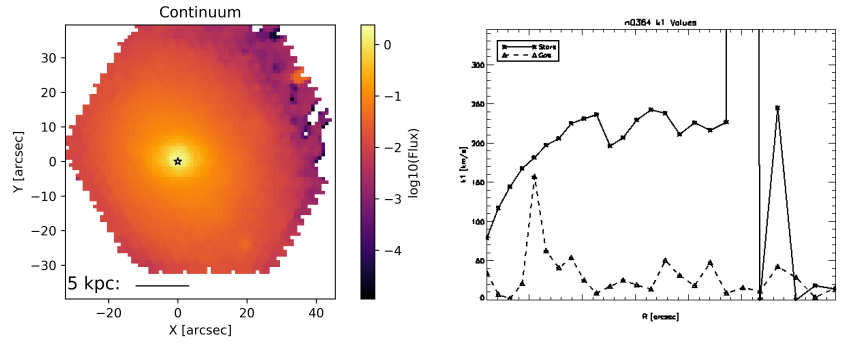


Figure 46 Top row, left to right: Name and characteristic parameters, continuum flux, and radial k_1 profiles for stars (solid) and gas (dashed), respectively. Bottom row, left to right: stellar kinematics, gas kinematics, and the difference between stellar and gas kinematics, respectively. The curves containing the data points are the convex hulls used to define the 'edge' of the map. The brightest continuum pixel (used as the center for kinemetry) is marked by a white star. The solid and dashed line in the stellar and gas velocity map, respectively, is the median position angle along which kinemetry coefficients were determined. The number value of this position angle is given at the top right of the plot. A scale bar is given along the bottom of each velocity map.

NGC 0364

$\log(\text{Stellar Mass}): 10.962$
 $D = 68.3 \text{ Mpc}$
 $M_r = -21.561 \text{ mag}$
 Redshift: 0.017
 $r_e = 15.84 \text{ arcsec}$
 AGN activity: No
 λ_R value at r_e : 0.609
 Residual asymmetry: 0.827



NGC 0472

$\log(\text{Stellar Mass}): 10.965$
 $D = 71.2 \text{ Mpc}$
 $M_r = -21.104 \text{ mag}$
 Redshift: 0.000
 $r_e = 4.620 \text{ arcsec}$
 AGN activity: No
 λ_R value at r_e : 0.661
 Residual asymmetry: 0.778

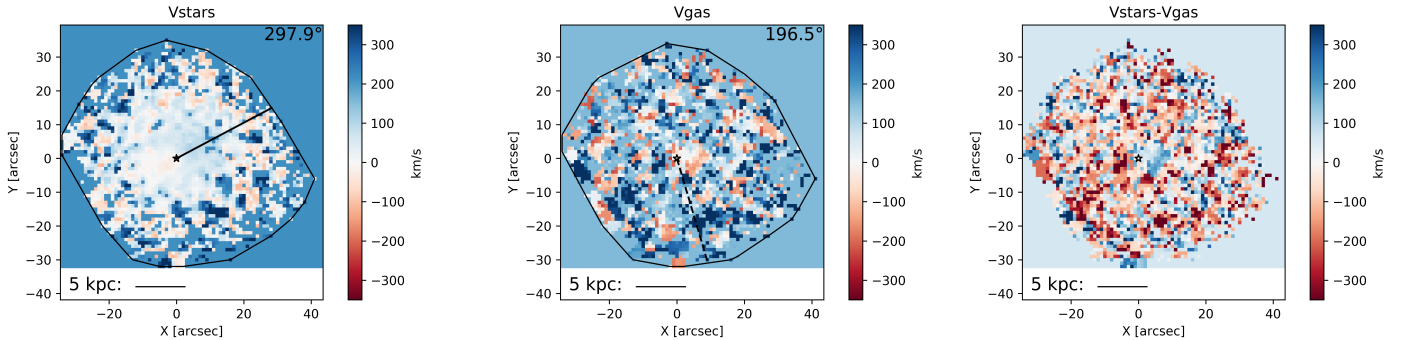
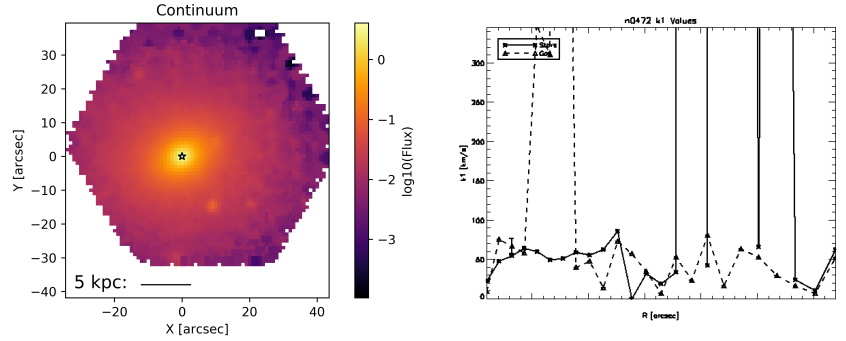


Figure 47 Top row, left to right: Name and characteristic parameters, continuum flux, and radial k_1 profiles for stars (solid) and gas (dashed), respectively. Bottom row, left to right: stellar kinematics, gas kinematics, and the difference between stellar and gas kinematics, respectively. The curves containing the data points are the convex hulls used to define the 'edge' of the map. The brightest continuum pixel (used as the center for kinemetry) is marked by a white star. The solid and dashed line in the stellar and gas velocity map, respectively, is the median position angle along which kinemetry coefficients were determined. The number value of this position angle is given at the top right of the plot. A scale bar is given along the bottom of each velocity map.

NGC 0499

$\log(\text{Stellar Mass}): 11.401$

$D = 59.1 \text{ Mpc}$

$M_r = -22.482 \text{ mag}$

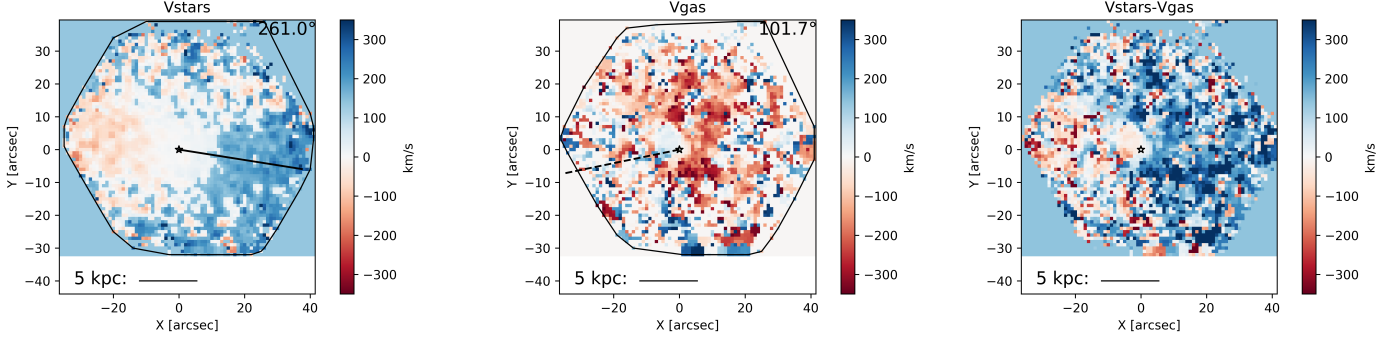
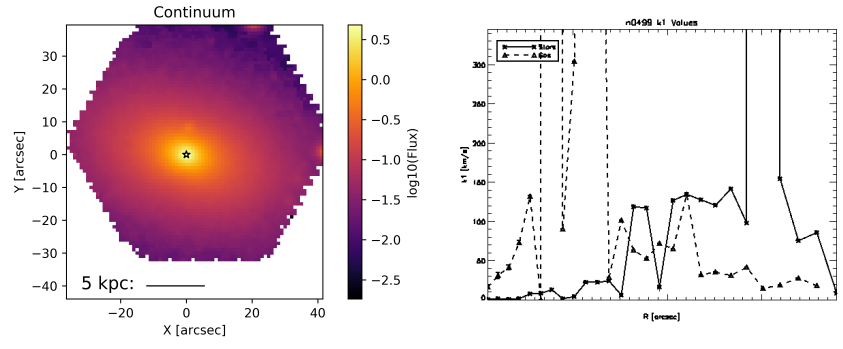
Redshift: 0.015

$r_e = 21.384 \text{ arcsec}$

AGN activity: No

λ_R value at r_e : 0.378

Residual asymmetry: 0.719



NGC 0517

$\log(\text{Stellar Mass}): 10.822$

$D = 56.5 \text{ Mpc}$

$M_r = -21.352 \text{ mag}$

Redshift: 0.014

$r_e = 10.296 \text{ arcsec}$

AGN activity: No

λ_R value at r_e : 0.572

Residual asymmetry: 0.822

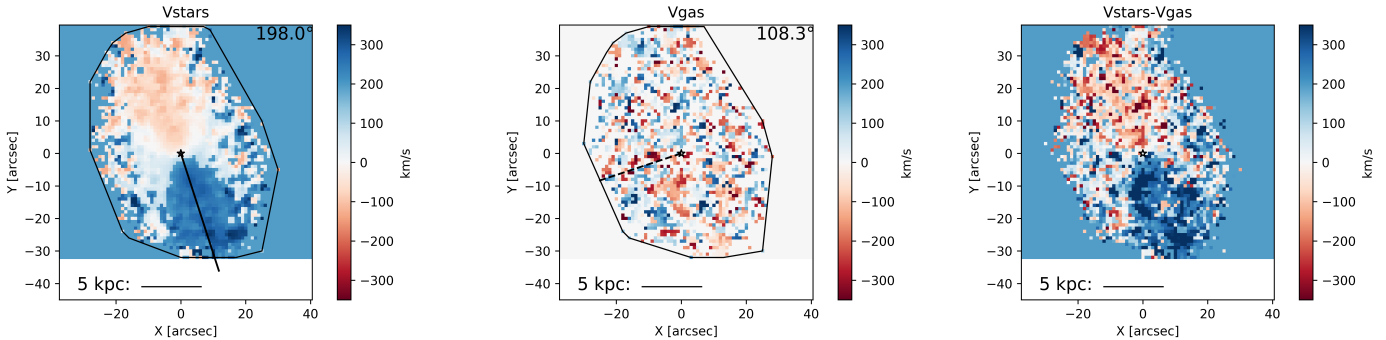
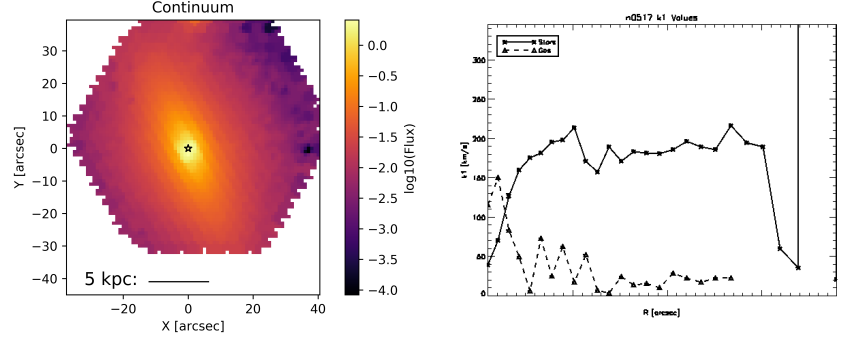


Figure 48 Top row, left to right: Name and characteristic parameters, continuum flux, and radial k_1 profiles for stars (solid) and gas (dashed), respectively. Bottom row, left to right: stellar kinematics, gas kinematics, and the difference between stellar and gas kinematics, respectively. The curves containing the data points are the convex hulls used to define the 'edge' of the map. The brightest continuum pixel (used as the center for kinemetry) is marked by a white star. The solid and dashed line in the stellar and gas velocity map, respectively, is the median position angle along which kinemetry coefficients were determined. The number value of this position angle is given at the top right of the plot. A scale bar is given along the bottom of each velocity map.

NGC 0528

$\log(\text{Stellar Mass}): 10.874$

$D = 64.5 \text{ Mpc}$

$M_r = -21.697 \text{ mag}$

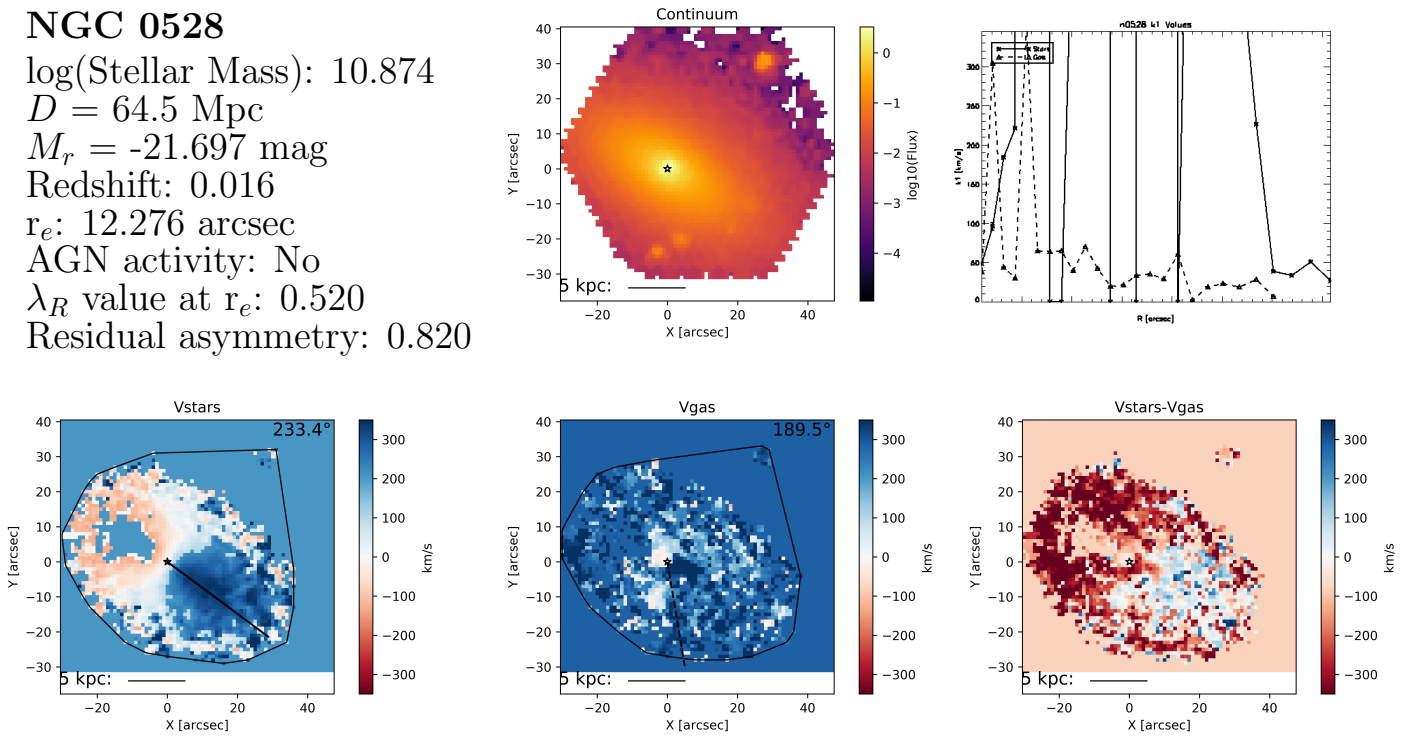
Redshift: 0.016

$r_e: 12.276 \text{ arcsec}$

AGN activity: No

λ_R value at $r_e: 0.520$

Residual asymmetry: 0.820



NGC 0529

$\log(\text{Stellar Mass}): 11.088$

$D = 64.7 \text{ Mpc}$

$M_r = -22.271 \text{ mag}$

Redshift: 0.016

$r_e: 12.672 \text{ arcsec}$

AGN activity: No

λ_R value at $r_e: 0.541$

Residual asymmetry: 0.784

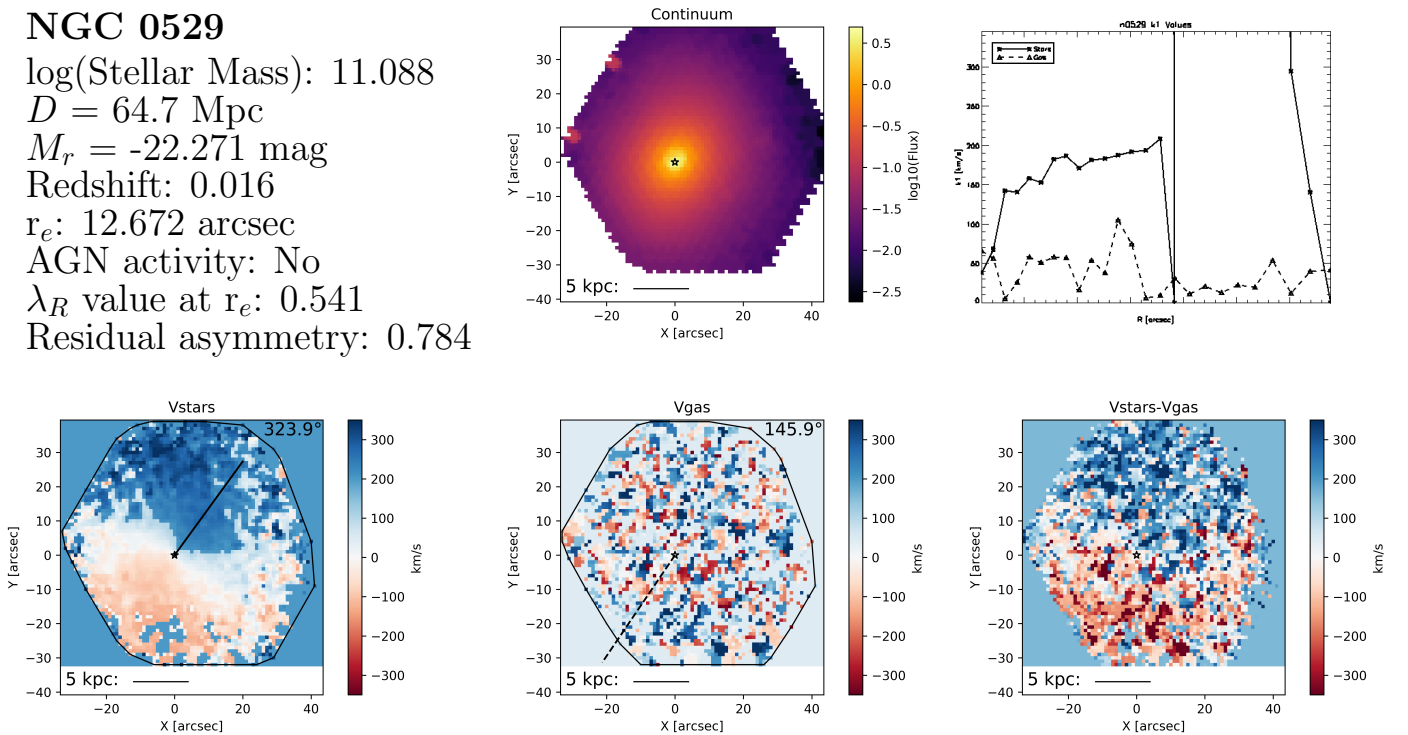


Figure 49 Top row, left to right: Name and characteristic parameters, continuum flux, and radial k_1 profiles for stars (solid) and gas (dashed), respectively. Bottom row, left to right: stellar kinematics, gas kinematics, and the difference between stellar and gas kinematics, respectively. The curves containing the data points are the convex hulls used to define the 'edge' of the map. The brightest continuum pixel (used as the center for kinemetry) is marked by a white star. The solid and dashed line in the stellar and gas velocity map, respectively, is the median position angle along which kinemetry coefficients were determined. The number value of this position angle is given at the top right of the plot. A scale bar is given along the bottom of each velocity map.

NGC 0677

$\log(\text{Stellar Mass}): 11.291$

$D = 67.6 \text{ Mpc}$

$M_r = -22.574 \text{ mag}$

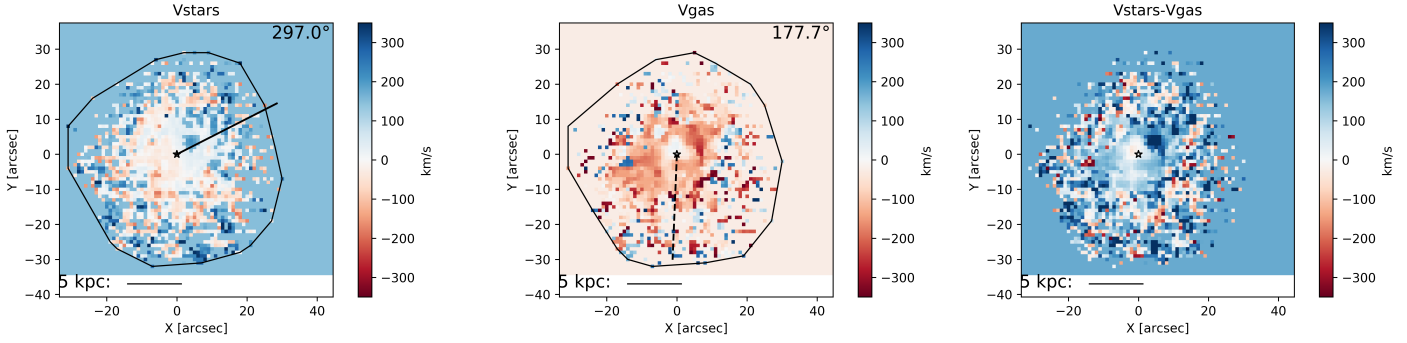
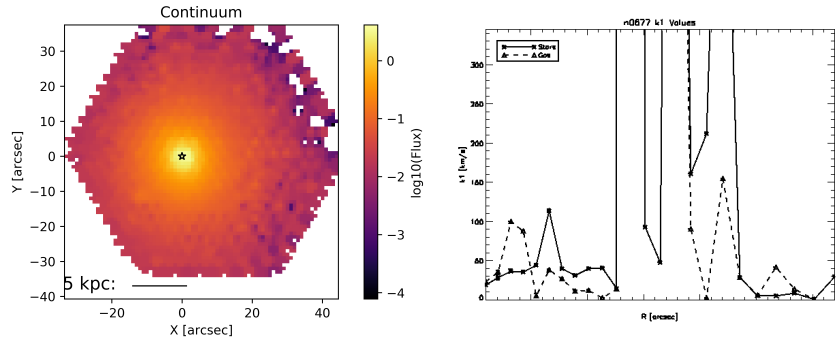
Redshift: 0.017

$r_e = 34.056 \text{ arcsec}$

AGN activity: No

λ_R value at r_e : N/A

Residual asymmetry: 0.978



NGC 0731

$\log(\text{Stellar Mass}): 10.903$

$D = 50.8 \text{ Mpc}$

$M_r = -21.776 \text{ mag}$

Redshift: 0.013

$r_e = 11.484 \text{ arcsec}$

AGN activity: No

λ_R value at r_e : 0.558

Residual asymmetry: 0.834

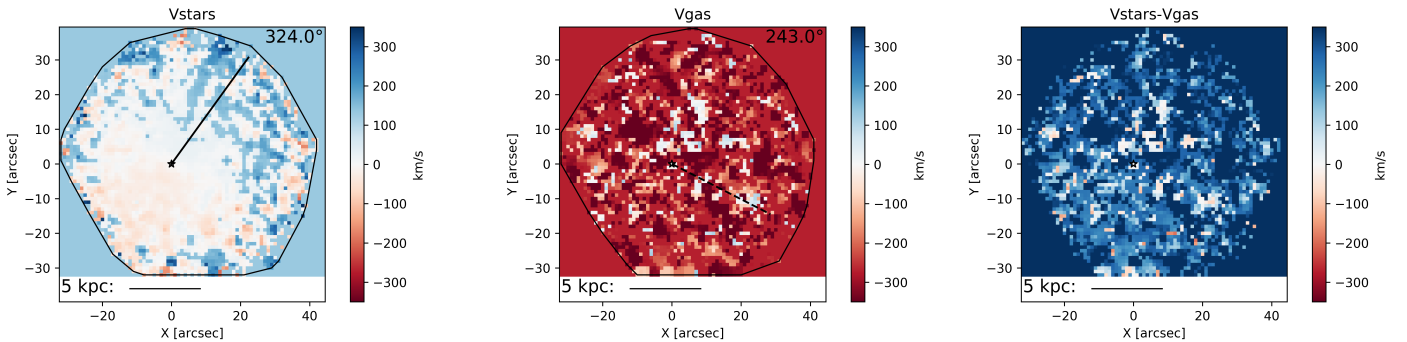
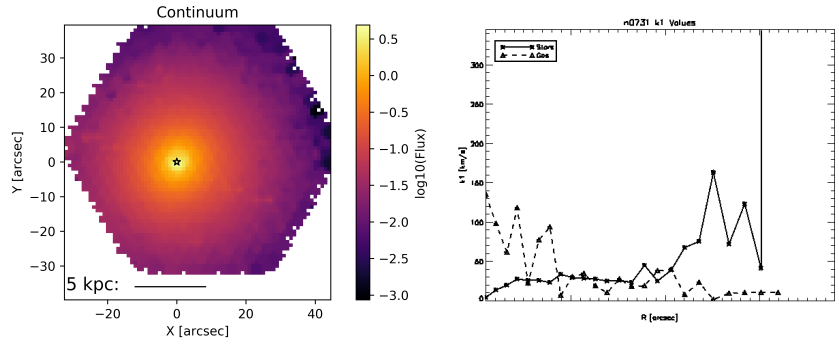
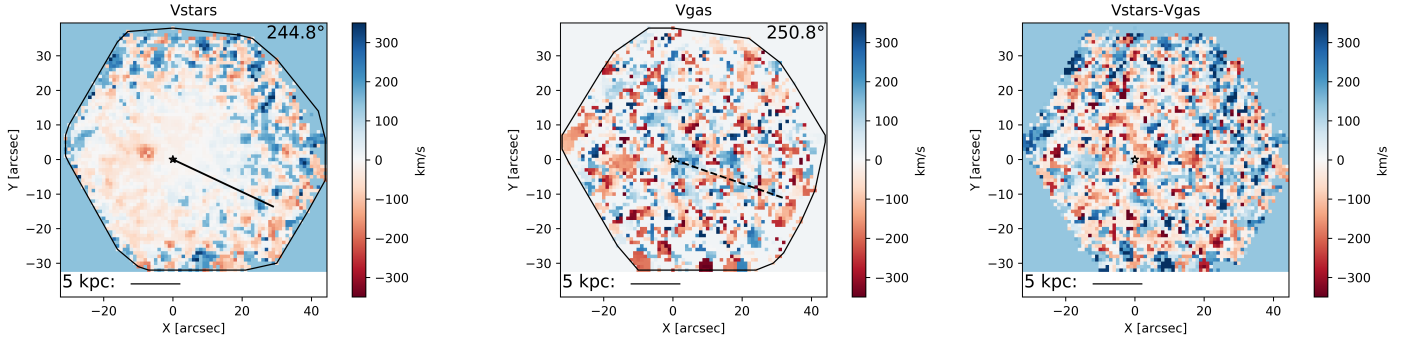
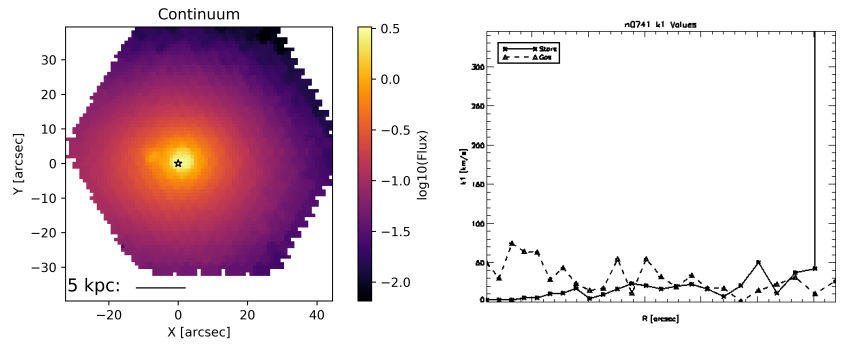


Figure 50 Top row, left to right: Name and characteristic parameters, continuum flux, and radial k_1 profiles for stars (solid) and gas (dashed), respectively. Bottom row, left to right: stellar kinematics, gas kinematics, and the difference between stellar and gas kinematics, respectively. The curves containing the data points are the convex hulls used to define the 'edge' of the map. The brightest continuum pixel (used as the center for kinemetry) is marked by a white star. The solid and dashed line in the stellar and gas velocity map, respectively, is the median position angle along which kinemetry coefficients were determined. The number value of this position angle is given at the top right of the plot. A scale bar is given along the bottom of each velocity map.

NGC 0741

$\log(\text{Stellar Mass}): 11.517$
 $D = 73.7 \text{ Mpc}$
 $M_r = -23.465 \text{ mag}$
 Redshift: 0.019
 $r_e: 35.244 \text{ arcsec}$
 AGN activity: No
 λ_R value at r_e : N/A
 Residual asymmetry: 0.804



NGC 0774

$\log(\text{Stellar Mass}): 10.924$
 $D = 61.2 \text{ Mpc}$
 $M_r = -21.554 \text{ mag}$
 Redshift: 0.015
 $r_e: 12.276 \text{ arcsec}$
 AGN activity: No
 λ_R value at r_e : 0.562
 Residual asymmetry: 0.885

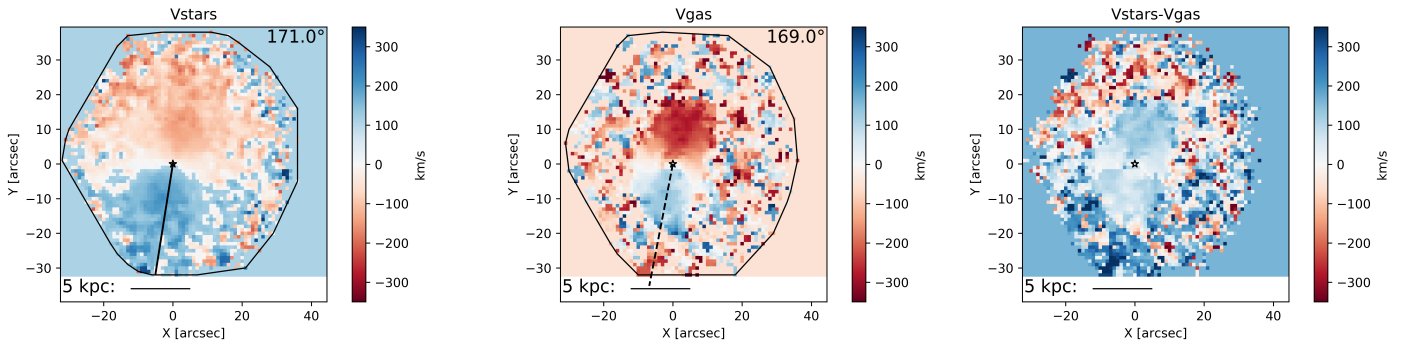
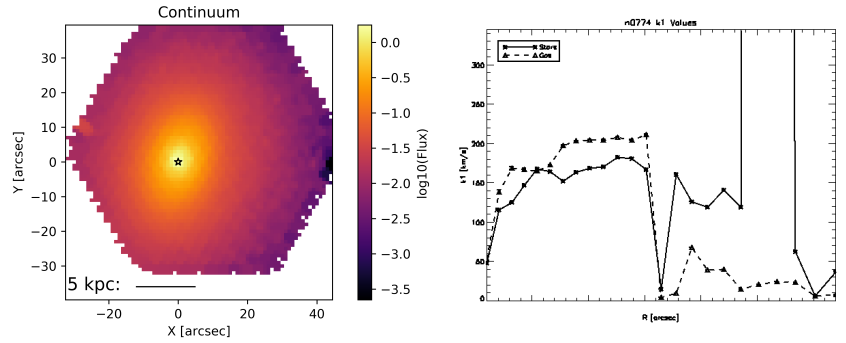
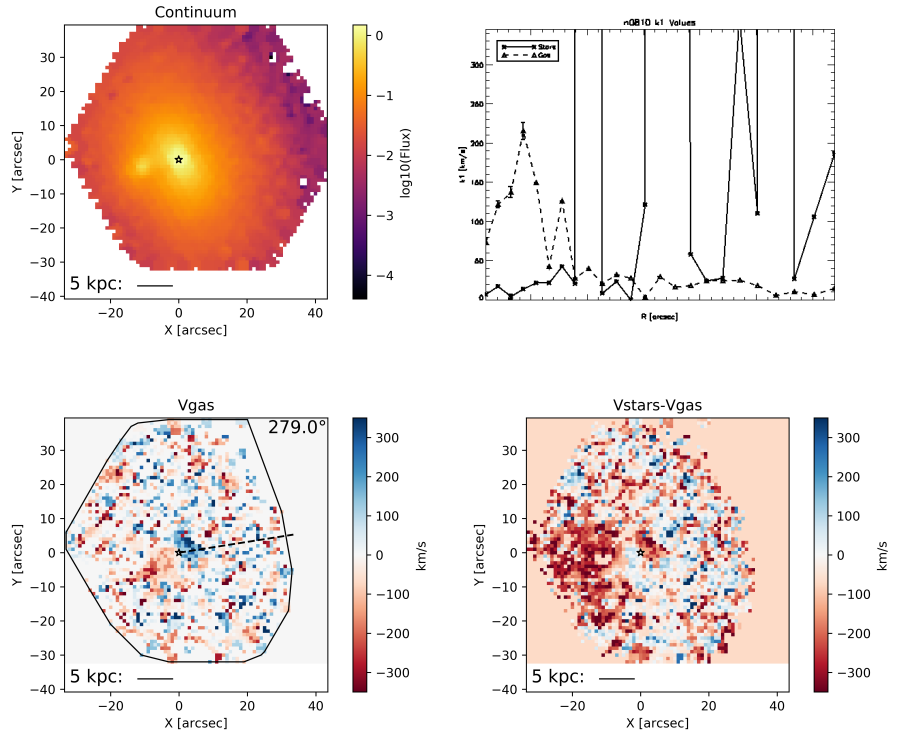


Figure 51 Top row, left to right: Name and characteristic parameters, continuum flux, and radial k_1 profiles for stars (solid) and gas (dashed), respectively. Bottom row, left to right: stellar kinematics, gas kinematics, and the difference between stellar and gas kinematics, respectively. The curves containing the data points are the convex hulls used to define the 'edge' of the map. The brightest continuum pixel (used as the center for kinemetry) is marked by a white star. The solid and dashed line in the stellar and gas velocity map, respectively, is the median position angle along which kinemetry coefficients were determined. The number value of this position angle is given at the top right of the plot. A scale bar is given along the bottom of each velocity map.

NGC 0810

$\log(\text{Stellar Mass}): 11.552$
 $D = 102.0 \text{ Mpc}$
 $M_r = -22.839 \text{ mag}$
 Redshift: 0.026
 $r_e = 17.424 \text{ arcsec}$
 AGN activity: No
 λ_R value at r_e : 0.324
 Residual asymmetry: 0.846



NGC 0842

$\log(\text{Stellar Mass}): 10.74$
 $D = 51.1 \text{ Mpc}$
 $M_r = -21.392 \text{ mag}$
 Redshift: 0.013
 $r_e = 11.484 \text{ arcsec}$
 AGN activity: No
 λ_R value at r_e : 0.534
 Residual asymmetry: 0.960

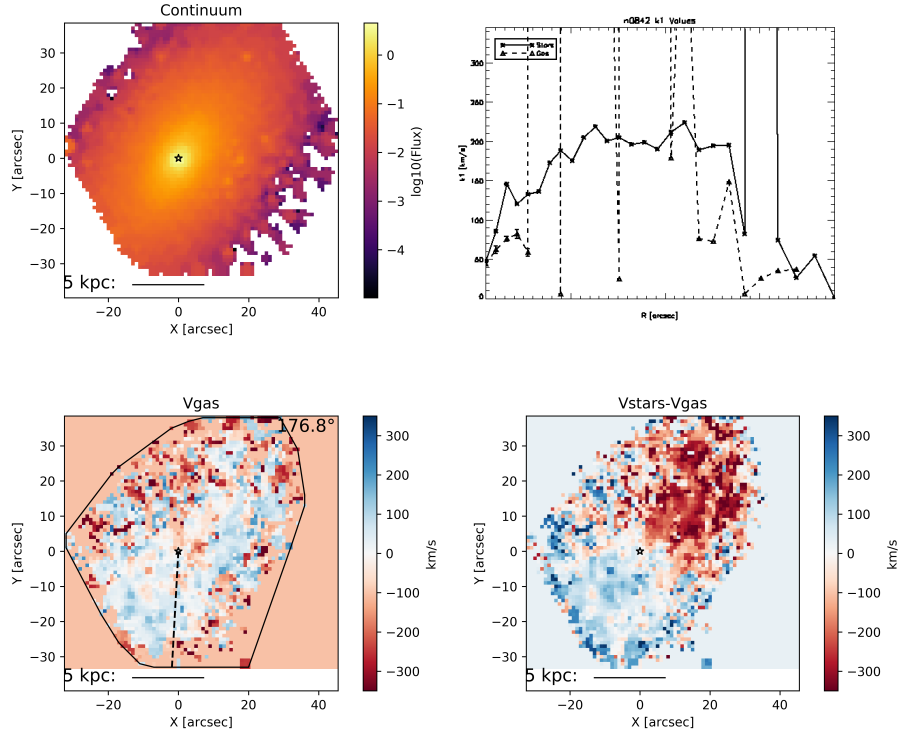
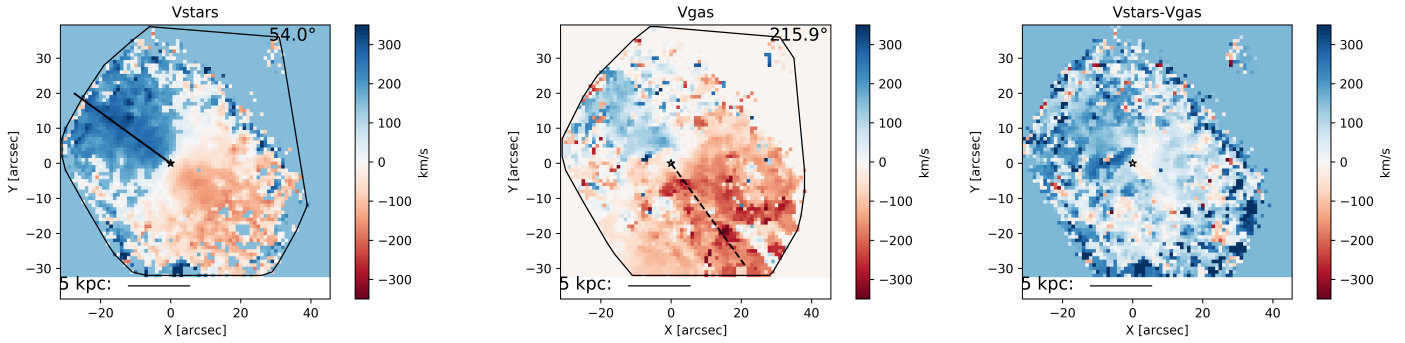
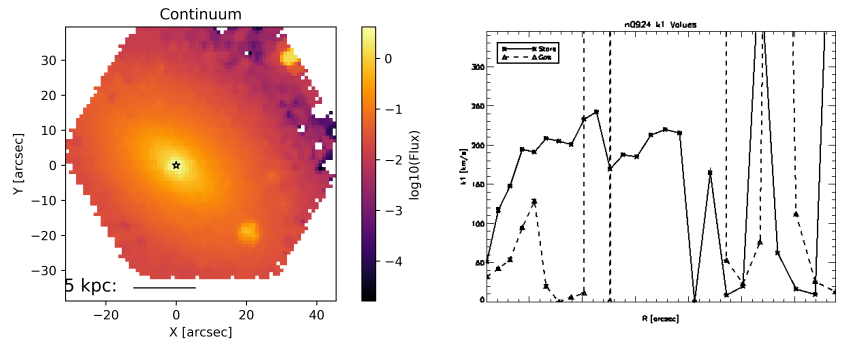


Figure 52 Top row, left to right: Name and characteristic parameters, continuum flux, and radial k_1 profiles for stars (solid) and gas (dashed), respectively. Bottom row, left to right: stellar kinematics, gas kinematics, and the difference between stellar and gas kinematics, respectively. The curves containing the data points are the convex hulls used to define the 'edge' of the map. The brightest continuum pixel (used as the center for kinemetry) is marked by a white star. The solid and dashed line in the stellar and gas velocity map, respectively, is the median position angle along which kinemetry coefficients were determined. The number value of this position angle is given at the top right of the plot. A scale bar is given along the bottom of each velocity map.

NGC 0924

$\log(\text{Stellar Mass}): 10.856$
 $D = 59.2 \text{ Mpc}$
 $M_r = -21.896 \text{ mag}$
 Redshift: 0.015
 $r_e: 12.672 \text{ arcsec}$
 AGN activity: No
 λ_R value at $r_e: 0.638$
 Residual asymmetry: 0.995



NGC 0932

$\log(\text{Stellar Mass}): 10.964$
 $D = 54.1 \text{ Mpc}$
 $M_r = -22.099 \text{ mag}$
 Redshift: 0.014
 $r_e: 18.612 \text{ arcsec}$
 AGN activity: Yes
 λ_R value at $r_e: 0.462$
 Residual asymmetry: 0.769

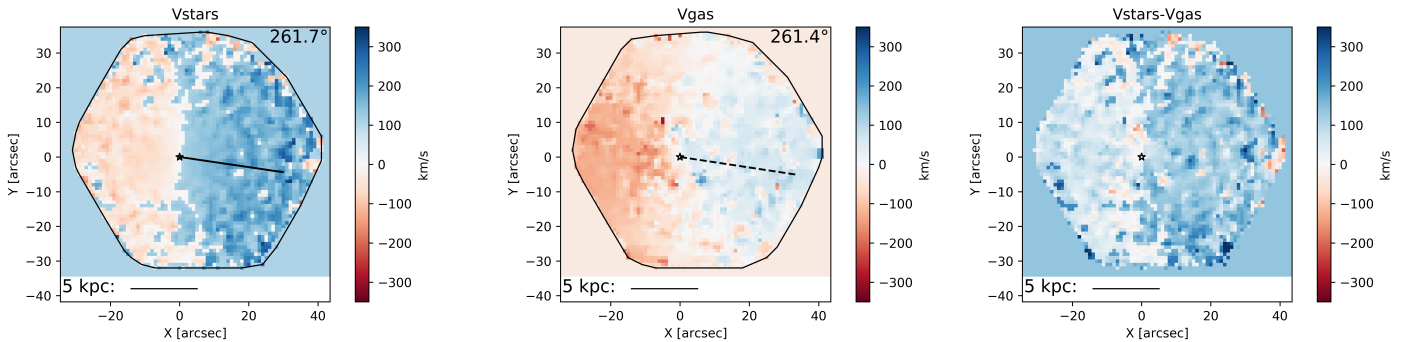
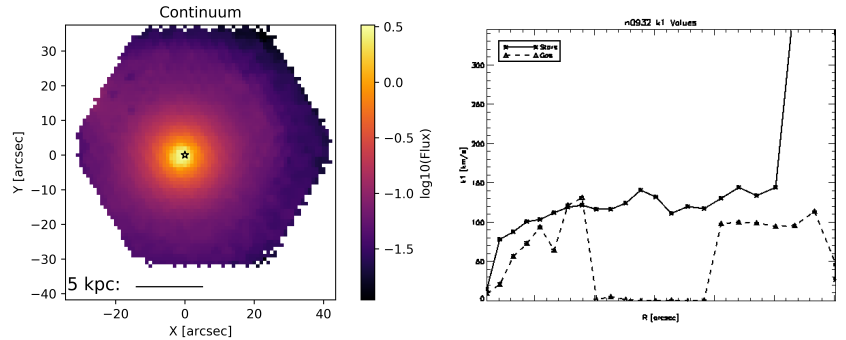


Figure 53 Top row, left to right: Name and characteristic parameters, continuum flux, and radial k_1 profiles for stars (solid) and gas (dashed), respectively. Bottom row, left to right: stellar kinematics, gas kinematics, and the difference between stellar and gas kinematics, respectively. The curves containing the data points are the convex hulls used to define the 'edge' of the map. The brightest continuum pixel (used as the center for kinemetry) is marked by a white star. The solid and dashed line in the stellar and gas velocity map, respectively, is the median position angle along which kinemetry coefficients were determined. The number value of this position angle is given at the top right of the plot. A scale bar is given along the bottom of each velocity map.

NGC 0938

$\log(\text{Stellar Mass}): 10.965$

$D = 54.6 \text{ Mpc}$

$M_r = -21.721 \text{ mag}$

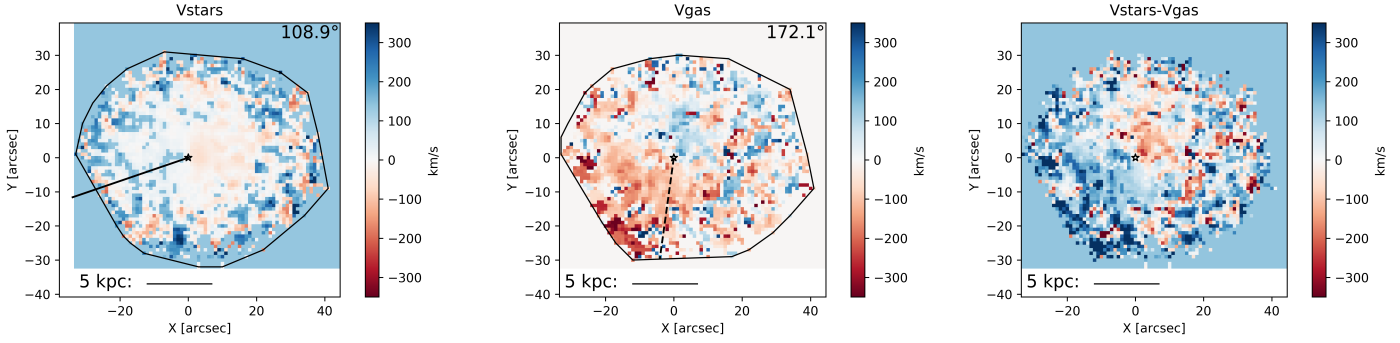
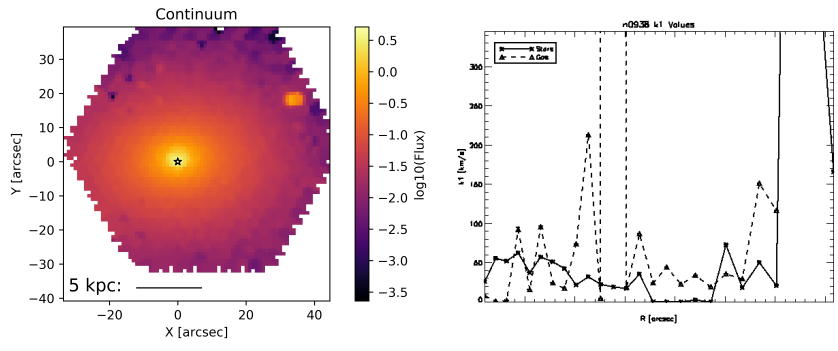
Redshift: 0.014

$r_e = 13.86 \text{ arcsec}$

AGN activity: No

λ_R value at r_e : 0.526

Residual asymmetry: 0.796



NGC 0962

$\log(\text{Stellar Mass}): 11.043$

$D = 61.4 \text{ Mpc}$

$M_r = -21.982 \text{ mag}$

Redshift: 0.016

$r_e = 13.86 \text{ arcsec}$

AGN activity: No

λ_R value at r_e : 0.472

Residual asymmetry: 0.782

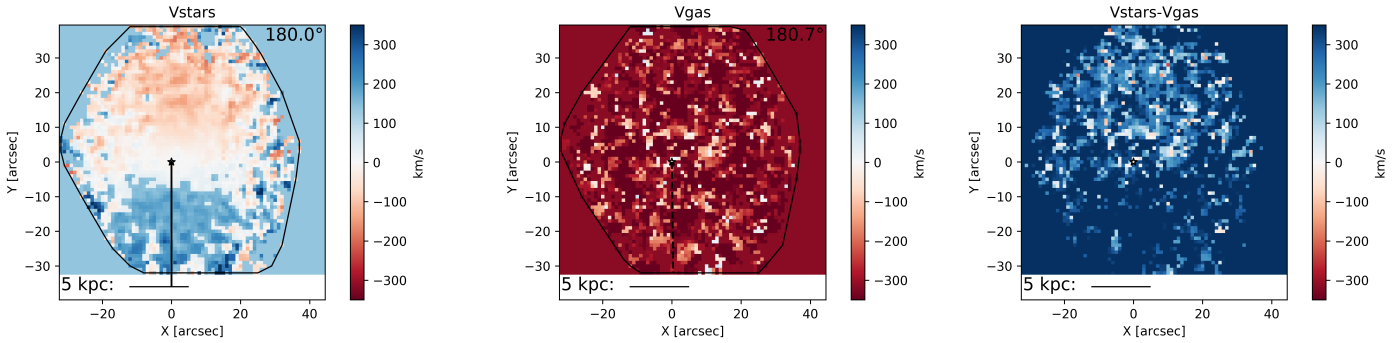
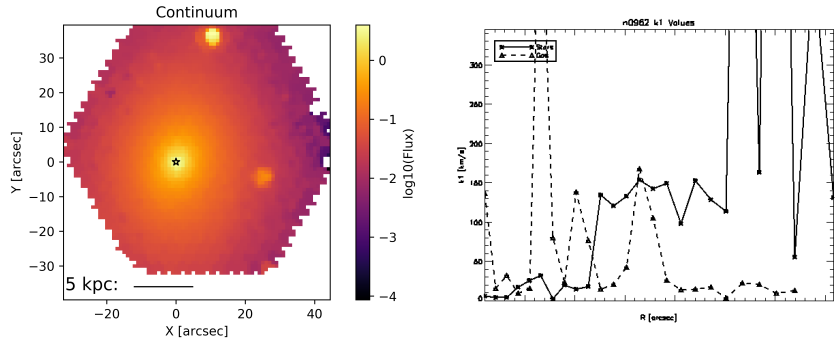


Figure 54 Top row, left to right: Name and characteristic parameters, continuum flux, and radial k_1 profiles for stars (solid) and gas (dashed), respectively. Bottom row, left to right: stellar kinematics, gas kinematics, and the difference between stellar and gas kinematics, respectively. The curves containing the data points are the convex hulls used to define the 'edge' of the map. The brightest continuum pixel (used as the center for kinemetry) is marked by a white star. The solid and dashed line in the stellar and gas velocity map, respectively, is the median position angle along which kinemetry coefficients were determined. The number value of this position angle is given at the top right of the plot. A scale bar is given along the bottom of each velocity map.

NGC 1056

$\log(\text{Stellar Mass}): 10.020$

$D = 21.4 \text{ Mpc}$

$M_r = -19.942 \text{ mag}$

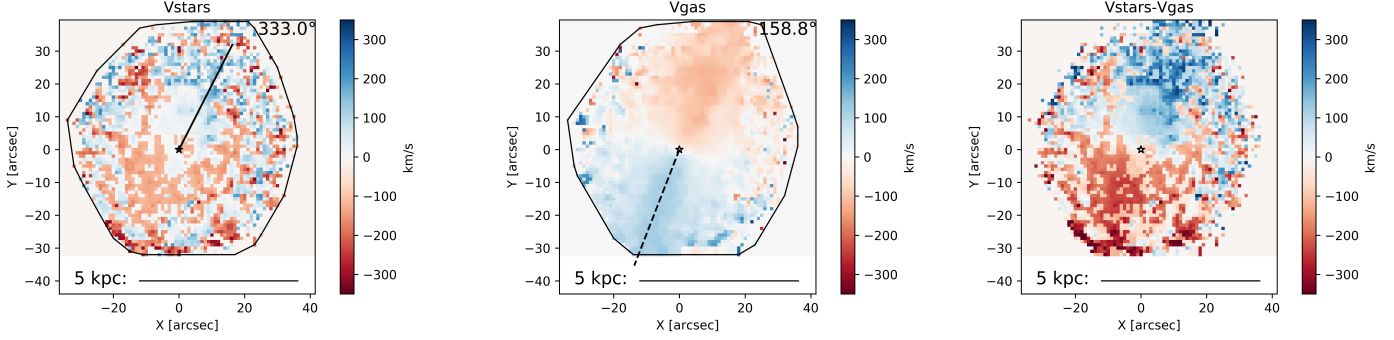
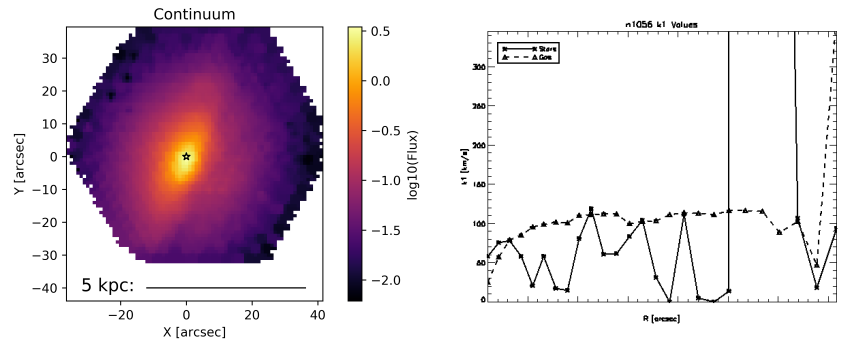
Redshift: 0.017

$r_e = 14.256 \text{ arcsec}$

AGN activity: No

λ_R value at r_e : 0.308

Residual asymmetry: 0.861



NGC 1060

$\log(\text{Stellar Mass}): 11.846$

$D = 69.3 \text{ Mpc}$

$M_r = -23.617 \text{ mag}$

Redshift: 0.017

$r_e = 27.324 \text{ arcsec}$

AGN activity: No

λ_R value at r_e : 0.415

Residual asymmetry: 0.778

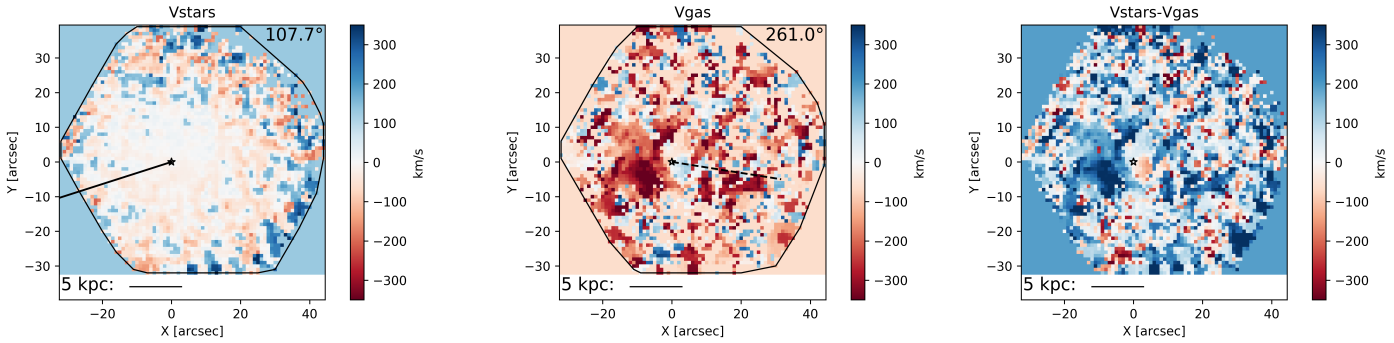
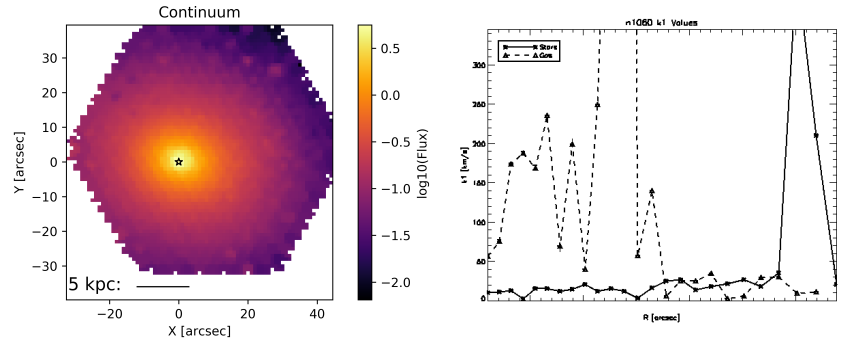
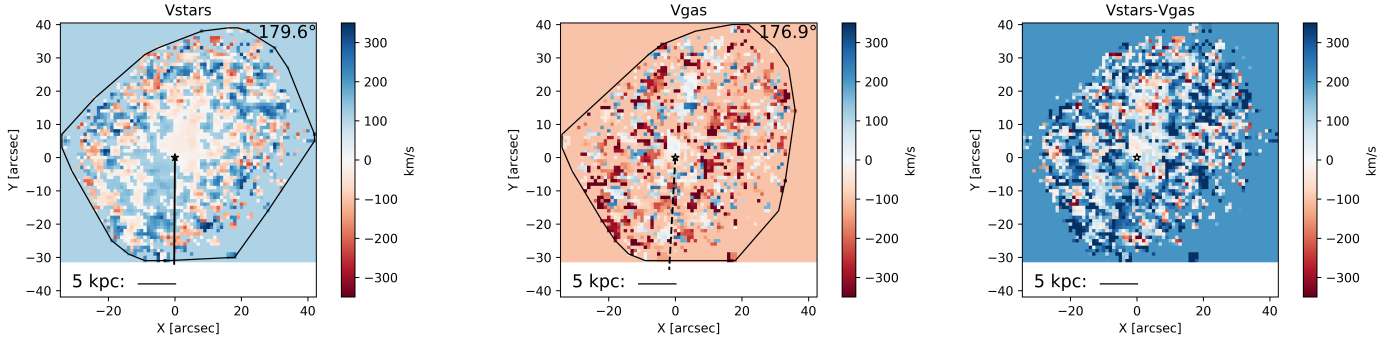
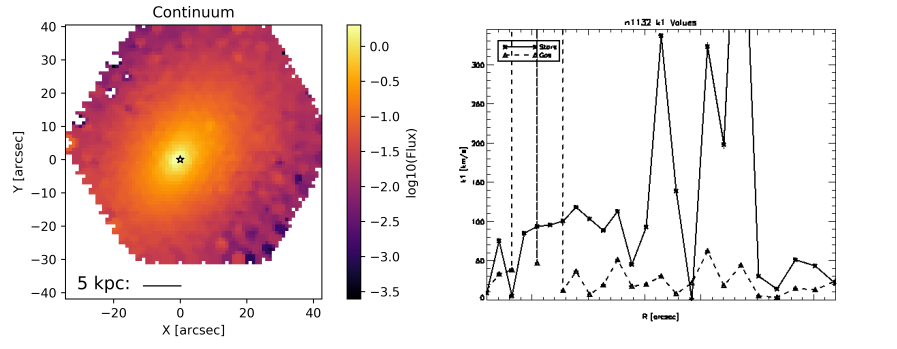


Figure 56 Top row, left to right: Name and characteristic parameters, continuum flux, and radial k_1 profiles for stars (solid) and gas (dashed), respectively. Bottom row, left to right: stellar kinematics, gas kinematics, and the difference between stellar and gas kinematics, respectively. The curves containing the data points are the convex hulls used to define the 'edge' of the map. The brightest continuum pixel (used as the center for kinemetry) is marked by a white star. The solid and dashed line in the stellar and gas velocity map, respectively, is the median position angle along which kinemetry coefficients were determined. The number value of this position angle is given at the top right of the plot. A scale bar is given along the bottom of each velocity map.

NGC 1132

$\log(\text{Stellar Mass}): 11.713$
 $D = 92.2 \text{ Mpc}$
 $M_r = -23.151 \text{ mag}$
 Redshift: 0.023
 $r_e: 32.868 \text{ arcsec}$
 AGN activity: No
 λ_R value at $r_e: 0.369$
 Residual asymmetry: 0.883



NGC 1167

$\log(\text{Stellar Mass}): 11.692$
 $D = 70.4 \text{ (DR3) Mpc}$
 $M_r = -22.980 \text{ mag}$
 Redshift: 0.016
 $r_e: 24.948 \text{ arcsec}$
 AGN activity: No
 λ_R value at $r_e: 0.339$
 Residual asymmetry: 0.782

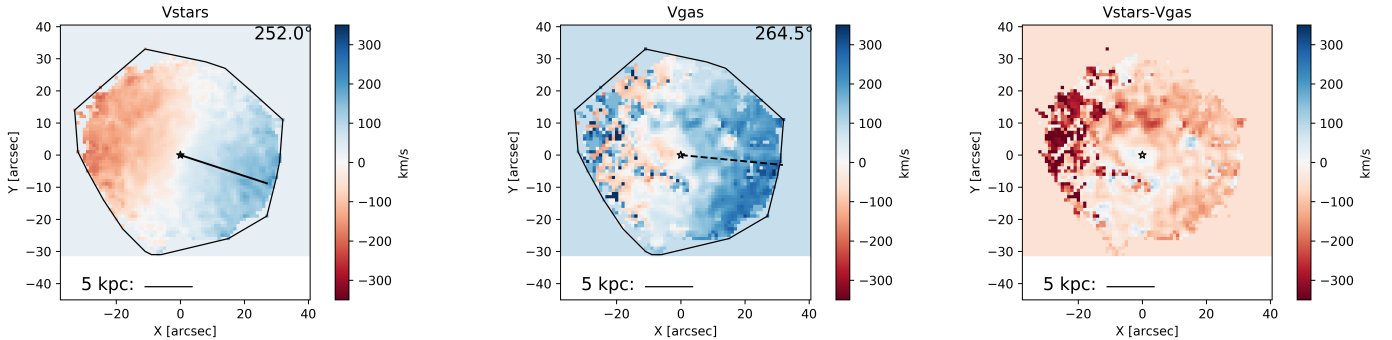
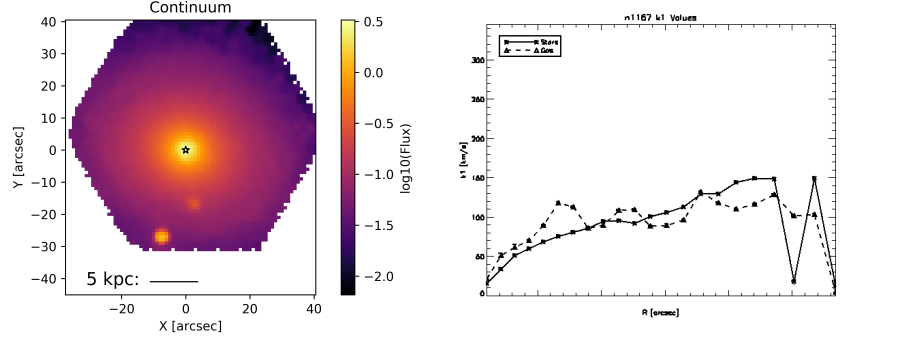


Figure 57 Top row, left to right: Name and characteristic parameters, continuum flux, and radial k_1 profiles for stars (solid) and gas (dashed), respectively. Bottom row, left to right: stellar kinematics, gas kinematics, and the difference between stellar and gas kinematics, respectively. The curves containing the data points are the convex hulls used to define the 'edge' of the map. The brightest continuum pixel (used as the center for kinemetry) is marked by a white star. The solid and dashed line in the stellar and gas velocity map, respectively, is the median position angle along which kinemetry coefficients were determined. The number value of this position angle is given at the top right of the plot. A scale bar is given along the bottom of each velocity map.

NGC 1270

$\log(\text{Stellar Mass}): 11.151$

$D = 66.9 \text{ Mpc}$

$M_r = -21.705 \text{ mag}$

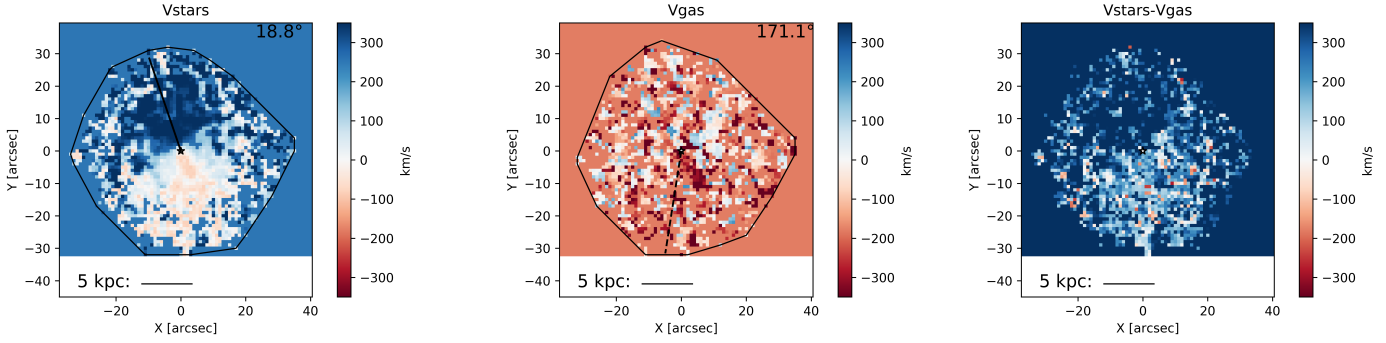
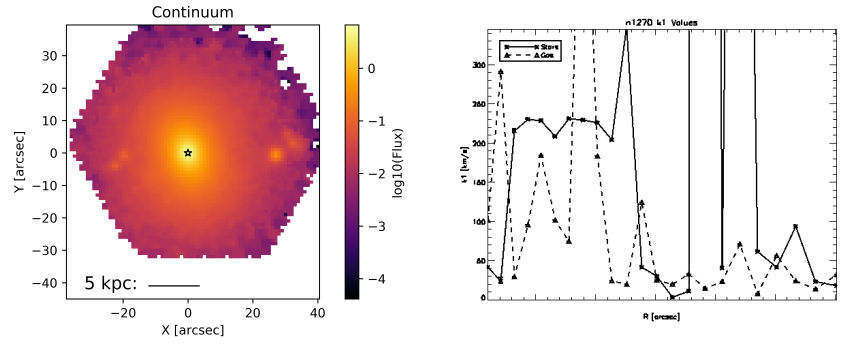
Redshift: 0.000

$r_e = 5.048 \text{ arcsec}$

AGN activity: No

λ_R value at r_e : 0.466

Residual asymmetry: 0.758



NGC 1349

$\log(\text{Stellar Mass}): 10.928$

$D = 94.2 \text{ (DR3) Mpc}$

$M_r = -22.442 \text{ mag}$

Redshift: 0.022

$r_e = 17.028 \text{ arcsec}$

AGN activity: Yes

λ_R value at r_e : 0.251

Residual asymmetry: 0.818

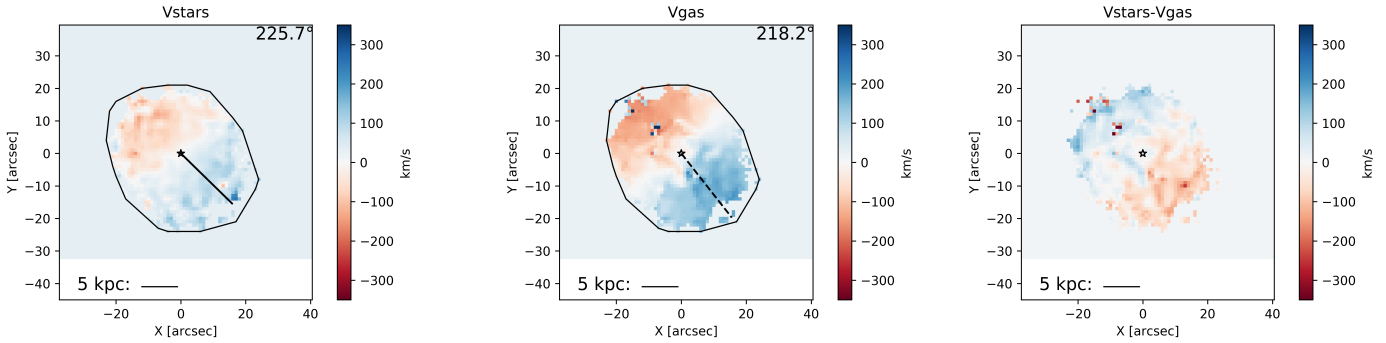
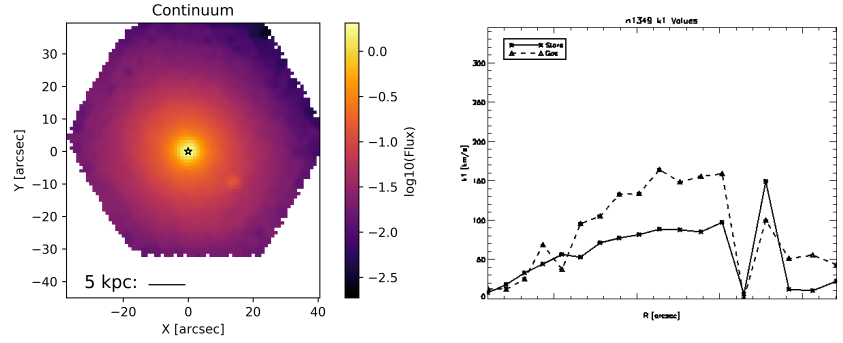
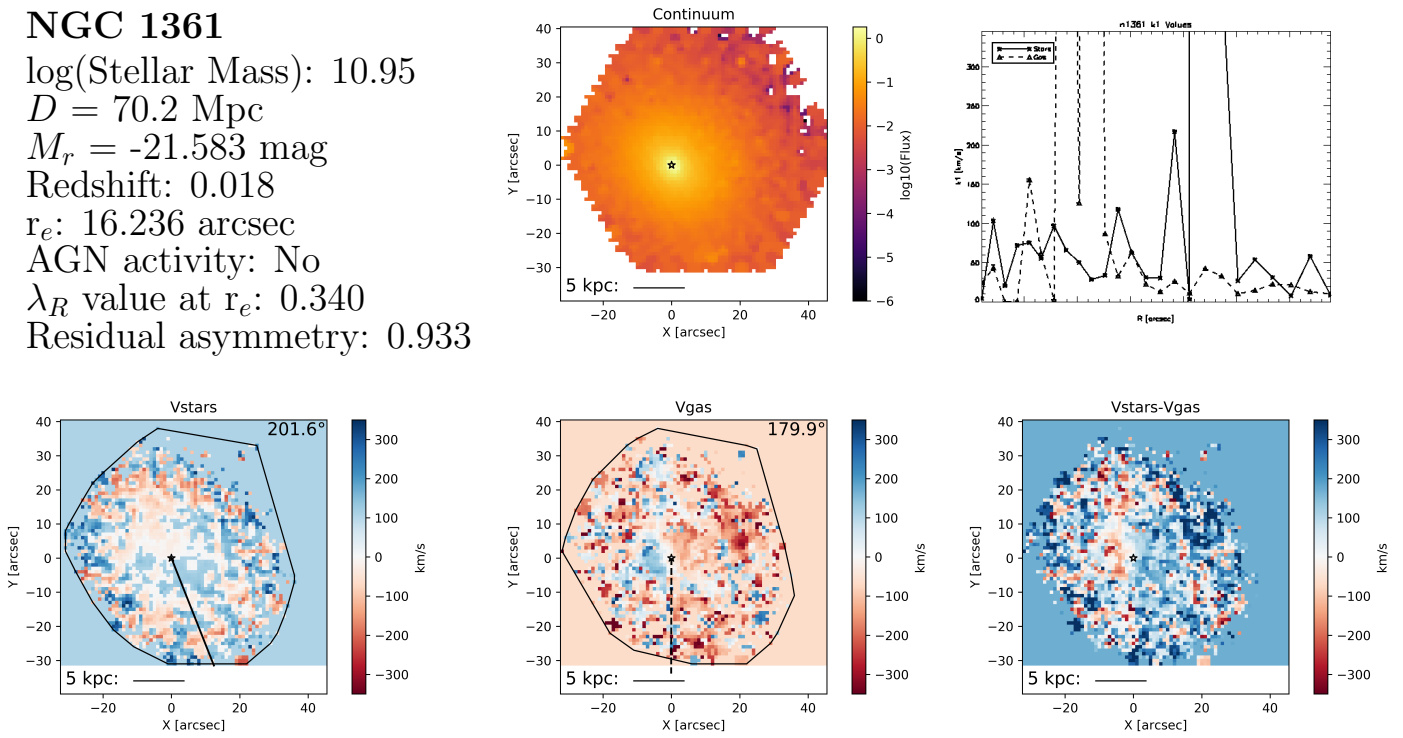


Figure 58 Top row, left to right: Name and characteristic parameters, continuum flux, and radial k_1 profiles for stars (solid) and gas (dashed), respectively. Bottom row, left to right: stellar kinematics, gas kinematics, and the difference between stellar and gas kinematics, respectively. The curves containing the data points are the convex hulls used to define the 'edge' of the map. The brightest continuum pixel (used as the center for kinemetry) is marked by a white star. The solid and dashed line in the stellar and gas velocity map, respectively, is the median position angle along which kinemetry coefficients were determined. The number value of this position angle is given at the top right of the plot. A scale bar is given along the bottom of each velocity map.

NGC 1361

$\log(\text{Stellar Mass}): 10.95$
 $D = 70.2 \text{ Mpc}$
 $M_r = -21.583 \text{ mag}$
 Redshift: 0.018
 $r_e: 16.236 \text{ arcsec}$
 AGN activity: No
 λ_R value at $r_e: 0.340$
 Residual asymmetry: 0.933



NGC 1656

$\log(\text{Stellar Mass}): 10.623$
 $D = 50.7 \text{ Mpc}$
 $M_r = -21.453 \text{ mag}$
 Redshift: 0.013
 $r_e: 17.424 \text{ arcsec}$
 AGN activity: No
 λ_R value at $r_e: 0.679$
 Residual asymmetry: 0.826

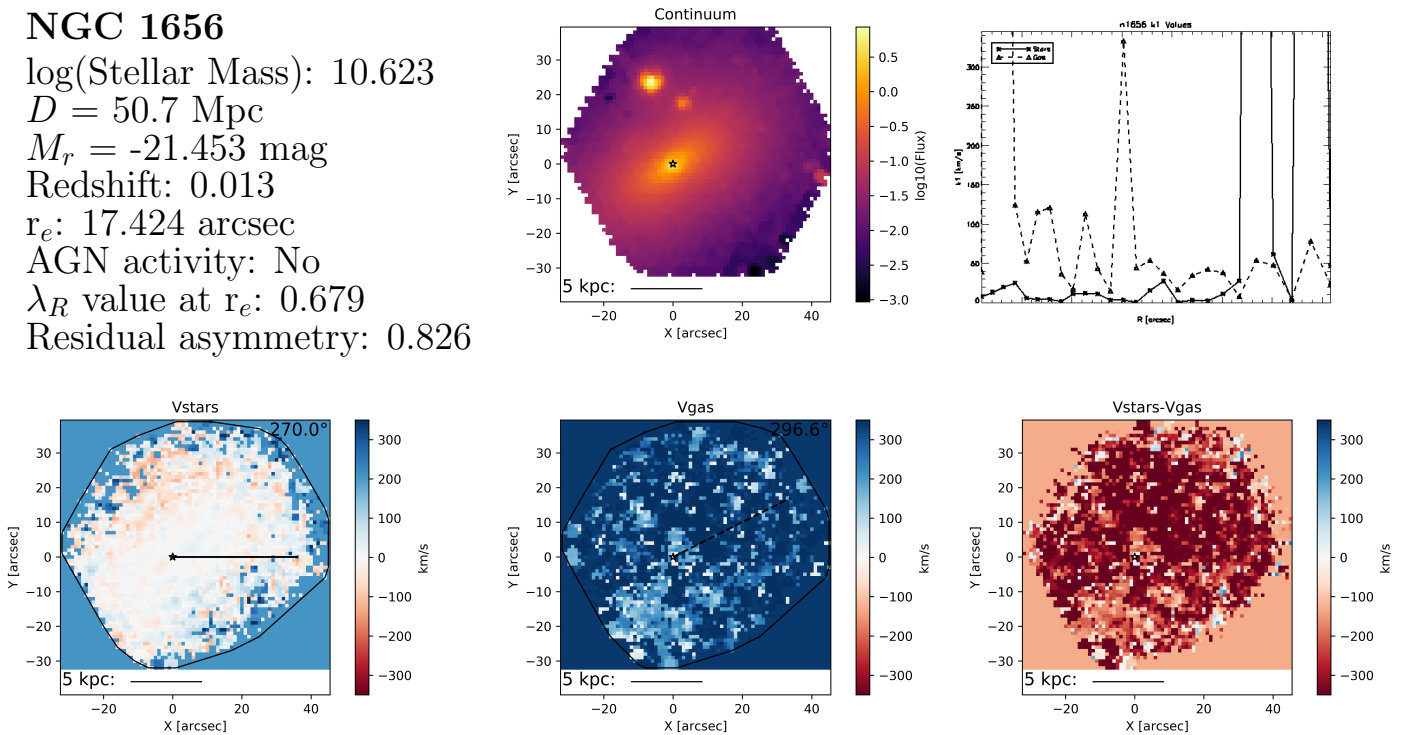
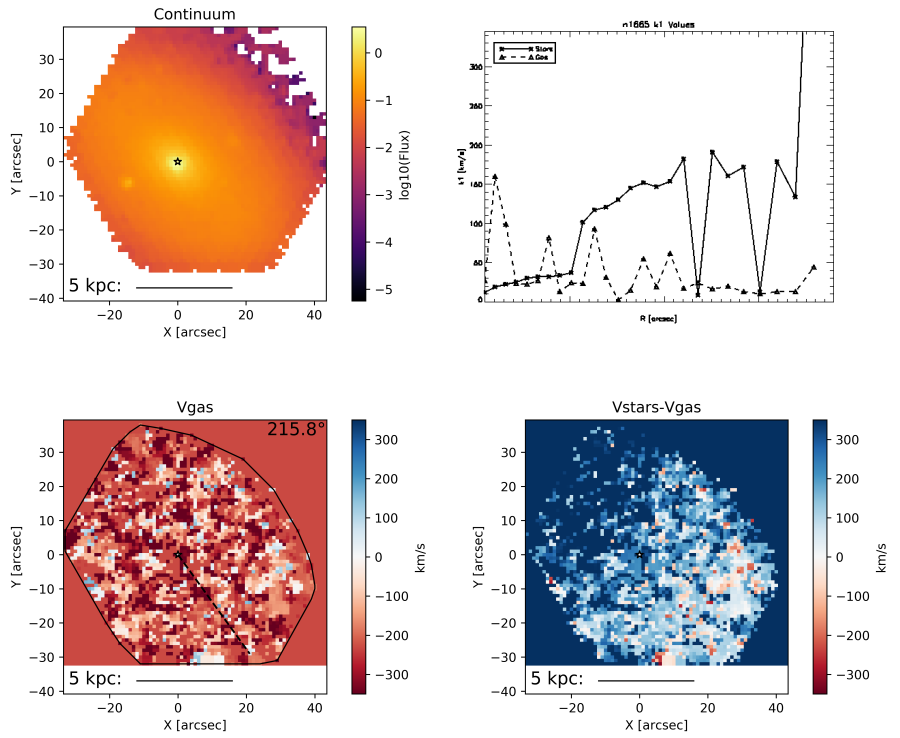


Figure 59 Top row, left to right: Name and characteristic parameters, continuum flux, and radial k_1 profiles for stars (solid) and gas (dashed), respectively. Bottom row, left to right: stellar kinematics, gas kinematics, and the difference between stellar and gas kinematics, respectively. The curves containing the data points are the convex hulls used to define the 'edge' of the map. The brightest continuum pixel (used as the center for kinemetry) is marked by a white star. The solid and dashed line in the stellar and gas velocity map, respectively, is the median position angle along which kinemetry coefficients were determined. The number value of this position angle is given at the top right of the plot. A scale bar is given along the bottom of each velocity map.

NGC 1665

$\log(\text{Stellar Mass}): 10.577$
 $D = 37.0 \text{ Mpc}$
 $M_r = -20.927 \text{ mag}$
 Redshift: 0.009
 $r_e = 23.76 \text{ arcsec}$
 AGN activity: No
 λ_R value at r_e : 0.631
 Residual asymmetry: 0.787



NGC 1666

$\log(\text{Stellar Mass}): 10.471$
 $D = 37.1 \text{ Mpc}$
 $M_r = -20.869 \text{ mag}$
 Redshift: 0.009
 $r_e = 12.276 \text{ arcsec}$
 AGN activity: No
 λ_R value at r_e : 0.621
 Residual asymmetry: 0.993

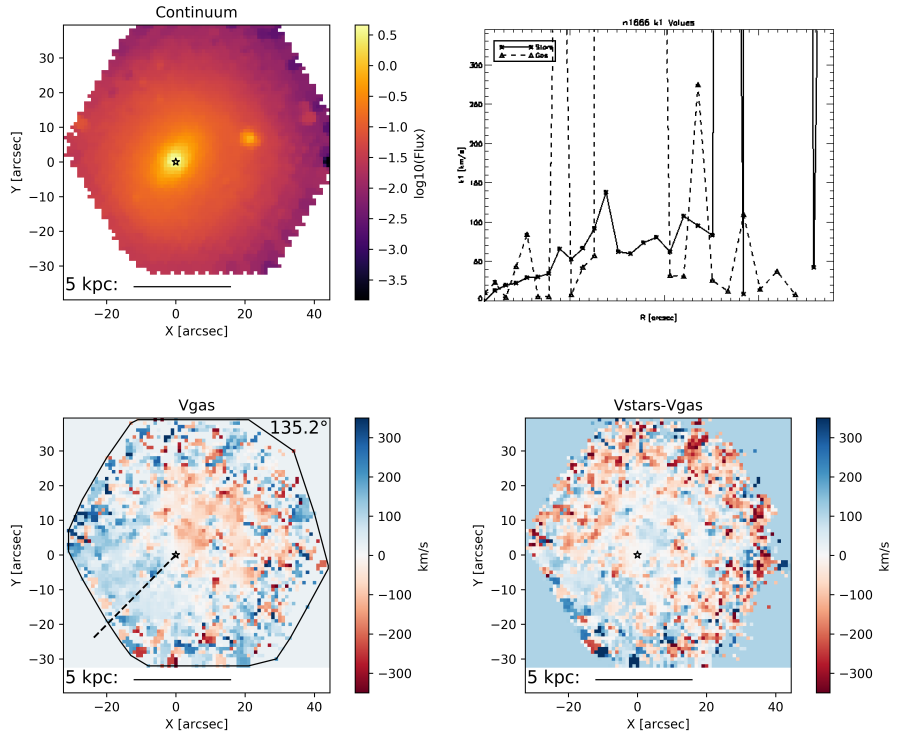
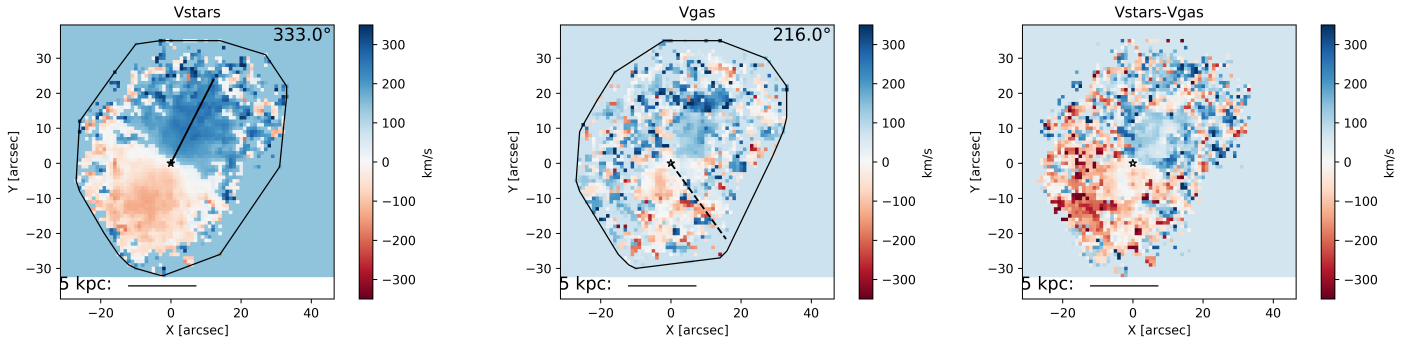
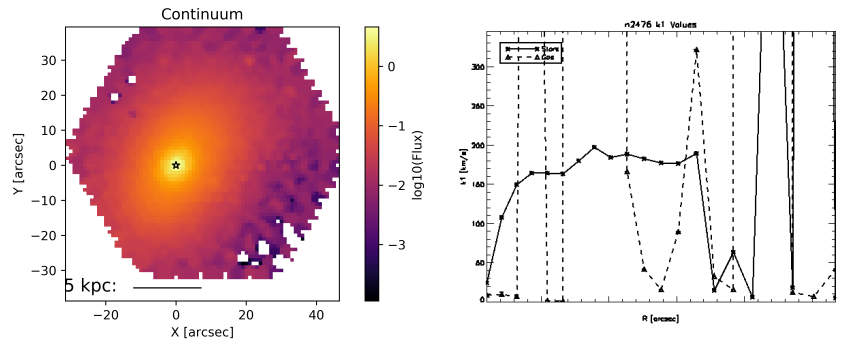


Figure 60 Top row, left to right: Name and characteristic parameters, continuum flux, and radial $k1$ profiles for stars (solid) and gas (dashed), respectively. Bottom row, left to right: stellar kinematics, gas kinematics, and the difference between stellar and gas kinematics, respectively. The curves containing the data points are the convex hulls used to define the 'edge' of the map. The brightest continuum pixel (used as the center for kinemetry) is marked by a white star. The solid and dashed line in the stellar and gas velocity map, respectively, is the median position angle along which kinemetry coefficients were determined. The number value of this position angle is given at the top right of the plot. A scale bar is given along the bottom of each velocity map.

NGC 2476

$\log(\text{Stellar Mass}): 10.801$
 $D = 54.0 \text{ Mpc}$
 $M_r = -21.581 \text{ mag}$
 Redshift: 0.012
 $r_e = 9.504 \text{ arcsec}$
 AGN activity: No
 λ_R value at r_e : 0.564
 Residual asymmetry: 1.000



NGC 2507

$\log(\text{Stellar Mass}): 11.277$
 $D = 65.3 \text{ Mpc}$
 $M_r = -22.556 \text{ mag}$
 Redshift: 0.015
 $r_e = 19.8 \text{ arcsec}$
 AGN activity: No
 λ_R value at r_e : 0.472
 Residual asymmetry: 0.922

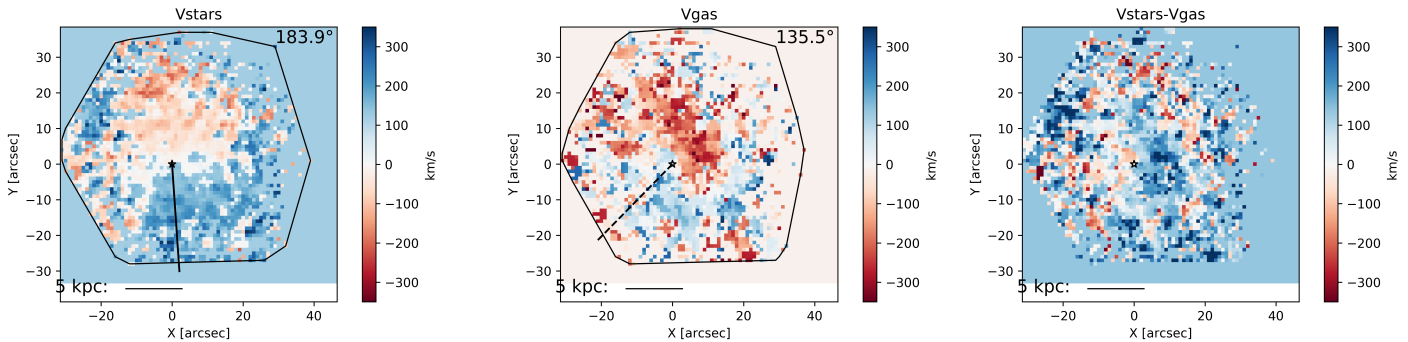
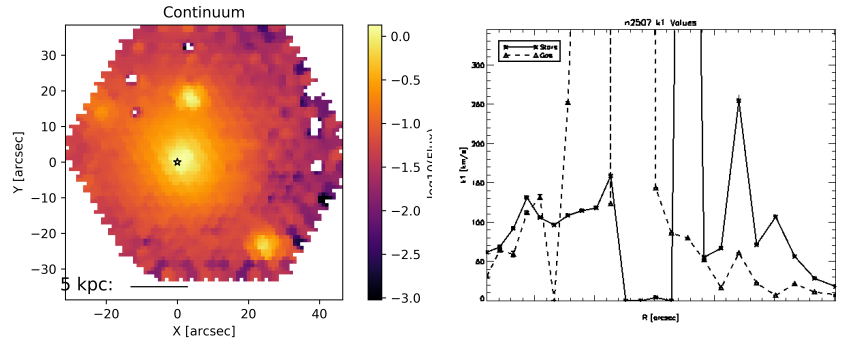
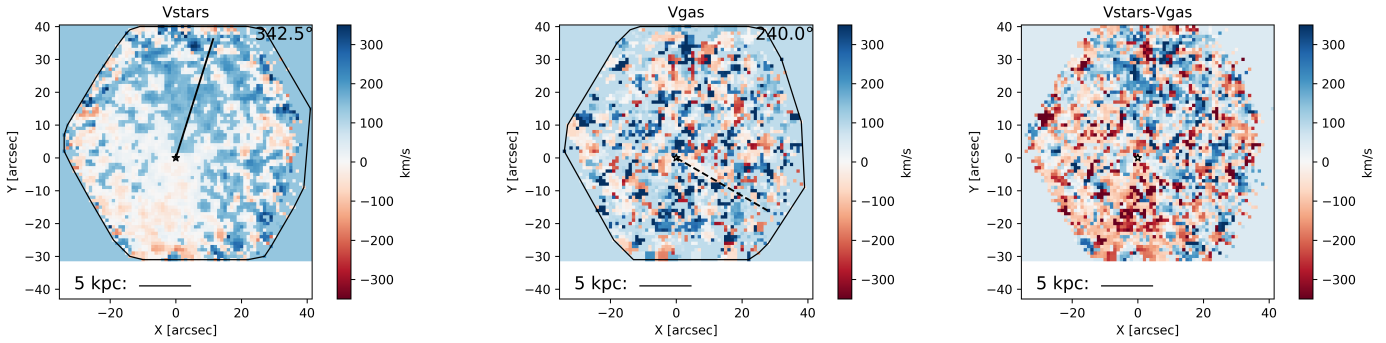
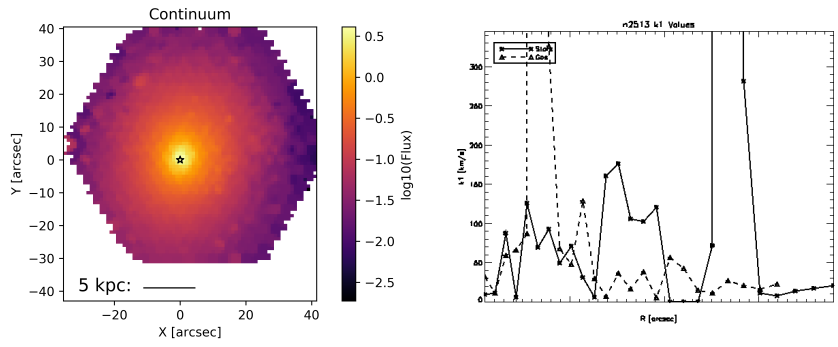


Figure 61 Top row, left to right: Name and characteristic parameters, continuum flux, and radial k_1 profiles for stars (solid) and gas (dashed), respectively. Bottom row, left to right: stellar kinematics, gas kinematics, and the difference between stellar and gas kinematics, respectively. The curves containing the data points are the convex hulls used to define the 'edge' of the map. The brightest continuum pixel (used as the center for kinemetry) is marked by a white star. The solid and dashed line in the stellar and gas velocity map, respectively, is the median position angle along which kinemetry coefficients were determined. The number value of this position angle is given at the top right of the plot. A scale bar is given along the bottom of each velocity map.

NGC 2513

$\log(\text{Stellar Mass}): 11.539$
 $D = 67.1 \text{ Mpc}$
 $M_r = -22.860 \text{ mag}$
 Redshift: 0.016
 $r_e = 26.532 \text{ arcsec}$
 AGN activity: No
 λ_R value at r_e : 0.298
 Residual asymmetry: 0.762



NGC 2577

$\log(\text{Stellar Mass}): 10.606$
 $D = 31.7 \text{ Mpc}$
 $M_r = -20.854 \text{ mag}$
 Redshift: 0.007
 $r_e = 17.424 \text{ arcsec}$
 AGN activity: No
 λ_R value at r_e : 0.573
 Residual asymmetry: 0.835

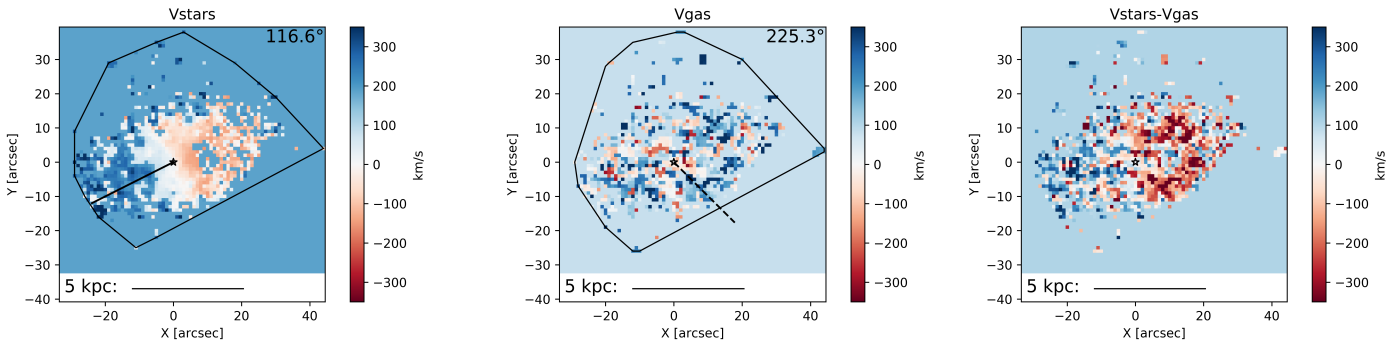
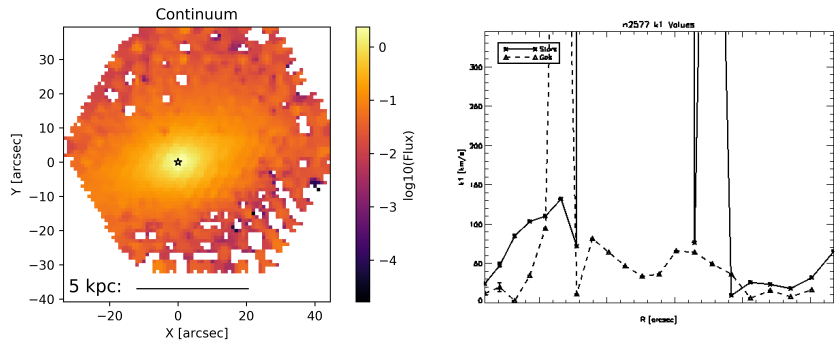
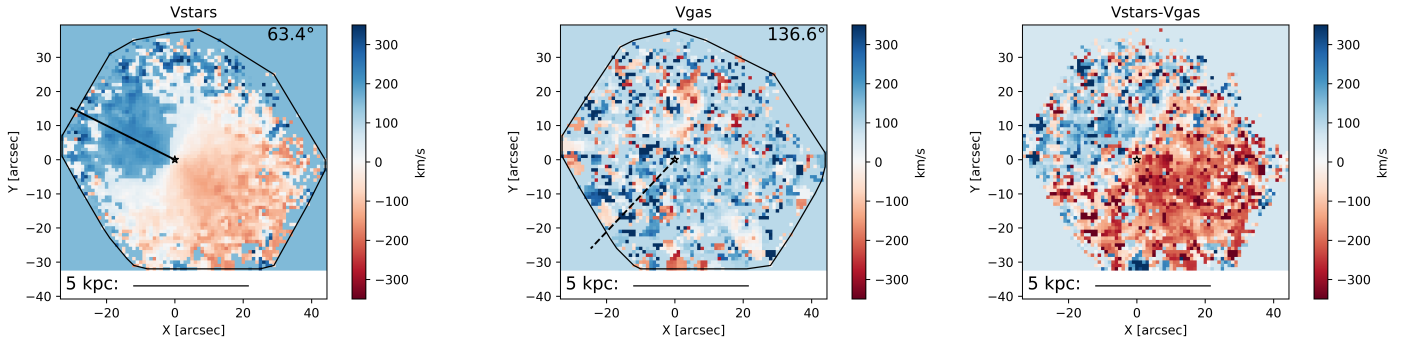
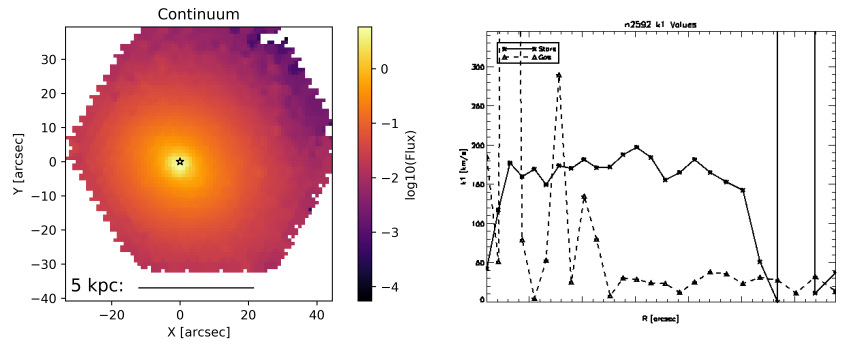


Figure 62 Top row, left to right: Name and characteristic parameters, continuum flux, and radial k_1 profiles for stars (solid) and gas (dashed), respectively. Bottom row, left to right: stellar kinematics, gas kinematics, and the difference between stellar and gas kinematics, respectively. The curves containing the data points are the convex hulls used to define the 'edge' of the map. The brightest continuum pixel (used as the center for kinemetry) is marked by a white star. The solid and dashed line in the stellar and gas velocity map, respectively, is the median position angle along which kinemetry coefficients were determined. The number value of this position angle is given at the top right of the plot. A scale bar is given along the bottom of each velocity map.

NGC 2592

$\log(\text{Stellar Mass}): 10.618$
 $D = 30.8 \text{ Mpc}$
 $M_r = -20.719 \text{ mag}$
 Redshift: 0.007
 $r_e: 9.9 \text{ arcsec}$
 AGN activity: No
 λ_R value at $r_e: 0.563$
 Residual asymmetry: 0.824



NGC 2767

$\log(\text{Stellar Mass}): 10.75$
 $D = 71.2 \text{ Mpc}$
 $M_r = -20.874 \text{ mag}$
 Redshift: 0.016
 $r_e: 5.716 \text{ arcsec}$
 AGN activity: No
 λ_R value at $r_e: 0.568$
 Residual asymmetry: 0.907

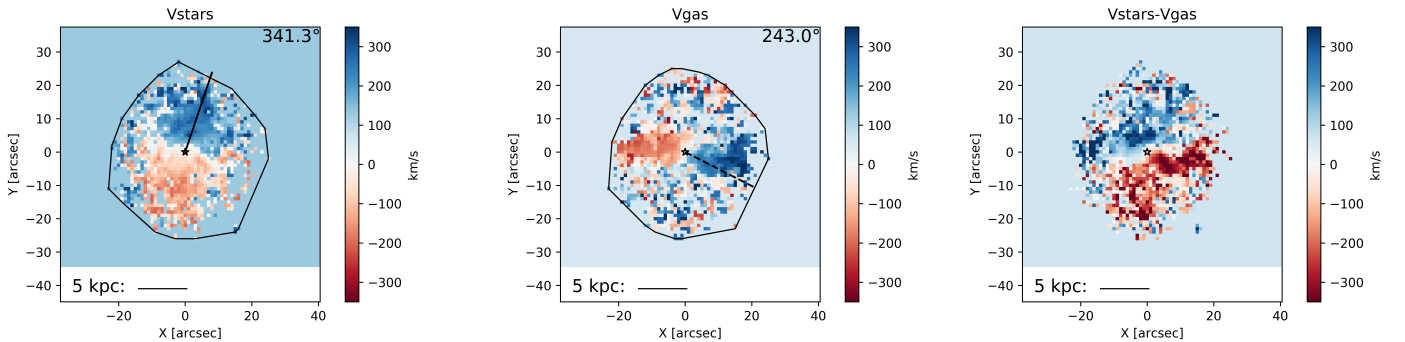
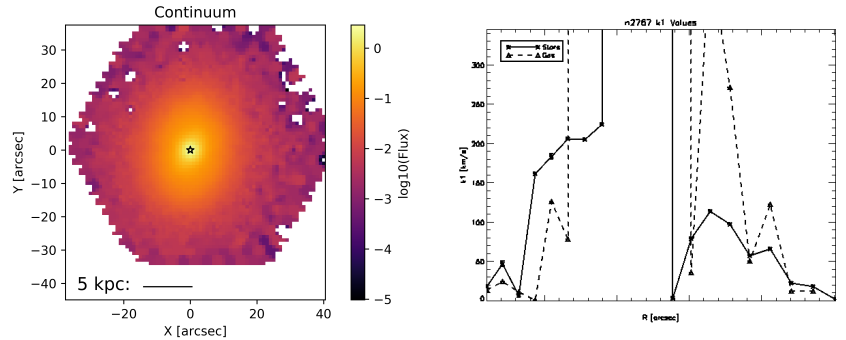
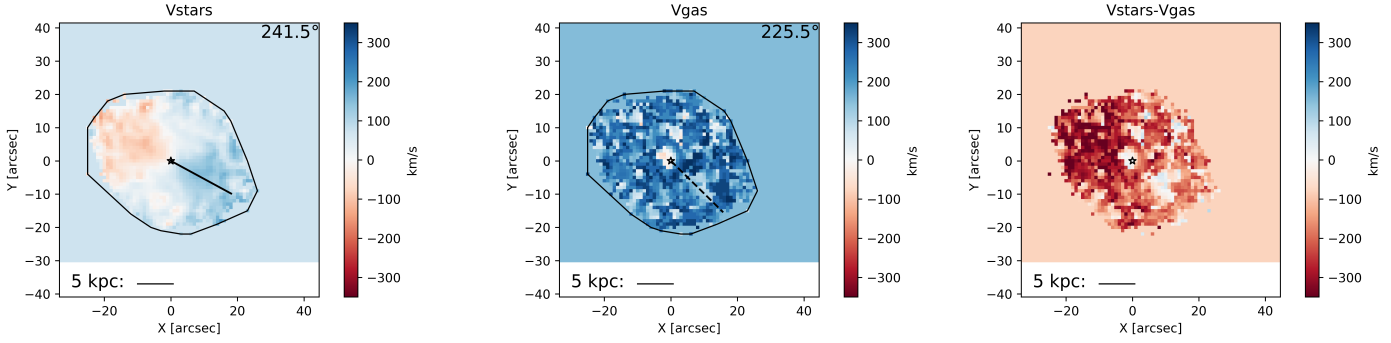
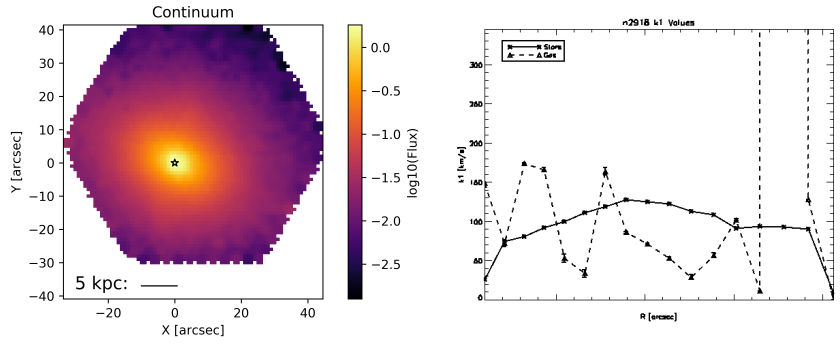


Figure 63 Top row, left to right: Name and characteristic parameters, continuum flux, and radial k_1 profiles for stars (solid) and gas (dashed), respectively. Bottom row, left to right: stellar kinematics, gas kinematics, and the difference between stellar and gas kinematics, respectively. The curves containing the data points are the convex hulls used to define the 'edge' of the map. The brightest continuum pixel (used as the center for kinemetry) is marked by a white star. The solid and dashed line in the stellar and gas velocity map, respectively, is the median position angle along which kinemetry coefficients were determined. The number value of this position angle is given at the top right of the plot. A scale bar is given along the bottom of each velocity map.

NGC 2918

$\log(\text{Stellar Mass}): 11.443$
 $D = 96.6$ (DR3) Mpc
 $M_r = -22.776$ mag
 Redshift: 0.023
 $r_e = 12.276$ arcsec
 AGN activity: No
 λ_R value at r_e : 0.269
 Residual asymmetry: 0.919



NGC 3106

$\log(\text{Stellar Mass}): 11.212$
 $D = 88.7$ (DR3) Mpc
 $M_r = -22.794$ mag
 Redshift: 0.021
 $r_e = 21.384$ arcsec
 AGN activity: Yes
 λ_R value at r_e : 0.200
 Residual asymmetry: 0.834

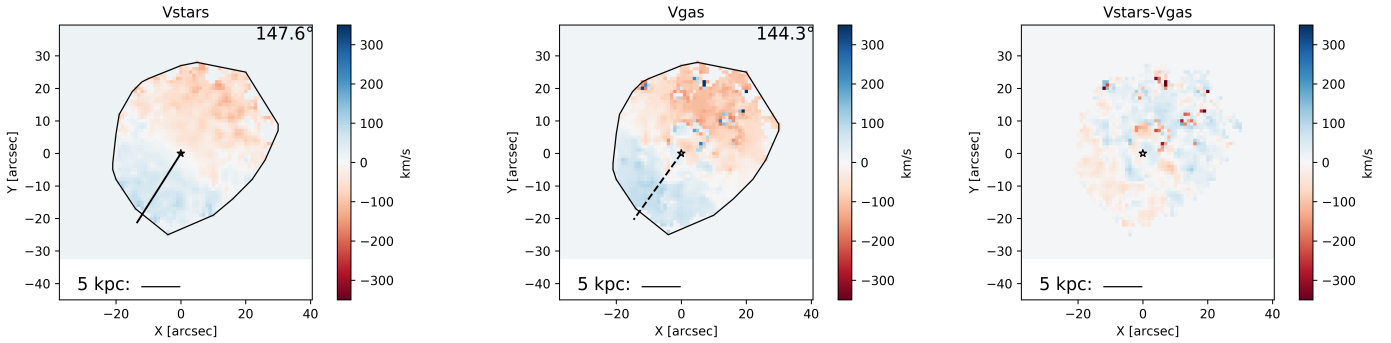
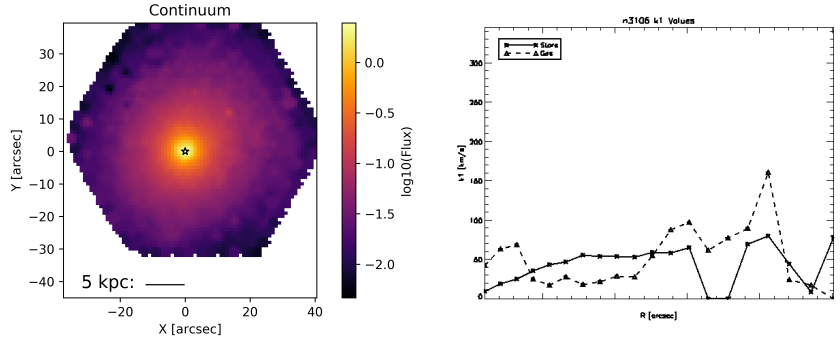
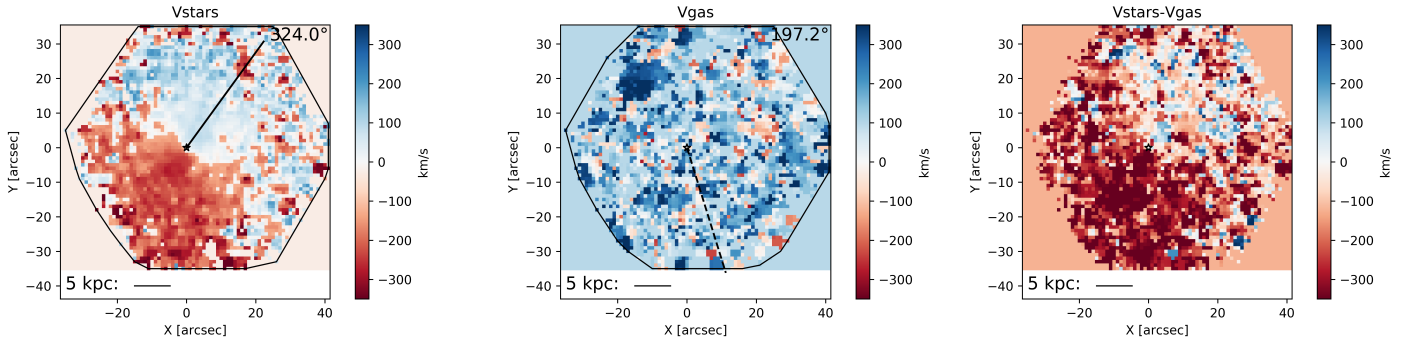
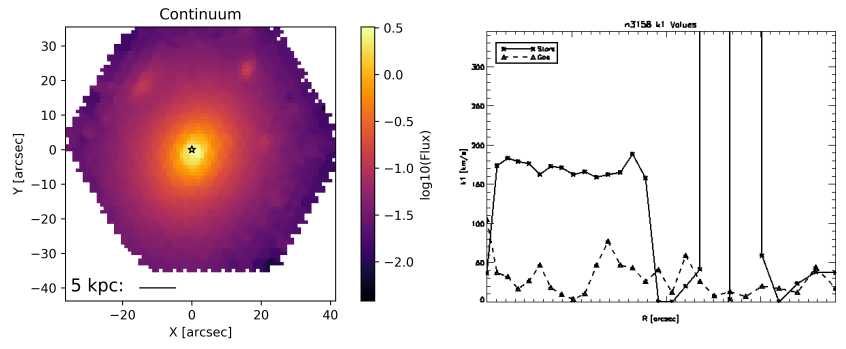


Figure 64 Top row, left to right: Name and characteristic parameters, continuum flux, and radial k_1 profiles for stars (solid) and gas (dashed), respectively. Bottom row, left to right: stellar kinematics, gas kinematics, and the difference between stellar and gas kinematics, respectively. The curves containing the data points are the convex hulls used to define the 'edge' of the map. The brightest continuum pixel (used as the center for kinemetry) is marked by a white star. The solid and dashed line in the stellar and gas velocity map, respectively, is the median position angle along which kinemetry coefficients were determined. The number value of this position angle is given at the top right of the plot. A scale bar is given along the bottom of each velocity map.

NGC 3158

$\log(\text{Stellar Mass}): 11.738$
 $D = 100.6 \text{ Mpc}$
 $M_r = -23.704 \text{ mag}$
 Redshift: 0.023
 $r_e: 32.472 \text{ arcsec}$
 AGN activity: No
 λ_R value at $r_e: 0.388$
 Residual asymmetry: 0.800



NGC 3182

$\log(\text{Stellar Mass}): 10.399$
 $D = 34.5 \text{ Mpc}$
 $M_r = -20.833 \text{ mag}$
 Redshift: 0.007
 $r_e: 17.424 \text{ arcsec}$
 AGN activity: No
 λ_R value at $r_e: 0.454$
 Residual asymmetry: 0.988

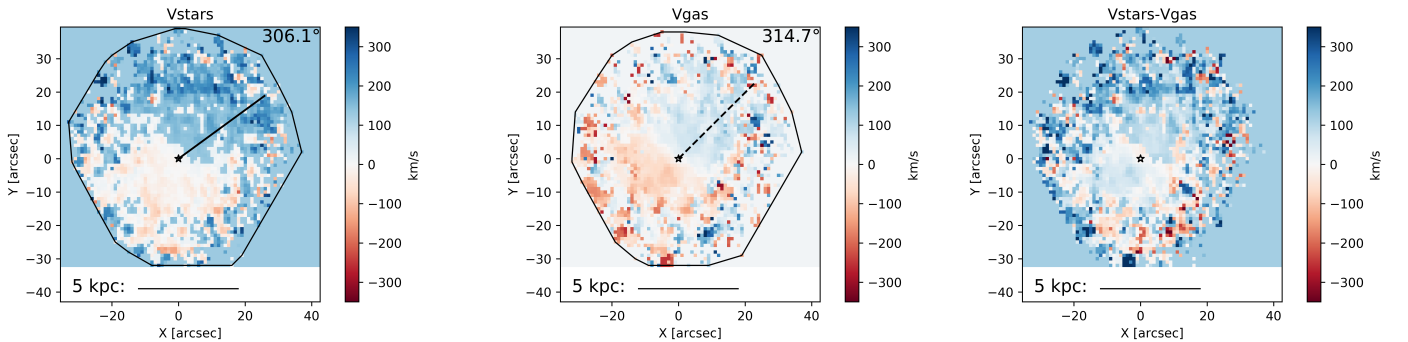
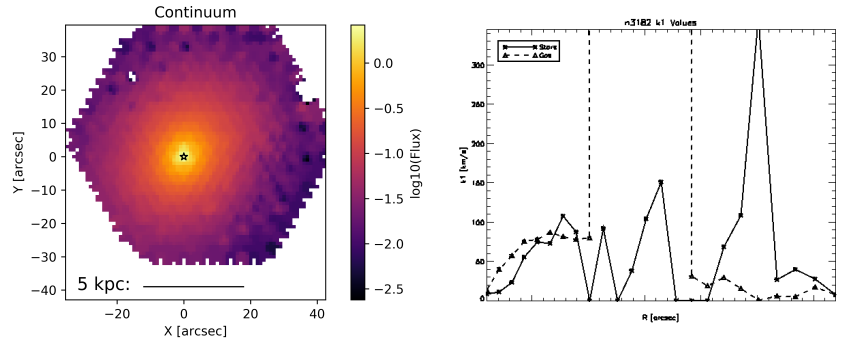
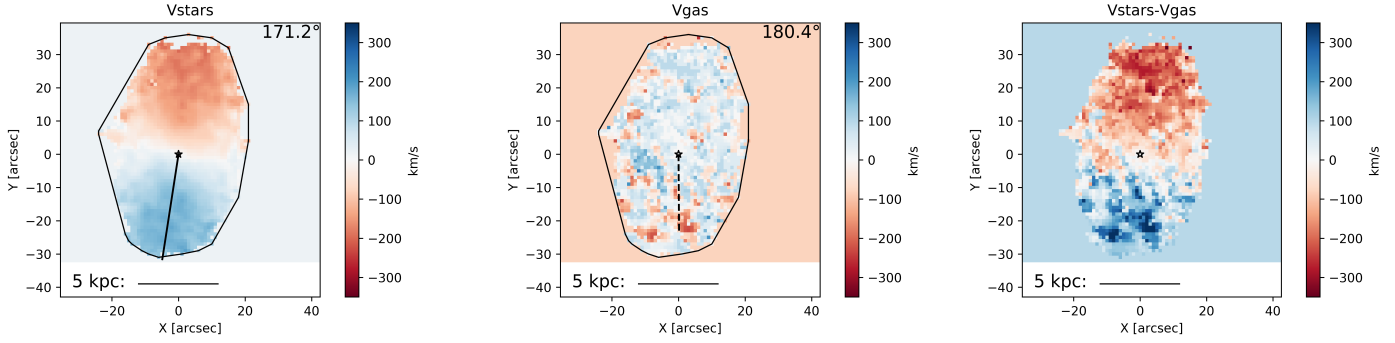
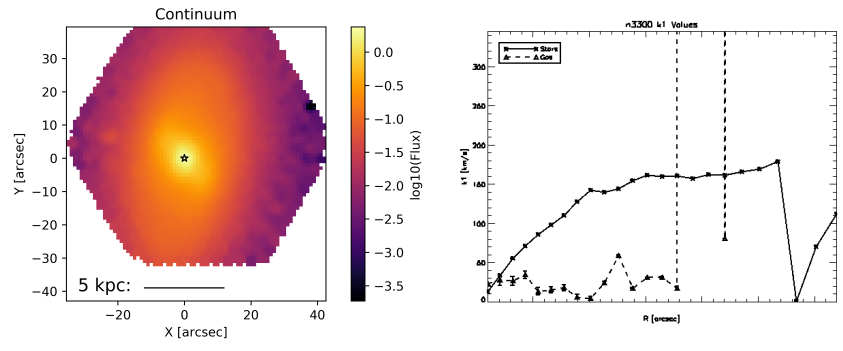


Figure 65 Top row, left to right: Name and characteristic parameters, continuum flux, and radial k_1 profiles for stars (solid) and gas (dashed), respectively. Bottom row, left to right: stellar kinematics, gas kinematics, and the difference between stellar and gas kinematics, respectively. The curves containing the data points are the convex hulls used to define the 'edge' of the map. The brightest continuum pixel (used as the center for kinemetry) is marked by a white star. The solid and dashed line in the stellar and gas velocity map, respectively, is the median position angle along which kinemetry coefficients were determined. The number value of this position angle is given at the top right of the plot. A scale bar is given along the bottom of each velocity map.

NGC 3300

$\log(\text{Stellar Mass}): 10.762$
 $D = 43.2$ (DR3) Mpc
 $M_r = -21.410$ mag
 Redshift: 0.010
 $r_e = 13.86$ arcsec
 AGN activity: No
 λ_R value at r_e : 0.391
 Residual asymmetry: 0.945



NGC 3610

$\log(\text{Stellar Mass}): 10.9$
 $D = 29.6$ Mpc
 $M_r = -21.918$ mag
 Redshift: 0.006
 $r_e = 13.86$ arcsec
 AGN activity: No
 λ_R value at r_e : 0.512
 Residual asymmetry: 0.793

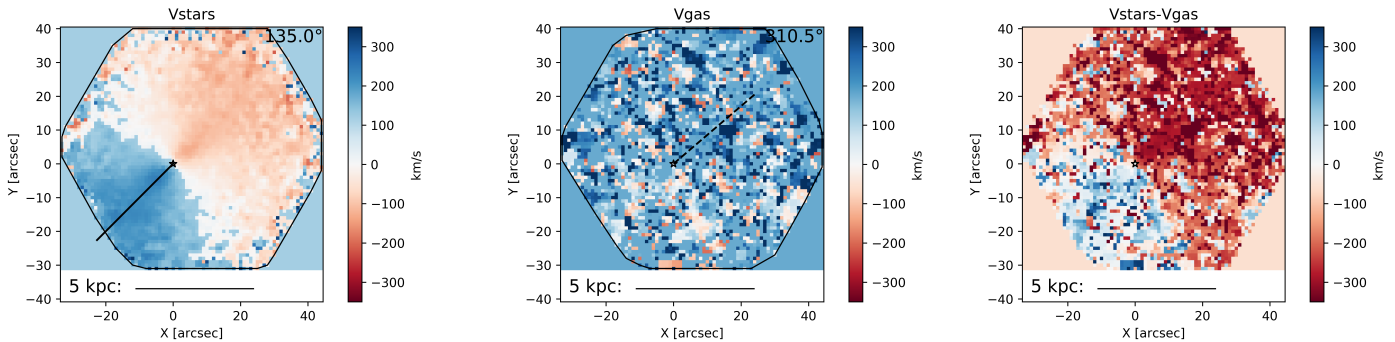
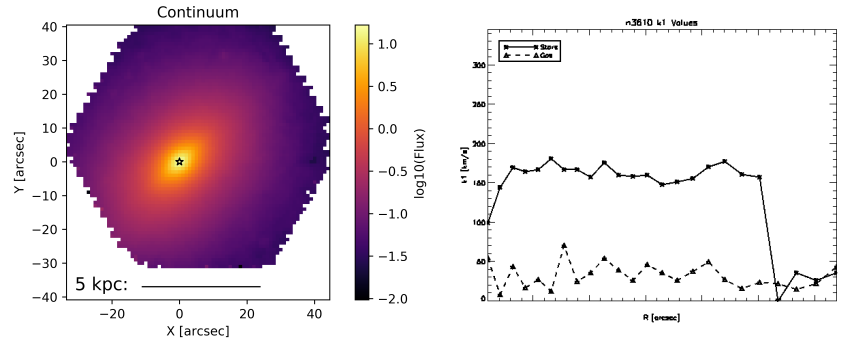
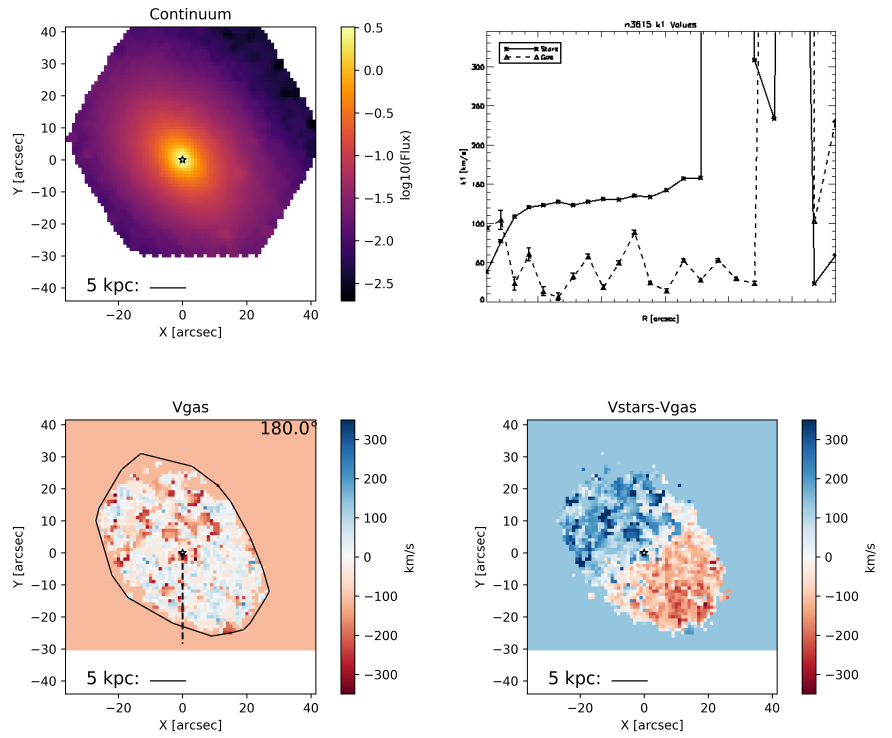


Figure 66 Top row, left to right: Name and characteristic parameters, continuum flux, and radial k_1 profiles for stars (solid) and gas (dashed), respectively. Bottom row, left to right: stellar kinematics, gas kinematics, and the difference between stellar and gas kinematics, respectively. The curves containing the data points are the convex hulls used to define the 'edge' of the map. The brightest continuum pixel (used as the center for kinemetry) is marked by a white star. The solid and dashed line in the stellar and gas velocity map, respectively, is the median position angle along which kinemetry coefficients were determined. The number value of this position angle is given at the top right of the plot. A scale bar is given along the bottom of each velocity map.

NGC 3615

$\log(\text{Stellar Mass}): 11.383$
 $D = 94.6$ (DR3) Mpc
 $M_r = -22.977$ mag
 Redshift: 0.022
 $r_e: 15.444$ arcsec
 AGN activity: No
 λ_R value at $r_e: 0.317$
 Residual asymmetry: 0.835



NGC 3619

$\log(\text{Stellar Mass}): 10.583$
 $D = 27.7$ Mpc
 $M_r = -21.165$ mag
 Redshift: 0.005
 $r_e: 28.116$ arcsec
 AGN activity: Yes
 λ_R value at $r_e: 0.403$
 Residual asymmetry: 0.982

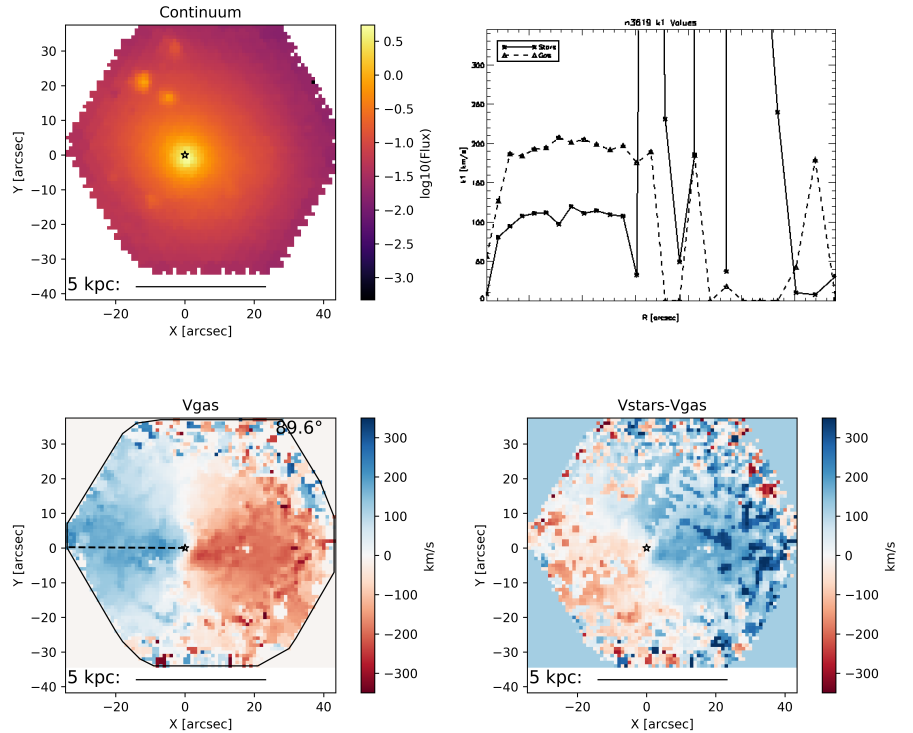


Figure 67 Top row, left to right: Name and characteristic parameters, continuum flux, and radial k_1 profiles for stars (solid) and gas (dashed), respectively. Bottom row, left to right: stellar kinematics, gas kinematics, and the difference between stellar and gas kinematics, respectively. The curves containing the data points are the convex hulls used to define the 'edge' of the map. The brightest continuum pixel (used as the center for kinemetry) is marked by a white star. The solid and dashed line in the stellar and gas velocity map, respectively, is the median position angle along which kinemetry coefficients were determined. The number value of this position angle is given at the top right of the plot. A scale bar is given along the bottom of each velocity map.

NGC 3990

$\log(\text{Stellar Mass}): 9.942$

$D = 14.37 \text{ Mpc}$

$M_r = -19.373 \text{ mag}$

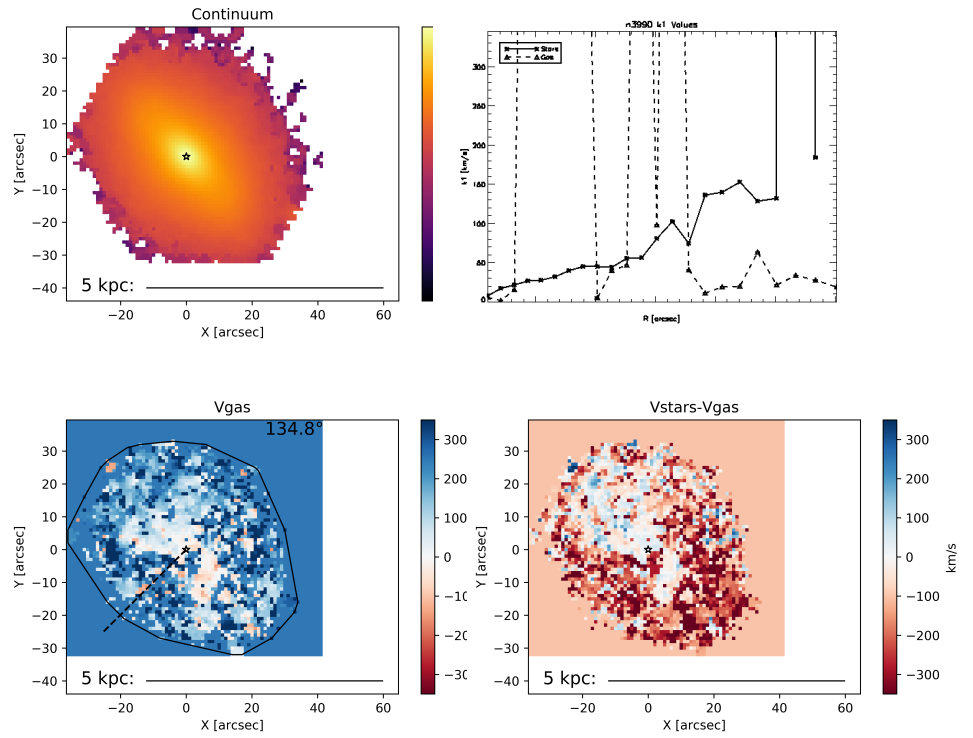
Redshift: 0.000

$r_e: 5.918 \text{ arcsec}$

AGN activity: No

λ_R value at r_e : 0.647

Residual asymmetry: 0.764



NGC 4003

$\log(\text{Stellar Mass}): 11.073$

$D = 93.8 \text{ (DR3) Mpc}$

$M_r = -22.000 \text{ mag}$

Redshift: 0.022

$r_e: 14.256 \text{ arcsec}$

AGN activity: No

λ_R value at r_e : 0.416

Residual asymmetry: 0.943

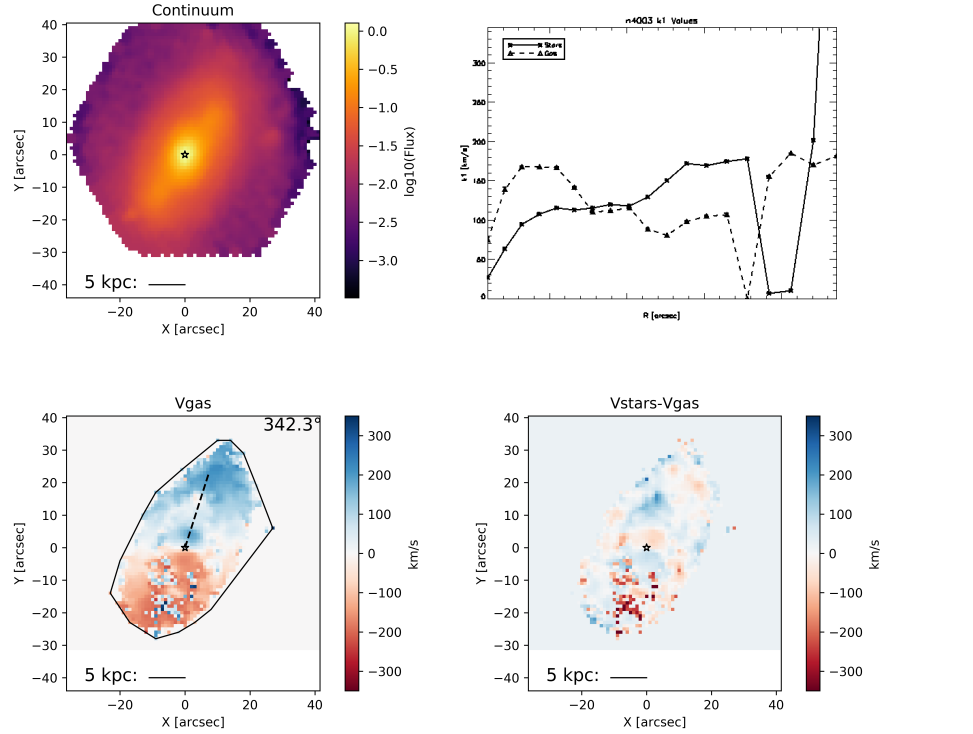
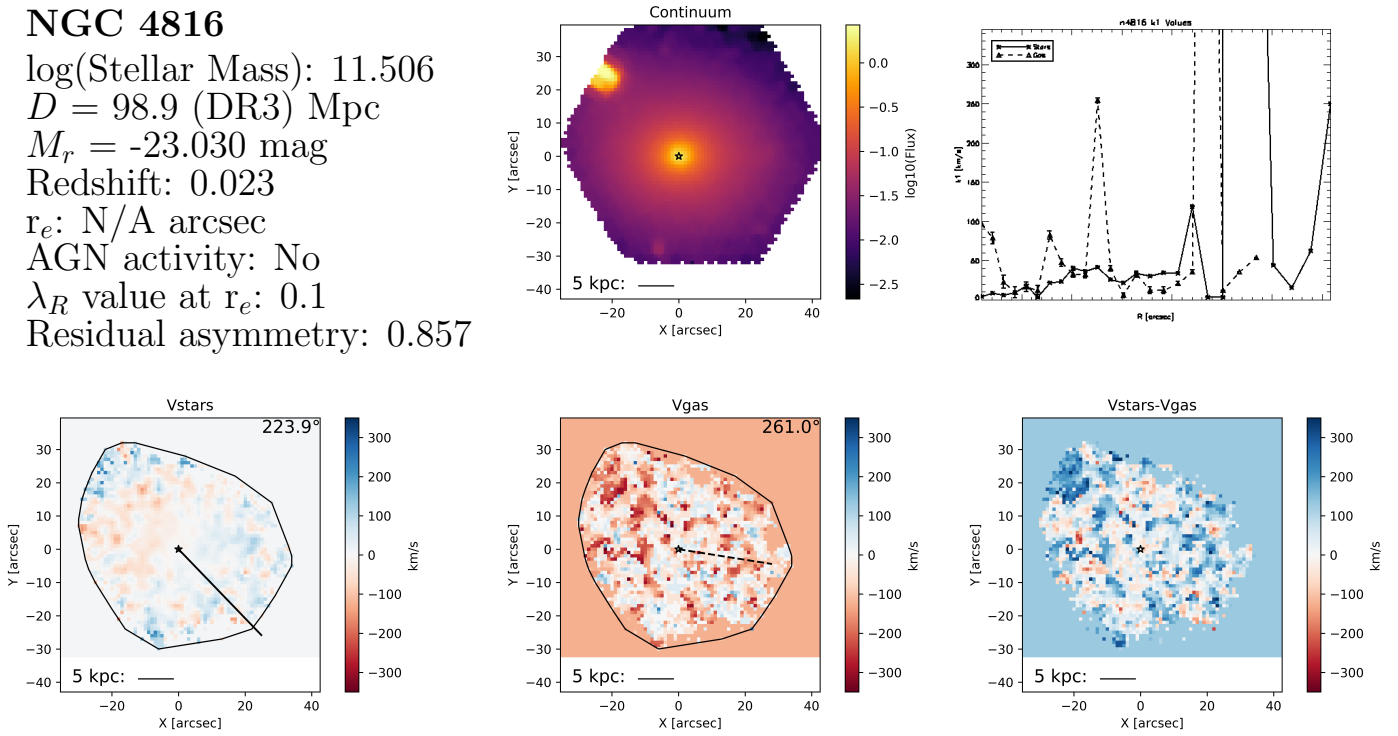


Figure 68 Top row, left to right: Name and characteristic parameters, continuum flux, and radial $k1$ profiles for stars (solid) and gas (dashed), respectively. Bottom row, left to right: stellar kinematics, gas kinematics, and the difference between stellar and gas kinematics, respectively. The curves containing the data points are the convex hulls used to define the 'edge' of the map. The brightest continuum pixel (used as the center for kinemetry) is marked by a white star. The solid and dashed line in the stellar and gas velocity map, respectively, is the median position angle along which kinemetry coefficients were determined. The number value of this position angle is given at the top right of the plot. A scale bar is given along the bottom of each velocity map.

NGC 4816

$\log(\text{Stellar Mass}): 11.506$
 $D = 98.9$ (DR3) Mpc
 $M_r = -23.030$ mag
 Redshift: 0.023
 r_e : N/A arcsec
 AGN activity: No
 λ_R value at r_e : 0.1
 Residual asymmetry: 0.857



NGC 4841a

$\log(\text{Stellar Mass}): 11.546$
 $D = 100.7$ Mpc
 $M_r = -22.825$ mag
 Redshift: 0.023
 r_e : 20.592 arcsec
 AGN activity: No
 λ_R value at r_e : 0.242
 Residual asymmetry: 0.779

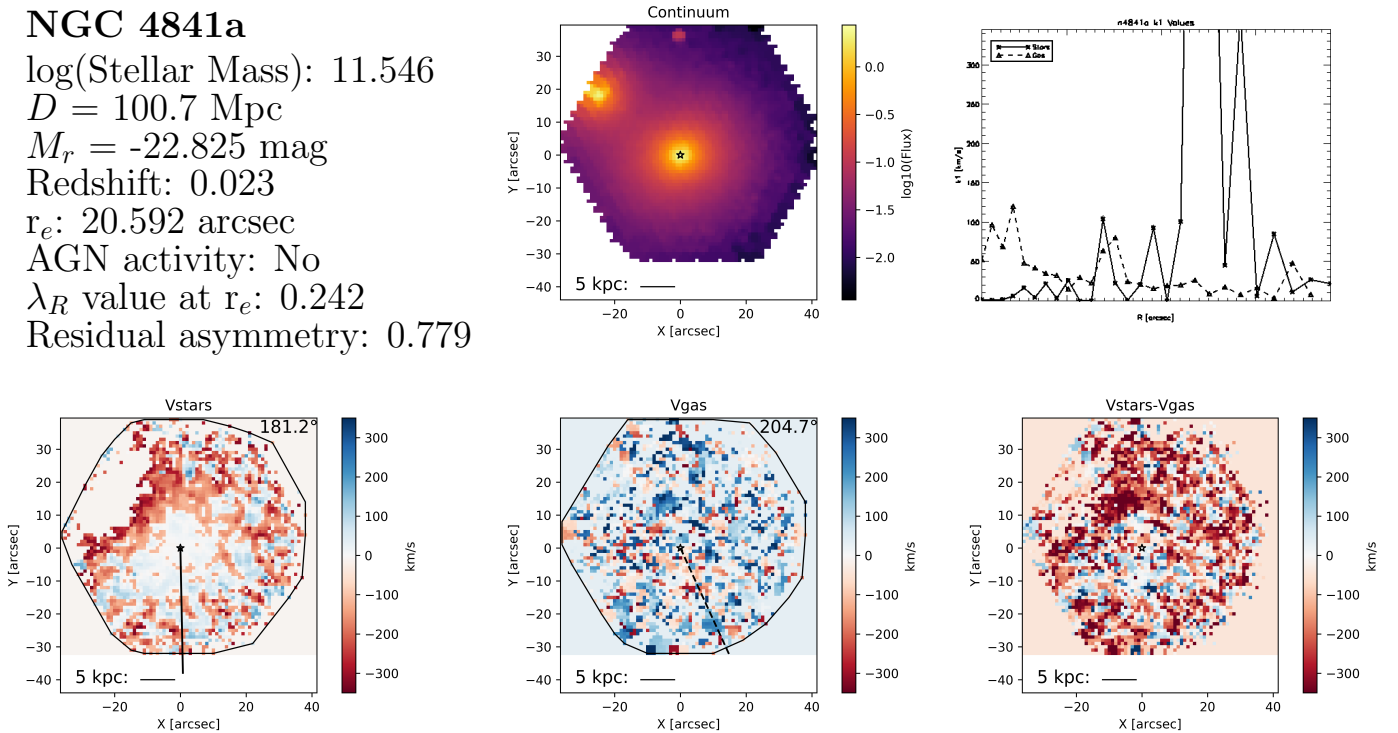


Figure 69 Top row, left to right: Name and characteristic parameters, continuum flux, and radial k_1 profiles for stars (solid) and gas (dashed), respectively. Bottom row, left to right: stellar kinematics, gas kinematics, and the difference between stellar and gas kinematics, respectively. The curves containing the data points are the convex hulls used to define the 'edge' of the map. The brightest continuum pixel (used as the center for kinemetry) is marked by a white star. The solid and dashed line in the stellar and gas velocity map, respectively, is the median position angle along which kinemetry coefficients were determined. The number value of this position angle is given at the top right of the plot. A scale bar is given along the bottom of each velocity map.

NGC 4874

$\log(\text{Stellar Mass}): 11.695$

$D = 106.2 \text{ Mpc}$

$M_r = -24.113 \text{ mag}$

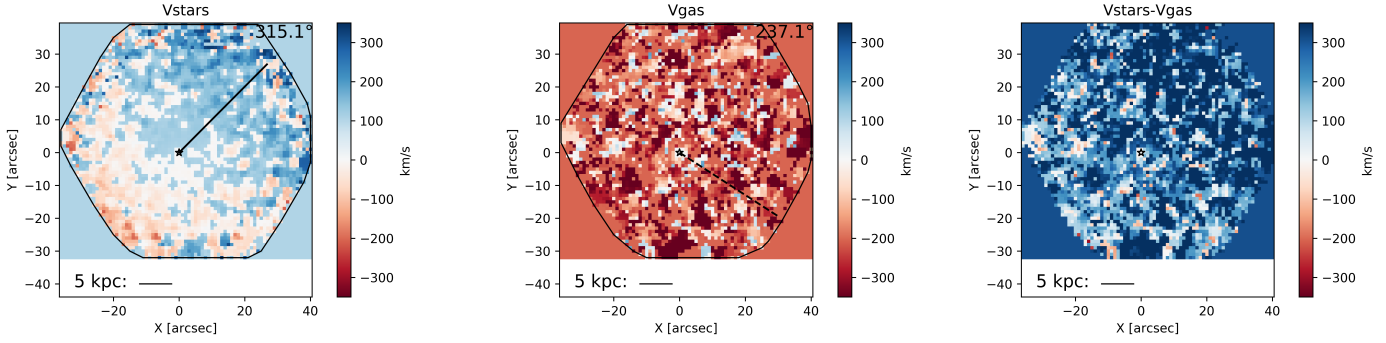
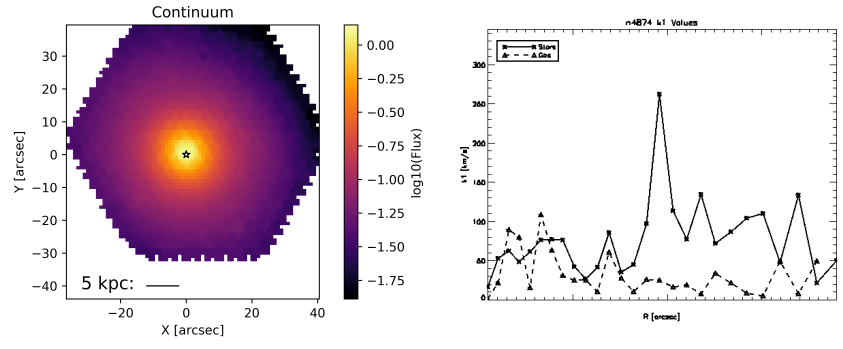
Redshift: 0.024

$r_e: 55.044 \text{ arcsec}$

AGN activity: No

λ_R value at r_e : N/A

Residual asymmetry: 0.800



NGC 4956

$\log(\text{Stellar Mass}): 10.986$

$D = 72.8 \text{ Mpc}$

$M_r = -22.381 \text{ mag}$

Redshift: 0.016

$r_e: 9.504 \text{ arcsec}$

AGN activity: No

λ_R value at r_e : 0.491

Residual asymmetry: 0.971

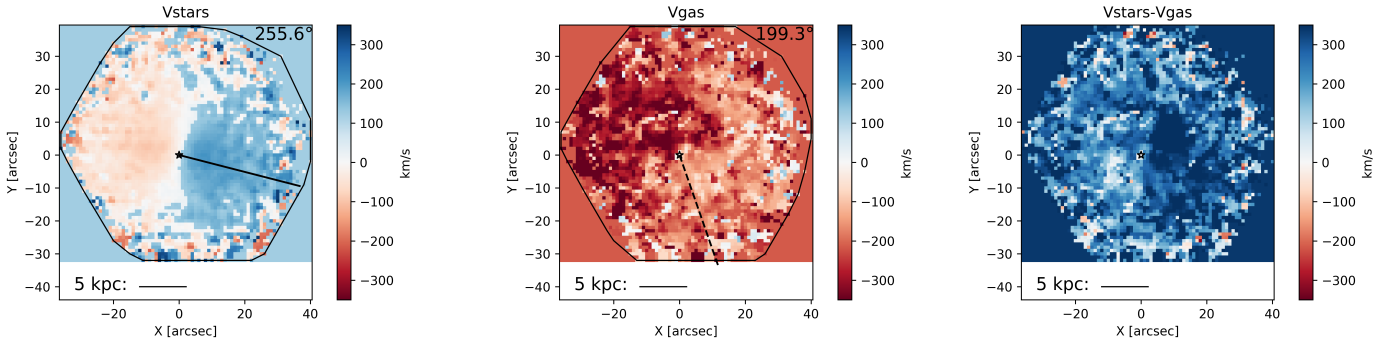
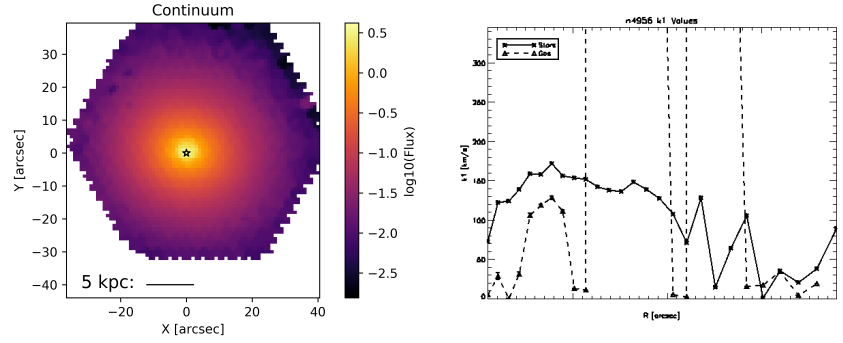
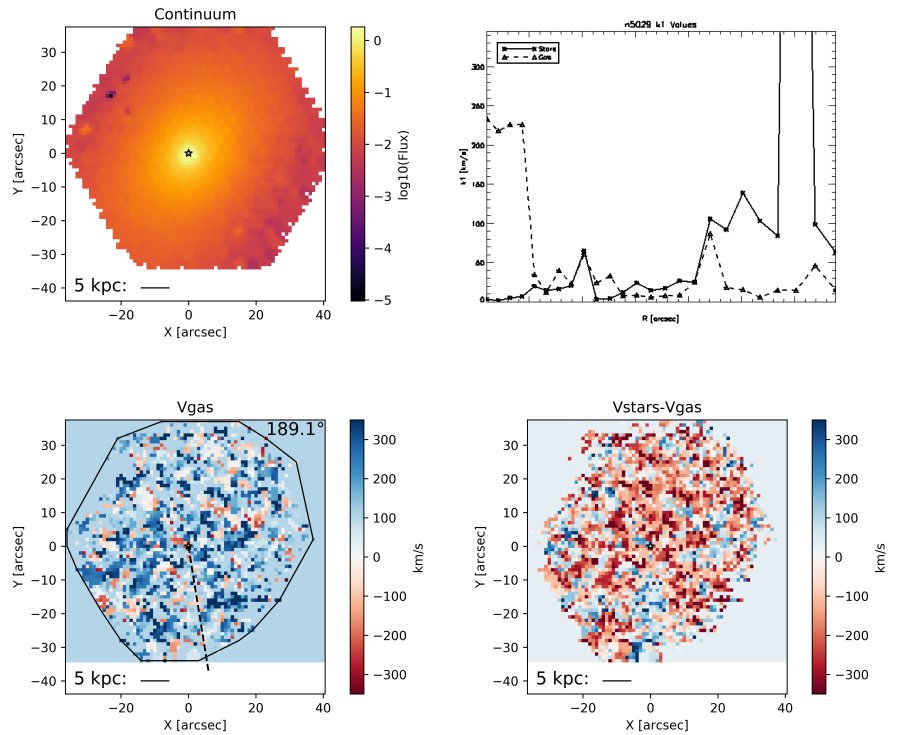


Figure 70 Top row, left to right: Name and characteristic parameters, continuum flux, and radial k_1 profiles for stars (solid) and gas (dashed), respectively. Bottom row, left to right: stellar kinematics, gas kinematics, and the difference between stellar and gas kinematics, respectively. The curves containing the data points are the convex hulls used to define the 'edge' of the map. The brightest continuum pixel (used as the center for kinemetry) is marked by a white star. The solid and dashed line in the stellar and gas velocity map, respectively, is the median position angle along which kinemetry coefficients were determined. The number value of this position angle is given at the top right of the plot. A scale bar is given along the bottom of each velocity map.

NGC 5029

$\log(\text{Stellar Mass}): 11.502$
 $D = 126.2 \text{ Mpc}$
 $M_r = -23.229 \text{ mag}$
 Redshift: 0.029
 $r_e: 25.344 \text{ arcsec}$
 AGN activity: No
 λ_R value at $r_e: 0.417$
 Residual asymmetry: 0.757



NGC 5198

$\log(\text{Stellar Mass}): 10.994$
 $D = 41.9 \text{ Mpc}$
 $M_r = -21.695 \text{ mag}$
 Redshift: 0.009
 $r_e: 16.236 \text{ arcsec}$
 AGN activity: No
 λ_R value at $r_e: 0.391$
 Residual asymmetry: 0.854

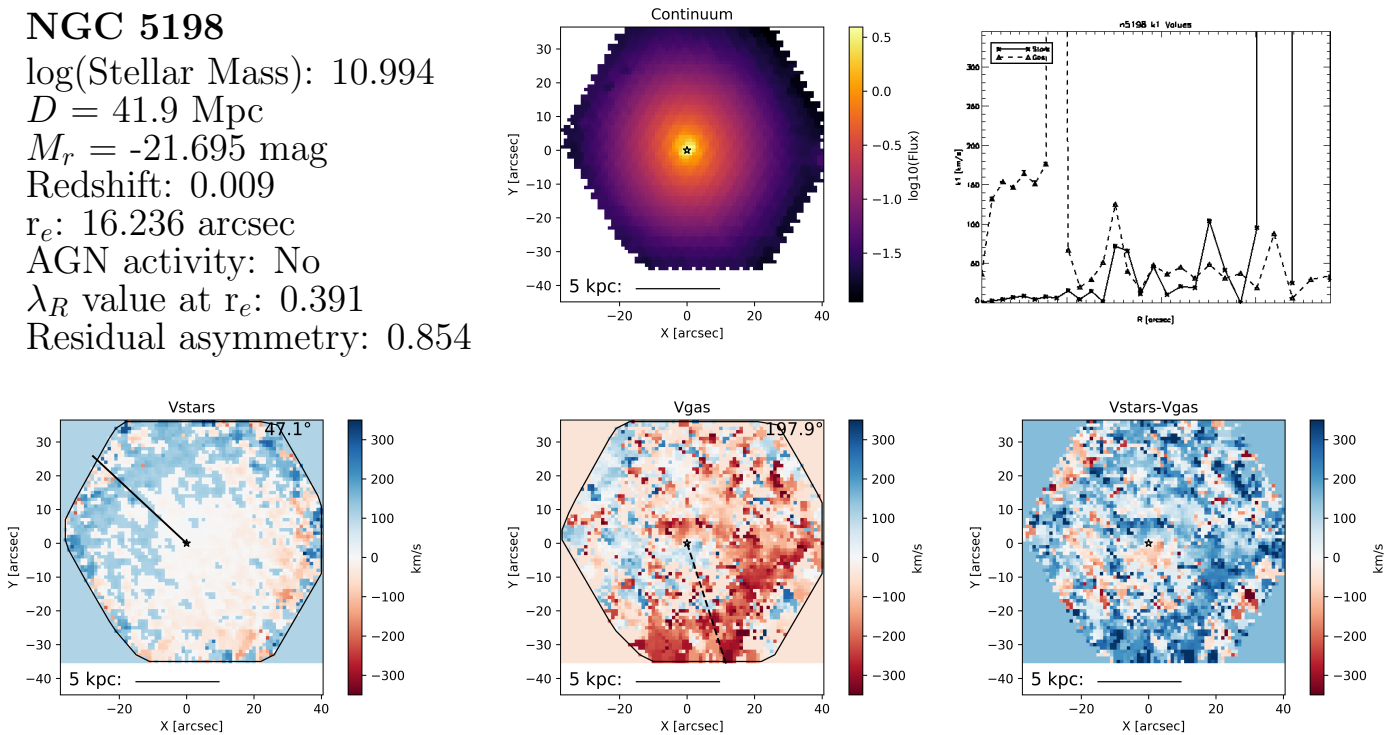


Figure 71 Top row, left to right: Name and characteristic parameters, continuum flux, and radial k_1 profiles for stars (solid) and gas (dashed), respectively. Bottom row, left to right: stellar kinematics, gas kinematics, and the difference between stellar and gas kinematics, respectively. The curves containing the data points are the convex hulls used to define the 'edge' of the map. The brightest continuum pixel (used as the center for kinemetry) is marked by a white star. The solid and dashed line in the stellar and gas velocity map, respectively, is the median position angle along which kinemetry coefficients were determined. The number value of this position angle is given at the top right of the plot. A scale bar is given along the bottom of each velocity map.

NGC 5216

$\log(\text{Stellar Mass}): 10.505$

$D = 46.4 \text{ Mpc}$

$M_r = -21.065 \text{ mag}$

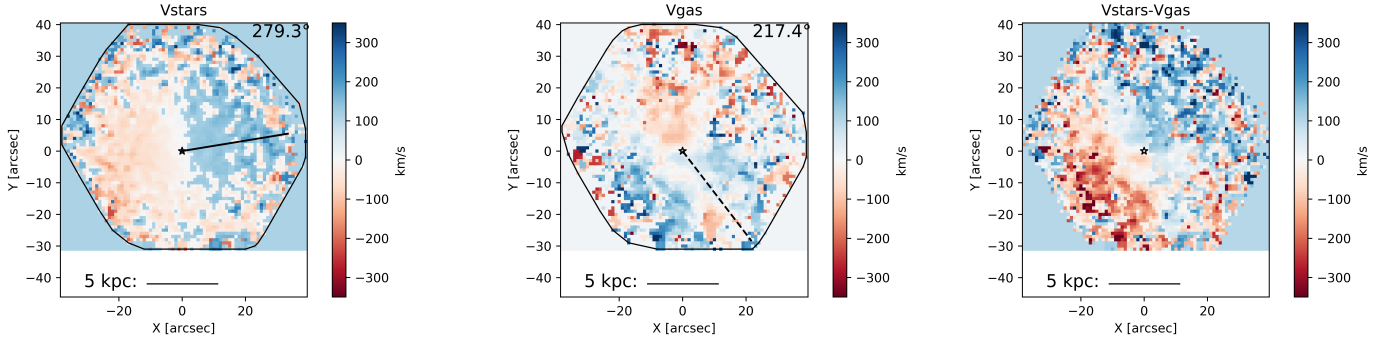
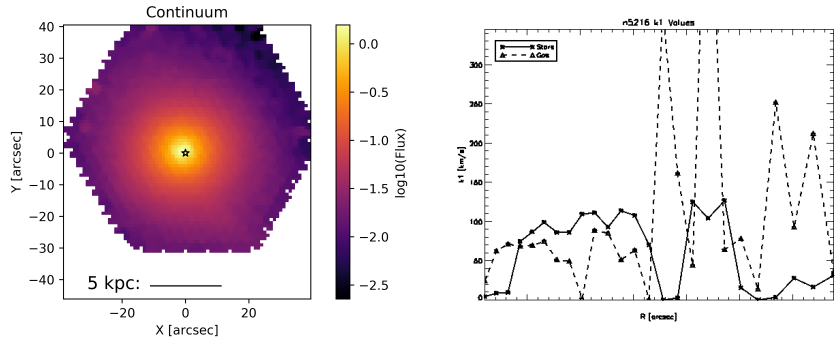
Redshift: 0.010

$r_e = 20.196 \text{ arcsec}$

AGN activity: No

λ_R value at r_e : 0.483

Residual asymmetry: 0.840



NGC 5423

$\log(\text{Stellar Mass}): 11.437$

$D = 90.2 \text{ Mpc}$

$M_r = -22.643 \text{ mag}$

Redshift: 0.020

$r_e = 15.444 \text{ arcsec}$

AGN activity: No

λ_R value at r_e : 0.393

Residual asymmetry: 0.898

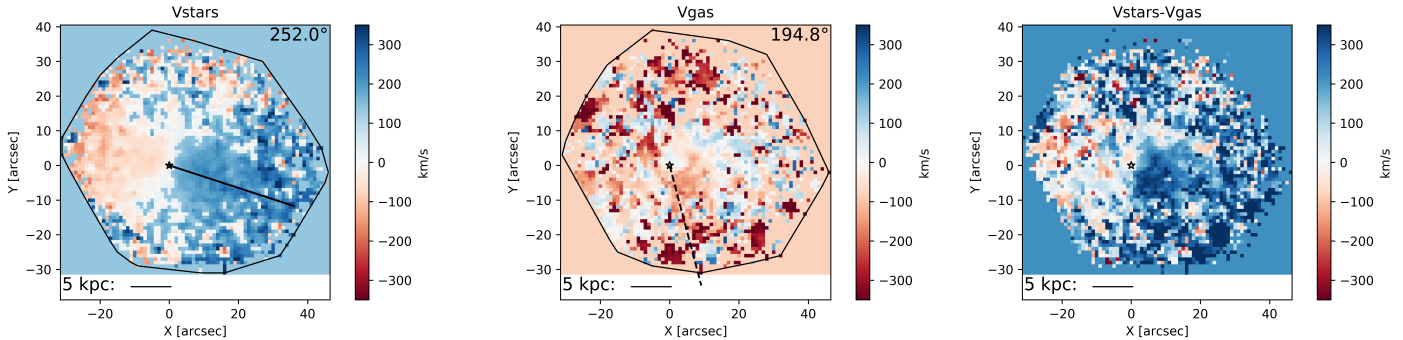
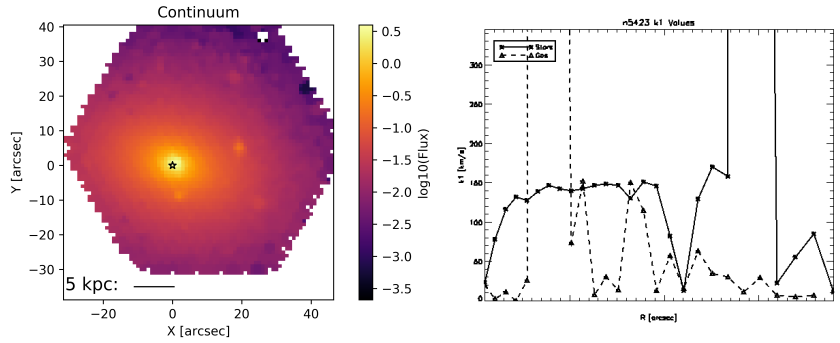
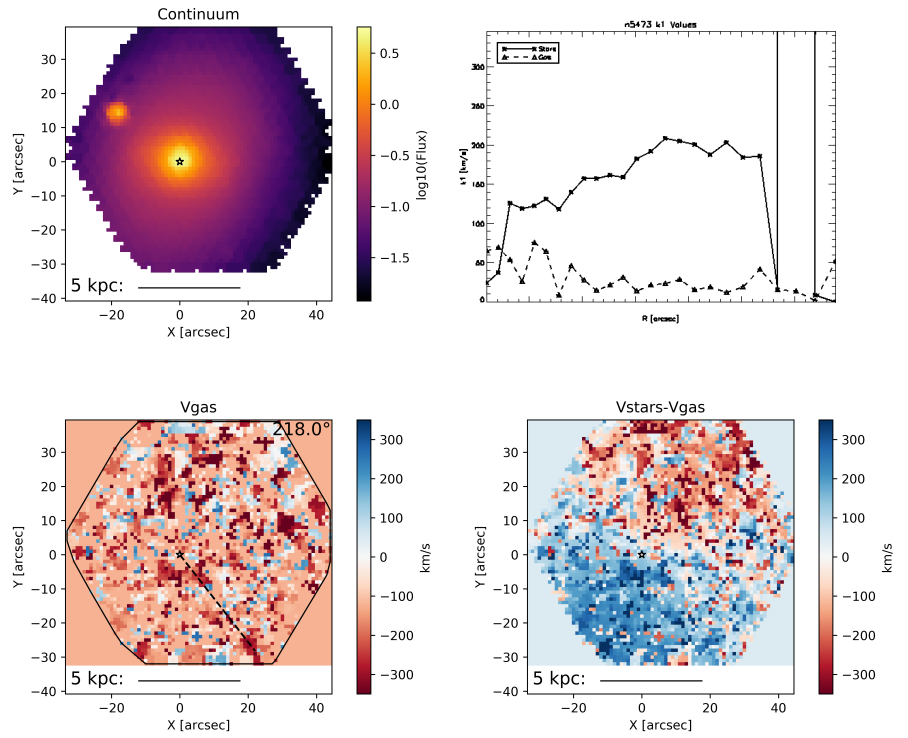


Figure 72 Top row, left to right: Name and characteristic parameters, continuum flux, and radial k_1 profiles for stars (solid) and gas (dashed), respectively. Bottom row, left to right: stellar kinematics, gas kinematics, and the difference between stellar and gas kinematics, respectively. The curves containing the data points are the convex hulls used to define the 'edge' of the map. The brightest continuum pixel (used as the center for kinemetry) is marked by a white star. The solid and dashed line in the stellar and gas velocity map, respectively, is the median position angle along which kinemetry coefficients were determined. The number value of this position angle is given at the top right of the plot. A scale bar is given along the bottom of each velocity map.

NGC 5473

$\log(\text{Stellar Mass}): 10.871$
 $D = 34.9 \text{ Mpc}$
 $M_r = -21.717 \text{ mag}$
 Redshift: 0.007
 $r_e: 17.82 \text{ arcsec}$
 AGN activity: No
 λ_R value at $r_e: 0.418$
 Residual asymmetry: 0.822



NGC 5481

$\log(\text{Stellar Mass}): 10.281$
 $D = 34.7 \text{ Mpc}$
 $M_r = -19.799 \text{ mag}$
 Redshift: 0.000
 $r_e: 5.918 \text{ arcsec}$
 AGN activity: No
 λ_R value at $r_e: 0.291$
 Residual asymmetry: 0.956

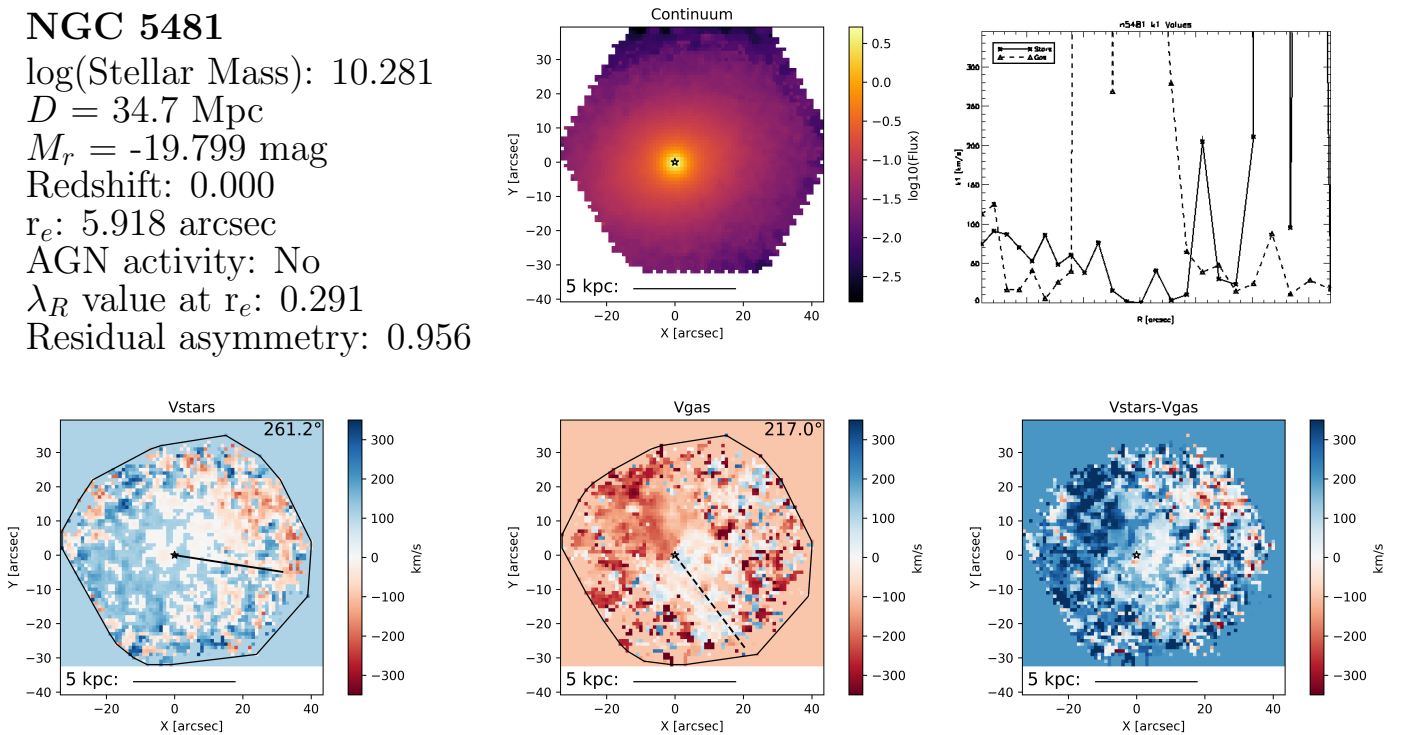


Figure 73 Top row, left to right: Name and characteristic parameters, continuum flux, and radial k_1 profiles for stars (solid) and gas (dashed), respectively. Bottom row, left to right: stellar kinematics, gas kinematics, and the difference between stellar and gas kinematics, respectively. The curves containing the data points are the convex hulls used to define the 'edge' of the map. The brightest continuum pixel (used as the center for kinemetry) is marked by a white star. The solid and dashed line in the stellar and gas velocity map, respectively, is the median position angle along which kinemetry coefficients were determined. The number value of this position angle is given at the top right of the plot. A scale bar is given along the bottom of each velocity map.

NGC 5485

$\log(\text{Stellar Mass}): 11.024$

$D = 33.6 \text{ Mpc}$

$M_r = -21.950 \text{ mag}$

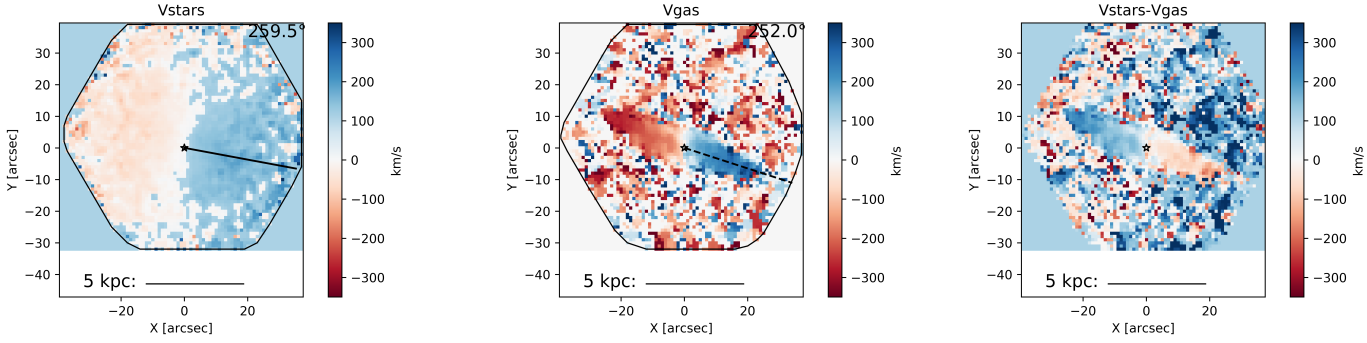
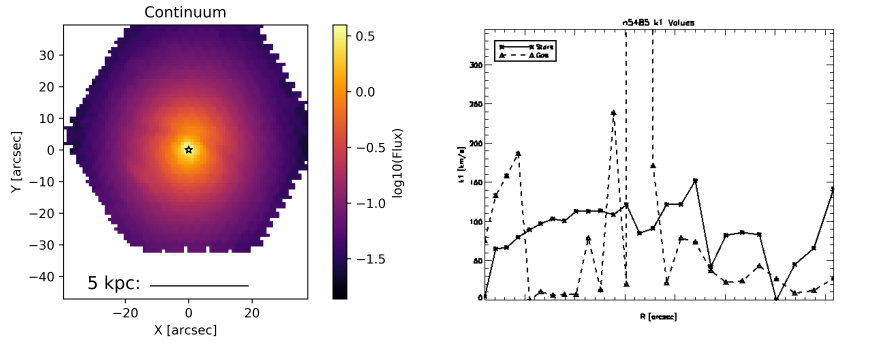
Redshift: 0.006

$r_e: 31.68 \text{ arcsec}$

AGN activity: No

λ_R value at r_e : 0.391

Residual asymmetry: 0.815



NGC 5513

$\log(\text{Stellar Mass}): 11.231$

$D = 77.2 \text{ Mpc}$

$M_r = -22.498 \text{ mag}$

Redshift: 0.017

$r_e: 15.84 \text{ arcsec}$

AGN activity: No

λ_R value at r_e : 0.535

Residual asymmetry: 0.766

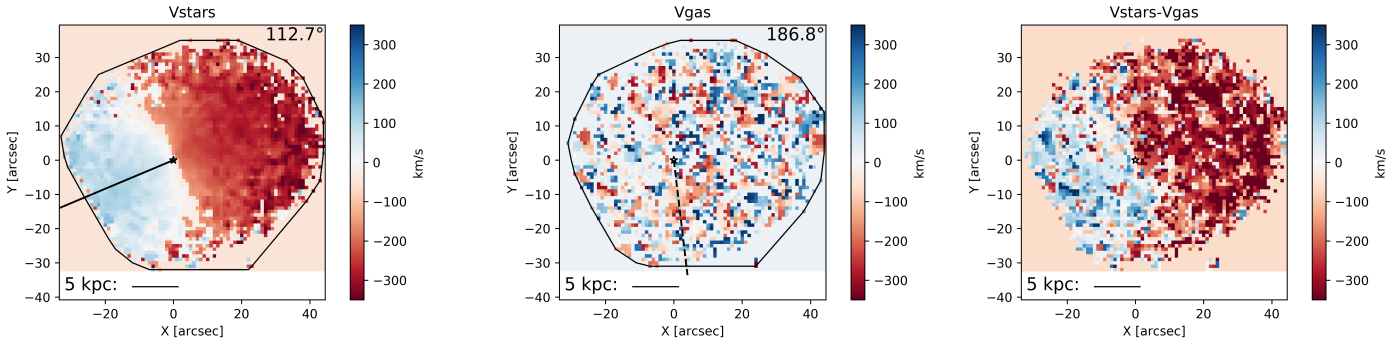
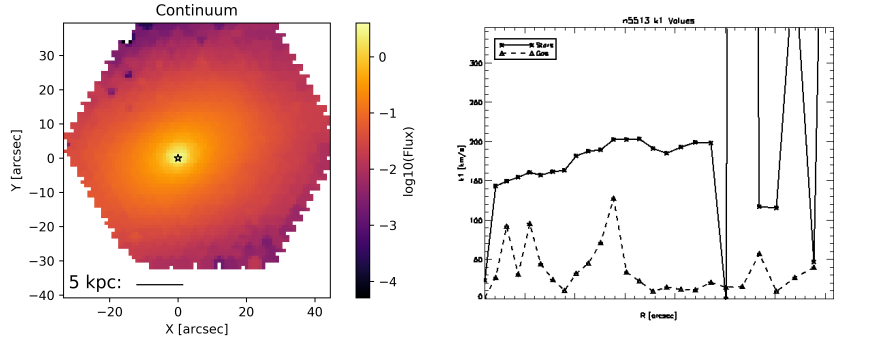
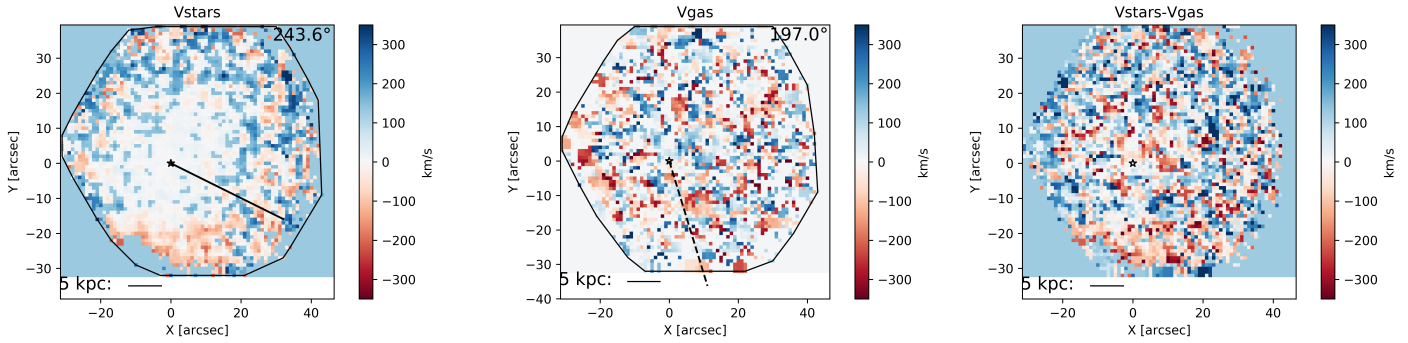
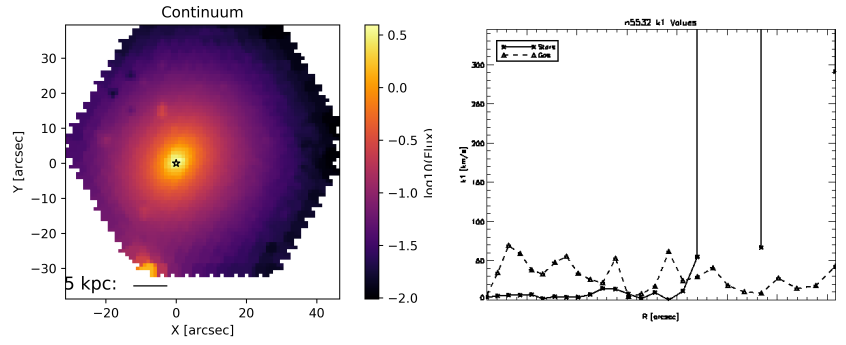


Figure 74 Top row, left to right: Name and characteristic parameters, continuum flux, and radial k_1 profiles for stars (solid) and gas (dashed), respectively. Bottom row, left to right: stellar kinematics, gas kinematics, and the difference between stellar and gas kinematics, respectively. The curves containing the data points are the convex hulls used to define the 'edge' of the map. The brightest continuum pixel (used as the center for kinemetry) is marked by a white star. The solid and dashed line in the stellar and gas velocity map, respectively, is the median position angle along which kinemetry coefficients were determined. The number value of this position angle is given at the top right of the plot. A scale bar is given along the bottom of each velocity map.

NGC 5532

$\log(\text{Stellar Mass}): 11.851$
 $D = 110.5 \text{ Mpc}$
 $M_r = -23.938 \text{ mag}$
 Redshift: 0.025
 $r_e: 24.552 \text{ arcsec}$
 AGN activity: No
 λ_R value at $r_e: 0.341$
 Residual asymmetry: 0.811



NGC 5546

$\log(\text{Stellar Mass}): 11.59$
 $D = 109.5 \text{ Mpc}$
 $M_r = -23.307 \text{ mag}$
 Redshift: 0.025
 $r_e: 17.424 \text{ arcsec}$
 AGN activity: No
 λ_R value at $r_e: 0.327$
 Residual asymmetry: 0.864

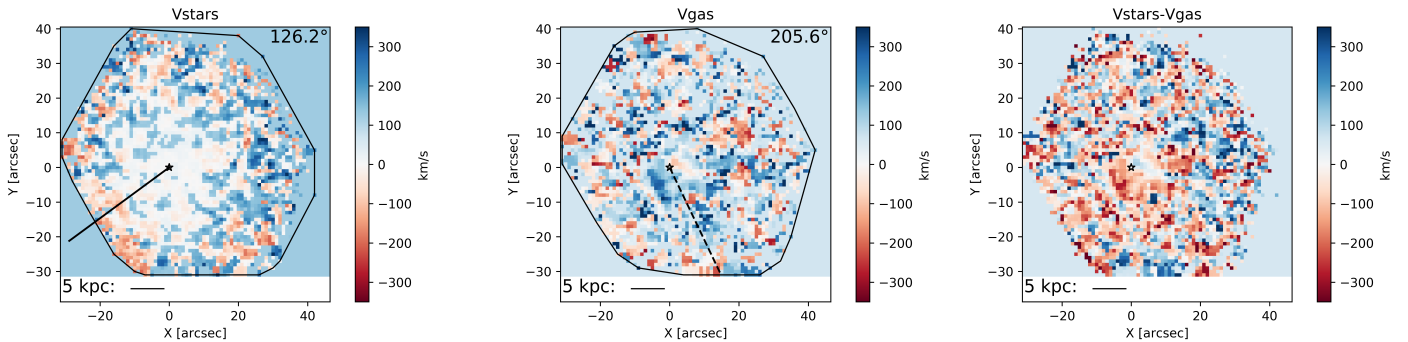
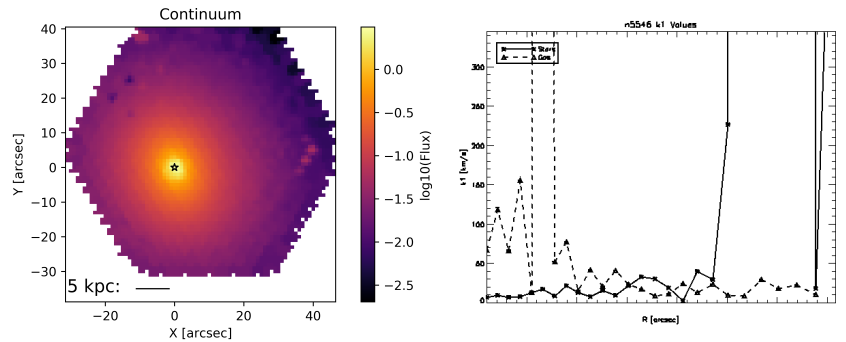


Figure 75 Top row, left to right: Name and characteristic parameters, continuum flux, and radial k_1 profiles for stars (solid) and gas (dashed), respectively. Bottom row, left to right: stellar kinematics, gas kinematics, and the difference between stellar and gas kinematics, respectively. The curves containing the data points are the convex hulls used to define the 'edge' of the map. The brightest continuum pixel (used as the center for kinemetry) is marked by a white star. The solid and dashed line in the stellar and gas velocity map, respectively, is the median position angle along which kinemetry coefficients were determined. The number value of this position angle is given at the top right of the plot. A scale bar is given along the bottom of each velocity map.

NGC 5549

$\log(\text{Stellar Mass}): 11.629$

$D = 114.7 \text{ Mpc}$

$M_r = -23.169 \text{ mag}$

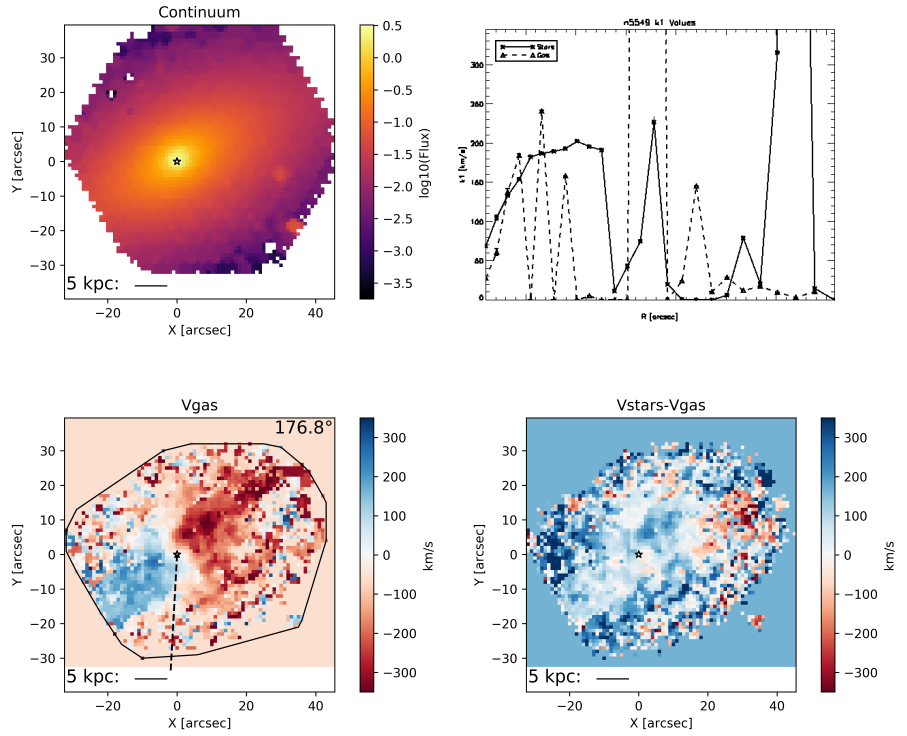
Redshift: 0.026

$r_e = 14.652 \text{ arcsec}$

AGN activity: No

λ_R value at r_e : 0.454

Residual asymmetry: 0.917



NGC 5557

$\log(\text{Stellar Mass}): 11.282$

$D = 52.1 \text{ Mpc}$

$M_r = -22.886 \text{ mag}$

Redshift: 0.011

$r_e = 24.552 \text{ arcsec}$

AGN activity: No

λ_R value at r_e : 0.363

Residual asymmetry: 0.758

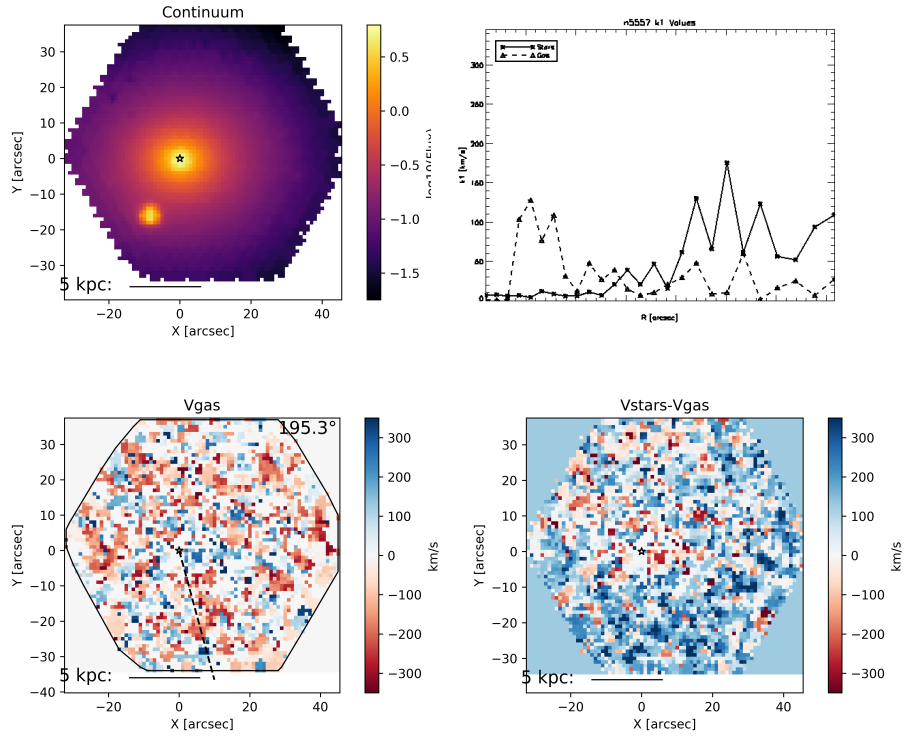
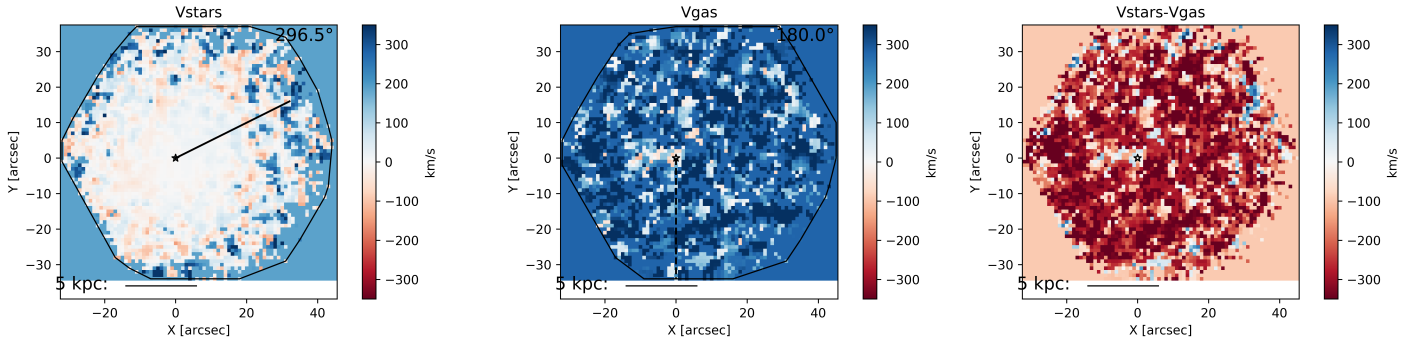
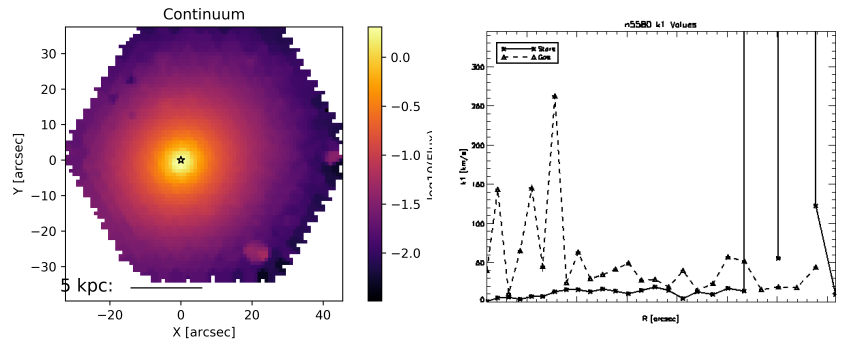


Figure 76 Top row, left to right: Name and characteristic parameters, continuum flux, and radial k_1 profiles for stars (solid) and gas (dashed), respectively. Bottom row, left to right: stellar kinematics, gas kinematics, and the difference between stellar and gas kinematics, respectively. The curves containing the data points are the convex hulls used to define the 'edge' of the map. The brightest continuum pixel (used as the center for kinemetry) is marked by a white star. The solid and dashed line in the stellar and gas velocity map, respectively, is the median position angle along which kinemetry coefficients were determined. The number value of this position angle is given at the top right of the plot. A scale bar is given along the bottom of each velocity map.

NGC 5580

$\log(\text{Stellar Mass}): 10.798$
 $D = 52.0 \text{ Mpc}$
 $M_r = -21.58 \text{ mag}$
 Redshift: 0.011
 $r_e = 15.048 \text{ arcsec}$
 AGN activity: No
 λ_R value at r_e : 0.625
 Residual asymmetry: 0.785



NGC 5598

$\log(\text{Stellar Mass}): 11.126$
 $D = 82.6 \text{ Mpc}$
 $M_r = -21.957 \text{ mag}$
 Redshift: 0.018
 $r_e = 9.108 \text{ arcsec}$
 AGN activity: No
 λ_R value at r_e : 0.442
 Residual asymmetry: 0.809

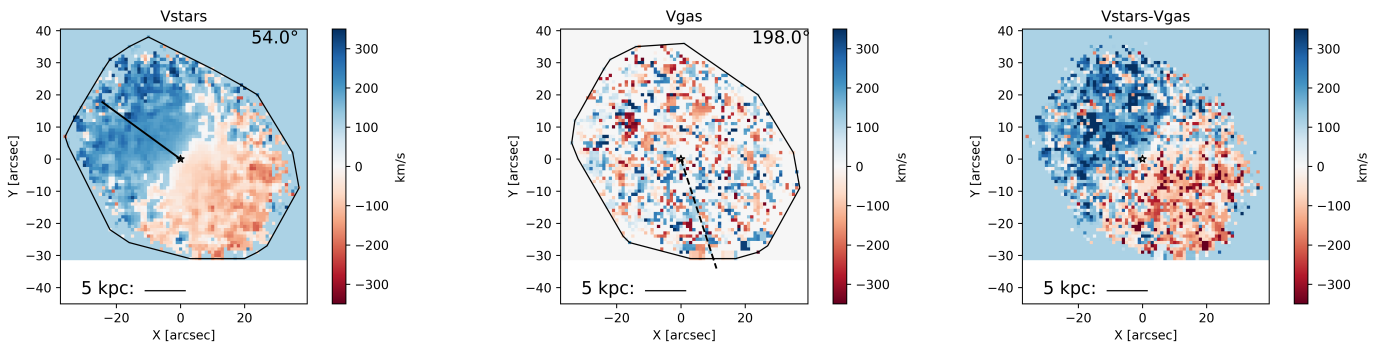
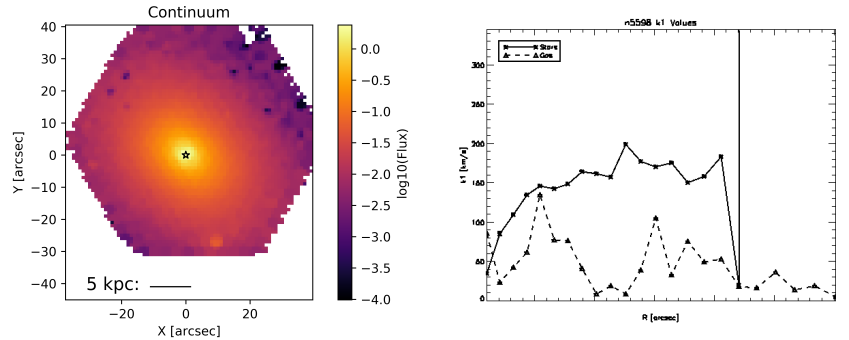
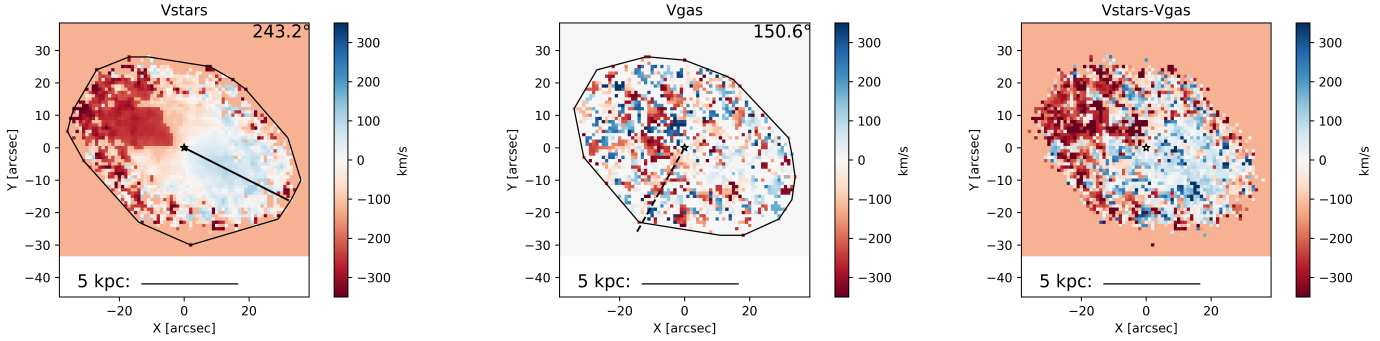
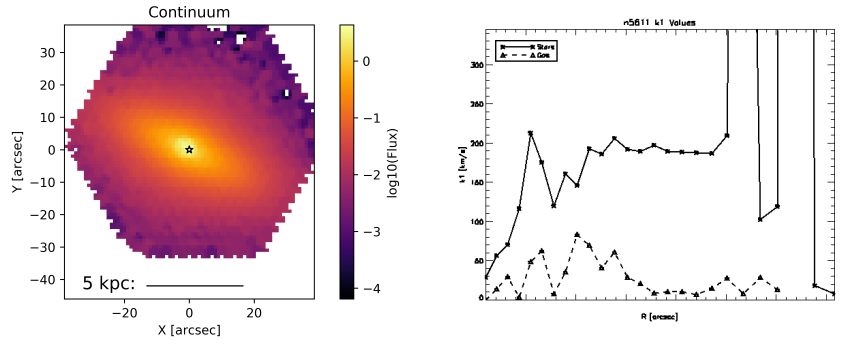


Figure 77 Top row, left to right: Name and characteristic parameters, continuum flux, and radial k_1 profiles for stars (solid) and gas (dashed), respectively. Bottom row, left to right: stellar kinematics, gas kinematics, and the difference between stellar and gas kinematics, respectively. The curves containing the data points are the convex hulls used to define the 'edge' of the map. The brightest continuum pixel (used as the center for kinemetry) is marked by a white star. The solid and dashed line in the stellar and gas velocity map, respectively, is the median position angle along which kinemetry coefficients were determined. The number value of this position angle is given at the top right of the plot. A scale bar is given along the bottom of each velocity map.

NGC 5611

$\log(\text{Stellar Mass}): 10.347$
 $D = 35.0 \text{ Mpc}$
 $M_r = -20.444 \text{ mag}$
 Redshift: 0.006
 $r_e = 7.92 \text{ arcsec}$
 AGN activity: No
 λ_R value at r_e : 0.464
 Residual asymmetry: 0.965



NGC 5623

$\log(\text{Stellar Mass}): 10.849$
 $D = 54.1 \text{ Mpc}$
 $M_r = -21.681 \text{ mag}$
 Redshift: 0.011
 $r_e = 15.444 \text{ arcsec}$
 AGN activity: No
 λ_R value at r_e : 0.277
 Residual asymmetry: 0.866

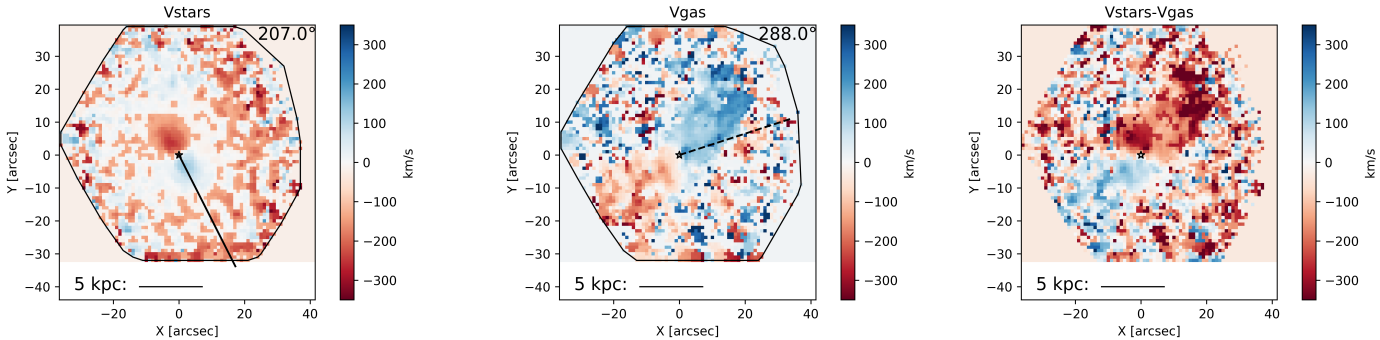
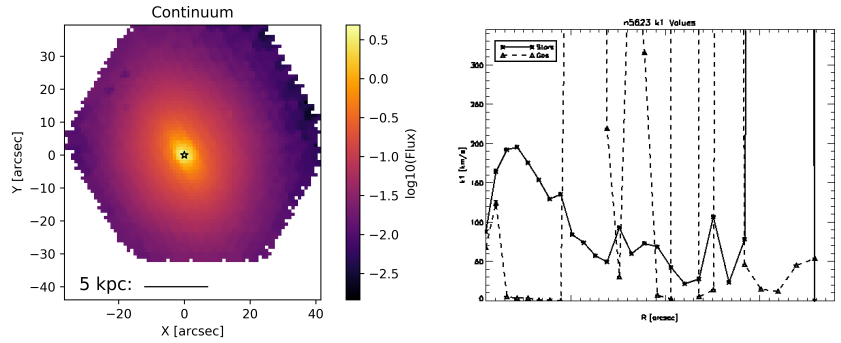
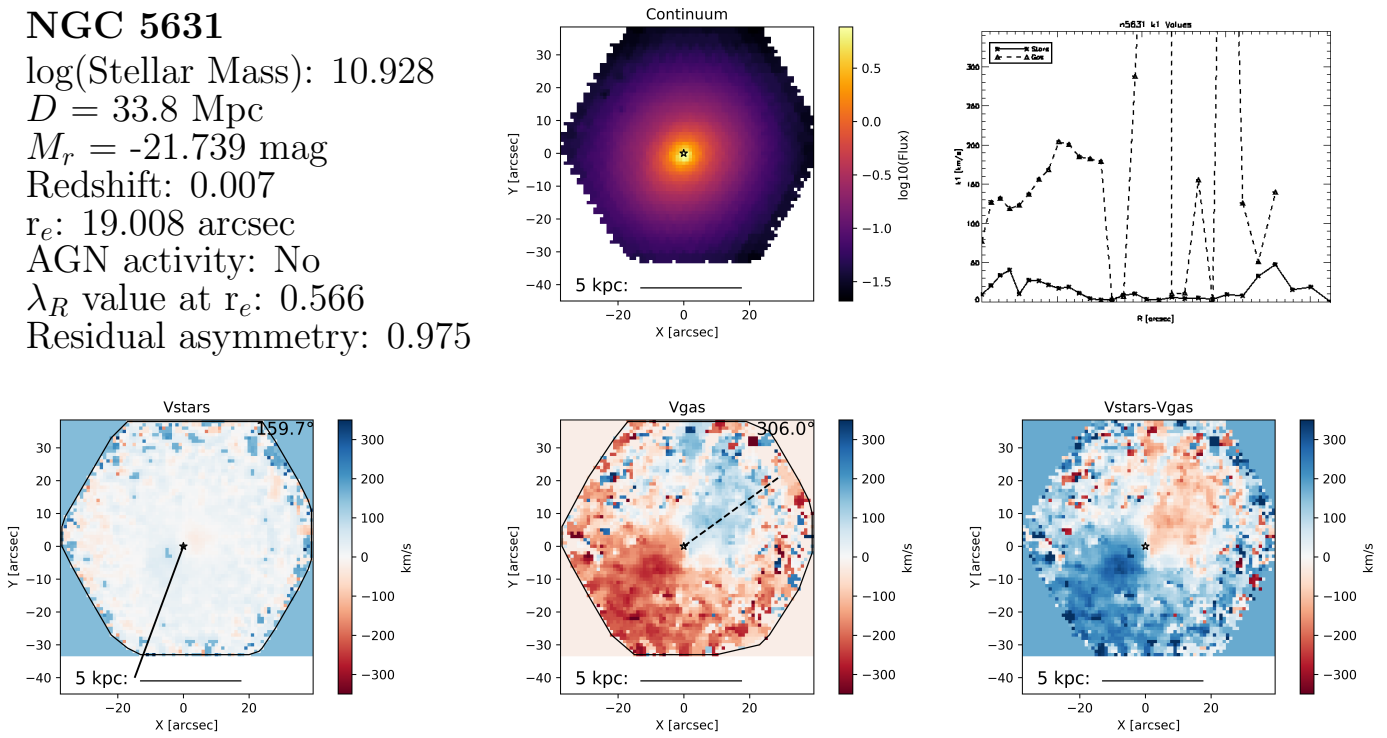


Figure 78 Top row, left to right: Name and characteristic parameters, continuum flux, and radial k_1 profiles for stars (solid) and gas (dashed), respectively. Bottom row, left to right: stellar kinematics, gas kinematics, and the difference between stellar and gas kinematics, respectively. The curves containing the data points are the convex hulls used to define the 'edge' of the map. The brightest continuum pixel (used as the center for kinemetry) is marked by a white star. The solid and dashed line in the stellar and gas velocity map, respectively, is the median position angle along which kinemetry coefficients were determined. The number value of this position angle is given at the top right of the plot. A scale bar is given along the bottom of each velocity map.

NGC 5631

$\log(\text{Stellar Mass}): 10.928$
 $D = 33.8 \text{ Mpc}$
 $M_r = -21.739 \text{ mag}$
 Redshift: 0.007
 $r_e: 19.008 \text{ arcsec}$
 AGN activity: No
 λ_R value at $r_e: 0.566$
 Residual asymmetry: 0.975



NGC 5642

$\log(\text{Stellar Mass}): 11.294$
 $D = 67.3 \text{ Mpc}$
 $M_r = -22.358 \text{ mag}$
 Redshift: 0.014
 $r_e: 18.612 \text{ arcsec}$
 AGN activity: No
 λ_R value at $r_e: 0.267$
 Residual asymmetry: 0.799

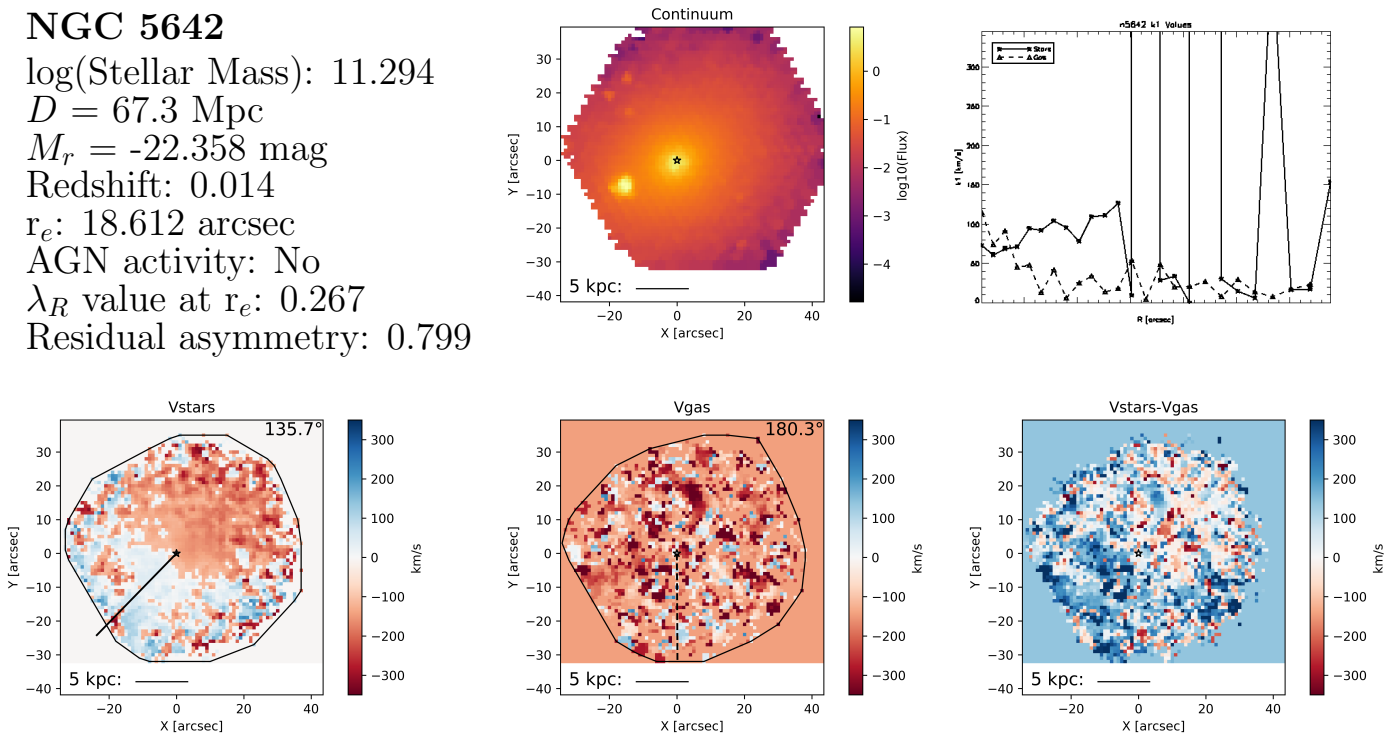
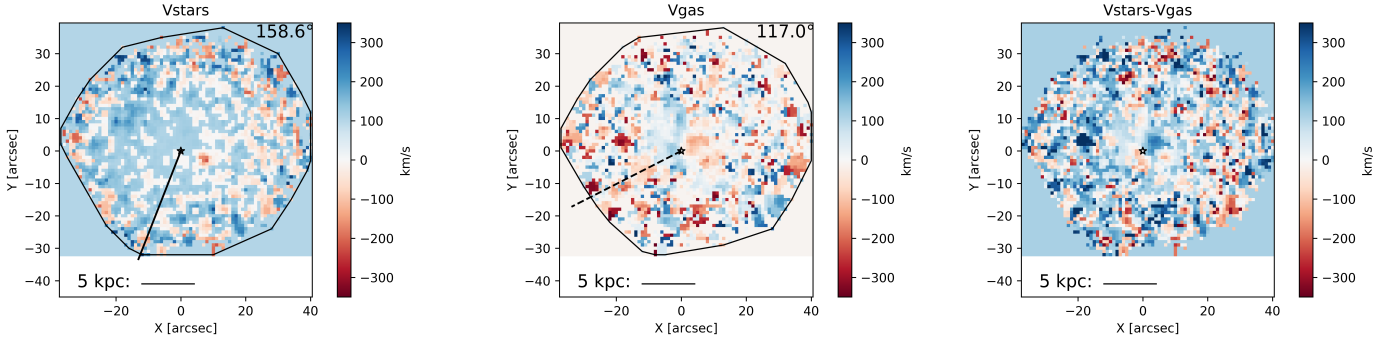
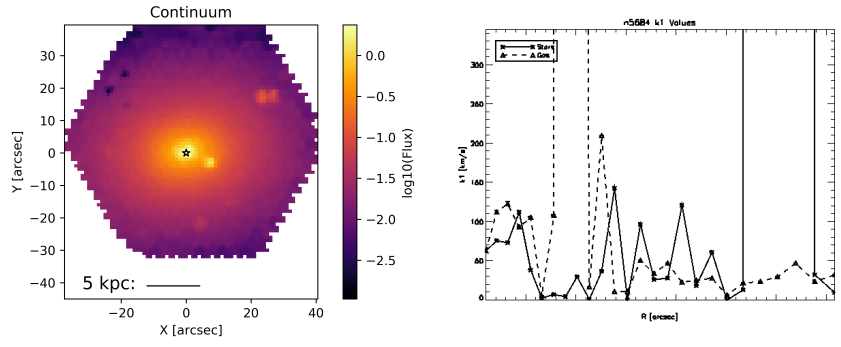


Figure 79 Top row, left to right: Name and characteristic parameters, continuum flux, and radial k_1 profiles for stars (solid) and gas (dashed), respectively. Bottom row, left to right: stellar kinematics, gas kinematics, and the difference between stellar and gas kinematics, respectively. The curves containing the data points are the convex hulls used to define the 'edge' of the map. The brightest continuum pixel (used as the center for kinemetry) is marked by a white star. The solid and dashed line in the stellar and gas velocity map, respectively, is the median position angle along which kinemetry coefficients were determined. The number value of this position angle is given at the top right of the plot. A scale bar is given along the bottom of each velocity map.

NGC 5684

$\log(\text{Stellar Mass}): 10.955$
 $D = 63.9 \text{ Mpc}$
 $M_r = -21.802 \text{ mag}$
 Redshift: 0.014
 $r_e: 17.82 \text{ arcsec}$
 AGN activity: No
 λ_R value at r_e : 0.260
 Residual asymmetry: 0.943



NGC 5687

$\log(\text{Stellar Mass}): 10.913$
 $D = 36.6 \text{ Mpc}$
 $M_r = -21.421 \text{ mag}$
 Redshift: 0.007
 $r_e: 25.344 \text{ arcsec}$
 AGN activity: No
 λ_R value at r_e : 0.297
 Residual asymmetry: 0.760

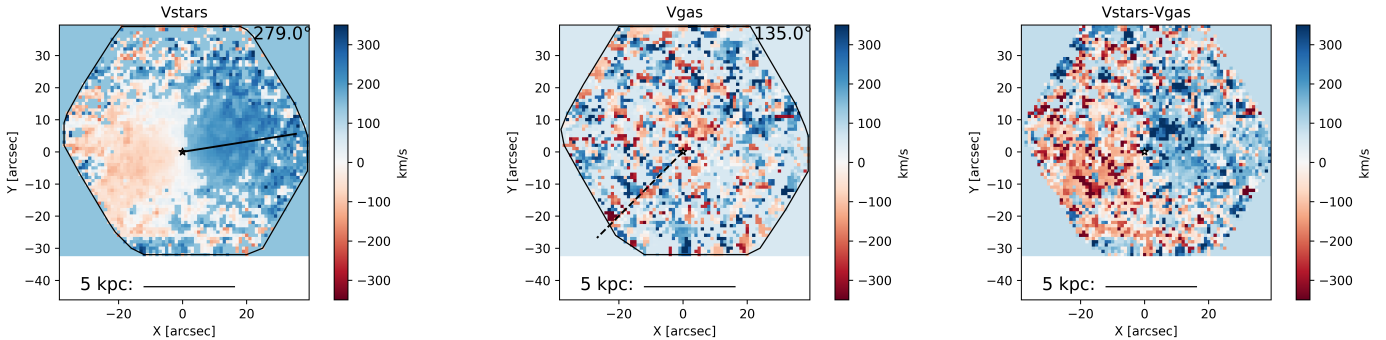
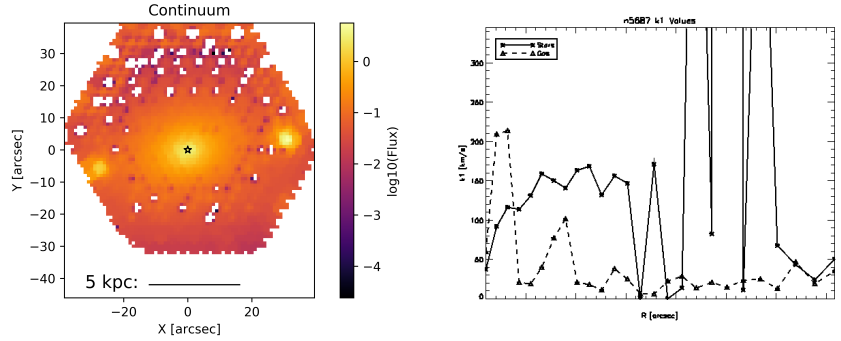
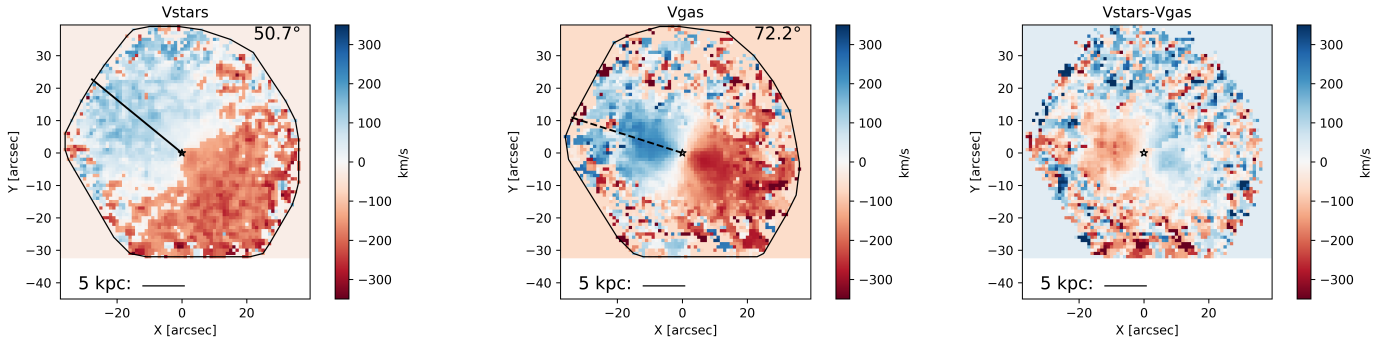
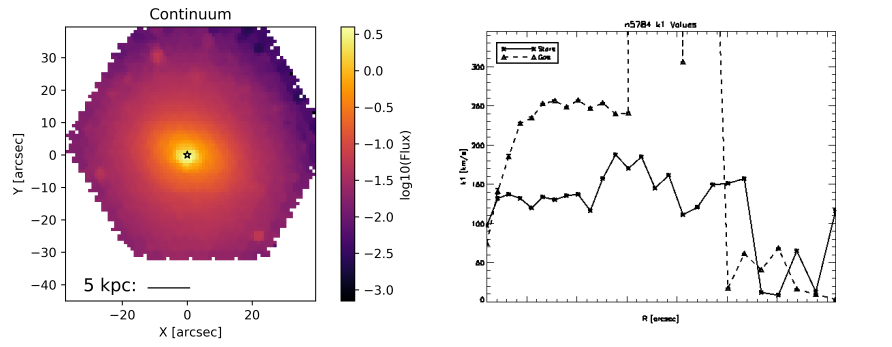


Figure 80 Top row, left to right: Name and characteristic parameters, continuum flux, and radial k1 profiles for stars (solid) and gas (dashed), respectively. Bottom row, left to right: stellar kinematics, gas kinematics, and the difference between stellar and gas kinematics, respectively. The curves containing the data points are the convex hulls used to define the 'edge' of the map. The brightest continuum pixel (used as the center for kinemetry) is marked by a white star. The solid and dashed line in the stellar and gas velocity map, respectively, is the median position angle along which kinemetry coefficients were determined. The number value of this position angle is given at the top right of the plot. A scale bar is given along the bottom of each velocity map.

NGC 5784

$\log(\text{Stellar Mass}): 11.216$
 $D = 81.1 \text{ Mpc}$
 $M_r = -22.615 \text{ mag}$
 Redshift: 0.018
 $r_e: 13.464 \text{ arcsec}$
 AGN activity: No
 λ_R value at $r_e: 0.369$
 Residual asymmetry: 0.954



NGC 5797

$\log(\text{Stellar Mass}): 10.846$
 $D = 61.7 \text{ Mpc}$
 $M_r = -22.129 \text{ mag}$
 Redshift: 0.013
 $r_e: 18.612 \text{ arcsec}$
 AGN activity: No
 λ_R value at $r_e: 0.539$
 Residual asymmetry: 0.784

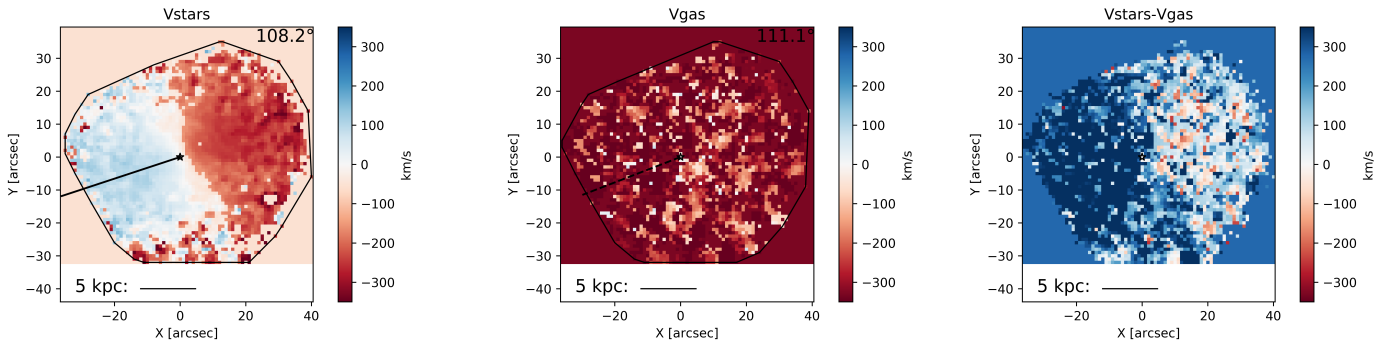
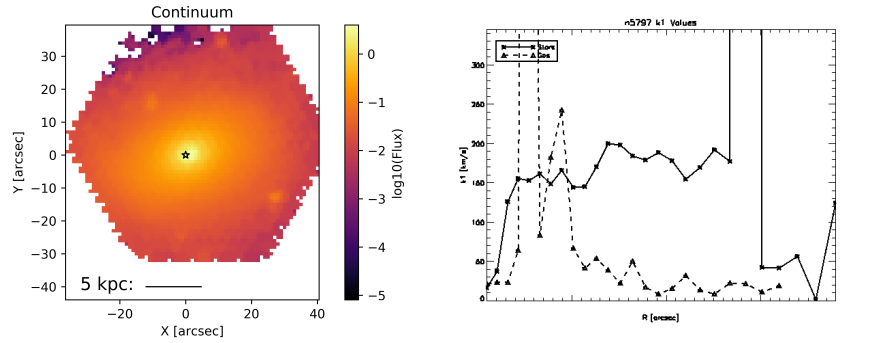
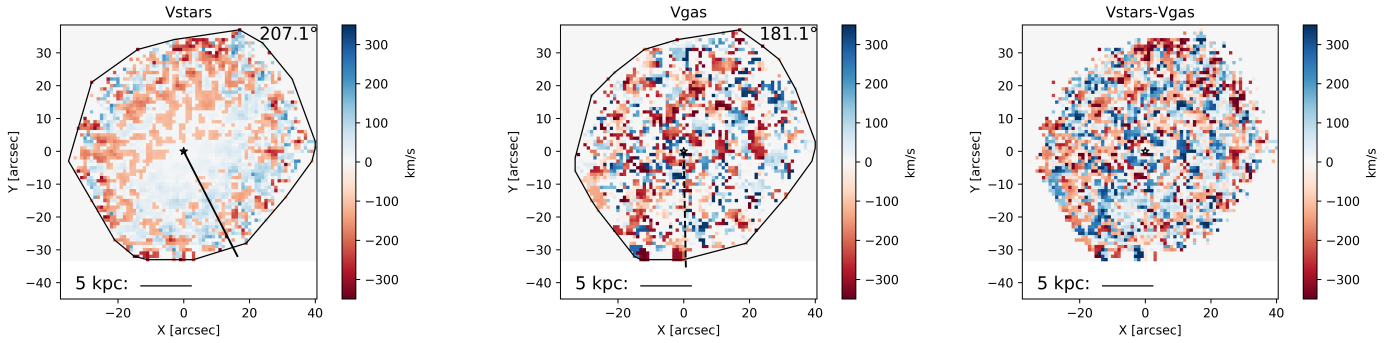


Figure 81 Top row, left to right: Name and characteristic parameters, continuum flux, and radial k_1 profiles for stars (solid) and gas (dashed), respectively. Bottom row, left to right: stellar kinematics, gas kinematics, and the difference between stellar and gas kinematics, respectively. The curves containing the data points are the convex hulls used to define the 'edge' of the map. The brightest continuum pixel (used as the center for kinemetry) is marked by a white star. The solid and dashed line in the stellar and gas velocity map, respectively, is the median position angle along which kinemetry coefficients were determined. The number value of this position angle is given at the top right of the plot. A scale bar is given along the bottom of each velocity map.

NGC 6020

$\log(\text{Stellar Mass}): 11.001$
 $D = 67.4 \text{ Mpc}$
 $M_r = -22.081 \text{ mag}$
 Redshift: 0.014
 $r_e: 19.008 \text{ arcsec}$
 AGN activity: No
 λ_R value at $r_e: 0.195$
 Residual asymmetry: 0.800



NGC 6021

$\log(\text{Stellar Mass}): 11.006$
 $D = 73.6 \text{ Mpc}$
 $M_r = -21.883 \text{ mag}$
 Redshift: 0.016
 $r_e: 9.504 \text{ arcsec}$
 AGN activity: No
 λ_R value at $r_e: 0.420$
 Residual asymmetry: 0.920

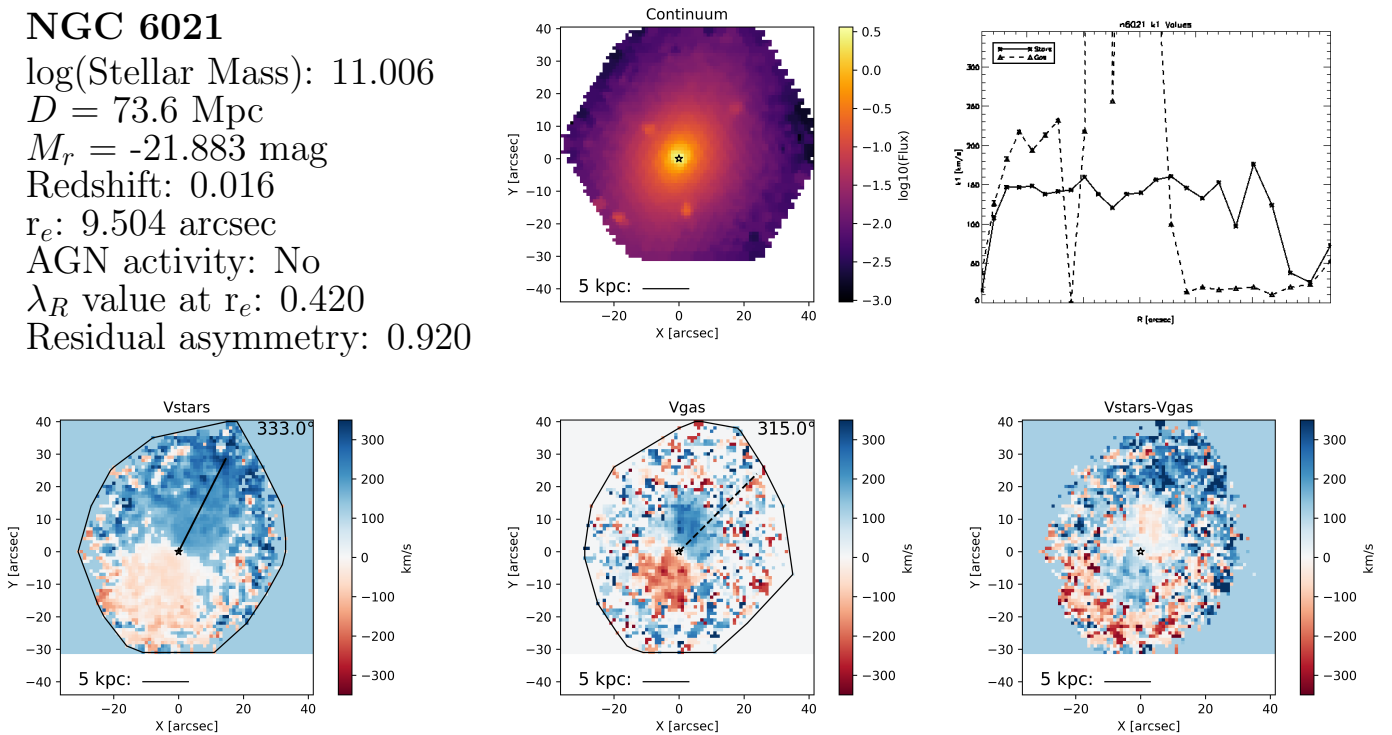
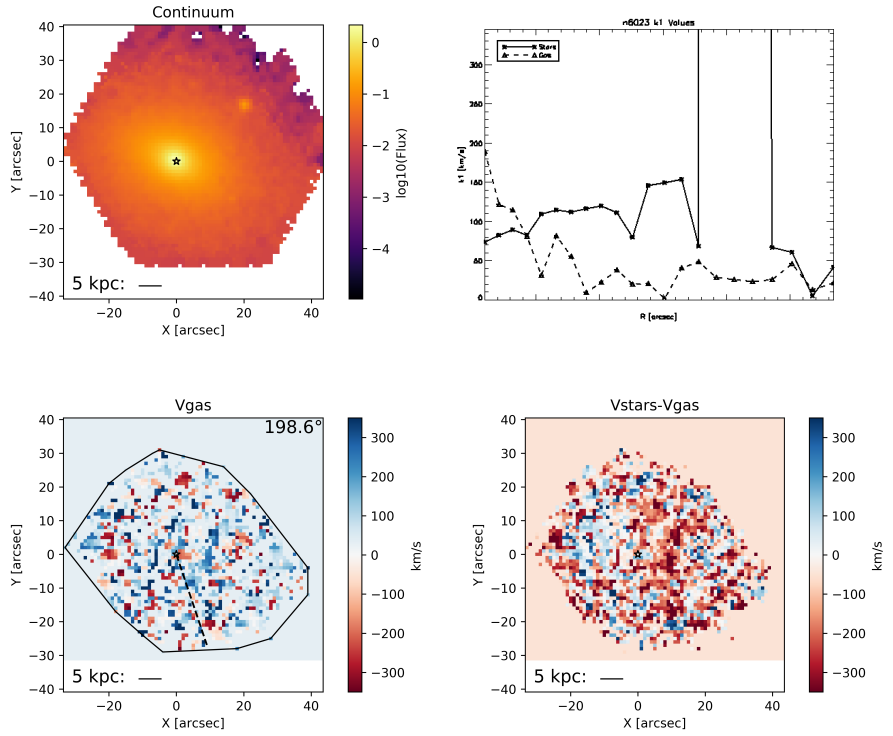


Figure 83 Top row, left to right: Name and characteristic parameters, continuum flux, and radial k_1 profiles for stars (solid) and gas (dashed), respectively. Bottom row, left to right: stellar kinematics, gas kinematics, and the difference between stellar and gas kinematics, respectively. The curves containing the data points are the convex hulls used to define the 'edge' of the map. The brightest continuum pixel (used as the center for kinemetry) is marked by a white star. The solid and dashed line in the stellar and gas velocity map, respectively, is the median position angle along which kinemetry coefficients were determined. The number value of this position angle is given at the top right of the plot. A scale bar is given along the bottom of each velocity map.

NGC 6023

$\log(\text{Stellar Mass}): 11.864$
 $D = 160.2 \text{ Mpc}$
 $M_r = -22.899 \text{ mag}$
 Redshift: 0.037
 $r_e = 8.940 \text{ arcsec}$
 AGN activity: No
 λ_R value at r_e : 0.180
 Residual asymmetry: 0.834



NGC 6081

$\log(\text{Stellar Mass}): 11.118$
 $D = 73.1 \text{ (DR3) Mpc}$
 $M_r = -21.949 \text{ mag}$
 Redshift: 0.017
 $r_e = 12.276 \text{ arcsec}$
 AGN activity: No
 λ_R value at r_e : 0.357
 Residual asymmetry: 0.705

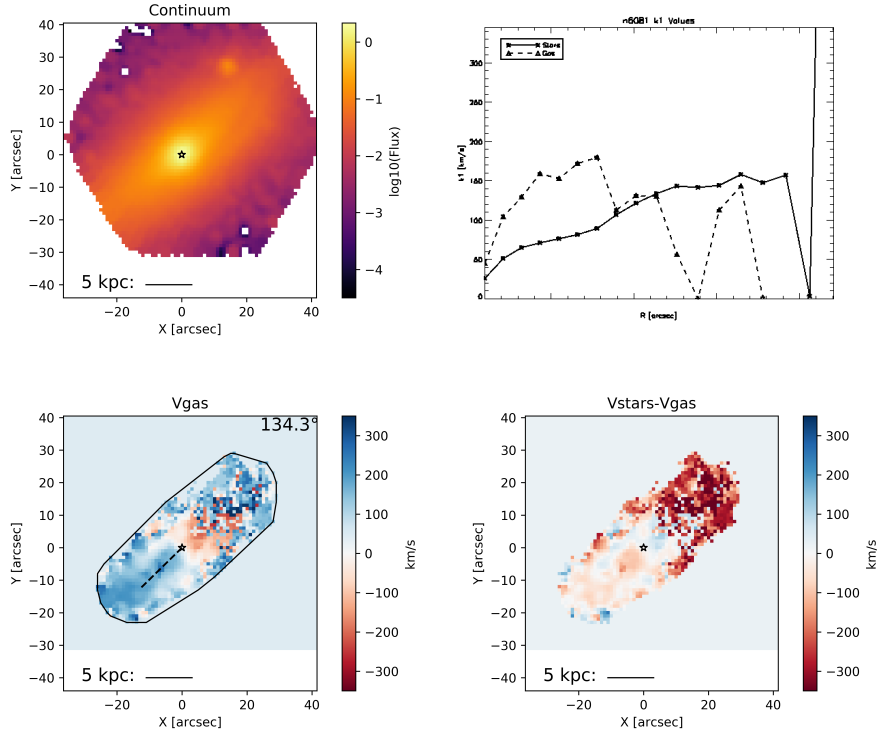
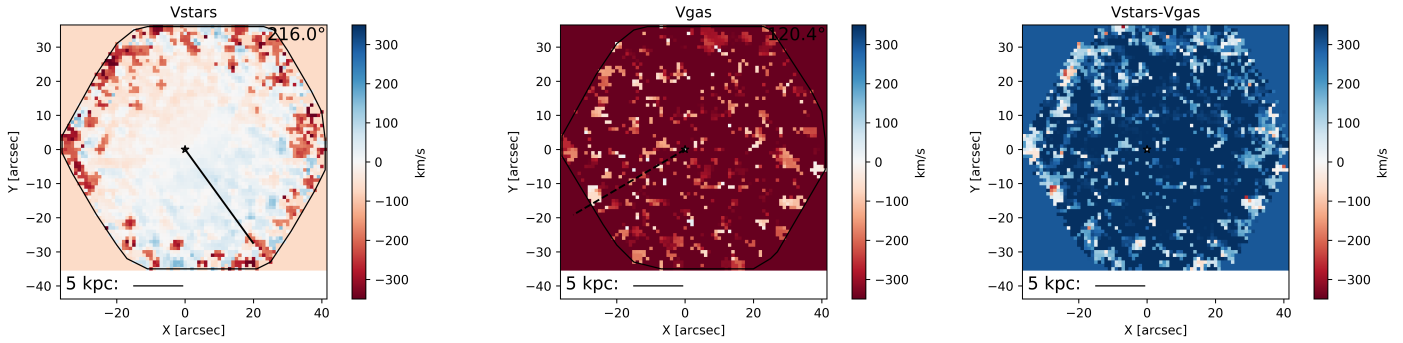
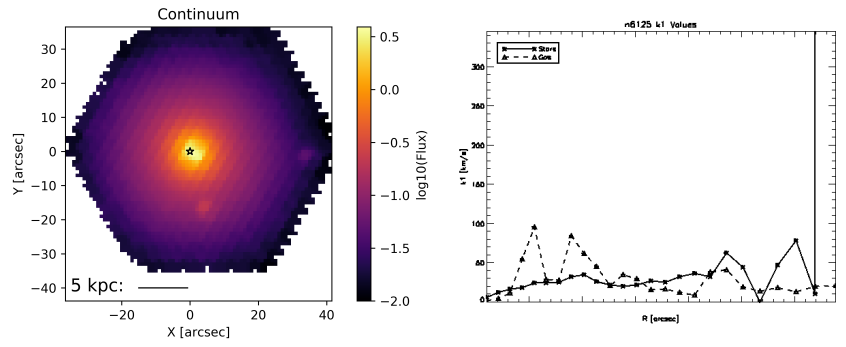


Figure 84 Top row, left to right: Name and characteristic parameters, continuum flux, and radial k_1 profiles for stars (solid) and gas (dashed), respectively. Bottom row, left to right: stellar kinematics, gas kinematics, and the difference between stellar and gas kinematics, respectively. The curves containing the data points are the convex hulls used to define the 'edge' of the map. The brightest continuum pixel (used as the center for kinemetry) is marked by a white star. The solid and dashed line in the stellar and gas velocity map, respectively, is the median position angle along which kinemetry coefficients were determined. The number value of this position angle is given at the top right of the plot. A scale bar is given along the bottom of each velocity map.

NGC 6125

$\log(\text{Stellar Mass}): 11.384$
 $D = 72.2 \text{ Mpc}$
 $M_r = -22.858 \text{ mag}$
 Redshift: 0.015
 $r_e: 21.78 \text{ arcsec}$
 AGN activity: No
 λ_R value at $r_e: 0.267$
 Residual asymmetry: 0.772



NGC 6146

$\log(\text{Stellar Mass}): 11.629$
 $D = 125.1 \text{ (DR3) Mpc}$
 $M_r = -23.482 \text{ mag}$
 Redshift: 0.029
 $r_e: 15.048 \text{ arcsec}$
 AGN activity: No
 λ_R value at $r_e: 0.211$
 Residual asymmetry: 0.991

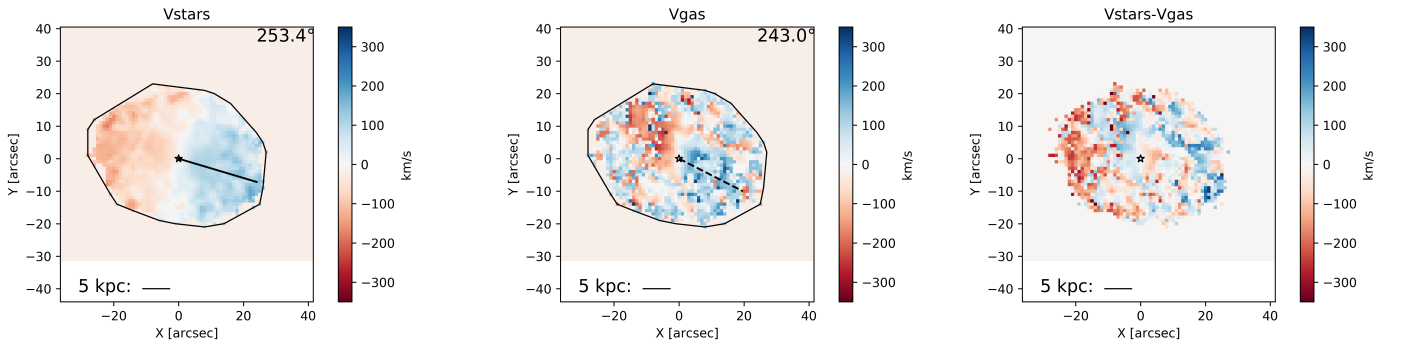
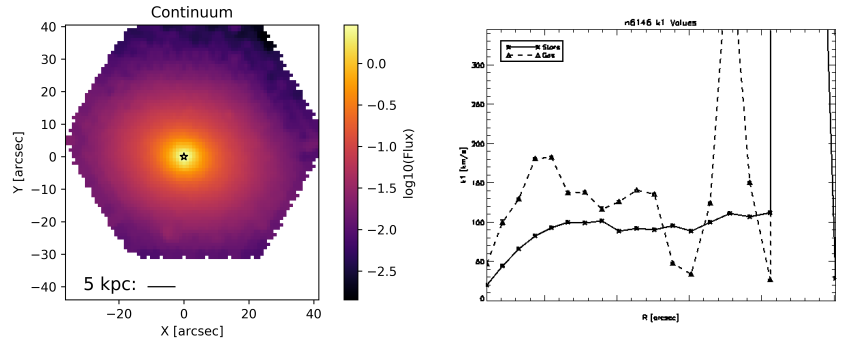
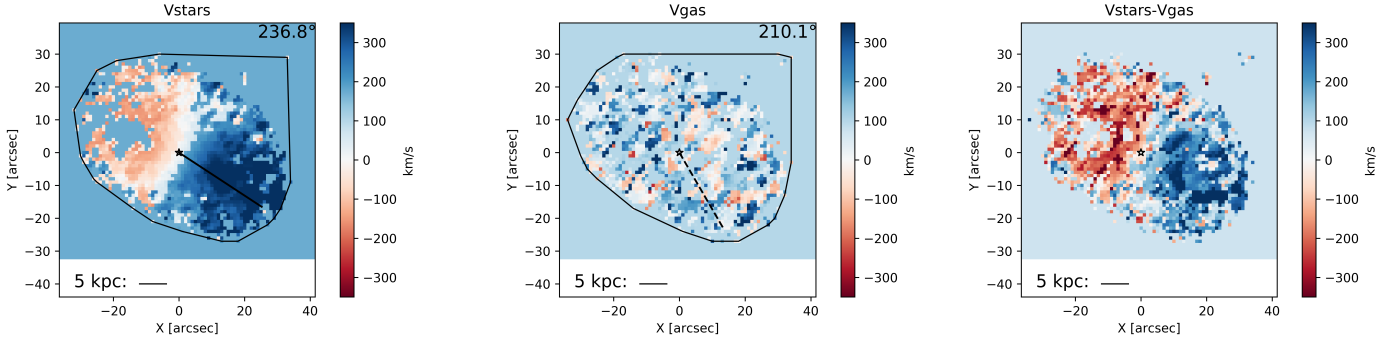
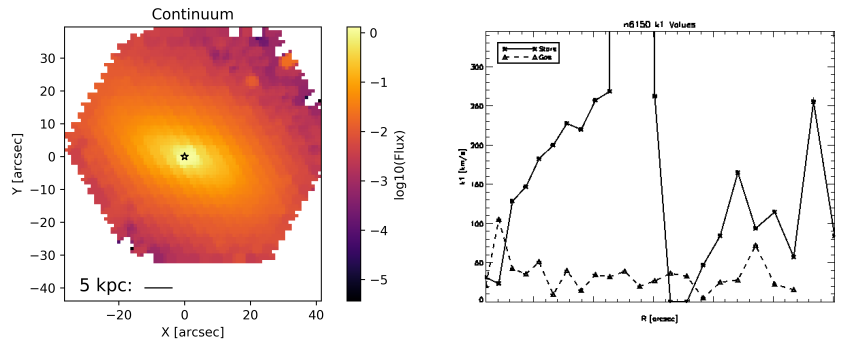


Figure 85 Top row, left to right: Name and characteristic parameters, continuum flux, and radial k_1 profiles for stars (solid) and gas (dashed), respectively. Bottom row, left to right: stellar kinematics, gas kinematics, and the difference between stellar and gas kinematics, respectively. The curves containing the data points are the convex hulls used to define the 'edge' of the map. The brightest continuum pixel (used as the center for kinemetry) is marked by a white star. The solid and dashed line in the stellar and gas velocity map, respectively, is the median position angle along which kinemetry coefficients were determined. The number value of this position angle is given at the top right of the plot. A scale bar is given along the bottom of each velocity map.

NGC 6150

$\log(\text{Stellar Mass}): 11.426$
 $D = 126.0 \text{ Mpc}$
 $M_r = -22.645 \text{ mag}$
 Redshift: 0.029
 $r_e: 11.88 \text{ arcsec}$
 AGN activity: No
 λ_R value at r_e : 0.535
 Residual asymmetry: 0.825



NGC 6173

$\log(\text{Stellar Mass}): 11.725$
 $D = 126.9 \text{ Mpc}$
 $M_r = -23.846 \text{ mag}$
 Redshift: 0.029
 $r_e: 38.016 \text{ arcsec}$
 AGN activity: No
 λ_R value at r_e : N/A
 Residual asymmetry: 0.809

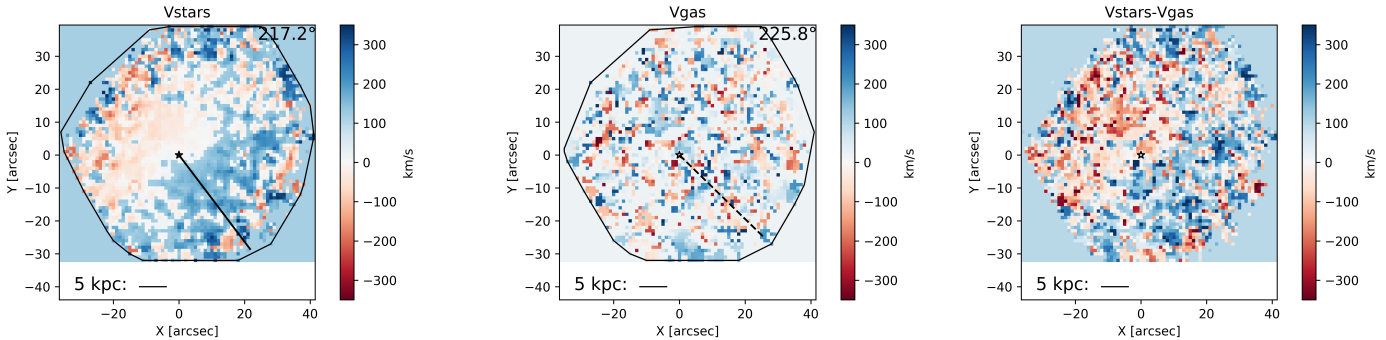
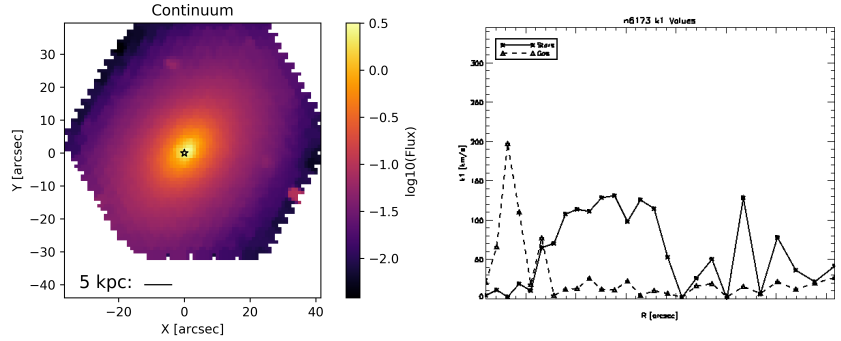
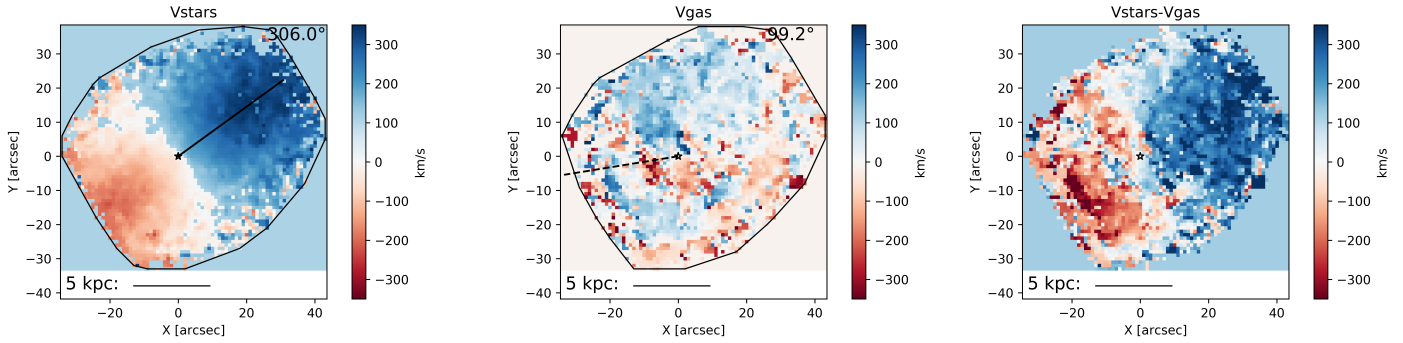
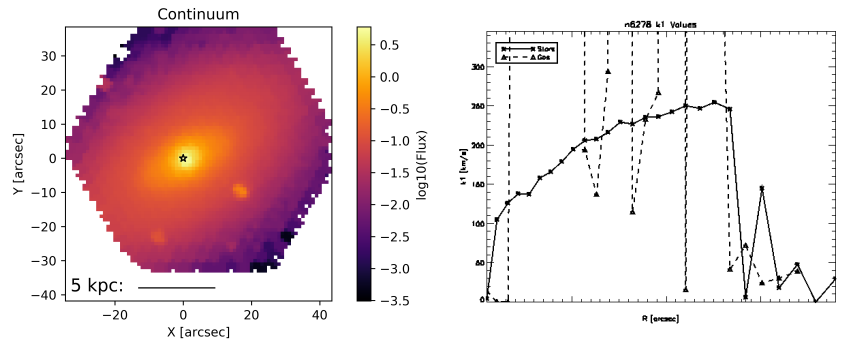


Figure 86 Top row, left to right: Name and characteristic parameters, continuum flux, and radial k_1 profiles for stars (solid) and gas (dashed), respectively. Bottom row, left to right: stellar kinematics, gas kinematics, and the difference between stellar and gas kinematics, respectively. The curves containing the data points are the convex hulls used to define the 'edge' of the map. The brightest continuum pixel (used as the center for kinemetry) is marked by a white star. The solid and dashed line in the stellar and gas velocity map, respectively, is the median position angle along which kinemetry coefficients were determined. The number value of this position angle is given at the top right of the plot. A scale bar is given along the bottom of each velocity map.

NGC 6278

$\log(\text{Stellar Mass}): 10.919$
 $D = 46.4 \text{ Mpc}$
 $M_r = -21.486 \text{ mag}$
 Redshift: 0.009
 $r_e: 11.088 \text{ arcsec}$
 AGN activity: No
 λ_R value at $r_e: 0.487$
 Residual asymmetry: 0.925



NGC 6338

$\log(\text{Stellar Mass}): 11.691$
 $D = 117.0 \text{ Mpc}$
 $M_r = -23.477 \text{ mag}$
 Redshift: 0.027
 $r_e: 28.116 \text{ arcsec}$
 AGN activity: No
 λ_R value at $r_e: 0.311$
 Residual asymmetry: 0.855

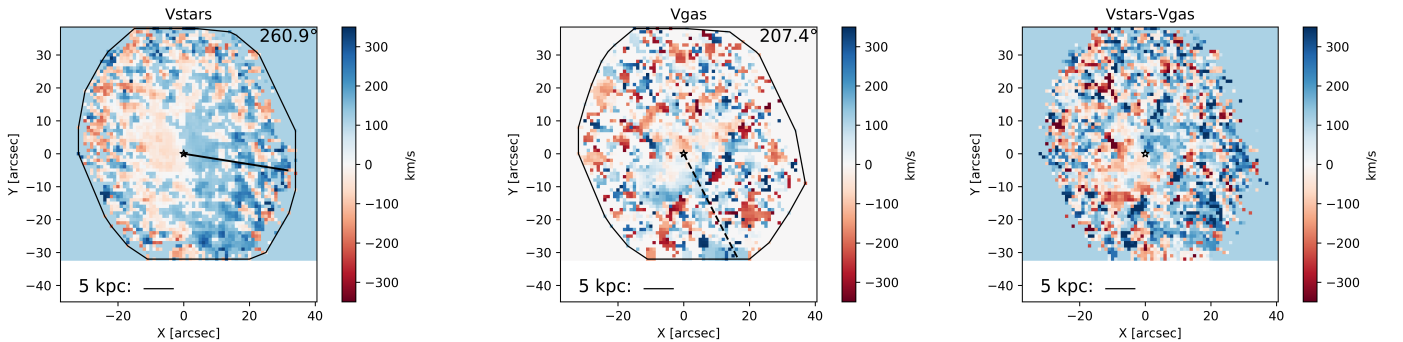
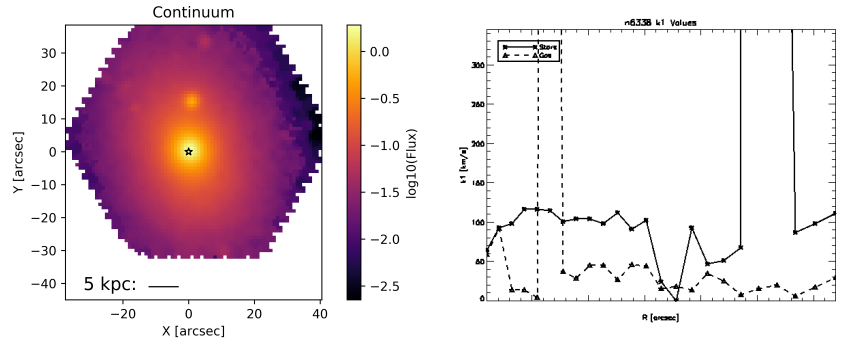
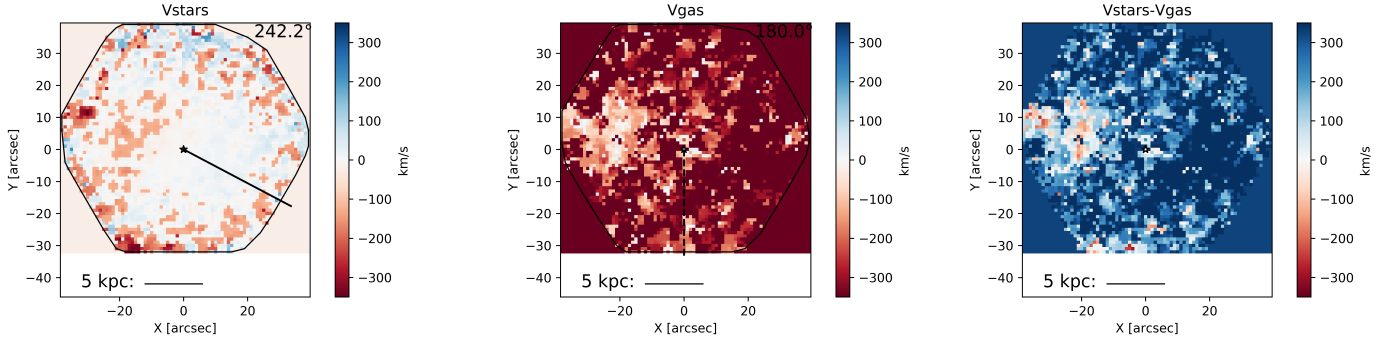
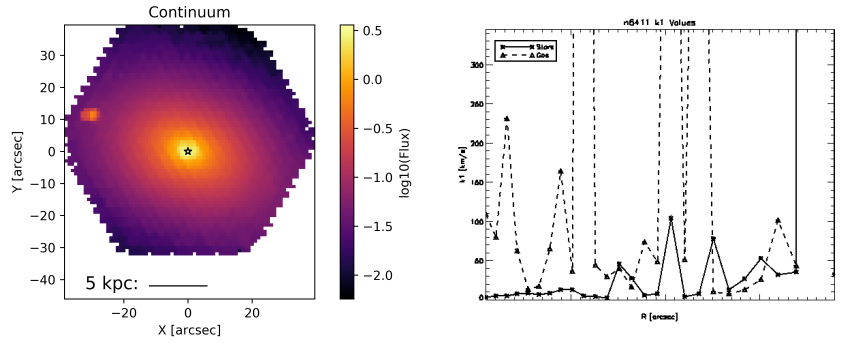


Figure 87 Top row, left to right: Name and characteristic parameters, continuum flux, and radial k_1 profiles for stars (solid) and gas (dashed), respectively. Bottom row, left to right: stellar kinematics, gas kinematics, and the difference between stellar and gas kinematics, respectively. The curves containing the data points are the convex hulls used to define the 'edge' of the map. The brightest continuum pixel (used as the center for kinemetry) is marked by a white star. The solid and dashed line in the stellar and gas velocity map, respectively, is the median position angle along which kinemetry coefficients were determined. The number value of this position angle is given at the top right of the plot. A scale bar is given along the bottom of each velocity map.

NGC 6411

$\log(\text{Stellar Mass}): 11.082$
 $D = 57.6 \text{ Mpc}$
 $M_r = -22.417 \text{ mag}$
 Redshift: 0.012
 $r_e = 34.056 \text{ arcsec}$
 AGN activity: No
 λ_R value at r_e : 0.223
 Residual asymmetry: 0.774



NGC 6427

$\log(\text{Stellar Mass}): 10.751$
 $D = 51.3 \text{ Mpc}$
 $M_r = -21.370 \text{ mag}$
 Redshift: 0.011
 $r_e = 8.316 \text{ arcsec}$
 AGN activity: No
 λ_R value at r_e : 0.466
 Residual asymmetry: 0.818

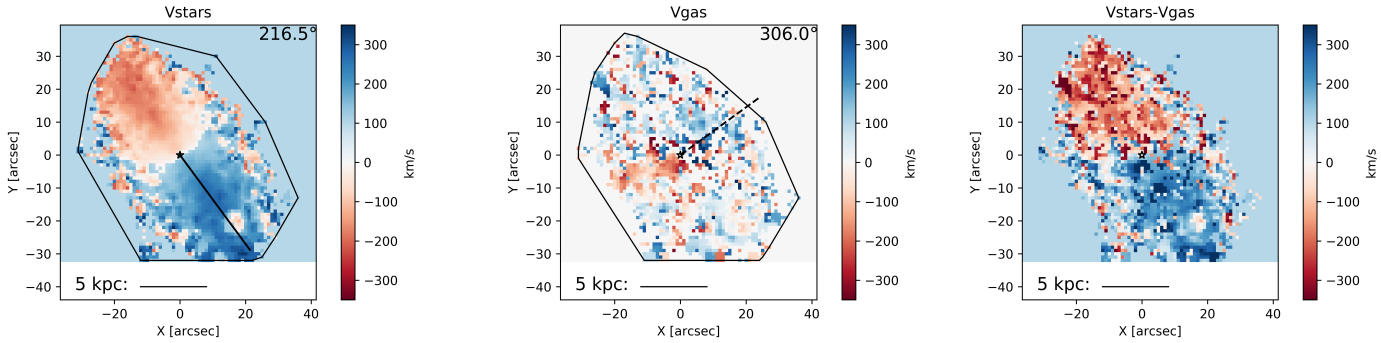
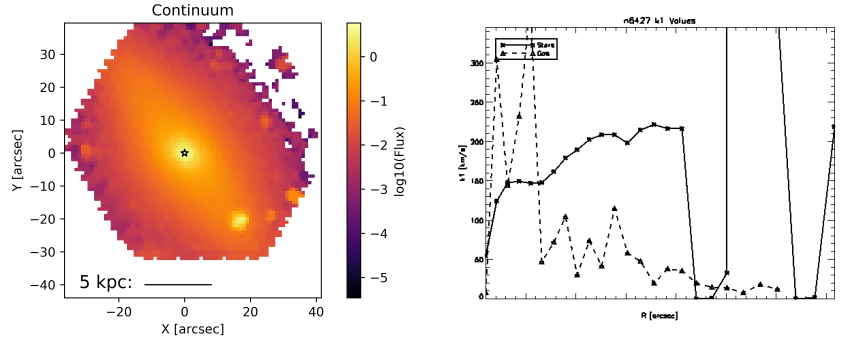
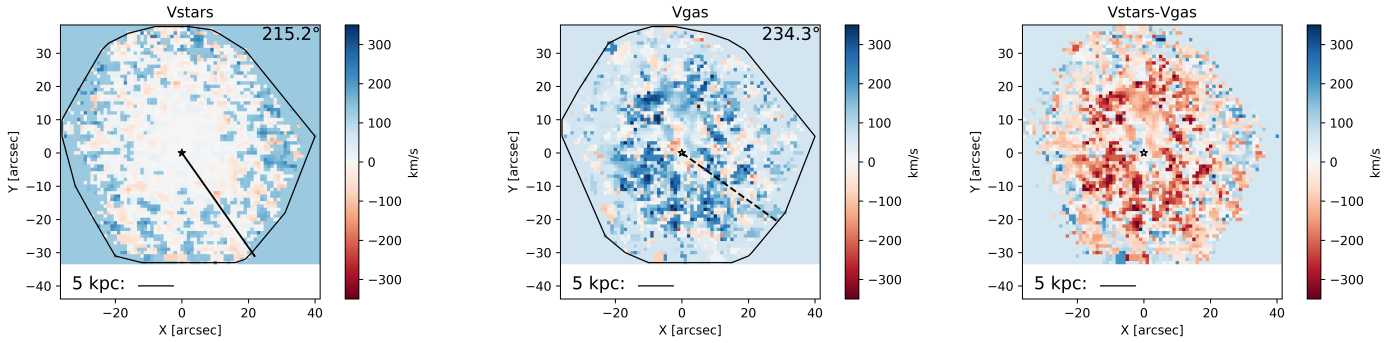
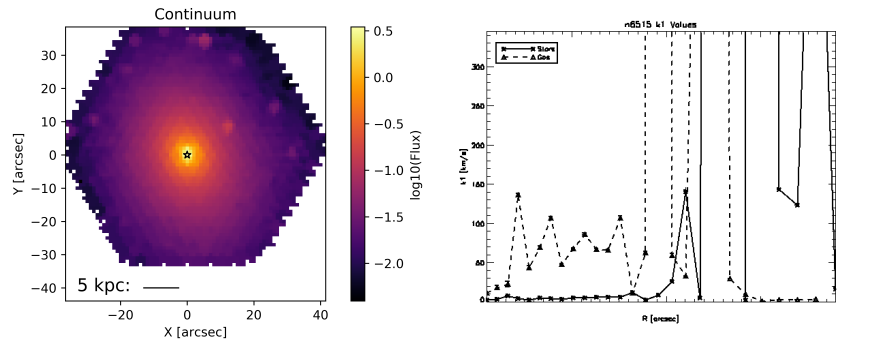


Figure 88 Top row, left to right: Name and characteristic parameters, continuum flux, and radial k_1 profiles for stars (solid) and gas (dashed), respectively. Bottom row, left to right: stellar kinematics, gas kinematics, and the difference between stellar and gas kinematics, respectively. The curves containing the data points are the convex hulls used to define the 'edge' of the map. The brightest continuum pixel (used as the center for kinemetry) is marked by a white star. The solid and dashed line in the stellar and gas velocity map, respectively, is the median position angle along which kinemetry coefficients were determined. The number value of this position angle is given at the top right of the plot. A scale bar is given along the bottom of each velocity map.

NGC 6515

$\log(\text{Stellar Mass}): 11.193$
 $D = 99.0 \text{ Mpc}$
 $M_r = -22.725 \text{ mag}$
 Redshift: 0.023
 $r_e: 19.008 \text{ arcsec}$
 AGN activity: No
 λ_R value at $r_e: 0.478$
 Residual asymmetry: 0.965



NGC 6762

$\log(\text{Stellar Mass}): 10.383$
 $D = 41.8 \text{ (DR3) Mpc}$
 $M_r = -20.464 \text{ mag}$
 Redshift: 0.010
 $r_e: 9.504 \text{ arcsec}$
 AGN activity: No
 λ_R value at $r_e: 0.376$
 Residual asymmetry: 0.992

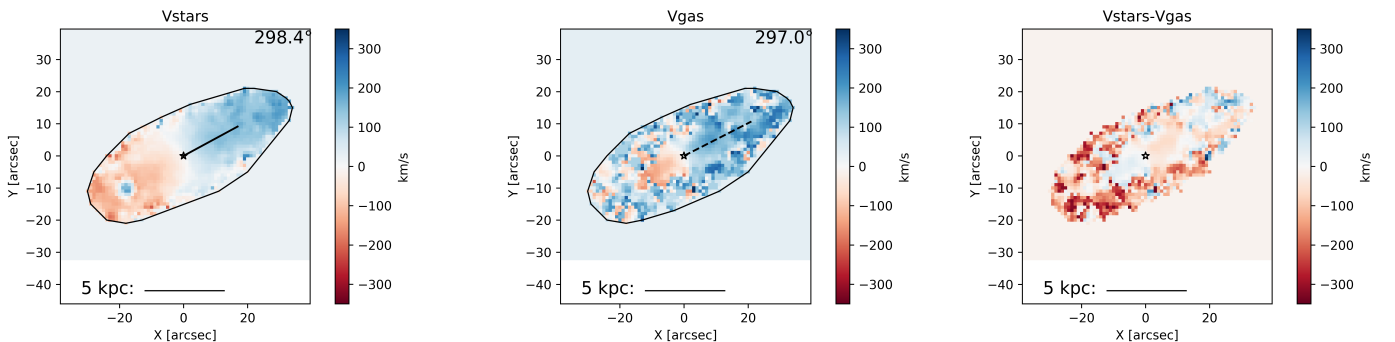
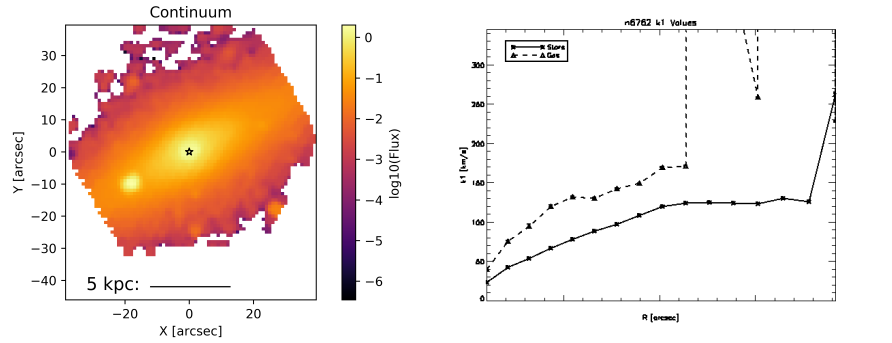
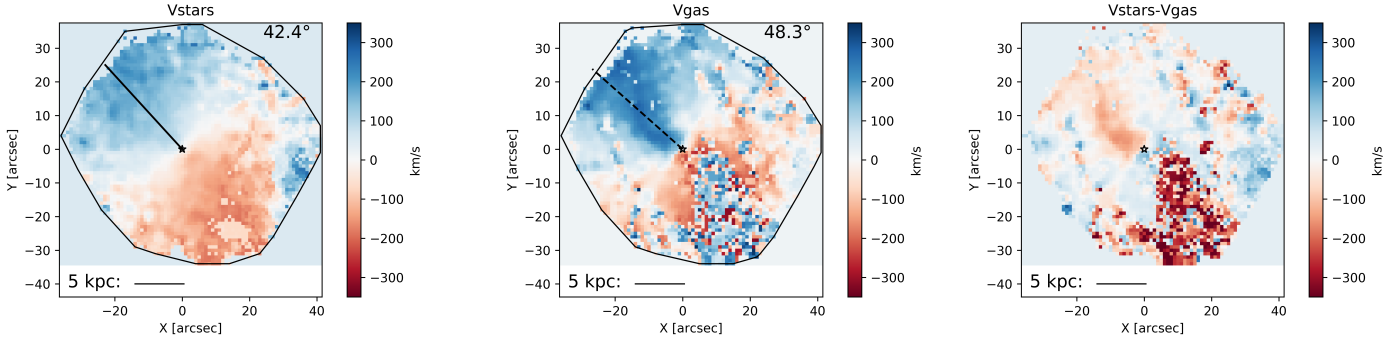
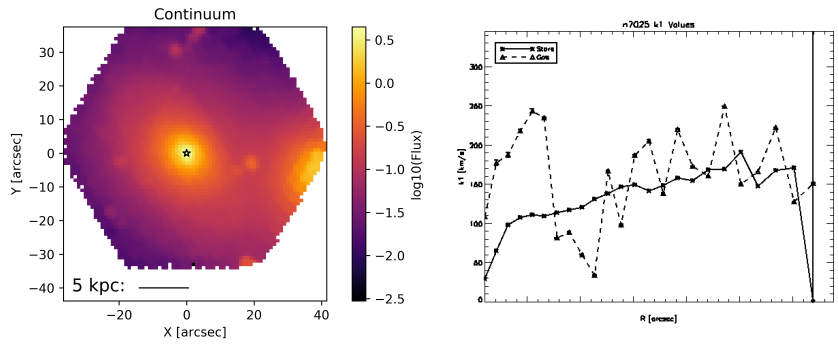


Figure 89 Top row, left to right: Name and characteristic parameters, continuum flux, and radial k_1 profiles for stars (solid) and gas (dashed), respectively. Bottom row, left to right: stellar kinematics, gas kinematics, and the difference between stellar and gas kinematics, respectively. The curves containing the data points are the convex hulls used to define the 'edge' of the map. The brightest continuum pixel (used as the center for kinemetry) is marked by a white star. The solid and dashed line in the stellar and gas velocity map, respectively, is the median position angle along which kinemetry coefficients were determined. The number value of this position angle is given at the top right of the plot. A scale bar is given along the bottom of each velocity map.

NGC 7025

$\log(\text{Stellar Mass}): 11.527$
 $D = 71.0$ (DR3) Mpc
 $M_r = -22.734$ mag
 Redshift: 0.017
 $r_e = 13.464$ arcsec
 AGN activity: No
 λ_R value at r_e : 0.314
 Residual asymmetry: 0.735



NGC 7194

$\log(\text{Stellar Mass}): 11.445$
 $D = 110.7$ Mpc
 $M_r = -23.049$ mag
 Redshift: 0.027
 $r_e = 17.82$ arcsec
 AGN activity: No
 λ_R value at r_e : 0.509
 Residual asymmetry: 0.800

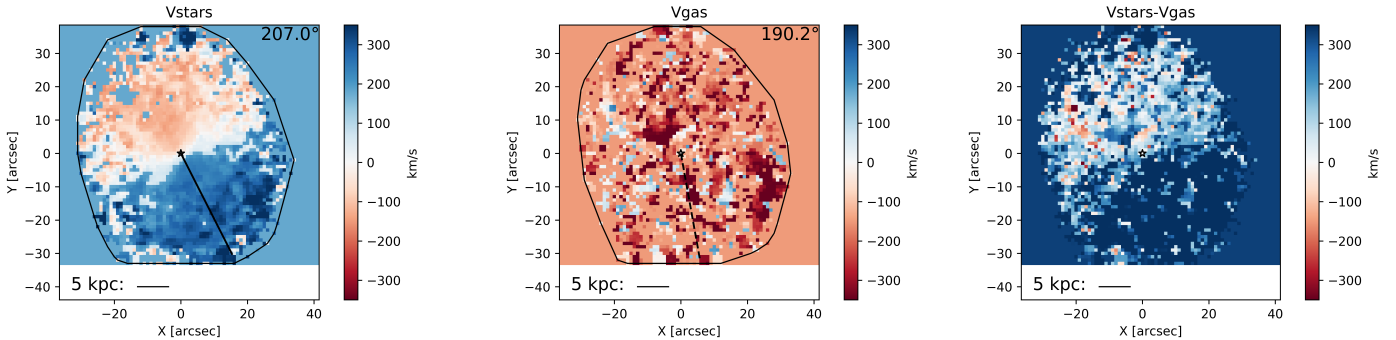
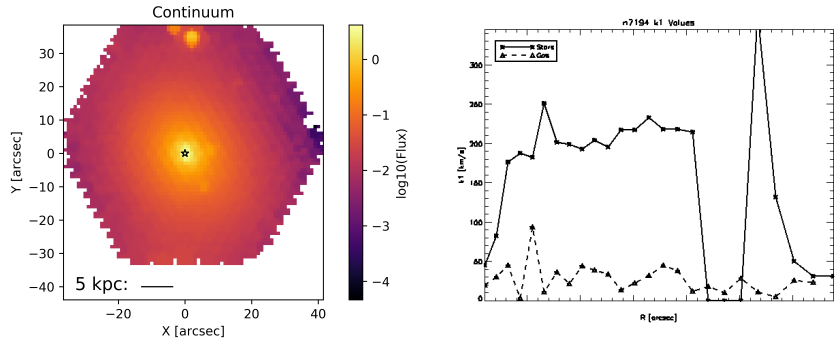
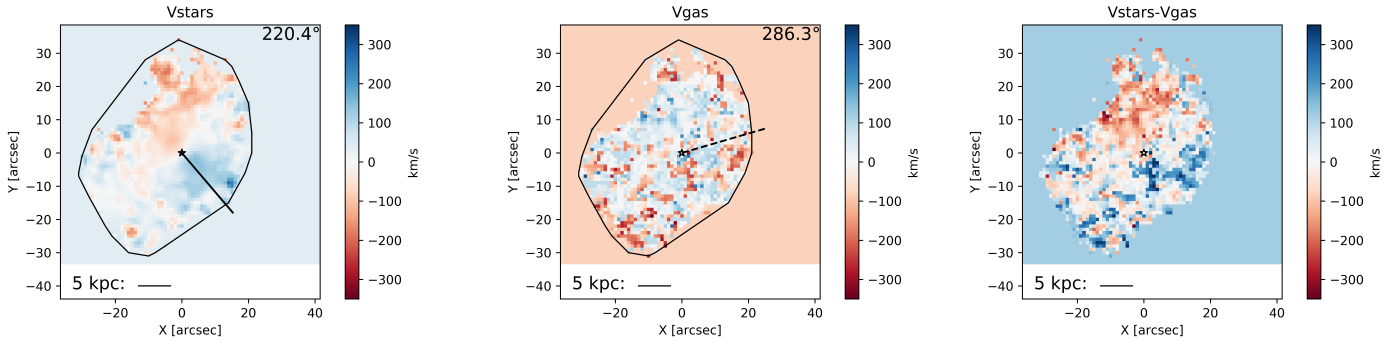
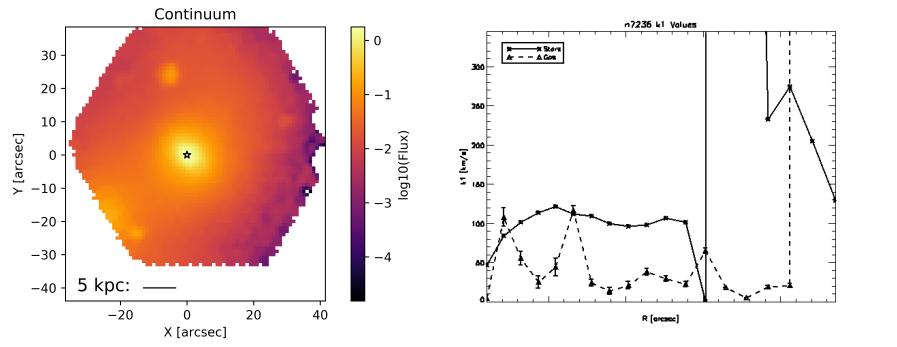


Figure 90 Top row, left to right: Name and characteristic parameters, continuum flux, and radial k1 profiles for stars (solid) and gas (dashed), respectively. Bottom row, left to right: stellar kinematics, gas kinematics, and the difference between stellar and gas kinematics, respectively. The curves containing the data points are the convex hulls used to define the 'edge' of the map. The brightest continuum pixel (used as the center for kinemetry) is marked by a white star. The solid and dashed line in the stellar and gas velocity map, respectively, is the median position angle along which kinemetry coefficients were determined. The number value of this position angle is given at the top right of the plot. A scale bar is given along the bottom of each velocity map.

NGC 7236

$\log(\text{Stellar Mass}): 11.347$
 $D = 107.6$ (2MASS) Mpc
 $M_r = -22.745$ mag
 Redshift: 0.026
 $r_e: 14.652$ arcsec
 AGN activity: No
 λ_R value at $r_e: 0.259$
 Residual asymmetry: 0.997



NGC 7436b

$\log(\text{Stellar Mass}): 11.914$
 $D = 105.4$ (DR3) Mpc
 $M_r = -23.495$ mag
 Redshift: 0.025
 $r_e: 27.72$ arcsec
 AGN activity: No
 λ_R value at $r_e: 0.193$
 Residual asymmetry: 0.966

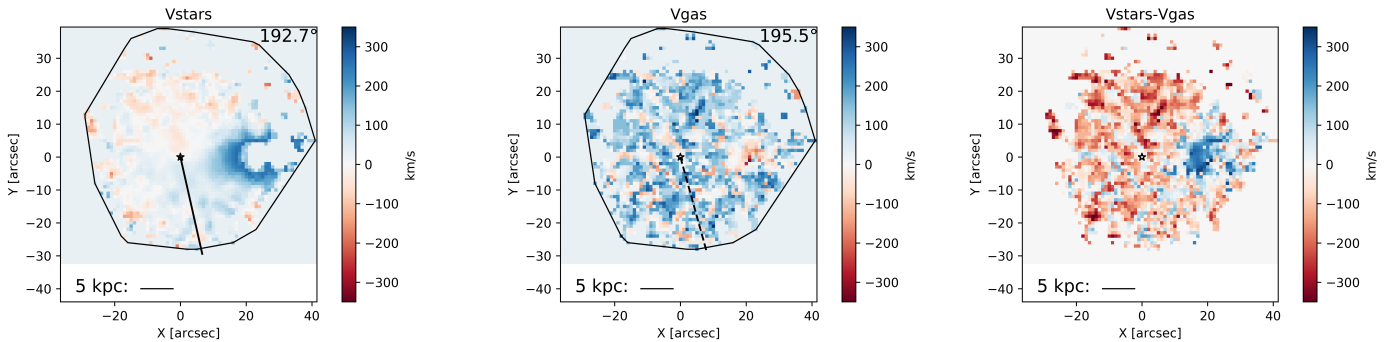
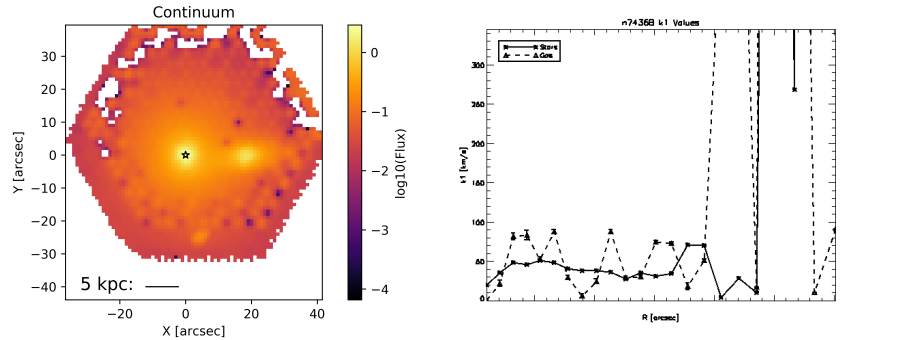
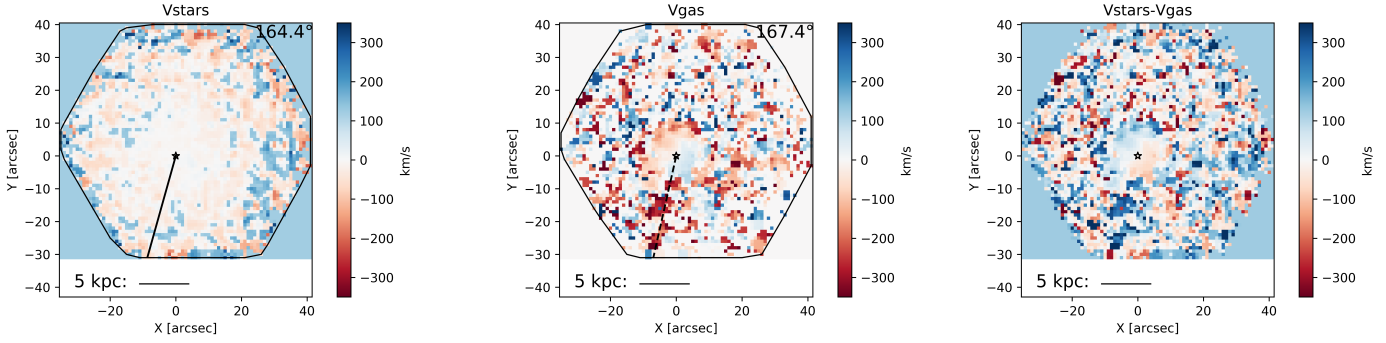
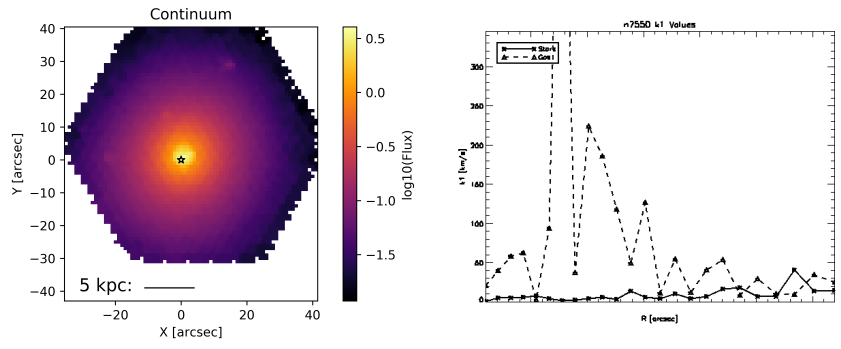


Figure 91 Top row, left to right: Name and characteristic parameters, continuum flux, and radial k_1 profiles for stars (solid) and gas (dashed), respectively. Bottom row, left to right: stellar kinematics, gas kinematics, and the difference between stellar and gas kinematics, respectively. The curves containing the data points are the convex hulls used to define the 'edge' of the map. The brightest continuum pixel (used as the center for kinemetry) is marked by a white star. The solid and dashed line in the stellar and gas velocity map, respectively, is the median position angle along which kinemetry coefficients were determined. The number value of this position angle is given at the top right of the plot. A scale bar is given along the bottom of each velocity map.

NGC 7550

$\log(\text{Stellar Mass}): 11.432$
 $D = 69.2 \text{ Mpc}$
 $M_r = -22.890 \text{ mag}$
 Redshift: 0.017
 $r_e = 24.552 \text{ arcsec}$
 AGN activity: No
 λ_R value at r_e : 0.468
 Residual asymmetry: 0.831



NGC 7559b

$\log(\text{Stellar Mass}): 10.842$
 $D = 62.8 \text{ Mpc}$
 $M_r = -21.145 \text{ mag}$
 Redshift: 0.015
 $r_e = 9.957 \text{ arcsec}$
 AGN activity: No
 λ_R value at r_e : 0.666
 Residual asymmetry: 0.775

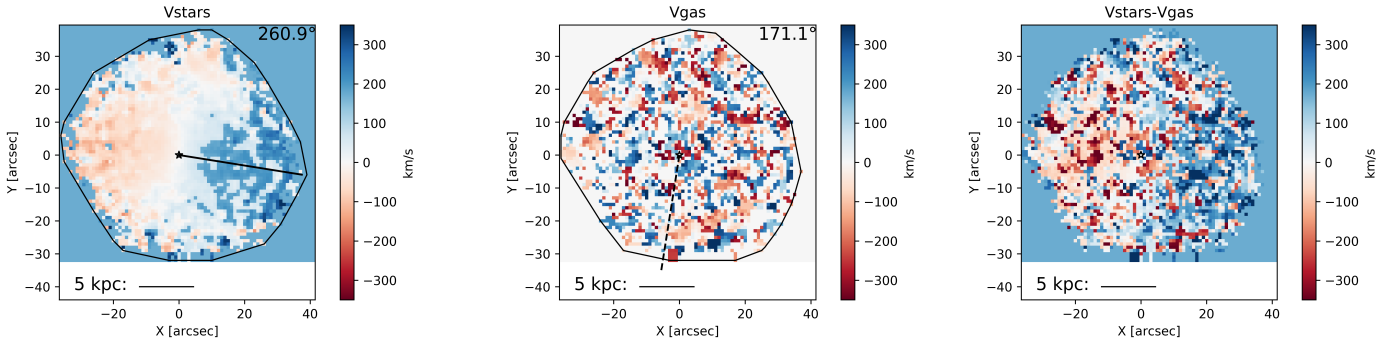
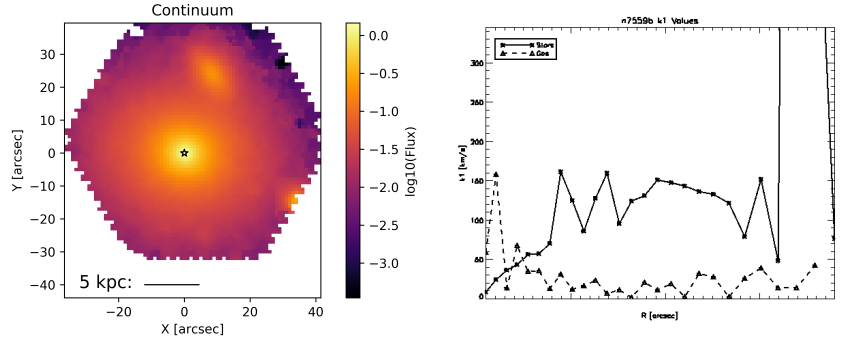
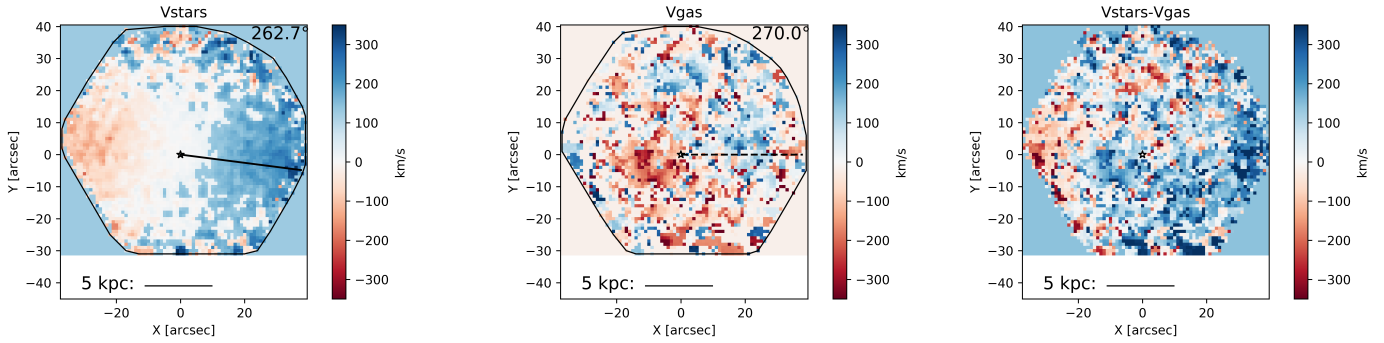
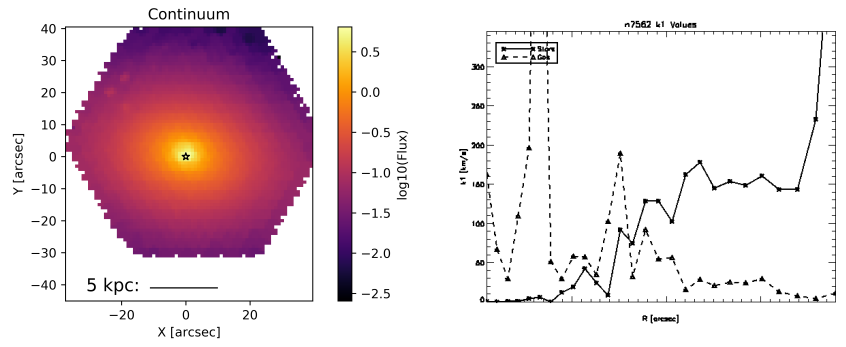


Figure 92 Top row, left to right: Name and characteristic parameters, continuum flux, and radial k_1 profiles for stars (solid) and gas (dashed), respectively. Bottom row, left to right: stellar kinematics, gas kinematics, and the difference between stellar and gas kinematics, respectively. The curves containing the data points are the convex hulls used to define the 'edge' of the map. The brightest continuum pixel (used as the center for kinemetry) is marked by a white star. The solid and dashed line in the stellar and gas velocity map, respectively, is the median position angle along which kinemetry coefficients were determined. The number value of this position angle is given at the top right of the plot. A scale bar is given along the bottom of each velocity map.

NGC 7562

$\log(\text{Stellar Mass}): 11.247$
 $D = 49.6 \text{ Mpc}$
 $M_r = -22.542 \text{ mag}$
 Redshift: 0.012
 $r_e: 20.988 \text{ arcsec}$
 AGN activity: No
 λ_R value at $r_e: 0.383$
 Residual asymmetry: 0.826



NGC 7611

$\log(\text{Stellar Mass}): 10.899$
 $D = 44.9 \text{ Mpc}$
 $M_r = -21.324 \text{ mag}$
 Redshift: 0.011
 $r_e: 11.088 \text{ arcsec}$
 AGN activity: No
 λ_R value at $r_e: 0.633$
 Residual asymmetry: 0.828

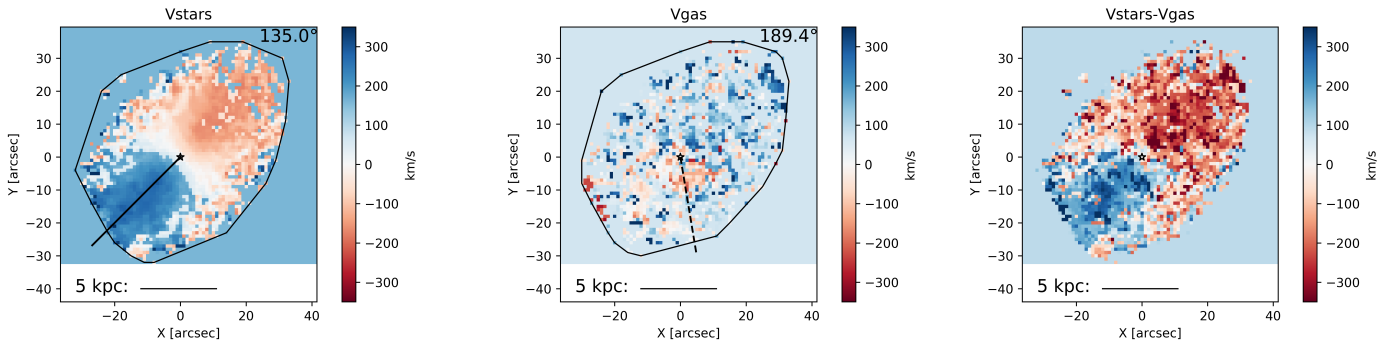
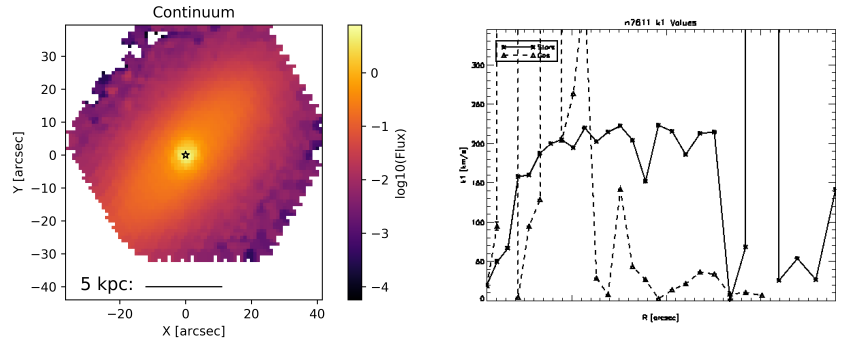
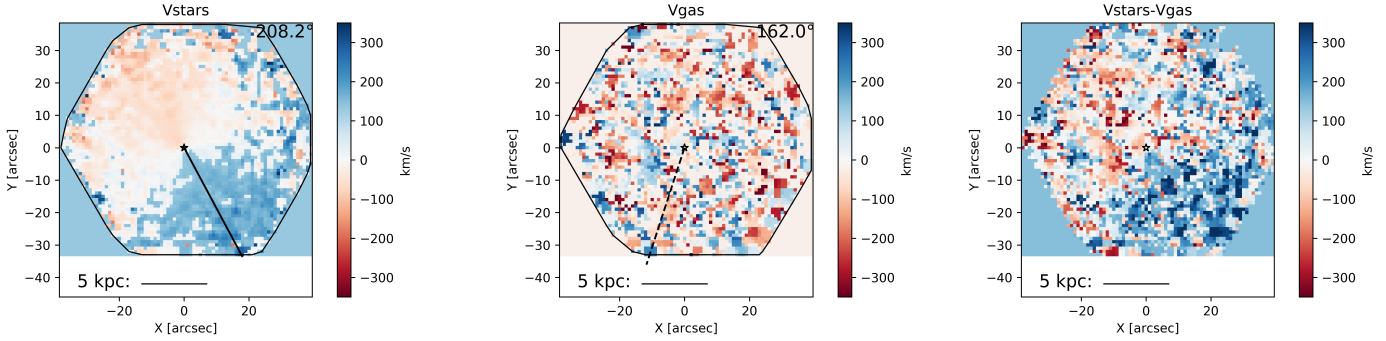
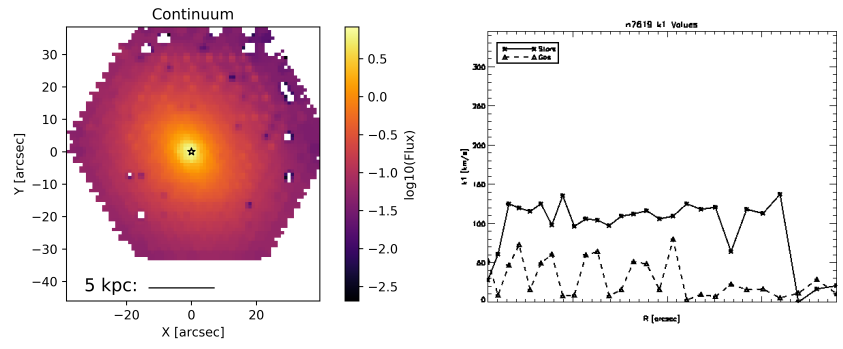


Figure 93 Top row, left to right: Name and characteristic parameters, continuum flux, and radial k_1 profiles for stars (solid) and gas (dashed), respectively. Bottom row, left to right: stellar kinematics, gas kinematics, and the difference between stellar and gas kinematics, respectively. The curves containing the data points are the convex hulls used to define the 'edge' of the map. The brightest continuum pixel (used as the center for kinemetry) is marked by a white star. The solid and dashed line in the stellar and gas velocity map, respectively, is the median position angle along which kinemetry coefficients were determined. The number value of this position angle is given at the top right of the plot. A scale bar is given along the bottom of each velocity map.

NGC 7619

$\log(\text{Stellar Mass}): 10.944$
 $D = 51.6 \text{ Mpc}$
 $M_r = -22.694 \text{ mag}$
 Redshift: 0.013
 $r_e = 35.64 \text{ arcsec}$
 AGN activity: No
 λ_R value at r_e : 0.389
 Residual asymmetry: 0.772



NGC 7671

$\log(\text{Stellar Mass}): 10.956$
 $D = 56.4 \text{ Mpc}$
 $M_r = -21.764 \text{ mag}$
 Redshift: 0.014
 $r_e = 11.088 \text{ arcsec}$
 AGN activity: No
 λ_R value at r_e : 0.356
 Residual asymmetry: 0.722

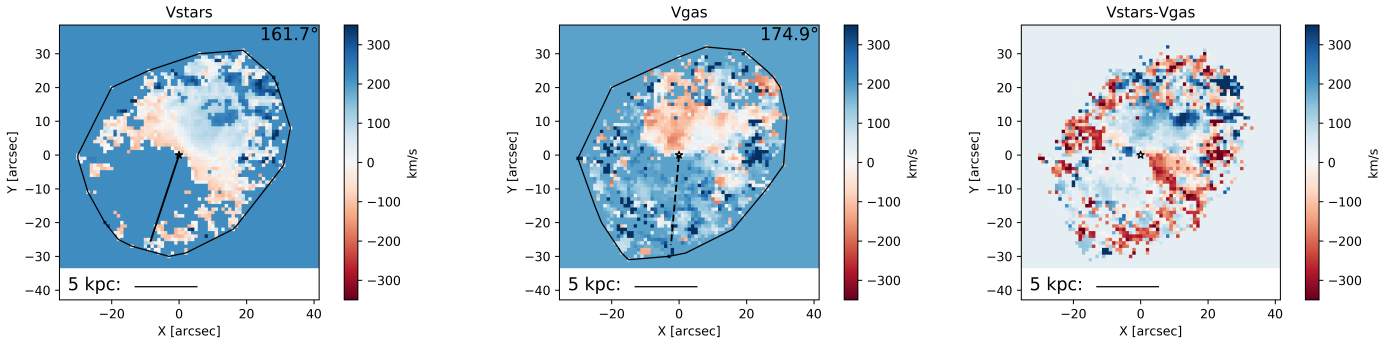
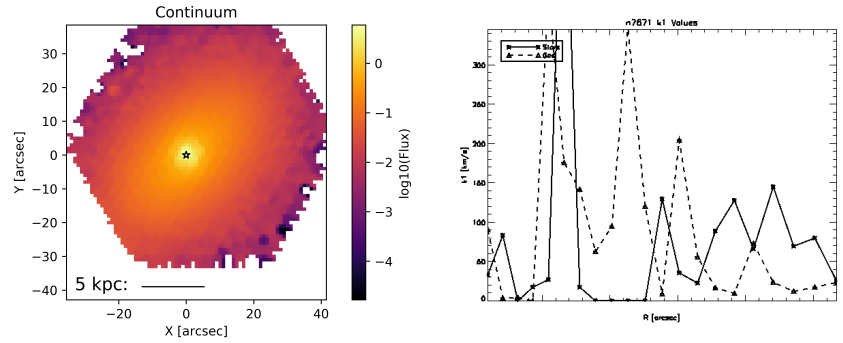
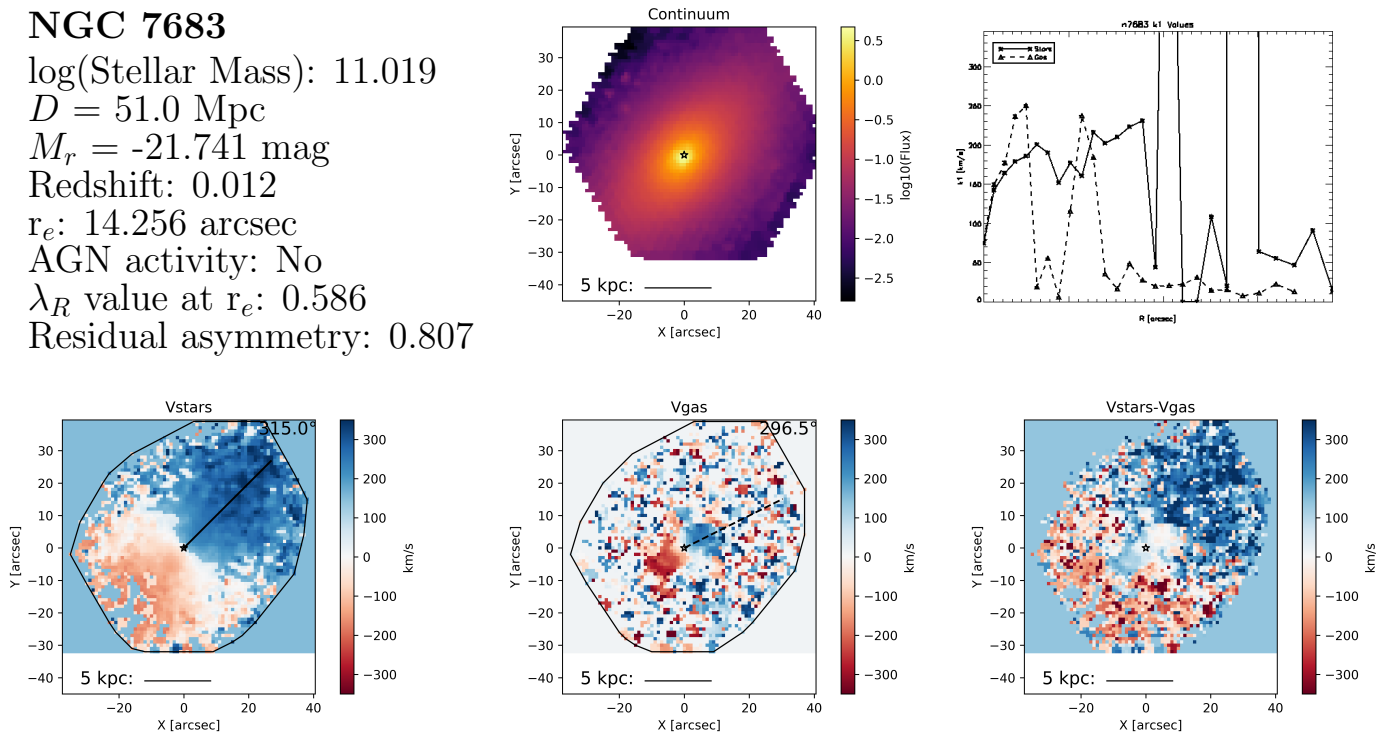


Figure 94 Top row, left to right: Name and characteristic parameters, continuum flux, and radial k1 profiles for stars (solid) and gas (dashed), respectively. Bottom row, left to right: stellar kinematics, gas kinematics, and the difference between stellar and gas kinematics, respectively. The curves containing the data points are the convex hulls used to define the 'edge' of the map. The brightest continuum pixel (used as the center for kinemetry) is marked by a white star. The solid and dashed line in the stellar and gas velocity map, respectively, is the median position angle along which kinemetry coefficients were determined. The number value of this position angle is given at the top right of the plot. A scale bar is given along the bottom of each velocity map.

NGC 7683

$\log(\text{Stellar Mass}): 11.019$
 $D = 51.0 \text{ Mpc}$
 $M_r = -21.741 \text{ mag}$
 Redshift: 0.012
 $r_e: 14.256 \text{ arcsec}$
 AGN activity: No
 λ_R value at $r_e: 0.586$
 Residual asymmetry: 0.807



NGC 7711

$\log(\text{Stellar Mass}): 11.053$
 $D = 55.3 \text{ Mpc}$
 $M_r = -22.019 \text{ mag}$
 Redshift: 0.014
 $r_e: 15.048 \text{ arcsec}$
 AGN activity: No
 λ_R value at $r_e: 0.472$
 Residual asymmetry: 0.904

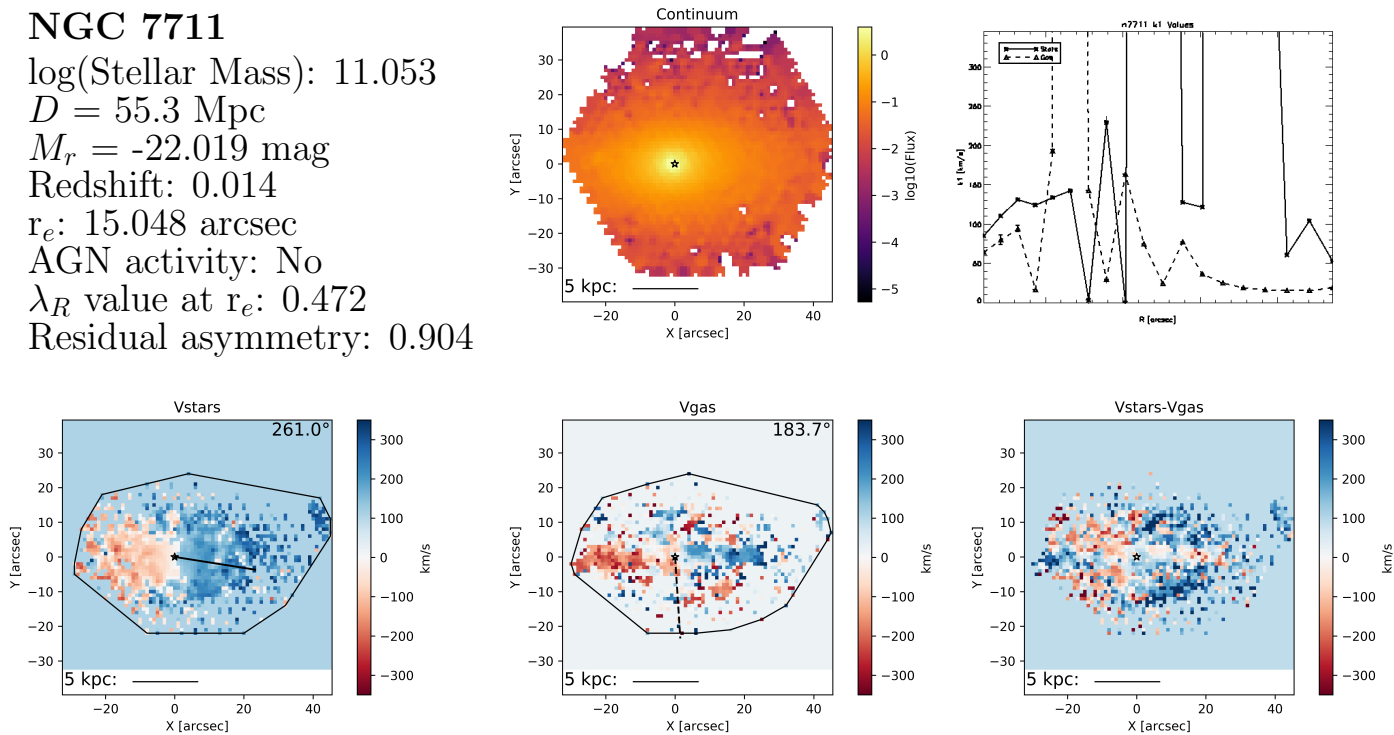
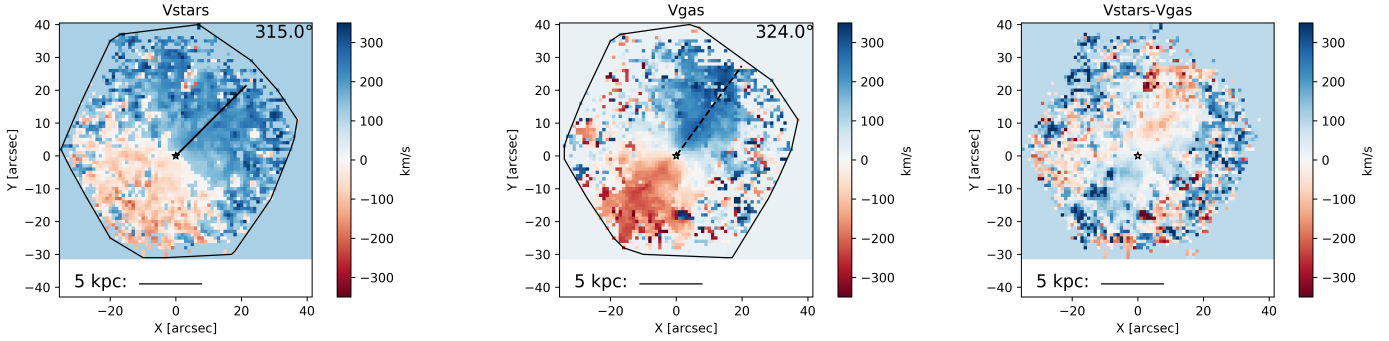
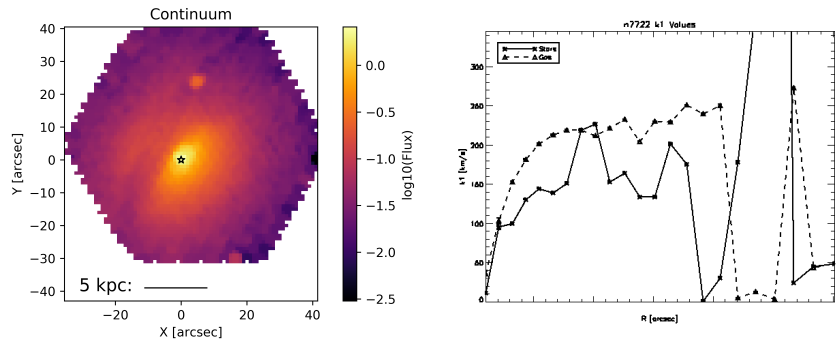


Figure 95 Top row, left to right: Name and characteristic parameters, continuum flux, and radial k_1 profiles for stars (solid) and gas (dashed), respectively. Bottom row, left to right: stellar kinematics, gas kinematics, and the difference between stellar and gas kinematics, respectively. The curves containing the data points are the convex hulls used to define the 'edge' of the map. The brightest continuum pixel (used as the center for kinemetry) is marked by a white star. The solid and dashed line in the stellar and gas velocity map, respectively, is the median position angle along which kinemetry coefficients were determined. The number value of this position angle is given at the top right of the plot. A scale bar is given along the bottom of each velocity map.

NGC 7722

$\log(\text{Stellar Mass}): 11.245$
 $D = 54.9 \text{ Mpc}$
 $M_r = -22.053 \text{ mag}$
 Redshift: 0.013
 $r_e = 21.384 \text{ arcsec}$
 AGN activity: No
 λ_R value at r_e : 0.499
 Residual asymmetry: 0.806



UGC 0029

$\log(\text{Stellar Mass}): 11.036$
 $D = 118.5 \text{ Mpc}$
 $M_r = -22.661 \text{ mag}$
 Redshift: 0.029
 $r_e = 17.028 \text{ arcsec}$
 AGN activity: No
 λ_R value at r_e : 0.294
 Residual asymmetry: 0.825

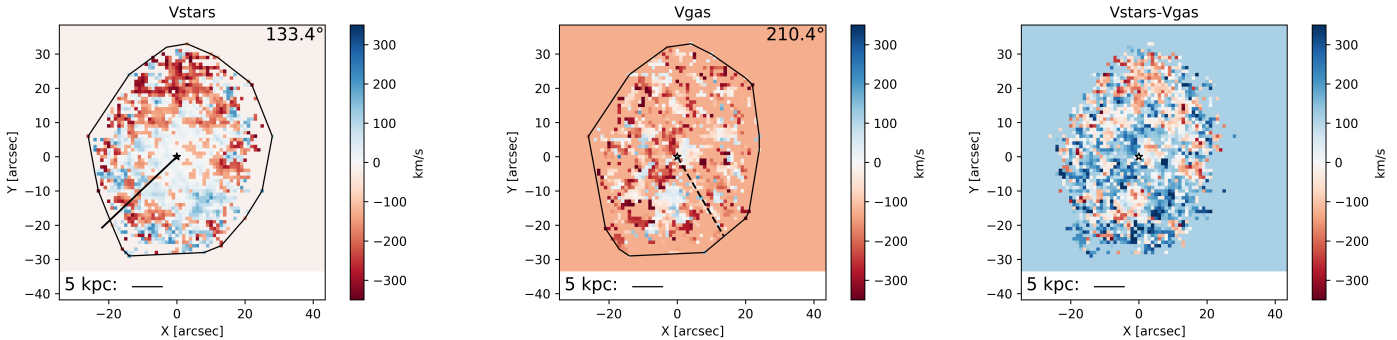
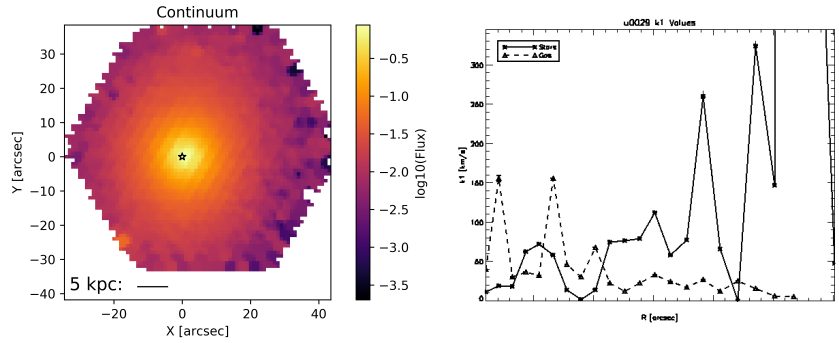
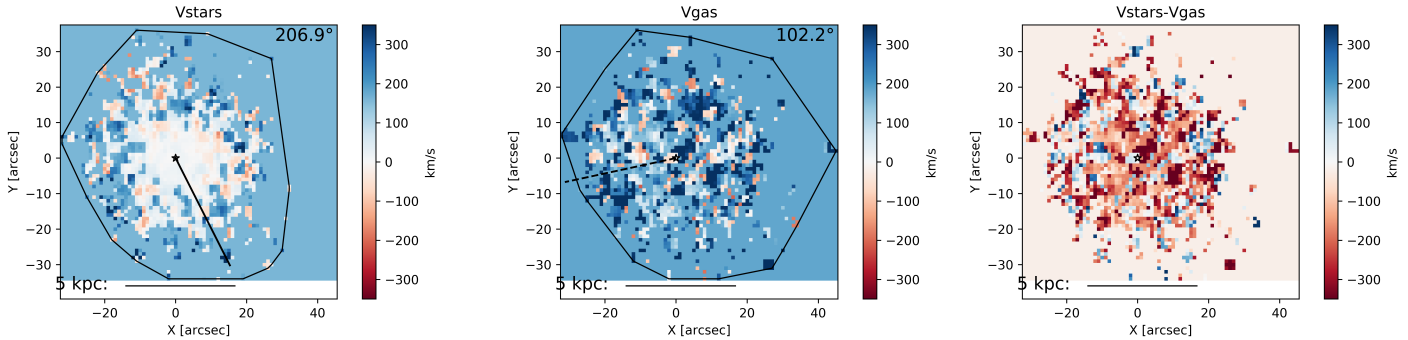
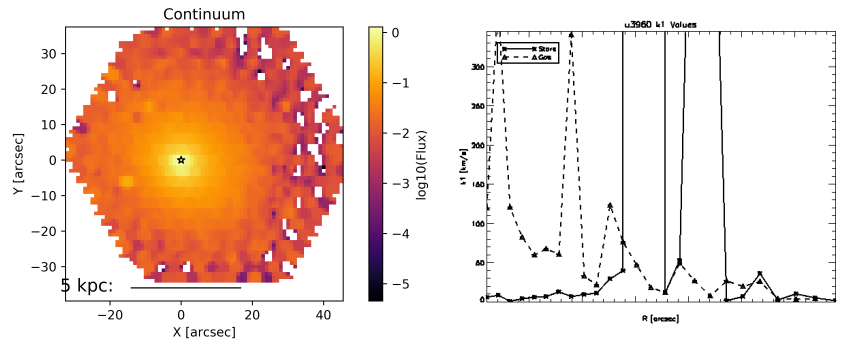


Figure 96 Top row, left to right: Name and characteristic parameters, continuum flux, and radial k_1 profiles for stars (solid) and gas (dashed), respectively. Bottom row, left to right: stellar kinematics, gas kinematics, and the difference between stellar and gas kinematics, respectively. The curves containing the data points are the convex hulls used to define the 'edge' of the map. The brightest continuum pixel (used as the center for kinemetry) is marked by a white star. The solid and dashed line in the stellar and gas velocity map, respectively, is the median position angle along which kinemetry coefficients were determined. The number value of this position angle is given at the top right of the plot. A scale bar is given along the bottom of each velocity map.

UGC 3960

$\log(\text{Stellar Mass}): 9.849$
 $D = 33.6 \text{ Mpc}$
 $M_r = -19.096 \text{ mag}$
 Redshift: 0.008
 $r_e: 8.879 \text{ arcsec}$
 AGN activity: No
 λ_R value at $r_e: 0.638$
 Residual asymmetry: 0.825



UGC 5771

$\log(\text{Stellar Mass}): 11.317$
 $D = 106.6 \text{ (DR3) Mpc}$
 $M_r = -22.351 \text{ mag}$
 Redshift: 0.025
 $r_e: 12.672 \text{ arcsec}$
 AGN activity: No
 λ_R value at $r_e: 0.355$
 Residual asymmetry: 0.852

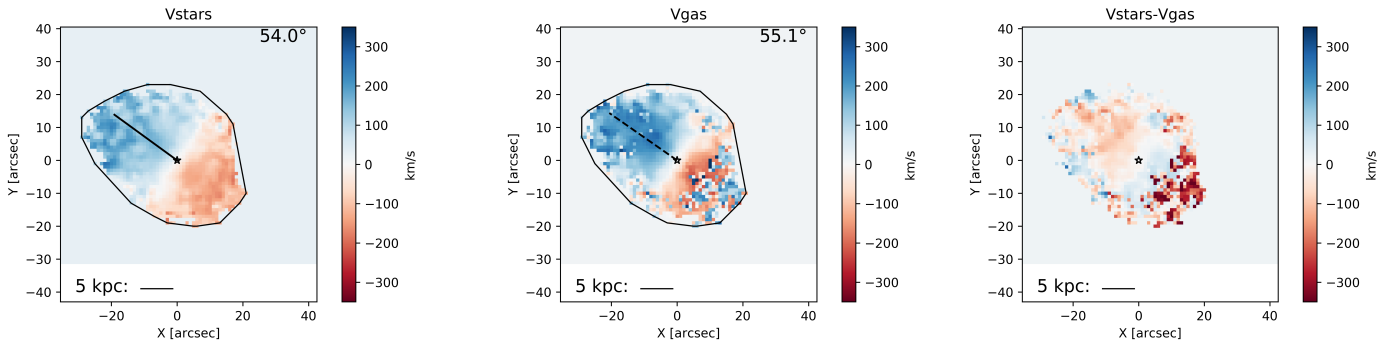
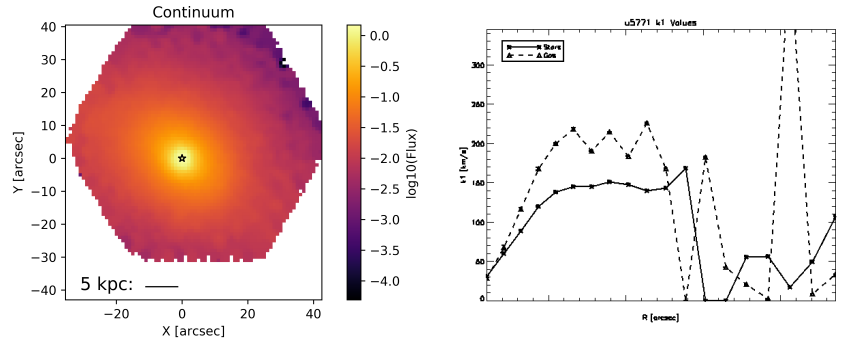
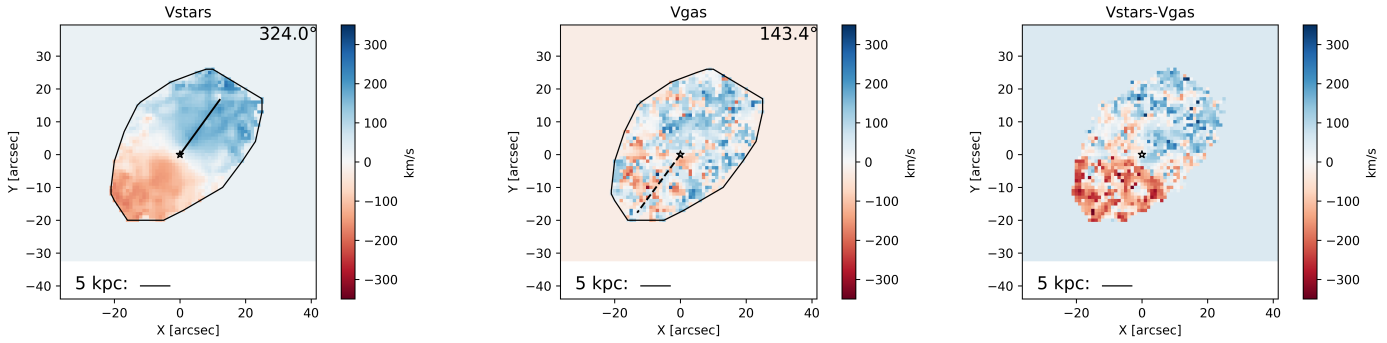
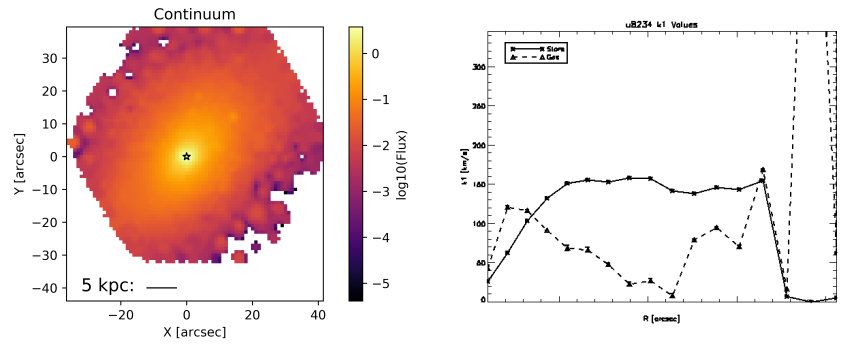


Figure 97 Top row, left to right: Name and characteristic parameters, continuum flux, and radial k_1 profiles for stars (solid) and gas (dashed), respectively. Bottom row, left to right: stellar kinematics, gas kinematics, and the difference between stellar and gas kinematics, respectively. The curves containing the data points are the convex hulls used to define the 'edge' of the map. The brightest continuum pixel (used as the center for kinemetry) is marked by a white star. The solid and dashed line in the stellar and gas velocity map, respectively, is the median position angle along which kinemetry coefficients were determined. The number value of this position angle is given at the top right of the plot. A scale bar is given along the bottom of each velocity map.

UGC 8234

$\log(\text{Stellar Mass}): 11.135$
 $D = 115.8$ (DR3) Mpc
 $M_r = -22.763$ mag
 Redshift: 0.027
 $r_e: 8.316$ arcsec
 AGN activity: No
 λ_R value at $r_e: 0.353$
 Residual asymmetry: 0.957



UGC 9518

$\log(\text{Stellar Mass}): 11.524$
 $D = 127.2$ Mpc
 $M_r = -22.947$ mag
 Redshift: 0.029
 $r_e: 11.484$ arcsec
 AGN activity: No
 λ_R value at $r_e: 0.438$
 Residual asymmetry: 0.817

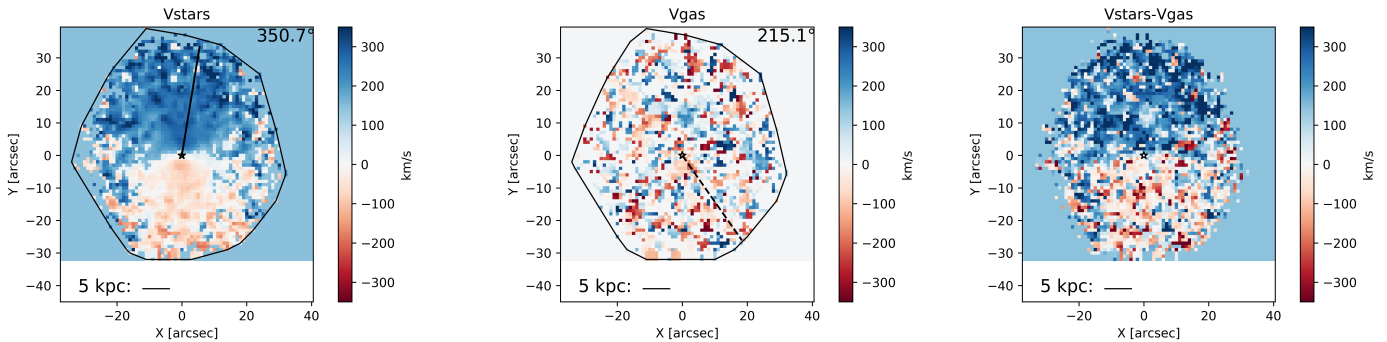
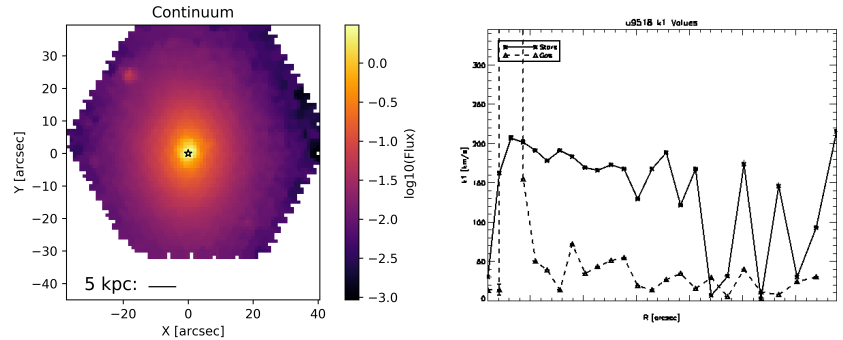
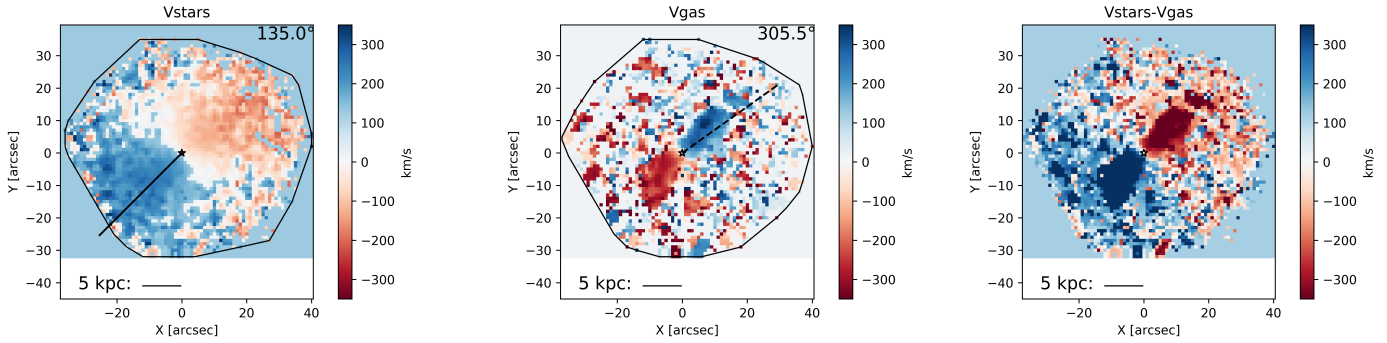
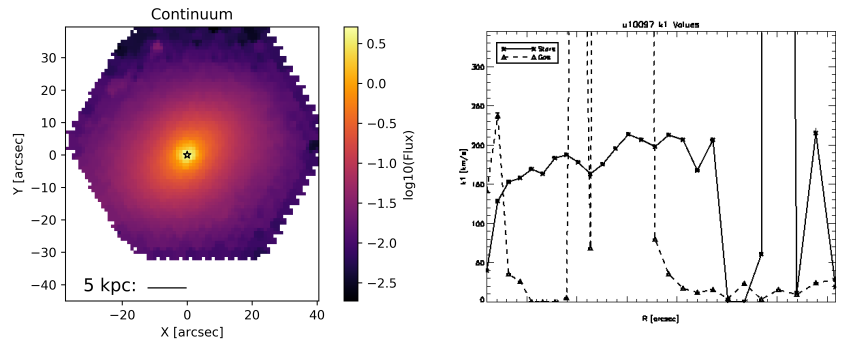


Figure 98 Top row, left to right: Name and characteristic parameters, continuum flux, and radial k_1 profiles for stars (solid) and gas (dashed), respectively. Bottom row, left to right: stellar kinematics, gas kinematics, and the difference between stellar and gas kinematics, respectively. The curves containing the data points are the convex hulls used to define the 'edge' of the map. The brightest continuum pixel (used as the center for kinemetry) is marked by a white star. The solid and dashed line in the stellar and gas velocity map, respectively, is the median position angle along which kinemetry coefficients were determined. The number value of this position angle is given at the top right of the plot. A scale bar is given along the bottom of each velocity map.

UGC 10097

$\log(\text{Stellar Mass}): 11.458$
 $D = 88.4 \text{ Mpc}$
 $M_r = -22.725 \text{ mag}$
 Redshift: 0.020
 $r_e: 14.652 \text{ arcsec}$
 AGN activity: No
 λ_R value at $r_e: 0.454$
 Residual asymmetry: 0.842



UGC 10205

$\log(\text{Stellar Mass}): 10.997$
 $D = 93.9 \text{ (DR3) Mpc}$
 $M_r = -22.317 \text{ mag}$
 Redshift: 0.022
 $r_e: 19.404 \text{ arcsec}$
 AGN activity: Yes
 λ_R value at $r_e: 0.248$
 Residual asymmetry: 0.906

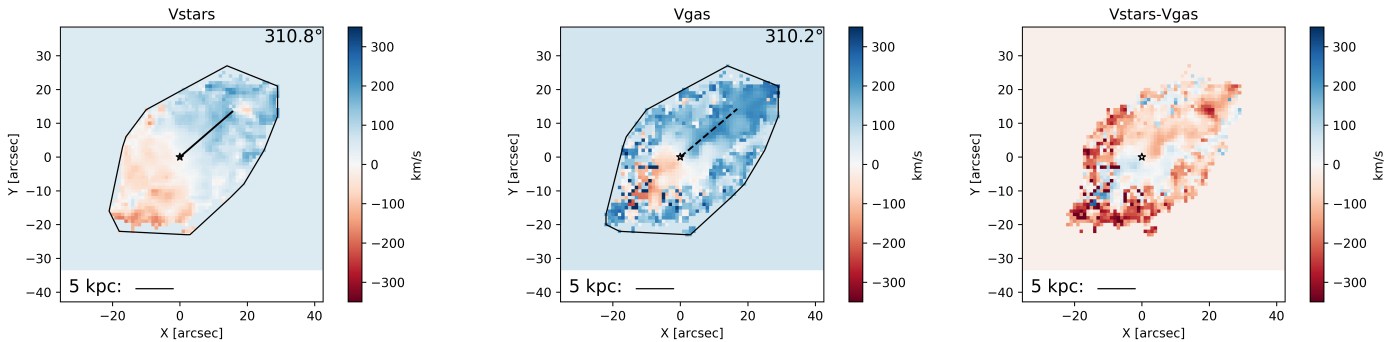
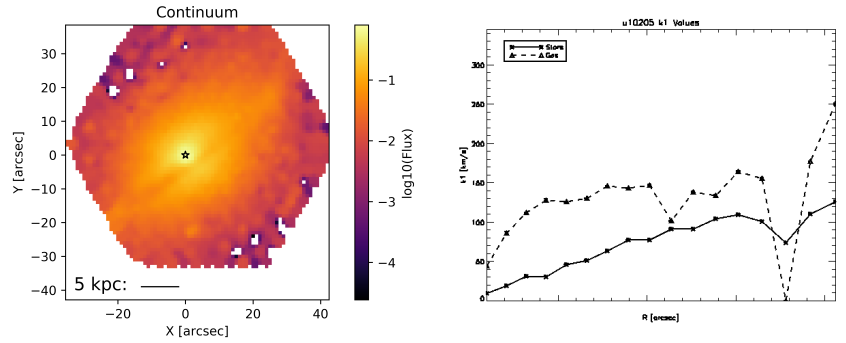
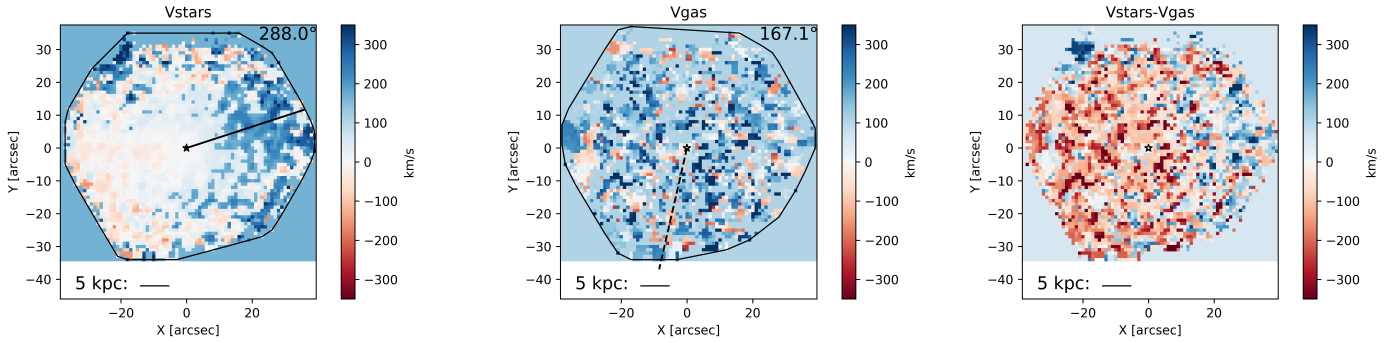
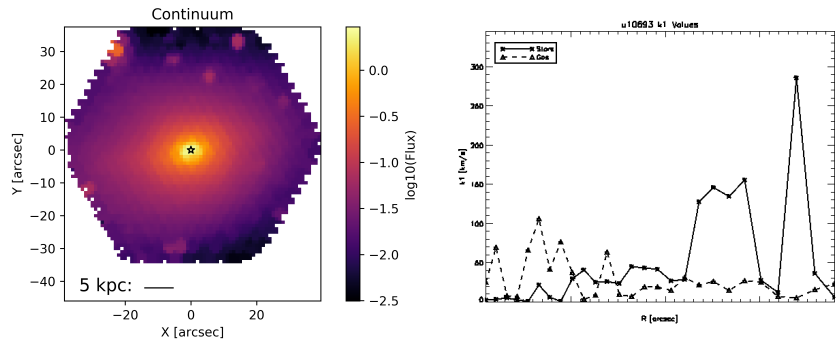


Figure 99 Top row, left to right: Name and characteristic parameters, continuum flux, and radial k_1 profiles for stars (solid) and gas (dashed), respectively. Bottom row, left to right: stellar kinematics, gas kinematics, and the difference between stellar and gas kinematics, respectively. The curves containing the data points are the convex hulls used to define the 'edge' of the map. The brightest continuum pixel (used as the center for kinemetry) is marked by a white star. The solid and dashed line in the stellar and gas velocity map, respectively, is the median position angle along which kinemetry coefficients were determined. The number value of this position angle is given at the top right of the plot. A scale bar is given along the bottom of each velocity map.

UGC 10693

$\log(\text{Stellar Mass}): 11.507$
 $D = 120.5 \text{ Mpc}$
 $M_r = -23.385 \text{ mag}$
 Redshift: 0.028
 $r_e = 22.968 \text{ arcsec}$
 AGN activity: No
 λ_R value at r_e : 0.452
 Residual asymmetry: 0.780



UGC 10695

$\log(\text{Stellar Mass}): 11.300$
 $D = 120.1 \text{ Mpc}$
 $M_r = -22.703 \text{ mag}$
 Redshift: 0.028
 $r_e = 24.552 \text{ arcsec}$
 AGN activity: No
 λ_R value at r_e : 0.667
 Residual asymmetry: 0.795

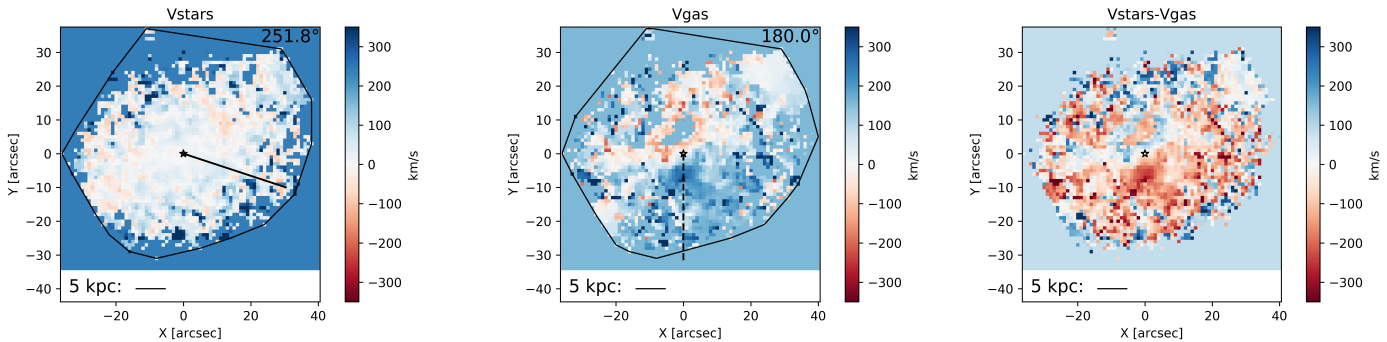
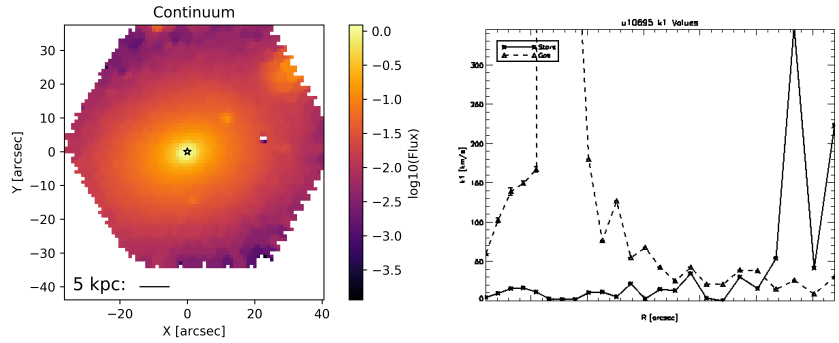
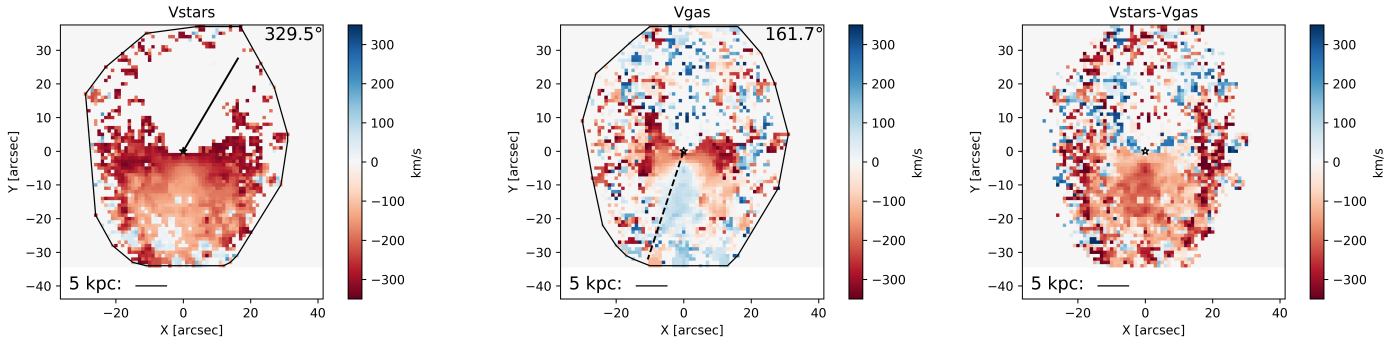
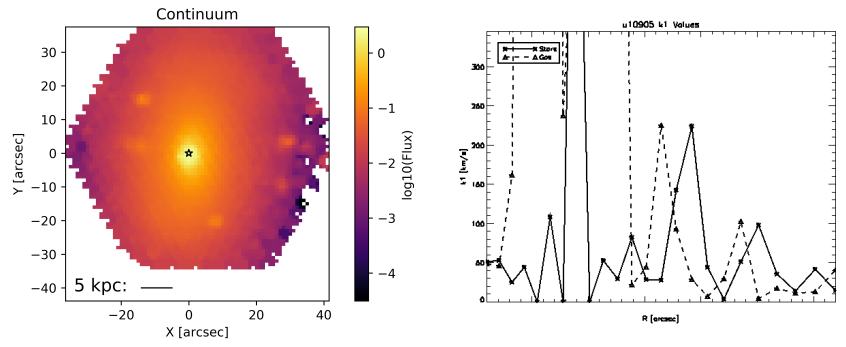


Figure 100 Top row, left to right: Name and characteristic parameters, continuum flux, and radial k_1 profiles for stars (solid) and gas (dashed), respectively. Bottom row, left to right: stellar kinematics, gas kinematics, and the difference between stellar and gas kinematics, respectively. The curves containing the data points are the convex hulls used to define the 'edge' of the map. The brightest continuum pixel (used as the center for kinemetry) is marked by a white star. The solid and dashed line in the stellar and gas velocity map, respectively, is the median position angle along which kinemetry coefficients were determined. The number value of this position angle is given at the top right of the plot. A scale bar is given along the bottom of each velocity map.

UGC 10905

$\log(\text{Stellar Mass}): 11.607$
 $D = 114.1 \text{ Mpc}$
 $M_r = -22.915 \text{ mag}$
 Redshift: 0.027
 $r_e: 15.444 \text{ arcsec}$
 AGN activity: No
 λ_R value at $r_e: 0.367$
 Residual asymmetry: 0.834



UGC 11228

$\log(\text{Stellar Mass}): 11.093$
 $D = 84.5 \text{ Mpc}$
 $M_r = -22.096 \text{ mag}$
 Redshift: 0.019
 $r_e: 12.276 \text{ arcsec}$
 AGN activity: No
 λ_R value at $r_e: 0.486$
 Residual asymmetry: 0.810

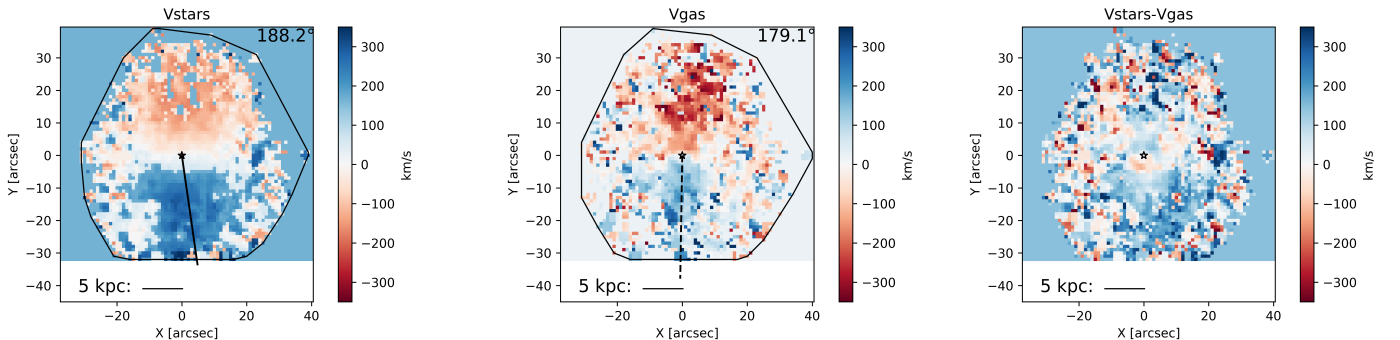
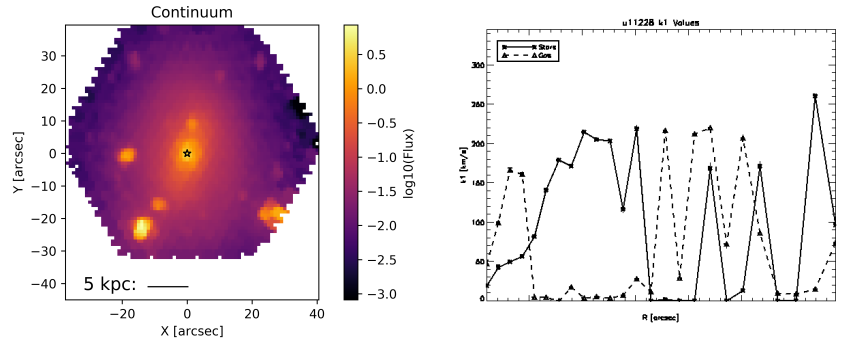
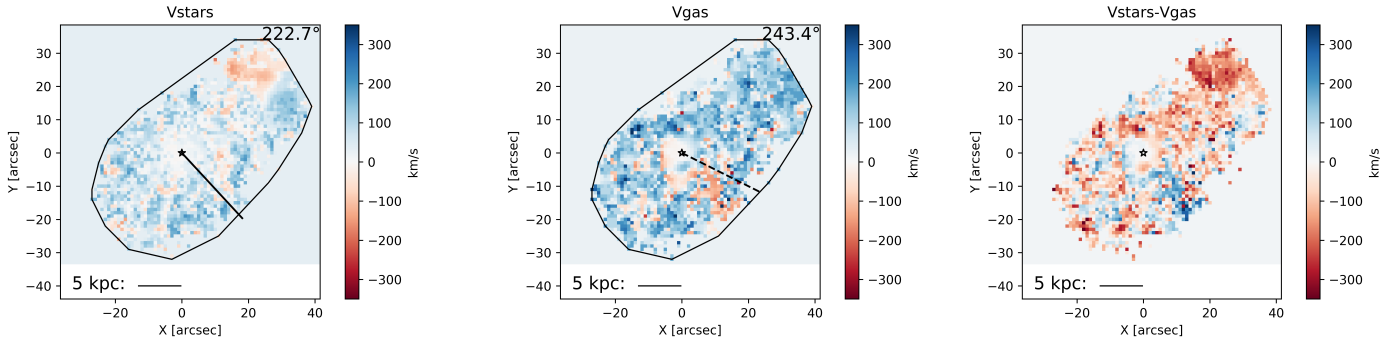
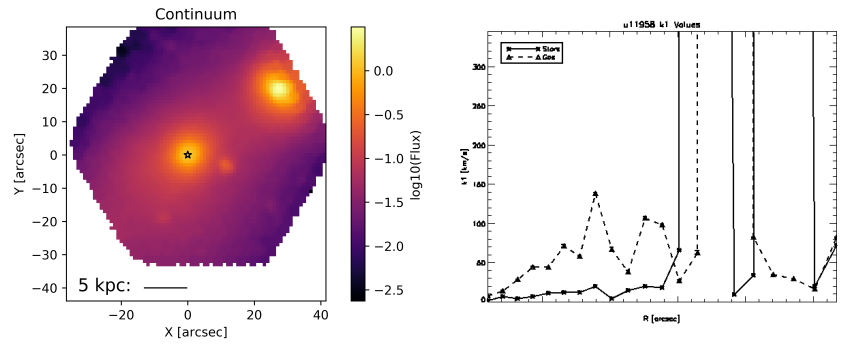


Figure 101 Top row, left to right: Name and characteristic parameters, continuum flux, and radial k_1 profiles for stars (solid) and gas (dashed), respectively. Bottom row, left to right: stellar kinematics, gas kinematics, and the difference between stellar and gas kinematics, respectively. The curves containing the data points are the convex hulls used to define the 'edge' of the map. The brightest continuum pixel (used as the center for kinemetry) is marked by a white star. The solid and dashed line in the stellar and gas velocity map, respectively, is the median position angle along which kinemetry coefficients were determined. The number value of this position angle is given at the top right of the plot. A scale bar is given along the bottom of each velocity map.

UGC 11958

$\log(\text{Stellar Mass}): 11.306$
 $D = 81.5 \text{ Mpc}$
 $M_r = -21.893 \text{ mag}$
 Redshift: 0.026
 $r_e: 13.464 \text{ arcsec}$
 AGN activity: No
 λ_R value at r_e : 0.268
 Residual asymmetry: 0.998



UGC 12127

$\log(\text{Stellar Mass}): 11.369$
 $D = 113.2 \text{ Mpc}$
 $M_r = -23.468 \text{ mag}$
 Redshift: 0.027
 $r_e: 36.432 \text{ arcsec}$
 AGN activity: No
 λ_R value at r_e : 0.272
 Residual asymmetry: 0.780

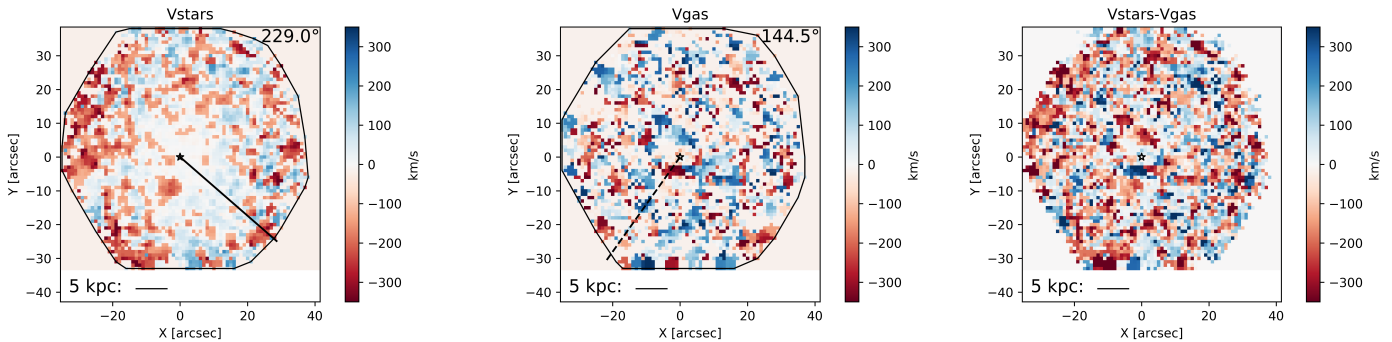
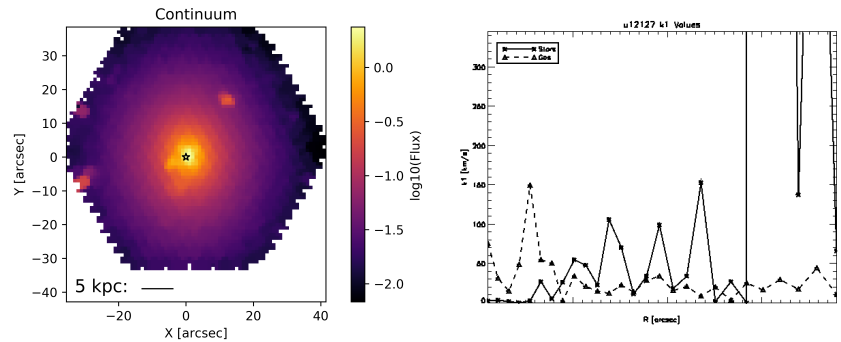


Figure 102 Top row, left to right: Name and characteristic parameters, continuum flux, and radial k_1 profiles for stars (solid) and gas (dashed), respectively. Bottom row, left to right: stellar kinematics, gas kinematics, and the difference between stellar and gas kinematics, respectively. The curves containing the data points are the convex hulls used to define the 'edge' of the map. The brightest continuum pixel (used as the center for kinemetry) is marked by a white star. The solid and dashed line in the stellar and gas velocity map, respectively, is the median position angle along which kinemetry coefficients were determined. The number value of this position angle is given at the top right of the plot. A scale bar is given along the bottom of each velocity map.

References

- O. Agertz and A. V. Kravtsov. On the Interplay between Star Formation and Feedback in Galaxy Formation Simulations. *Astrophysical Journal*, 804:18, May 2015. doi: 10.1088/0004-637X/804/1/18.
- O. Agertz, B. Moore, J. Stadel, D. Potter, F. Miniati, J. Read, L. Mayer, A. Gawryszczak, A. Kravtsov, Å. Nordlund, F. Pearce, V. Quilis, D. Rudd, V. Springel, J. Stone, E. Tasker, R. Teyssier, J. Wadsley, and R. Walder. Fundamental differences between SPH and grid methods. *Monthly Notices of the RAS*, 380:963–978, September 2007. doi: 10.1111/j.1365-2966.2007.12183.x.
- O. Agertz, A. V. Kravtsov, S. N. Leitner, and N. Y. Gnedin. Toward a Complete Accounting of Energy and Momentum from Stellar Feedback in Galaxy Formation Simulations. *Astrophysical Journal*, 770:25, June 2013. doi: 10.1088/0004-637X/770/1/25.
- N. Arav, B. Borguet, C. Chamberlain, D. Edmonds, and C. Danforth. Quasar outflows and AGN feedback in the extreme UV: HST/COS observations of HE 0238-1904. *Monthly Notices of the RAS*, 436:3286–3305, December 2013. doi: 10.1093/mnras/stt1812.
- S. Arribas, E. Mediavilla, B. García-Lorenzo, and C. del Burgo. Stellar and Ionized-Gas Kinematics of the Seyfert 1 Galaxy NGC 3516. *Astrophysical Journal*, 490: 227–237, November 1997. doi: 10.1086/304849.
- M. Aumer, S. D. M. White, T. Naab, and C. Scannapieco. Towards a more realistic population of bright spiral galaxies in cosmological simulations. *Monthly Notices of the RAS*, 434:3142–3164, October 2013a. doi: 10.1093/mnras/stt1230.
- M. Aumer, S. D. M. White, T. Naab, and C. Scannapieco. Towards a more realistic population of bright spiral galaxies in cosmological simulations. *Monthly Notices of the RAS*, 434:3142–3164, October 2013b. doi: 10.1093/mnras/stt1230.
- R. Bacon, G. Adam, A. Baranne, G. Courtes, D. Dubet, J. P. Dubois, E. Emsellem, P. Ferruit, Y. Georgelin, G. Monnet, E. Pecontal, A. Rousset, and F. Say. 3D spectrography at high spatial resolution. I. Concept and realization of the integral field spectrograph TIGER. *Astronomy and Astrophysics, Supplement*, 113:347, October 1995.
- R. Bacon, Y. Copin, G. Monnet, B. W. Miller, J. R. Allington-Smith, M. Bureau, C. M. Carollo, R. L. Davies, E. Emsellem, H. Kuntschner, R. F. Peletier, E. K. Verolme, and P. T. de Zeeuw. The SAURON project - I. The panoramic integral-field spectrograph. *Monthly Notices of the RAS*, 326:23–35, September 2001. doi: 10.1046/j.1365-8711.2001.04612.x.

- J. A. Baldwin, M. M. Phillips, and R. Terlevich. Classification parameters for the emission-line spectra of extragalactic objects. *Publications of the ASP*, 93:5–19, February 1981. doi: 10.1086/130766.
- J. Barnes and P. Hut. A hierarchical $O(N \log N)$ force-calculation algorithm. *Nature*, 324:446–449, December 1986. doi: 10.1038/324446a0.
- P. S. Behroozi, C. Conroy, and R. H. Wechsler. A Comprehensive Analysis of Uncertainties Affecting the Stellar Mass-Halo Mass Relation for $0 < z < 4$. *Astrophysical Journal*, 717:379–403, July 2010. doi: 10.1088/0004-637X/717/1/379.
- F. Belfiore, R. Maiolino, C. Maraston, E. Emsellem, M. A. Bershadsky, K. L. Masters, R. Yan, D. Bizyaev, M. Boquien, J. R. Brownstein, K. Bundy, N. Drory, T. M. Heckman, D. R. Law, A. Roman-Lopes, K. Pan, L. Stanghellini, D. Thomas, A.-M. Weijmans, and K. B. Westfall. SDSS IV MaNGA - spatially resolved diagnostic diagrams: a proof that many galaxies are LIERs. *Monthly Notices of the RAS*, 461:3111–3134, September 2016. doi: 10.1093/mnras/stw1234.
- R. Bender. Velocity anisotropies and isophote shapes in elliptical galaxies. *Astronomy and Astrophysics*, 193:L7–L10, March 1988.
- A. J. Benson. Galaxy formation theory. *Physics Reports*, 495:33–86, October 2010. doi: 10.1016/j.physrep.2010.06.001.
- M. A. Bershadsky, M. A. W. Verheijen, R. A. Swaters, D. R. Andersen, K. B. Westfall, and T. Martinsson. The DiskMass Survey. I. Overview. *Astrophysical Journal*, 716:198–233, June 2010. doi: 10.1088/0004-637X/716/1/198.
- E. Bertschinger. Simulations of Structure Formation in the Universe. *Annual Review of Astron and Astrophys*, 36:599–654, 1998. doi: 10.1146/annurev.astro.36.1.599.
- L. Binette, C. G. Magris, G. Stasińska, and A. G. Bruzual. Photoionization in elliptical galaxies by old stars. *Astronomy and Astrophysics*, 292:13–19, December 1994.
- J. Binney. On the rotation of elliptical galaxies. *Monthly Notices of the RAS*, 183:501–514, May 1978. doi: 10.1093/mnras/183.3.501.
- J. Binney and S. Tremaine. *Galactic dynamics*. 1987.
- J. Binney and S. Tremaine. *Galactic Dynamics: Second Edition*. Princeton University Press, 2008.
- H. Bondi. On spherically symmetrical accretion. *Monthly Notices of the RAS*, 112:195, 1952. doi: 10.1093/mnras/112.2.195.

- C. M. Booth and J. Schaye. Cosmological simulations of the growth of supermassive black holes and feedback from active galactic nuclei: method and tests. *Monthly Notices of the RAS*, 398:53–74, September 2009. doi: 10.1111/j.1365-2966.2009.15043.x.
- A. Bosma. *The distribution and kinematics of neutral hydrogen in spiral galaxies of various morphological types*. PhD thesis, PhD Thesis, Groningen Univ., (1978), 1978.
- G. L. Bryan, M. L. Norman, B. W. O’Shea, T. Abel, J. H. Wise, M. J. Turk, D. R. Reynolds, D. C. Collins, P. Wang, S. W. Skillman, B. Smith, R. P. Harkness, J. Bordner, J.-h. Kim, M. Kuhlen, H. Xu, N. Goldbaum, C. Hummels, A. G. Kritsuk, E. Tasker, S. Skory, C. M. Simpson, O. Hahn, J. S. Oishi, G. C. So, F. Zhao, R. Cen, Y. Li, and Enzo Collaboration. ENZO: An Adaptive Mesh Refinement Code for Astrophysics. *Astrophysical Journal, Supplement*, 211:19, April 2014. doi: 10.1088/0067-0049/211/2/19.
- J. J. Bryant, M. S. Owers, A. S. G. Robotham, S. M. Croom, S. P. Driver, M. J. Drinkwater, N. P. F. Lorente, L. Cortese, N. Scott, M. Colless, A. Schaefer, E. N. Taylor, I. S. Konstantopoulos, J. T. Allen, I. Baldry, L. Barnes, A. E. Bauer, J. Bland-Hawthorn, J. V. Bloom, A. M. Brooks, S. Brough, G. Cecil, W. Couch, D. Croton, R. Davies, S. Ellis, L. M. R. Fogarty, C. Foster, K. Glazebrook, M. Goodwin, A. Green, M. L. Gunawardhana, E. Hampton, I.-T. Ho, A. M. Hopkins, L. Kewley, J. S. Lawrence, S. G. Leon-Saval, S. Leslie, R. McElroy, G. Lewis, J. Liske, Á. R. López-Sánchez, S. Mahajan, A. M. Medling, N. Metcalfe, M. Meyer, J. Mould, D. Obreschkow, S. O’Toole, M. Pracy, S. N. Richards, T. Shanks, R. Sharp, S. M. Sweet, A. D. Thomas, C. Tonini, and C. J. Walcher. The SAMI Galaxy Survey: instrument specification and target selection. *Monthly Notices of the RAS*, 447:2857–2879, March 2015. doi: 10.1093/mnras/stu2635.
- K. Bundy, M. A. Bershady, D. R. Law, R. Yan, N. Drory, N. MacDon-ald, D. A. Wake, B. Cherinka, J. R. Sánchez-Gallego, A.-M. Weijmans, D. Thomas, C. Tremonti, K. Masters, L. Coccato, A. M. Diamond-Stanic, A. Aragón-Salamanca, V. Avila-Reese, C. Badenes, J. Falcón-Barroso, F. Belfiore, D. Bizyaev, G. A. Blanc, J. Bland-Hawthorn, M. R. Blanton, J. R. Brownstein, N. Byler, M. Cappellari, C. Conroy, A. A. Dutton, E. Emsellem, J. Etherington, P. M. Frinchaboy, H. Fu, J. E. Gunn, P. Harding, E. J. Johnston, G. Kauffmann, K. Kinemuchi, M. A. Klaene, J. H. Knapen, A. Leauthaud, C. Li, L. Lin, R. Maiolino, V. Malanushenko, E. Malanushenko, S. Mao, C. Maraston, R. M. McDermid, M. R. Merrifield, R. C. Nichol, D. Oravetz, K. Pan, J. K. Parejko, S. F. Sanchez, D. Schlegel, A. Simmons, O. Steele, M. Steinmetz, K. Thanjavur, B. A. Thompson, J. L. Tinker, R. C. E. van den Bosch, K. B. Westfall, D. Wilkinson, S. Wright, T. Xiao, and K. Zhang. Overview of the SDSS-IV MaNGA Survey:

- Mapping nearby Galaxies at Apache Point Observatory. *Astrophysical Journal*, 798:7, January 2015. doi: 10.1088/0004-637X/798/1/7.
- N. Caon, M. Capaccioli, and M. D’Onofrio. On the Shape of the Light Profiles of Early Type Galaxies. *Monthly Notices of the RAS*, 265:1013, December 1993. doi: 10.1093/mnras/265.4.1013.
- M. Capaccioli. Photometry of early-type galaxies and the $R \propto r^{1/4}$ law. In H. G. Corwin, Jr. and L. Bottinelli, editors, *World of Galaxies (Le Monde des Galaxies)*, pages 208–227, 1989.
- M. Cappellari. Structure and Kinematics of Early-Type Galaxies from Integral Field Spectroscopy. *Annual Review of Astron and Astrophys*, 54:597–665, September 2016. doi: 10.1146/annurev-astro-082214-122432.
- M. Cappellari and Y. Copin. Adaptive spatial binning of integral-field spectroscopic data using Voronoi tessellations. *Monthly Notices of the RAS*, 342:345–354, June 2003. doi: 10.1046/j.1365-8711.2003.06541.x.
- M. Cappellari, E. Emsellem, R. Bacon, M. Bureau, R. L. Davies, P. T. de Zeeuw, J. Falcón-Barroso, D. Krajnović, H. Kuntschner, R. M. McDermid, R. F. Peletier, M. Sarzi, R. C. E. van den Bosch, and G. van de Ven. The SAURON project - X. The orbital anisotropy of elliptical and lenticular galaxies: revisiting the $(V/\sigma, \epsilon)$ diagram with integral-field stellar kinematics. *Monthly Notices of the RAS*, 379: 418–444, August 2007. doi: 10.1111/j.1365-2966.2007.11963.x.
- M. Cappellari, E. Emsellem, D. Krajnović, R. M. McDermid, N. Scott, G. A. Verdoes Kleijn, L. M. Young, K. Alatalo, R. Bacon, L. Blitz, M. Bois, F. Bournaud, M. Bureau, R. L. Davies, T. A. Davis, P. T. de Zeeuw, P.-A. Duc, S. Khochfar, H. Kuntschner, P.-Y. Lablanche, R. Morganti, T. Naab, T. Oosterloo, M. Sarzi, P. Serra, and A.-M. Weijmans. The ATLAS^{3D} project - I. A volume-limited sample of 260 nearby early-type galaxies: science goals and selection criteria. *Monthly Notices of the RAS*, 413:813–836, May 2011a. doi: 10.1111/j.1365-2966.2010.18174.x.
- M. Cappellari, E. Emsellem, D. Krajnović, R. M. McDermid, P. Serra, K. Alatalo, L. Blitz, M. Bois, F. Bournaud, M. Bureau, R. L. Davies, T. A. Davis, P. T. de Zeeuw, S. Khochfar, H. Kuntschner, P.-Y. Lablanche, R. Morganti, T. Naab, T. Oosterloo, M. Sarzi, N. Scott, A.-M. Weijmans, and L. M. Young. The ATLAS^{3D} project - VII. A new look at the morphology of nearby galaxies: the kinematic morphology-density relation. *Monthly Notices of the RAS*, 416: 1680–1696, September 2011b. doi: 10.1111/j.1365-2966.2011.18600.x.
- E. Choi, J. P. Ostriker, T. Naab, L. Oser, and B. P. Moster. The impact of mechanical AGN feedback on the formation of massive early-type galaxies. *Monthly Notices of the RAS*, 449:4105–4116, June 2015. doi: 10.1093/mnras/stv575.

- E. Choi, J. P. Ostriker, T. Naab, R. S. Somerville, M. Hirschmann, A. Núñez, C.-Y. Hu, and L. Oser. Physics of Galactic Metals: Evolutionary Effects due to Production, Distribution, Feedback & Interaction with Black Holes. *ArXiv e-prints*, October 2016.
- R. Cid Fernandes, A. Mateus, L. Sodré, G. Stasińska, and J. M. Gomes. Semi-empirical analysis of Sloan Digital Sky Survey galaxies - I. Spectral synthesis method. *Monthly Notices of the RAS*, 358:363–378, April 2005. doi: 10.1111/j.1365-2966.2005.08752.x.
- R. Cid Fernandes, G. Stasińska, M. S. Schlickmann, A. Mateus, N. Vale Asari, W. Schoenell, and L. Sodré. Alternative diagnostic diagrams and the ‘forgotten’ population of weak line galaxies in the SDSS. *Monthly Notices of the RAS*, 403:1036–1053, April 2010. doi: 10.1111/j.1365-2966.2009.16185.x.
- R. Cid Fernandes, G. Stasińska, A. Mateus, and N. Vale Asari. A comprehensive classification of galaxies in the Sloan Digital Sky Survey: how to tell true from fake AGN? *Monthly Notices of the RAS*, 413:1687–1699, May 2011. doi: 10.1111/j.1365-2966.2011.18244.x.
- P. Colella and P. R. Woodward. The Piecewise Parabolic Method (PPM) for Gas-Dynamical Simulations. *Journal of Computational Physics*, 54:174–201, September 1984. doi: 10.1016/0021-9991(84)90143-8.
- C. J. Conselice, M. A. Bershadsky, and A. Jangren. The Asymmetry of Galaxies: Physical Morphology for Nearby and High-Redshift Galaxies. *Astrophysical Journal*, 529:886–910, February 2000. doi: 10.1086/308300.
- G. Courtes. An Integral Field Spectrograph (IFS) for Large Telescopes. In C. M. Humphries, editor, *IAU Colloq. 67: Instrumentation for Astronomy with Large Optical Telescopes*, volume 92 of *Astrophysics and Space Science Library*, page 123, 1982. doi: 10.1007/978-94-009-7787-7_16.
- A. C. Crook, J. P. Huchra, N. Martimbeau, K. L. Masters, T. Jarrett, and L. M. Macri. Groups of Galaxies in the Two Micron All Sky Redshift Survey. *Astrophysical Journal*, 655:790–813, February 2007. doi: 10.1086/510201.
- O. Daigle, C. Carignan, P. Amram, O. Hernandez, L. Chemin, C. Balkowski, and R. Kennicutt. H α kinematics of the SINGS nearby galaxies survey - I*. *Monthly Notices of the RAS*, 367:469–512, April 2006. doi: 10.1111/j.1365-2966.2006.10002.x.
- C. Dalla Vecchia and J. Schaye. Simulating galactic outflows with thermal supernova feedback. *Monthly Notices of the RAS*, 426:140–158, October 2012. doi: 10.1111/j.1365-2966.2012.21704.x.

- R. Davé, N. Katz, B. D. Oppenheimer, J. A. Kollmeier, and D. H. Weinberg. The neutral hydrogen content of galaxies in cosmological hydrodynamic simulations. *Monthly Notices of the RAS*, 434:2645–2663, September 2013. doi: 10.1093/mnras/stt1274.
- R. L. Davies, G. Efstathiou, S. M. Fall, G. Illingworth, and P. L. Schechter. The kinematic properties of faint elliptical galaxies. *Astrophysical Journal*, 266:41–57, March 1983. doi: 10.1086/160757.
- P. T. de Zeeuw, M. Bureau, E. Emsellem, R. Bacon, C. M. Carollo, Y. Copin, R. L. Davies, H. Kuntschner, B. W. Miller, G. Monnet, R. F. Peletier, and E. K. Verolme. The SAURON project - II. Sample and early results. *Monthly Notices of the RAS*, 329:513–530, January 2002. doi: 10.1046/j.1365-8711.2002.05059.x.
- T. Di Matteo, V. Springel, and L. Hernquist. Energy input from quasars regulates the growth and activity of black holes and their host galaxies. *Nature*, 433:604–607, February 2005. doi: 10.1038/nature03335.
- K. Dolag, S. Borgani, S. Schindler, A. Diaferio, and A. M. Bykov. Simulation Techniques for Cosmological Simulations. *Space Science Reviews*, 134:229–268, February 2008. doi: 10.1007/s11214-008-9316-5.
- M. A. Dopita and R. S. Sutherland. Spectral Signatures of Fast Shocks. II. Optical Diagnostic Diagrams. *Astrophysical Journal*, 455:468, December 1995. doi: 10.1086/176596.
- Y. Dubois, R. Gavazzi, S. Peirani, and J. Silk. AGN-driven quenching of star formation: morphological and dynamical implications for early-type galaxies. *Monthly Notices of the RAS*, 433:3297–3313, August 2013. doi: 10.1093/mnras/stt997.
- Y. Dubois, S. Peirani, C. Pichon, J. Devriendt, R. Gavazzi, C. Welker, and M. Volonteri. The HORIZON-AGN simulation: morphological diversity of galaxies promoted by AGN feedback. *Monthly Notices of the RAS*, 463:3948–3964, December 2016. doi: 10.1093/mnras/stw2265.
- G. Dumas, C. G. Mundell, E. Emsellem, and N. M. Nagar. Central kiloparsec of Seyfert and inactive host galaxies: a comparison of two-dimensional stellar and gaseous kinematics. *Monthly Notices of the RAS*, 379:1249–1278, August 2007. doi: 10.1111/j.1365-2966.2007.12014.x.
- D. J. Eisenstein and W. Hu. Power Spectra for Cold Dark Matter and Its Variants. *Astrophysical Journal*, 511:5–15, January 1999. doi: 10.1086/306640.
- E. Emsellem, M. Cappellari, R. F. Peletier, R. M. McDermid, R. Bacon, M. Bureau, Y. Copin, R. L. Davies, D. Krajnović, H. Kuntschner, B. W. Miller, and P. T. de Zeeuw. The SAURON project - III. Integral-field absorption-line kinematics

- of 48 elliptical and lenticular galaxies. *Monthly Notices of the RAS*, 352:721–743, August 2004. doi: 10.1111/j.1365-2966.2004.07948.x.
- E. Emsellem, M. Cappellari, D. Krajnović, G. van de Ven, R. Bacon, M. Bureau, R. L. Davies, P. T. de Zeeuw, J. Falcón-Barroso, H. Kuntschner, R. McDermid, R. F. Peletier, and M. Sarzi. The SAURON project - IX. A kinematic classification for early-type galaxies. *Monthly Notices of the RAS*, 379:401–417, August 2007. doi: 10.1111/j.1365-2966.2007.11752.x.
- E. Emsellem, M. Cappellari, D. Krajnović, K. Alatalo, L. Blitz, M. Bois, F. Bournaud, M. Bureau, R. L. Davies, T. A. Davis, P. T. de Zeeuw, S. Khochfar, H. Kuntschner, P.-Y. Lablanche, R. M. McDermid, R. Morganti, T. Naab, T. Oosterloo, M. Sarzi, N. Scott, P. Serra, G. van de Ven, A.-M. Weijmans, and L. M. Young. The ATLAS^{3D} project - III. A census of the stellar angular momentum within the effective radius of early-type galaxies: unveiling the distribution of fast and slow rotators. *Monthly Notices of the RAS*, 414:888–912, June 2011. doi: 10.1111/j.1365-2966.2011.18496.x.
- J. Falcón-Barroso, M. Lyubenova, and G. van de Ven. Angular Momentum across the Hubble sequence from the CALIFA survey. In M. Cappellari and S. Courteau, editors, *Galaxy Masses as Constraints of Formation Models*, volume 311 of *IAU Symposium*, pages 78–81, April 2015. doi: 10.1017/S1743921315003439.
- J. Falcón-Barroso, M. Lyubenova, G. van de Ven, J. Mendez-Abreu, J. A. L. Aguerri, B. García-Lorenzo, S. Bekeraité, S. F. Sánchez, B. Husemann, R. García-Benito, D. Mast, C. J. Walcher, S. Zibetti, J. K. Barrera-Ballesteros, L. Galbany, P. Sánchez-Blázquez, R. Singh, R. C. E. van den Bosch, V. Wild, L. Zhu, J. Bland-Hawthorn, R. Cid Fernandes, A. de Lorenzo-Cáceres, A. Gallazzi, R. M. González Delgado, R. A. Marino, I. Márquez, E. Pérez, I. Pérez, M. M. Roth, F. F. Rosales-Ortega, T. Ruiz-Lara, L. Wisotzki, B. Ziegler, and Califa Collaboration. Stellar kinematics across the Hubble sequence in the CALIFA survey: general properties and aperture corrections. *Astronomy and Astrophysics*, 597:A48, January 2017. doi: 10.1051/0004-6361/201628625.
- A. Feltre, S. Charlot, and J. Gutkin. Nuclear activity versus star formation: emission-line diagnostics at ultraviolet and optical wavelengths. *Monthly Notices of the RAS*, 456:3354–3374, March 2016. doi: 10.1093/mnras/stv2794.
- G. J. Ferland, R. L. Porter, P. A. M. van Hoof, R. J. R. Williams, N. P. Abel, M. L. Lykins, G. Shaw, W. J. Henney, and P. C. Stancil. The 2013 Release of Cloudy. *rmxaa*, 49:137–163, April 2013.
- M. Franx, G. Illingworth, and T. de Zeeuw. The ordered nature of elliptical galaxies - Implications for their intrinsic angular momenta and shapes. *Astrophysical Journal*, 383:112–134, December 1991. doi: 10.1086/170769.

- M. Gaspari, M. Ruszkowski, and S. P. Oh. Chaotic cold accretion on to black holes. *Monthly Notices of the RAS*, 432:3401–3422, July 2013. doi: 10.1093/mnras/stt692.
- J. M. Gomes, P. Papaderos, C. Kehrig, J. M. Vílchez, M. D. Lehnert, S. F. Sánchez, B. Ziegler, I. Breda, S. N. Dos Reis, J. Iglesias-Páramo, J. Bland-Hawthorn, L. Galbany, D. J. Bomans, F. F. Rosales-Ortega, R. Cid Fernandes, C. J. Walcher, J. Falcón-Barroso, R. García-Benito, I. Márquez, A. Del Olmo, J. Masegosa, M. Mollá, R. A. Marino, R. M. González Delgado, Á. R. López-Sánchez, and CALIFA Collaboration. Warm ionized gas in CALIFA early-type galaxies. 2D emission-line patterns and kinematics for 32 galaxies. *Astronomy and Astrophysics*, 588:A68, April 2016. doi: 10.1051/0004-6361/201525976.
- R. M. González Delgado, R. Cid Fernandes, R. García-Benito, E. Pérez, A. L. de Amorim, C. Cortijo-Ferrero, E. A. D. Lacerda, R. López Fernández, S. F. Sánchez, N. Vale Asari, J. Alves, J. Bland-Hawthorn, L. Galbany, A. Gallazzi, B. Husemann, S. Bekeraite, B. Jungwiert, A. R. López-Sánchez, A. de Lorenzo-Cáceres, R. A. Marino, D. Mast, M. Mollá, A. del Olmo, P. Sánchez-Blázquez, G. van de Ven, J. M. Vílchez, C. J. Walcher, L. Wisotzki, B. Ziegler, and C. Collaboration920. Insights on the Stellar Mass-Metallicity Relation from the CALIFA Survey. *Astrophysical Journal, Letters*, 791:L16, August 2014a. doi: 10.1088/2041-8205/791/1/L16.
- R. M. González Delgado, E. Pérez, R. Cid Fernandes, R. García-Benito, A. L. de Amorim, S. F. Sánchez, B. Husemann, C. Cortijo-Ferrero, R. López Fernández, P. Sánchez-Blázquez, S. Bekeraite, C. J. Walcher, J. Falcón-Barroso, A. Gallazzi, G. van de Ven, J. Alves, J. Bland-Hawthorn, R. C. Kennicutt, D. Kupko, M. Lyubenova, D. Mast, M. Mollá, R. A. Marino, A. Quirrenbach, J. M. Vílchez, and L. Wisotzki. The star formation history of CALIFA galaxies: Radial structures. *Astronomy and Astrophysics*, 562:A47, February 2014b. doi: 10.1051/0004-6361/201322011.
- F. Governato, B. Willman, L. Mayer, A. Brooks, G. Stinson, O. Valenzuela, J. Wadsley, and T. Quinn. Forming disc galaxies in Λ CDM simulations. *Monthly Notices of the RAS*, 374:1479–1494, February 2007. doi: 10.1111/j.1365-2966.2006.11266.x.
- F. Governato, C. Brook, L. Mayer, A. Brooks, G. Rhee, J. Wadsley, P. Jonsson, B. Willman, G. Stinson, T. Quinn, and P. Madau. Bulgeless dwarf galaxies and dark matter cores from supernova-driven outflows. *Nature*, 463:203–206, January 2010. doi: 10.1038/nature08640.
- A. W. Graham and R. Guzmán. HST Photometry of Dwarf Elliptical Galaxies in Coma, and an Explanation for the Alleged Structural Dichotomy between Dwarf and Bright Elliptical Galaxies. *Astronomical Journal*, 125:2936–2950, June 2003. doi: 10.1086/374992.

- J. Guedes, S. Callegari, P. Madau, and L. Mayer. Forming Realistic Late-type Spirals in a Λ CDM Universe: The Eris Simulation. *Astrophysical Journal*, 742:76, December 2011. doi: 10.1088/0004-637X/742/2/76.
- J. Gutkin, S. Charlot, and G. Bruzual. Modelling the nebular emission from primeval to present-day star-forming galaxies. *Monthly Notices of the RAS*, 462:1757–1774, October 2016. doi: 10.1093/mnras/stw1716.
- O. Hahn and T. Abel. Multi-scale initial conditions for cosmological simulations. *Monthly Notices of the RAS*, 415:2101–2121, August 2011. doi: 10.1111/j.1365-2966.2011.18820.x.
- T. M. Heckman. An optical and radio survey of the nuclei of bright galaxies - Activity in normal galactic nuclei. *Astronomy and Astrophysics*, 87:152–164, July 1980.
- M. Hirschmann, S. Charlot, A. Feltre, T. Naab, E. Choi, J. P. Ostriker, and R. S. Somerville. Synthetic nebular emission from massive galaxies - I: origin of the cosmic evolution of optical emission-line ratios. *Monthly Notices of the RAS*, 472:2468–2495, December 2017. doi: 10.1093/mnras/stx2180.
- L. C. Ho. LINERs as low-luminosity active galactic nuclei. *Advances in Space Research*, 23:813–822, 1999. doi: 10.1016/S0273-1177(99)00211-2.
- L. C. Ho, A. V. Filippenko, and W. L. W. Sargent. A Search for “Dwarf” Seyfert Nuclei. III. Spectroscopic Parameters and Properties of the Host Galaxies. *Astrophysical Journal, Supplement*, 112:315–390, October 1997. doi: 10.1086/313041.
- R. W. Hockney and J. W. Eastwood. *Computer simulation using particles*. 1988.
- P. F. Hopkins. A general class of Lagrangian smoothed particle hydrodynamics methods and implications for fluid mixing problems. *Monthly Notices of the RAS*, 428:2840–2856, February 2013. doi: 10.1093/mnras/sts210.
- P. F. Hopkins, D. Kereš, J. Oñorbe, C.-A. Faucher-Giguère, E. Quataert, N. Murray, and J. S. Bullock. Galaxies on FIRE (Feedback In Realistic Environments): stellar feedback explains cosmologically inefficient star formation. *Monthly Notices of the RAS*, 445:581–603, November 2014. doi: 10.1093/mnras/stu1738.
- F. Hoyle and R. A. Lyttleton. The effect of interstellar matter on climatic variation. *Proceedings of the Cambridge Philosophical Society*, 35:405, 1939. doi: 10.1017/S0305004100021150.
- C.-Y. Hu, T. Naab, S. Walch, B. P. Moster, and L. Oser. SPHGal: smoothed particle hydrodynamics with improved accuracy for galaxy simulations. *Monthly Notices of the RAS*, 443:1173–1191, September 2014. doi: 10.1093/mnras/stu1187.

- E. P. Hubble. Extragalactic nebulae. *Astrophysical Journal*, 64, December 1926. doi: 10.1086/143018.
- B. Husemann, K. Jahnke, S. F. Sánchez, D. Barrado, S. Bekeraité, D. J. Bomans, A. Castillo-Morales, C. Catalán-Torrecilla, R. Cid Fernandes, J. Falcón-Barroso, R. García-Benito, R. M. González Delgado, J. Iglesias-Páramo, B. D. Johnson, D. Kupko, R. López-Fernandez, M. Lyubenova, R. A. Marino, D. Mast, A. Miskolczi, A. Monreal-Ibero, A. Gil de Paz, E. Pérez, I. Pérez, F. F. Rosales-Ortega, T. Ruiz-Lara, U. Schilling, G. van de Ven, J. Walcher, J. Alves, A. L. de Amorim, N. Backsmann, J. K. Barrera-Ballesteros, J. Bland-Hawthorn, C. Cortijo, R.-J. Dettmar, M. Demleitner, A. I. Díaz, H. Enke, E. Florido, H. Flores, L. Galbany, A. Gallazzi, B. García-Lorenzo, J. M. Gomes, N. Gruel, T. Haines, L. Holmes, B. Jungwiert, V. Kalinova, C. Kehrig, R. C. Kennicutt, J. Klar, M. D. Lehnert, Á. R. López-Sánchez, A. de Lorenzo-Cáceres, E. Mármol-Queraltó, I. Márquez, J. Mendez-Abreu, M. Mollá, A. del Olmo, S. E. Meidt, P. Papaderos, J. Puschnig, A. Quirrenbach, M. M. Roth, P. Sánchez-Blázquez, K. Spekkens, R. Singh, V. Stanishev, S. C. Trager, J. M. Vilchez, V. Wild, L. Wisotzki, S. Zibetti, and B. Ziegler. CALIFA, the Calar Alto Legacy Integral Field Area survey. II. First public data release. *Astronomy and Astrophysics*, 549:A87, January 2013. doi: 10.1051/0004-6361/201220582.
- J. Iglesias-Páramo, J. M. Vilchez, L. Galbany, S. F. Sánchez, F. F. Rosales-Ortega, D. Mast, R. García-Benito, B. Husemann, J. A. L. Aguerri, J. Alves, S. Bekeraité, J. Bland-Hawthorn, C. Catalán-Torrecilla, A. L. de Amorim, A. de Lorenzo-Cáceres, S. Ellis, J. Falcón-Barroso, H. Flores, E. Florido, A. Gallazzi, J. M. Gomes, R. M. González Delgado, T. Haines, J. D. Hernández-Fernández, C. Kehrig, A. R. López-Sánchez, M. Lyubenova, R. A. Marino, M. Mollá, A. Monreal-Ibero, A. Mourão, P. Papaderos, M. Rodrigues, P. Sánchez-Blázquez, K. Spekkens, V. Stanishev, G. van de Ven, C. J. Walcher, L. Wisotzki, S. Zibetti, and B. Ziegler. Aperture corrections for disk galaxy properties derived from the CALIFA survey. Balmer emission lines in spiral galaxies. *Astronomy and Astrophysics*, 553:L7, May 2013. doi: 10.1051/0004-6361/201321460.
- G. Illingworth. Rotation in 13 elliptical galaxies. *Astrophysical Journal, Letters*, 218:L43–L47, December 1977. doi: 10.1086/182572.
- K. Iwamoto, F. Brachwitz, K. Nomoto, N. Kishimoto, H. Umeda, W. R. Hix, and F.-K. Thielemann. Nucleosynthesis in Chandrasekhar Mass Models for Type IA Supernovae and Constraints on Progenitor Systems and Burning-Front Propagation. *Astrophysical Journal, Supplement*, 125:439–462, December 1999. doi: 10.1086/313278.
- R. Jesseit, T. Naab, R. F. Peletier, and A. Burkert. 2D kinematics of simulated disc merger remnants. *Monthly Notices of the RAS*, 376:997–1020, April 2007. doi: 10.1111/j.1365-2966.2007.11524.x.

- R. Jesseit, M. Cappellari, T. Naab, E. Emsellem, and A. Burkert. Specific angular momentum of disc merger remnants and the λ_R -parameter. *Monthly Notices of the RAS*, 397:1202–1214, August 2009. doi: 10.1111/j.1365-2966.2009.14984.x.
- I. Kant. *Allgemeine Naturgeschichte und Theorie des Himmels*. 1755.
- A. I. Karakas. Updated stellar yields from asymptotic giant branch models. *Monthly Notices of the RAS*, 403:1413–1425, April 2010. doi: 10.1111/j.1365-2966.2009.16198.x.
- N. Katz. Dissipational galaxy formation. II - Effects of star formation. *Astrophysical Journal*, 391:502–517, June 1992. doi: 10.1086/171366.
- N. Katz, D. H. Weinberg, and L. Hernquist. Cosmological Simulations with TreeSPH. *Astrophysical Journal, Supplement*, 105:19, July 1996. doi: 10.1086/192305.
- G. Kauffmann, T. M. Heckman, C. Tremonti, J. Brinchmann, S. Charlot, S. D. M. White, S. E. Ridgway, J. Brinkmann, M. Fukugita, P. B. Hall, Ž. Ivezić, G. T. Richards, and D. P. Schneider. The host galaxies of active galactic nuclei. *Monthly Notices of the RAS*, 346:1055–1077, December 2003. doi: 10.1111/j.1365-2966.2003.07154.x.
- S. Kaviraj, S. Khochfar, K. Schawinski, S. K. Yi, E. Gawiser, J. Silk, S. N. Virani, C. N. Cardamone, P. G. van Dokkum, and C. M. Urry. The UV colours of high-redshift early-type galaxies: evidence for recent star formation and stellar mass assembly over the last 8 billion years. *Monthly Notices of the RAS*, 388:67–79, July 2008. doi: 10.1111/j.1365-2966.2008.13392.x.
- W. C. Keel, C. J. Lintott, K. Schawinski, V. N. Bennert, D. Thomas, A. Manning, S. D. Chojnowski, H. van Arkel, and S. Lynn. The History and Environment of a Faded Quasar: Hubble Space Telescope Observations of Hanny’s Voorwerp and IC 2497. *Astronomical Journal*, 144:66, August 2012. doi: 10.1088/0004-6256/144/2/66.
- C. Kehrig, A. Monreal-Ibero, P. Papaderos, J. M. Vílchez, J. M. Gomes, J. Masegosa, S. F. Sánchez, M. D. Lehnert, R. Cid Fernandes, J. Bland-Hawthorn, D. J. Bomans, I. Marquez, D. Mast, J. A. L. Aguerri, Á. R. López-Sánchez, R. A. Marino, A. Pasquali, I. Perez, M. M. Roth, P. Sánchez-Blázquez, and B. Ziegler. The ionized gas in the CALIFA early-type galaxies. I. Mapping two representative cases: NGC 6762 and NGC 5966. *Astronomy and Astrophysics*, 540:A11, April 2012. doi: 10.1051/0004-6361/201118357.
- A. Kelz, M. A. W. Verheijen, M. M. Roth, S. M. Bauer, T. Becker, J. Paschke, E. Popow, S. F. Sánchez, and U. Laux. PMAS: The Potsdam Multi-Aperture

- Spectrophotometer. II. The Wide Integral Field Unit PPak. *Publications of the ASP*, 118:129–145, January 2006. doi: 10.1086/497455.
- R. C. Kennicutt, Jr. The Global Schmidt Law in Star-forming Galaxies. *Astrophysical Journal*, 498:541–552, May 1998. doi: 10.1086/305588.
- L. J. Kewley, M. A. Dopita, R. S. Sutherland, C. A. Heisler, and J. Trevena. Theoretical Modeling of Starburst Galaxies. *Astrophysical Journal*, 556:121–140, July 2001. doi: 10.1086/321545.
- J. Kormendy and R. Bender. A Proposed Revision of the Hubble Sequence for Elliptical Galaxies. *Astrophysical Journal, Letters*, 464:L119, June 1996. doi: 10.1086/310095.
- J. Kormendy and G. Illingworth. Rotation of the bulge components of disk galaxies. *Astrophysical Journal*, 256:460–480, May 1982. doi: 10.1086/159923.
- D. Krajnović, M. Cappellari, P. T. de Zeeuw, and Y. Copin. Kinemetry: a generalization of photometry to the higher moments of the line-of-sight velocity distribution. *Monthly Notices of the RAS*, 366:787–802, March 2006. doi: 10.1111/j.1365-2966.2005.09902.x.
- D. Krajnović, E. Emsellem, M. Cappellari, K. Alatalo, L. Blitz, M. Bois, F. Bournaud, M. Bureau, R. L. Davies, T. A. Davis, P. T. de Zeeuw, S. Khochfar, H. Kuntschner, P.-Y. Lablanche, R. M. McDermid, R. Morganti, T. Naab, T. Oosterloo, M. Sarzi, N. Scott, P. Serra, A.-M. Weijmans, and L. M. Young. The ATLAS^{3D} project - II. Morphologies, kinematic features and alignment between photometric and kinematic axes of early-type galaxies. *Monthly Notices of the RAS*, 414:2923–2949, July 2011. doi: 10.1111/j.1365-2966.2011.18560.x.
- A. V. Kravtsov, A. A. Klypin, and A. M. Khokhlov. Adaptive Refinement Tree: A New High-Resolution N-Body Code for Cosmological Simulations. *Astrophysical Journal, Supplement*, 111:73–94, July 1997. doi: 10.1086/313015.
- J. H. Krolik. *Active galactic nuclei : from the central black hole to the galactic environment*. 1999.
- P. Kroupa. On the variation of the initial mass function. *Monthly Notices of the RAS*, 322:231–246, April 2001. doi: 10.1046/j.1365-8711.2001.04022.x.
- M. R. Krumholz, A. Dekel, and C. F. McKee. A Universal, Local Star Formation Law in Galactic Clouds, nearby Galaxies, High-redshift Disks, and Starbursts. *Astrophysical Journal*, 745:69, January 2012. doi: 10.1088/0004-637X/745/1/69.
- M. Kuhlen, M. R. Krumholz, P. Madau, B. D. Smith, and J. Wise. Dwarf Galaxy Formation with H₂-regulated Star Formation. *Astrophysical Journal*, 749:36, April 2012. doi: 10.1088/0004-637X/749/1/36.

- E. Kutdemir. *The Evolution of Spiral Galaxies in Clusters*. PhD thesis, University of Groningen, 2010.
- C. N. Lackner and J. E. Gunn. Astrophysically motivated bulge-disc decompositions of Sloan Digital Sky Survey galaxies. *Monthly Notices of the RAS*, 421:2277–2302, April 2012. doi: 10.1111/j.1365-2966.2012.20450.x.
- C. Leitherer, D. Schaerer, J. D. Goldader, R. M. G. Delgado, C. Robert, D. F. Kune, D. F. de Mello, D. Devost, and T. M. Heckman. Starburst99: Synthesis Models for Galaxies with Active Star Formation. *Astrophysical Journal, Supplement*, 123: 3–40, July 1999. doi: 10.1086/313233.
- A. K. Leroy, F. Walter, K. Sandstrom, A. Schruba, J.-C. Munoz-Mateos, F. Bigiel, A. Bolatto, E. Brinks, W. J. G. de Blok, S. Meidt, H.-W. Rix, E. Rosolowsky, E. Schinnerer, K.-F. Schuster, and A. Usero. Molecular Gas and Star Formation in nearby Disk Galaxies. *Astronomical Journal*, 146:19, August 2013. doi: 10.1088/0004-6256/146/2/19.
- F. Marinacci, R. Pakmor, and V. Springel. The formation of disc galaxies in high-resolution moving-mesh cosmological simulations. *Monthly Notices of the RAS*, 437:1750–1775, January 2014. doi: 10.1093/mnras/stt2003.
- D. Martizzi, Jimmy, R. Teyssier, and B. Moore. Brightest cluster galaxies in cosmological simulations with adaptive mesh refinement: successes and failures. *Monthly Notices of the RAS*, 443:1500–1508, September 2014. doi: 10.1093/mnras/stu1233.
- I. G. McCarthy, J. Schaye, T. J. Ponman, R. G. Bower, C. M. Booth, C. Dalla Vecchia, R. A. Crain, V. Springel, T. Theuns, and R. P. C. Wiersma. The case for AGN feedback in galaxy groups. *Monthly Notices of the RAS*, 406:822–839, August 2010. doi: 10.1111/j.1365-2966.2010.16750.x.
- C. F. McKee and E. C. Ostriker. Theory of Star Formation. *Annual Review of Astron and Astrophys*, 45:565–687, September 2007. doi: 10.1146/annurev.astro.45.051806.110602.
- C. F. McKee and J. P. Ostriker. A theory of the interstellar medium - Three components regulated by supernova explosions in an inhomogeneous substrate. *Astrophysical Journal*, 218:148–169, November 1977. doi: 10.1086/155667.
- J. J. Monaghan. Smoothed particle hydrodynamics. *Annual Review of Astron and Astrophys*, 30:543–574, 1992. doi: 10.1146/annurev.aa.30.090192.002551.
- N. Murray, E. Quataert, and T. A. Thompson. On the Maximum Luminosity of Galaxies and Their Central Black Holes: Feedback from Momentum-driven Winds. *Astrophysical Journal*, 618:569–585, January 2005. doi: 10.1086/426067.

- T. Naab and J. P. Ostriker. Theoretical Challenges in Galaxy Formation. *ArXiv e-prints*, December 2016.
- T. Naab, L. Oser, E. Emsellem, M. Cappellari, D. Krajnović, R. M. McDermid, K. Alatalo, E. Bayet, L. Blitz, M. Bois, F. Bournaud, M. Bureau, A. Crocker, R. L. Davies, T. A. Davis, P. T. de Zeeuw, P.-A. Duc, M. Hirschmann, P. H. Johansson, S. Khochfar, H. Kuntschner, R. Morganti, T. Oosterloo, M. Sarzi, N. Scott, P. Serra, G. van de Ven, A. Weijmans, and L. M. Young. The ATLAS^{3D} project - XXV. Two-dimensional kinematic analysis of simulated galaxies and the cosmological origin of fast and slow rotators. *Monthly Notices of the RAS*, 444: 3357–3387, November 2014. doi: 10.1093/mnras/stt1919.
- J. F. Navarro and S. D. M. White. Simulations of Dissipative Galaxy Formation in Hierarchically Clustering Universes - Part One - Tests of the Code. *Monthly Notices of the RAS*, 265:271, November 1993. doi: 10.1093/mnras/265.2.271.
- A. Núñez, J. P. Ostriker, T. Naab, L. Oser, C.-Y. Hu, and E. Choi. Modeling for Stellar Feedback in Galaxy Formation Simulations. *Astrophysical Journal*, 836: 204, February 2017. doi: 10.3847/1538-4357/836/2/204.
- B. D. Oppenheimer and R. Davé. Cosmological simulations of intergalactic medium enrichment from galactic outflows. *Monthly Notices of the RAS*, 373:1265–1292, December 2006. doi: 10.1111/j.1365-2966.2006.10989.x.
- L. Oser, J. P. Ostriker, T. Naab, P. H. Johansson, and A. Burkert. The Two Phases of Galaxy Formation. *Astrophysical Journal*, 725:2312–2323, December 2010. doi: 10.1088/0004-637X/725/2/2312.
- L. Oser, T. Naab, J. P. Ostriker, and P. H. Johansson. The Cosmological Size and Velocity Dispersion Evolution of Massive Early-type Galaxies. *Astrophysical Journal*, 744:63, January 2012. doi: 10.1088/0004-637X/744/1/63.
- P. Papaderos, J. M. Gomes, J. M. Vílchez, C. Kehrig, M. D. Lehnert, B. Ziegler, S. F. Sánchez, B. Husemann, A. Monreal-Ibero, R. García-Benito, J. Bland-Hawthorn, C. Cortijo-Ferrero, A. de Lorenzo-Cáceres, A. del Olmo, J. Falcón-Barroso, L. Galbany, J. Iglesias-Páramo, Á. R. López-Sánchez, I. Marquez, M. Mollá, D. Mast, G. van de Ven, and L. Wisotzki. Nebular emission and the Lyman continuum photon escape fraction in CALIFA early-type galaxies. *Astronomy and Astrophysics*, 555:L1, July 2013. doi: 10.1051/0004-6361/201321681.
- R. F. Peletier, R. L. Davies, G. D. Illingworth, L. E. Davis, and M. Cawson. CCD surface photometry of galaxies with dynamical data. II - UBR photometry of 39 elliptical galaxies. *Astronomical Journal*, 100:1091–1142, October 1990. doi: 10.1086/115582.

- B. W. Ritchie and P. A. Thomas. Multiphase smoothed-particle hydrodynamics. *Monthly Notices of the RAS*, 323:743–756, May 2001. doi: 10.1046/j.1365-8711.2001.04268.x.
- J. Rosdahl, J. Schaye, R. Teyssier, and O. Agertz. Galaxies that shine: radiation-hydrodynamical simulations of disc galaxies. *Monthly Notices of the RAS*, 451: 34–58, July 2015. doi: 10.1093/mnras/stv937.
- M. M. Roth, A. Kelz, T. Fechner, T. Hahn, S.-M. Bauer, T. Becker, P. Böhm, L. Christensen, F. Dionies, J. Paschke, E. Popow, D. Wolter, J. Schmoll, U. Laux, and W. Altmann. PMAS: The Potsdam Multi-Aperture Spectrophotometer. I. Design, Manufacture, and Performance. *Publications of the ASP*, 117:620–642, June 2005. doi: 10.1086/429877.
- T. R. Saitoh and J. Makino. A Density-independent Formulation of Smoothed Particle Hydrodynamics. *Astrophysical Journal*, 768:44, May 2013. doi: 10.1088/0004-637X/768/1/44.
- S. F. Sánchez, R. C. Kennicutt, A. Gil de Paz, G. van de Ven, J. M. Vílchez, L. Wisotzki, C. J. Walcher, D. Mast, J. A. L. Aguerri, S. Albiol-Pérez, A. Alonso-Herrero, J. Alves, J. Bakos, T. Bartáková, J. Bland-Hawthorn, A. Boselli, D. J. Bomans, A. Castillo-Morales, C. Cortijo-Ferrero, A. de Lorenzo-Cáceres, A. Del Olmo, R.-J. Dettmar, A. Díaz, S. Ellis, J. Falcón-Barroso, H. Flores, A. Galazzi, B. García-Lorenzo, R. González Delgado, N. Gruel, T. Haines, C. Hao, B. Husemann, J. Iglésias-Páramo, K. Jahnke, B. Johnson, B. Jungwiert, V. Kalinova, C. Kehrig, D. Kupko, Á. R. López-Sánchez, M. Lyubenova, R. A. Marino, E. Mármol-Queraltó, I. Márquez, J. Masegosa, S. Meidt, J. Mendez-Abreu, A. Monreal-Ibero, C. Montijo, A. M. Mourão, G. Palacios-Navarro, P. Papaderos, A. Pasquali, R. Peletier, E. Pérez, I. Pérez, A. Quirrenbach, M. Relaño, F. F. Rosales-Ortega, M. M. Roth, T. Ruiz-Lara, P. Sánchez-Blázquez, C. Sengupta, R. Singh, V. Stanishev, S. C. Trager, A. Vazdekis, K. Viironen, V. Wild, S. Zibetti, and B. Ziegler. CALIFA, the Calar Alto Legacy Integral Field Area survey. I. Survey presentation. *Astronomy and Astrophysics*, 538:A8, February 2012. doi: 10.1051/0004-6361/201117353.
- S. F. Sánchez, R. García-Benito, S. Zibetti, C. J. Walcher, B. Husemann, M. A. Mendoza, L. Galbany, J. Falcón-Barroso, D. Mast, J. Aceituno, J. A. L. Aguerri, J. Alves, A. L. Amorim, Y. Ascasibar, D. Barrado-Navascues, J. Barrera-Ballesteros, S. Bekeraïtè, J. Bland-Hawthorn, M. Cano Díaz, R. Cid Fernandes, O. Cavichia, C. Cortijo, H. Dannerbauer, M. Demleitner, A. Díaz, R. J. Dettmar, A. de Lorenzo-Cáceres, A. del Olmo, A. Galazzi, B. García-Lorenzo, A. Gil de Paz, R. González Delgado, L. Holmes, J. Iglésias-Páramo, C. Kehrig, A. Kelz, R. C. Kennicutt, B. Kleemann, E. A. D. Lacerda, R. López Fernández, A. R. López Sánchez, M. Lyubenova, R. Marino, I. Márquez, J. Mendez-Abreu, M. Mollá,

- A. Monreal-Ibero, R. Ortega Minakata, J. P. Torres-Papaqui, E. Pérez, F. F. Rosales-Ortega, M. M. Roth, P. Sánchez-Blázquez, U. Schilling, K. Spekkens, N. Vale Asari, R. C. E. van den Bosch, G. van de Ven, J. M. Vilchez, V. Wild, L. Wisotzki, A. Yıldırım, and B. Ziegler. CALIFA, the Calar Alto Legacy Integral Field Area survey. IV. Third public data release. *Astronomy and Astrophysics*, 594:A36, October 2016. doi: 10.1051/0004-6361/201628661.
- P. Sánchez-Blázquez, F. F. Rosales-Ortega, J. Méndez-Abreu, I. Pérez, S. F. Sánchez, S. Zibetti, J. A. L. Aguerri, J. Bland-Hawthorn, C. Catalán-Torrecilla, R. Cid Fernandes, A. de Amorim, A. de Lorenzo-Caceres, J. Falcón-Barroso, A. Galazzi, R. García Benito, A. Gil de Paz, R. González Delgado, B. Husemann, J. Iglesias-Páramo, B. Jungwiert, R. A. Marino, I. Márquez, D. Mast, M. A. Mendoza, M. Mollá, P. Papaderos, T. Ruiz-Lara, G. van de Ven, C. J. Walcher, and L. Wisotzki. Stellar population gradients in galaxy discs from the CALIFA survey. The influence of bars. *Astronomy and Astrophysics*, 570:A6, October 2014. doi: 10.1051/0004-6361/201423635.
- S. Y. Sazonov, J. P. Ostriker, and R. A. Sunyaev. Quasars: the characteristic spectrum and the induced radiative heating. *Monthly Notices of the RAS*, 347: 144–156, January 2004. doi: 10.1111/j.1365-2966.2004.07184.x.
- S. Y. Sazonov, J. P. Ostriker, L. Ciotti, and R. A. Sunyaev. Radiative feedback from quasars and the growth of massive black holes in stellar spheroids. *Monthly Notices of the RAS*, 358:168–180, March 2005. doi: 10.1111/j.1365-2966.2005.08763.x.
- C. Scannapieco, P. B. Tissera, S. D. M. White, and V. Springel. Feedback and metal enrichment in cosmological smoothed particle hydrodynamics simulations - I. A model for chemical enrichment. *Monthly Notices of the RAS*, 364:552–564, December 2005. doi: 10.1111/j.1365-2966.2005.09574.x.
- C. Scannapieco, P. B. Tissera, S. D. M. White, and V. Springel. Feedback and metal enrichment in cosmological SPH simulations - II. A multiphase model with supernova energy feedback. *Monthly Notices of the RAS*, 371:1125–1139, September 2006. doi: 10.1111/j.1365-2966.2006.10785.x.
- C. Scannapieco, M. Wadepuhl, O. H. Parry, J. F. Navarro, A. Jenkins, V. Springel, R. Teyssier, E. Carlson, H. M. P. Couchman, R. A. Crain, C. Dalla Vecchia, C. S. Frenk, C. Kobayashi, P. Monaco, G. Murante, T. Okamoto, T. Quinn, J. Schaye, G. S. Stinson, T. Theuns, J. Wadsley, S. D. M. White, and R. Woods. The Aquila comparison project: the effects of feedback and numerical methods on simulations of galaxy formation. *Monthly Notices of the RAS*, 423:1726–1749, June 2012. doi: 10.1111/j.1365-2966.2012.20993.x.
- J. Schaye, R. A. Crain, R. G. Bower, M. Furlong, M. Schaller, T. Theuns, C. Dalla Vecchia, C. S. Frenk, I. G. McCarthy, J. C. Helly, A. Jenkins, Y. M. Rosas-Guevara, S. D. M. White, M. Baes, C. M. Booth, P. Camps, J. F. Navarro, Y. Qu,

- A. Rahmati, T. Sawala, P. A. Thomas, and J. Trayford. The EAGLE project: simulating the evolution and assembly of galaxies and their environments. *Monthly Notices of the RAS*, 446:521–554, January 2015. doi: 10.1093/mnras/stu2058.
- M. Schmidt. The Rate of Star Formation. *Astrophysical Journal*, 129:243, March 1959. doi: 10.1086/146614.
- L. Searle. Evidence for Composition Gradients across the Disks of Spiral Galaxies. *Astrophysical Journal*, 168:327, September 1971. doi: 10.1086/151090.
- P. Serra, L. Oser, D. Krajnović, T. Naab, T. Oosterloo, R. Morganti, M. Cappellari, E. Emsellem, L. M. Young, L. Blitz, T. A. Davis, P.-A. Duc, M. Hirschmann, A.-M. Weijmans, K. Alatalo, E. Bayet, M. Bois, F. Bournaud, M. Bureau, A. F. Crocker, R. L. Davies, P. T. de Zeeuw, S. Khochfar, H. Kuntschner, P.-Y. Lablanche, R. M. McDermid, M. Sarzi, and N. Scott. The ATLAS^{3D} project - XXVI. H I discs in real and simulated fast and slow rotators. *Monthly Notices of the RAS*, 444:3388–3407, November 2014. doi: 10.1093/mnras/stt2496.
- J. L. Sersic. *Atlas de Galaxias Australes*. 1968.
- R. Sharp, J. T. Allen, L. M. R. Fogarty, S. M. Croom, L. Cortese, A. W. Green, J. Nielsen, S. N. Richards, N. Scott, E. N. Taylor, L. A. Barnes, A. E. Bauer, M. Birchall, J. Bland-Hawthorn, J. V. Bloom, S. Brough, J. J. Bryant, G. N. Cecil, M. Colless, W. J. Couch, M. J. Drinkwater, S. Driver, C. Foster, M. Goodwin, M. L. P. Gunawardhana, I.-T. Ho, E. J. Hampton, A. M. Hopkins, H. Jones, I. S. Konstantopoulos, J. S. Lawrence, S. K. Leslie, G. F. Lewis, J. Liske, Á. R. López-Sánchez, N. P. F. Lorente, R. McElroy, A. M. Medling, S. Mahajan, J. Mould, Q. Parker, M. B. Pracy, D. Obreschkow, M. S. Owers, A. L. Schaefer, S. M. Sweet, A. D. Thomas, C. Tonini, and C. J. Walcher. The SAMI Galaxy Survey: cubism and covariance, putting round pegs into square holes. *Monthly Notices of the RAS*, 446:1551–1566, January 2015. doi: 10.1093/mnras/stu2055.
- D. Sijacki, V. Springel, T. Di Matteo, and L. Hernquist. A unified model for AGN feedback in cosmological simulations of structure formation. *Monthly Notices of the RAS*, 380:877–900, September 2007. doi: 10.1111/j.1365-2966.2007.12153.x.
- O. K. Sil’chenko, V. V. Vlasyuk, and A. N. Burenkov. Decoupled nuclei and nuclear polar rings in regular spiral galaxies. NGC 2841. *Astronomy and Astrophysics*, 326:941–949, October 1997.
- R. Singh, G. van de Ven, K. Jahnke, M. Lyubenova, J. Falcón-Barroso, J. Alves, R. Cid Fernandes, L. Galbany, R. García-Benito, B. Husemann, R. C. Kennicutt, R. A. Marino, I. Márquez, J. Masegosa, D. Mast, A. Pasquali, S. F. Sánchez, J. Walcher, V. Wild, L. Wisotzki, and B. Ziegler. The nature of LINER galaxies: Ubiquitous hot old stars and rare accreting black holes. *Astronomy and Astrophysics*, 558:A43, October 2013. doi: 10.1051/0004-6361/201322062.

- A. Soltan. Masses of quasars. *Monthly Notices of the RAS*, 200:115–122, July 1982. doi: 10.1093/mnras/200.1.115.
- R. S. Somerville and R. Davé. Physical Models of Galaxy Formation in a Cosmological Framework. *Annual Review of Astron and Astrophys*, 53:51–113, August 2015. doi: 10.1146/annurev-astro-082812-140951.
- D. N. Spergel, R. Bean, O. Doré, M. R.olta, C. L. Bennett, J. Dunkley, G. Hinshaw, N. Jarosik, E. Komatsu, L. Page, H. V. Peiris, L. Verde, M. Halpern, R. S. Hill, A. Kogut, M. Limon, S. S. Meyer, N. Odegard, G. S. Tucker, J. L. Weiland, E. Wollack, and E. L. Wright. Three-Year Wilkinson Microwave Anisotropy Probe (WMAP) Observations: Implications for Cosmology. *Astrophysical Journal, Supplement*, 170:377–408, June 2007. doi: 10.1086/513700.
- V. Springel. The cosmological simulation code GADGET-2. *Monthly Notices of the RAS*, 364:1105–1134, December 2005. doi: 10.1111/j.1365-2966.2005.09655.x.
- V. Springel. E pur si muove: Galilean-invariant cosmological hydrodynamical simulations on a moving mesh. *Monthly Notices of the RAS*, 401:791–851, January 2010a. doi: 10.1111/j.1365-2966.2009.15715.x.
- V. Springel. Smoothed Particle Hydrodynamics in Astrophysics. *Annual Review of Astron and Astrophys*, 48:391–430, September 2010b. doi: 10.1146/annurev-astro-081309-130914.
- V. Springel and L. Hernquist. Cosmological smoothed particle hydrodynamics simulations: a hybrid multiphase model for star formation. *Monthly Notices of the RAS*, 339:289–311, February 2003. doi: 10.1046/j.1365-8711.2003.06206.x.
- V. Springel, T. Di Matteo, and L. Hernquist. Black Holes in Galaxy Mergers: The Formation of Red Elliptical Galaxies. *Astrophysical Journal, Letters*, 620:L79–L82, February 2005a. doi: 10.1086/428772.
- V. Springel, T. Di Matteo, and L. Hernquist. Modelling feedback from stars and black holes in galaxy mergers. *Monthly Notices of the RAS*, 361:776–794, August 2005b. doi: 10.1111/j.1365-2966.2005.09238.x.
- G. Stasińska, N. Vale Asari, R. Cid Fernandes, J. M. Gomes, M. Schlickmann, A. Mateus, W. Schoenell, L. Sodré, Jr., and Seagal Collaboration. Can retired galaxies mimic active galaxies? Clues from the Sloan Digital Sky Survey. *Monthly Notices of the RAS*, 391:L29–L33, November 2008. doi: 10.1111/j.1745-3933.2008.00550.x.
- G. Stinson, A. Seth, N. Katz, J. Wadsley, F. Governato, and T. Quinn. Star formation and feedback in smoothed particle hydrodynamic simulations - I. Isolated galaxies. *Monthly Notices of the RAS*, 373:1074–1090, December 2006. doi: 10.1111/j.1365-2966.2006.11097.x.

- G. S. Stinson, C. Brook, A. V. Macciò, J. Wadsley, T. R. Quinn, and H. M. P. Couchman. Making Galaxies In a Cosmological Context: the need for early stellar feedback. *Monthly Notices of the RAS*, 428:129–140, January 2013. doi: 10.1093/mnras/sts028.
- C. Struck. Galaxy collisions. *Physics Reports*, 321:1–137, 1999. doi: 10.1016/S0370-1573(99)00030-7.
- R. Teyssier. RAMSES: A new N-body and hydrodynamical code. Astrophysics Source Code Library, November 2010.
- B. Tremblay and D. Merritt. Evidence From Intrinsic Shapes for Two Families of Elliptical Galaxies. *Astronomical Journal*, 111:2243, June 1996. doi: 10.1086/117959.
- S. Veilleux and D. E. Osterbrock. Spectral classification of emission-line galaxies. *Astrophysical Journal, Supplement*, 63:295–310, February 1987. doi: 10.1086/191166.
- S. Veilleux, G. Cecil, and J. Bland-Hawthorn. Galactic Winds. *Annual Review of Astron and Astrophys*, 43:769–826, September 2005. doi: 10.1146/annurev.astro.43.072103.150610.
- J. C. Vernaleo and C. S. Reynolds. AGN Feedback and Cooling Flows: Problems with Simple Hydrodynamic Models. *Astrophysical Journal*, 645:83–94, July 2006. doi: 10.1086/504029.
- M. Vogelsberger, S. Genel, V. Springel, P. Torrey, D. Sijacki, D. Xu, G. Snyder, D. Nelson, and L. Hernquist. Introducing the Illustris Project: simulating the coevolution of dark and visible matter in the Universe. *Monthly Notices of the RAS*, 444:1518–1547, October 2014. doi: 10.1093/mnras/stu1536.
- M. Volonteri. Formation of supermassive black holes. *Astronomy and Astrophysics Reviews*, 18:279–315, July 2010. doi: 10.1007/s00159-010-0029-x.
- J. W. Wadsley, J. Stadel, and T. Quinn. Gasoline: a flexible, parallel implementation of TreeSPH. *New Astronomy*, 9:137–158, February 2004. doi: 10.1016/j.newast.2003.08.004.
- A. Wilkinson, R. M. Sharples, R. A. E. Fosbury, and P. T. Wallace. Stellar dynamics of CEN A. *Monthly Notices of the RAS*, 218:297–329, January 1986. doi: 10.1093/mnras/218.2.297.
- S. E. Woosley and T. A. Weaver. The Evolution and Explosion of Massive Stars. II. Explosive Hydrodynamics and Nucleosynthesis. *Astrophysical Journal, Supplement*, 101:181, November 1995. doi: 10.1086/192237.

- X. Wu, O. Gerhard, T. Naab, L. Oser, I. Martinez-Valpuesta, M. Hilz, E. Churazov, and N. Lyskova. The mass and angular momentum distribution of simulated massive early-type galaxies to large radii. *Monthly Notices of the RAS*, 438:2701–2715, March 2014. doi: 10.1093/mnras/stt2415.
- F. Yuan and R. Narayan. Hot Accretion Flows Around Black Holes. *Annual Review of Astron and Astrophys*, 52:529–588, August 2014. doi: 10.1146/annurev-astro-082812-141003.